



The
University
Of
Sheffield.

**The Effects of Composition on the Thermal, Mechanical and
Electrical Properties of Alumino-borosilicate Sealing Glasses for
Solid Oxide Fuel Cell (SOFC) Applications.**

By

Lawan Umar Grema

A thesis submitted for the degree of Doctor of Philosophy

The University of Sheffield

Faculty of Engineering

Department of Materials Science and Engineering

March 2018

Acknowledgements

I would like to start by expressing my sincere thanks to all the individuals who in one way or the other have helped me throughout the period of my PhD programme at the University of Sheffield.

I would like to thank endlessly the effort of my supervisor Prof Russell J Hand whose expertise, guidance, advice and support tremendously lead to the success of my project. I would also like to thank and appreciate the contribution of my secondary supervisor Prof Derek C Sinclair and my appreciation equally goes to Dr Fan for her guidance with the impedance spectroscopy.

My special appreciation goes to the technical staff in the Department of Materials Science and Engineering most especially Dr Lisa Hollands who has helped in melting all of the glasses I used for my PhD.

I most also thank the University of Sheffield for providing the enabling environment for my studies and Tertiary Education Trust Fund (TETFUND) for their financial support for my studies.

In conclusion I would like to appreciate and thank my lovely wife Yagana who accompanies me all along and gave me the necessary support throughout my study. My gratitude also goes to my children who always make me forget all the PhD stresses and be myself and of course to my mother and my late father and to all family members for their moral and financial support.

Abstract

Structural integrity and reliability of sealing materials for planar type solid oxide fuel cells (pSOFCs) is key to attaining the required functionality and subsequent commercialisation of such fuel cells. In this thesis a number of different series of alumino-borosilicate glasses containing alkaline earth modifiers, as well as ZnO and La₂O₃ are studied as potential sealant materials. The glass ceramics derived from these glasses were also studied. Vickers hardness indentation was used to assess the hardness and indentation fracture toughness of these glasses and acoustic measurements were used to determine their moduli. The results reveal a decrease in mechanical properties with modifier additions in all the series except for increasing La₂O₃ in xSi(20-x)La(Sr) with little variation of mechanical properties in the case of xB(15-x)Zn (10BaO-(15-x)ZnO-15La₂O₃-5Al₂O₃-(10+x)B₂O₃-45SiO₂ (X= 2.5, 5, 7.5, 10)) and xSi(20-x)Zn (10BaO-(20-x)ZnO-15La₂O₃-5Al₂O₃-10B₂O₃-(40+x)SiO₂ (X=2.5,5,7.5) mol%) hardness. Electrical conductivity of sealing glasses must be lower than 10⁻⁴ S cm⁻¹ and or > 10⁴Ω cm. Hence the electrical properties the electrical properties of these glasses were measured using impedance spectroscopy and the results indicated that all of the glass and glass ceramic samples studied are electrically resistive and show promise for use as sealing materials. Another important parameter is the thermal properties where the TEC of the sealing glass must be compatible with the other components because differences in TEC of sealing glasses and adjoining SOFC parts result in mismatch and induce thermal stresses during thermal cycling and this may generate cracks through which gas leakages occur. The TEC of xBa(10-x)Al series (10+x)BaO-5ZnO-20SrO-(10-x)Al₂O₃-20B₂O₃-35SiO₂ (X= 0, 2, 3, 4, 5) and some of xBa(40-x)Si samples (15+x)BaO-5ZnO-15La₂O₃-5Al₂O₃-20B₂O₃-(40+x)SiO₂ (X=2.5,5,7.5, 10) have fall within the requirement for sealing glasses. Apart from the TEC the T_g is also a determining factor as to the suitability or otherwise of a sealing glass to be a promising candidate due to the following reasons: (i) thermal stresses develop below the T_g where the glass is brittle therefore the T_g should be as low as possible; (ii) due to high temperature material degradation research efforts are on to reduce the operating temperatures of SOFCs to enhance materials service life and the opportunity for variety of materials selection to construct the SOFCs components. Heat treating series xB(15-x)Zn, xSi(20-x)Zn and xBa(40-x)Si lead to the formation of lanthanum borosilicate single phase. The evolution of these phase lead to not only increased in conductivity as mentioned above but also in the hardness as they are higher in the glass ceramics. However the TEC of the glass

ceramics compared with the parent glasses were slightly lower and its reported in this study that this is a good sign of thermal stability as the TEC did not exhibit the possibility of continues increase.

Table of contents

Acknowledgements.....	ii
Abstract.....	iii
List of Tables.....	viii
Table of figures.....	ix
1. Introduction.....	1
2. Literature review.....	5
2.1 Fuel cells.....	5
2.2 Types of fuel cells.....	7
2.2.1 Proton exchange membrane fuel cell (PEMFC).....	7
2.2.2 Alkaline Fuel Cells (AFC).....	8
2.2.3 Molten Carbonate Fuel Cells (MCFC).....	8
2.2.4 Solid Oxide Fuel Cells (SOFCs).....	8
2.3 Materials used in SOFCs.....	16
2.3.1 Electrolyte.....	16
2.3.2 Anode.....	17
2.3.3 Cathode.....	17
2.3.4 Interconnects.....	18
2.3.5 Sealing of SOFCs.....	20
2.4 Glass and glass-ceramic seals.....	22
2.4.1 Wetting and glass to metal seals.....	22
2.4.2 Bonding of glass to metal seals and coatings.....	24
2.5 Glass formation.....	26
2.5.1 The structural theory of glass formation.....	27
2.5.2 Kinetic theory of glass formation.....	28
2.6 Glass structure.....	28
2.6.1 Structure of silicate glasses.....	29
2.6.2 Structure of borosilicate glasses.....	30
2.6.3 Structure of alumino-silicate glasses.....	32
2.6.4 Modified rules for cation coordination and accepting NBOs in multi-oxide glasses.....	33
2.6.5 The roles of the oxides used in sealing glasses.....	34

2.7	Previously studied sealing glasses	37
2.7.1	Thermal stability requirements of sealing glasses	41
2.7.2	Mechanical properties of sealing glasses	42
2.7.3	Electrical properties of sealing glasses	44
2.7.4	Dielectric constant of sealing glasses.....	49
2.8	Mechanical property structure relationships for glasses	52
3	Experimental procedures	57
3.1	Glass melting	57
3.2	Density measurement.....	58
3.3	XRD analysis	59
3.4	X-ray fluorescence (XRF).....	61
3.5	Thermal analysis	64
3.6	FT-IR spectroscopy.....	65
3.7	Raman spectroscopy	70
3.8	Indentation measurements.....	75
3.9	Acoustic measurement of elastic moduli	77
3.10	Impedance spectroscopy	78
4.	Results 1: Physical, thermal and structural analysis	80
4.1.	Physical, thermal and structural analysis for $x\text{Ba}(40-x)\text{Si}$ series.....	80
4.2	Physical, thermal and structural analysis of $x\text{Ba}(10-x)\text{Al}$ glasses.	88
4.3	Physical, thermal and structural analysis of $x\text{B}(15-x)\text{Zn}$ glasses.	93
4.4	Physical, thermal and structural analysis of $x\text{Si}(20-x)\text{Zn}$ glasses.....	99
4.5	Physical, thermal and structural analysis of $x\text{Si}(20-x)\text{La}(\text{Ba})$ and $x\text{Si}(20-x)\text{La}(\text{Sr})$ glasses.....	104
4.6	Summary and conclusion of results	113
5	Results II: Electrical properties.....	115
5.1	Electrical properties of $x\text{Ba}(40-x)\text{Si}$ glasses and glass ceramics	116
5.2	Electrical properties of $x\text{Ba}(10-x)\text{Al}$ glasses	121
5.3	Electrical properties of $x\text{B}(15-x)\text{Zn}$ glasses and glass ceramics.....	124
5.4	Electrical properties of $x\text{Si}(20-x)\text{Zn}$ glass ceramics	128
5.5	General temperature and frequency dependent behaviour of glass and glass ceramics.....	130
5.6	Discussions of results.....	135
5.7	Summary and Conclusions.....	143

6 Results III: Mechanical properties	145
6.1 Mechanical properties of $x\text{Ba}(40-x)\text{Si}$ glasses.....	145
6.2 Mechanical properties of $x\text{Ba}(10-x)\text{Al}$ glasses.....	147
6.3 Mechanical properties of $x\text{B}(15-x)\text{Zn}$ glasses	149
6.4 Mechanical properties of $x\text{Si}(20-x)\text{Zn}$ glasses.....	151
6.5 Mechanical properties of $x\text{Si}(20-x)\text{La}(\text{Sr})$ glasses.....	152
6.6 Generalised correlations between mechanical properties of glasses.....	153
6.7 Indentation fracture toughness and hardness	155
6.8 Young's modulus and hardness	155
6.9 Brittleness and density	157
6.10 Relationships between fracture toughness, hardness, brittleness and Poisson's ratio	157
6.11 Correlations between mechanical properties and glass network structures	161
6.12 Summary and Conclusions	166
7. Discussion.....	168
7.1 $x\text{Ba}(40-x)\text{Si}$, $x\text{Ba}(10-x)\text{Al}$, $x\text{B}(15-x)\text{Zn}$, $x\text{Si}(20-x)\text{Zn}$, and $x\text{Si}(20-x)\text{La}(\text{Sr})$ glass and glass-ceramics	168
8. Conclusions and recommendation for future work.....	174
8.1 Recommendations for future work	176
References:.....	177
Appendix 1.....	191
Appendix 2.....	192
Appendix 5.....	195
Appendix 6.....	197
Appendix 7.....	198
Appendix 8.....	207

List of Tables

Table 2.1: Summary of fuel cells and their properties (Stambouli and Traversa 2002)	7
Table 2.2: Advantages and disadvantages of tubular and planar SOFC designs (Timurkutluk, Timurkutluk et al. 2016)	13
Table 2.3: Merits and Demerits of cell configurations (Minh 2004)	15
Table 2.4: Materials used in SOFCs and their reasons for selection	19
Table 2.5: Q ⁿ silicate groups and their nomenclature (Eden 2012)	30
Table 2.6: Summary of the oxide functions in glass.....	34
Table 2.7: Additional compositions used as sealants for SOFCs see section 2.7 and 2.7.2 for more details	40
Table 3.1: Nominal molar compositions for all series	58
Table 3.2: Raw materials used for glass batching.....	58
Table 3.3: Bracketed figures represent initial molar batched quantities in mol% and unbracketed numbers are XRF analysed data which is semi quantitative and serve as a guide to compositional error	63
Table 3.4: Comparison between FTIR and Raman spectroscopy (Rehman 2013)	66
Table 3.5: Summary of FTIR assignments	70
Table 3.6: Identified Q ⁿ species (Colomban 2003, Mahapatra, Lu et al. 2009).....	72
Table 3.7: Assignment of Raman peaks.....	75
Table 7.1: Electrical conductivity/resistivity of glasses and glass ceramics in this study and the requirement for SOFC application from the literature	140
Table 7.2: Activation energy for electrical conduction for glasses and glass ceramics produced in this study.....	141
Table 7.3: Electrical properties values for other glasses and glass ceramics in the literature.....	Error! Bookmark not defined.
	Bookmark not defined.

Table of figures

Figure 1-2 Schematic cell arrangement of SOFCs adopted from Mahapatra and Lu (2010)	3
Figure 2-1: Schematic operation activities in a SOFCs unit	11
Figure 2-2:SOFCs designs tubular top and planar bottom adopted from ref. (Timurkutluk, Timurkutluk et al. 2016)	12
Figure 2-3: Types of cell configurations for Planar SOFCs adopted from ref. (Minh 2004)	14
Figure 2-4: Contact angle θ (a) non-wetting (b) wetting adapted from ref (Donald 1993).....	23
Figure 2-5: depolymerisation of silicate glass backbone by a modifier (Na ₂ O)	29
Figure 2-6: Typical Q ⁿ species (a) completely isolated Q ⁰ ; (b) Q ² linked to 2 Q ¹ terminal tetrahedra units, (c) Q ³ linked with Q ¹ terminals and (d) Q ⁴ linked to other tetrahedral units. (Black and blue atoms are bridging and non-bridging oxygens). Adopted and modified from (Edén 2011).....	30
Figure 3 -1: Schematic diagram of X-ray diffraction in crystals	60
Figure 3-2: Schematic drawing of XRF functional structure.....	61
Figure 3-3: DTA graph showing an estimate of T _g (onset) and T _c (crystallization peak maximum).....	64
Figure 3-4: Michelson interferometer used in an IR spectrometer	67
Figure 3-5: Schematic diagram of Raman spectroscopy showing Rayleigh, Stokes and anti-Stokes scattering	71
Figure 3-6: Photograph of a Vicker's hardness indent where d_1 and d_2 are the diagonals of the indent	76
Figure 4-1: Density and molar volume versus Ba/Si ratio in xBa(40-x)Si glasses. For detailed compositions please see table 3.1	80
Figure 4-2:(a) XRD patterns of xBa(40-x)Si glass; (b) XRD patterns of xBa(40-x)Si samples crystallised at 800 °C for xBa(40-x)Si with increasing Ba/Si ratio (c) representative examples of the TEC for glass and glass obtained from TMA for 25BaSi30 exhibiting the differences in TEC and T _g positions in the two samples.....	82
Figure 4-3: DTA curves, (b) TEC of glass (blue line) and glass ceramic (red line) (c) T _g of xBa(40-x)Si glass and glass ceramics versus BaO/SiO ₂ ratio.	84
Figure 4-4: (a) Raman and (b) FTIR spectra for xBa(40-x)Si glasses	86
Figure 4-5: Deconvolution of (a) the silica unit (800-1200 cm ⁻¹) and (b) borate group (1250-1600 cm ⁻¹)	87
Figure 4-6: Area% of (a) Q ⁿ species and, (b) Boron species. (c) Raman and FTIR peak shift (RPS,FPS) of Si-O stretching unit and (d) polymerisation index for xBa(40-x)Si glasses.	88
Figure 4-7: (a) molar volume and (b) XRD patterns for xBa(10-x)Al glasses.	90
Figure 4-8: (a) DTA curves, (b) TEC and T _g of xBa(10-x)Al glasses	90
Figure 4-9: (a) Raman and (b) FTIR spectra for xBa(10-x)Al glasses.	92
Figure 4-10: Area% of (a) Si Q ⁿ species and, (b) boron species (c) Raman and FTIR peak shift (RPS, FPS) of Si-O stretching unit and (d) polymerisation index for xBa(10-x)Al glasses.	93
Figure 4-11: Density and molar volume change versus ZnO/B ₂ O ₃ ratio of xB(15-x)Zn.....	94
Figure 4-12: XRD pattern of xB(15-x)Zn (a) Glass and single phase crystalline during pouring (b) single phase crystalline at 800°C for 50hr for xB(15-x)Zn glasses.	95
Figure 4-13: (a) DTA curves, (b) TEC of glass (blue line) and glass ceramic (red line) (c) T _g of xB(15-x)Zn glass and glass ceramics.....	96
Figure 4-14: (a) Raman (b) FTIR spectra for xB(15-x)Zn glasses	98
Figure 4-15: Fraction of (a) Q ⁿ species and, (b) boron species, (c) Raman and FTIR peak shift (RPS, FPS) of Si-O stretching unit and (d) polymerisation index for xB(15-x)Zn glasses.....	99
Figure 4-16: Density and molar volume versus ZnO/SiO ₂ ratio of xSi(20-x)Zn glasses.....	100

Figure 4-17: XRD patterns of xSi(20-x)Zn (a) glasses and (b) glass ceramics	101
Figure 4-18: (a) DTA curves, (b) TEC of glass (blue data) and glass ceramic (red data) (c) T _g of xSi(20-x)Zn glasses and glass ceramics.....	102
Figure 4-19: (a) Raman and (b) FTIR Spectra of xSi(20-x)Zn glasses.....	103
Figure 4-20: Fraction of (a) Q ⁿ species and, (b) boron species, (c) Raman and FTIR peak shift of Si-O stretching unit and (d) polymerisation index of xSi(20-x)Zn glasses	104
Figure 4-21: (a) Density and (b) molar volume of xSi(20-x)La(Ba) blue line and xSi(20-x)La(Sr) red line glasses versus La ₂ O ₃ /SiO ₂ ratio.....	104
Figure 4-22: XRD patterns of un-dissolved quartz SiO ₂ PDF: no (01-085-1054) for crystalline part of xSi(20-x)La(Ba)4 with other amorphous samples (a) and (b) Amorphous xSi(20-x)La(Sr) series with increasing La/Si ratio	107
Figure 4-23: XRD patterns of apatite type lanthanum silicates (La _{9.33} Si ₆ O ₂₆) PDF 00-049-0443 and (b) Raman spectra of the same phase for 20LaSi40(Ba) and 20LaSi30(Sr) mol% with La/Si ratio 1:2 and 1:1.5 respectively. (c) Raman spectra of thermally treated xBa(40-x)Si, xB(15-x)Zn and xSi(20-x)Zn glasses showing the presence of lanthanum silicate boron oxide (La ₃ (Si ₂ O ₄) ₂ BO ₂).....	108
Figure 4-24: DTA curves (a) xSi(20-x)La(Ba) and (b) xSi(20-x)La(Sr)	109
Figure 4-25: Raman (b) FTIR spectra of xSi(20-x)La(Ba) glasses; (c) Raman and (d) FTIR spectra of xSi(20-x)La(Sr) glasses.....	110
Figure 4-26: Thermal stability plotted against (a) total divalent modifiers/total network formers and (b) total trivalent modifiers/ total network formers for all glass series.....	111
Figure 4-27: Fraction of Q ⁿ species (a) xSi(20-x)La(Ba), (b) xSi(20-x)La(Sr) and (c) polymerisation index for both xSi(20-x)La(Ba) blue line and xSi(20-x)La(Sr) glasses in red line	112
Figure 4-28: Area% of boron species (a) xSi(20-x)La(Ba) and (b) xSi(20-x)La(Sr) glasses.	113
Figure 5-1: Variation of conductivity with temperature and composition for (a) xBa(40-x)Si glasses (b) xBa(40-x)Si glass ceramics and (c) variation of activation energy for electrical conductivity (E _a) versus BaO/SiO ₂ for xBa(40-x)Si glasses blue line and glass ceramic red line.....	116
Figure 5-2: Frequency dependence of the dielectric constant of (a) xBa(40-x)Si glasses (b) xBa(40-x)Si glass ceramics and frequency dependence of the tangent loss of (c) xBa(40-x)Si glasses (d) xBa(40-x)Si glass ceramics. Measurement conditions 600±3°C and between 1 kHz to 1MHz. (Lines are guide to the eye).....	118
Figure 5-3: Conductivity (a) and dielectric constant (b) of xBa(40-x)Si glass and glass-ceramics versus total divalent modifier/total network formers. (c) Conductivity versus average Q ⁿ /N of xBa(40-x)Si series. Measurement conditions 600±3°C and between 1 kHz to 1MHz	119
Figure 5-4: Variation of conductivity with temperature and compositions for xBa(10-x)Al glasses (b) activation energies (E _a) for conductivity for xBa(10-x)Al glasses as a function of increasing BaO/Al ₂ O ₃ ratio	121
Figure 5-5: Frequency dependence for xBa(10-x)Al glasses of (a) the dielectric constant (b) tangent loss. Measurement conditions 600±3°C and between 1 kHz to 1MHz.	122
Figure 5-6: (a) Conductivity and (b) dielectric constant of xBa(10-x)Al glasses versus total divalent modifiers/total network formers. (c) Conductivity versus average Q ⁿ /N for xBa(10-x)Al glasses. Measurement conditions 600±3°C and between 1 kHz to 1MHz	123
Figure 5-8: Frequency dependence of the dielectric constant of xB(15-x)Zn (a) glasses and (b) glass-ceramics. Frequency dependence of the tangent loss of xB(15-x)Zn (c) glasses and (d) glass-ceramics. Measurement conditions 600±3°C and between 1 kHz to 1MHz	126

Figure 5-9: (a) Conductivity and (b) dielectric constant of $x\text{B}(15-x)\text{Zn}$ glasses and glass-ceramics versus total divalent modifier/total network formers. (c) Conductivity versus average Q^{p}/N for $x\text{B}(15-x)\text{Zn}$ series. Measurement conditions $600\pm 3^{\circ}\text{C}$ and between 1 kHz to 1MHz.	127
Figure 5-10: (a) Variation of conductivity with temperature and composition of $x\text{Si}(20-x)\text{Zn}$ glass ceramics; (b) variation of activation energies (E_a) as a function of increasing ZnO and frequency dependence of (c) dielectric constant and (d) tangent loss . Measurement conditions $600\pm 3^{\circ}\text{C}$ and between 1 kHz to 1MHz.	128
Figure 5-11: (a) Conductivity and (b) dielectric constant of $x\text{Si}(20-x)\text{Zn}$ glass ceramics versus total divalent modifier/total network formers. (c) Conductivity versus average Q^{p}/N of $x\text{Si}(20-x)\text{Zn}$ series. Measurement conditions $600\pm 3^{\circ}\text{C}$ and between 1 KHz to 1MHz	129
Figure 5-12: The temperature and frequency dependence of electrical conductivity of 25BaSi30 mol% (a) glass and (b) glass-ceramic. Dielectric constant (c) glass (d) glass-ceramic, Tangent loss (e) glass and (f) glass-ceramic.....	132
Figure 5-13: (a) Activation energy and (b) conductivity of $x\text{Ba}(40-x)\text{Si}$, $x\text{Ba}(10-x)\text{Al}$ glasses, and (c) Activation energy of $x\text{B}(15-x)\text{Zn}$ and (d) conductivity of $x\text{B}(15-x)\text{Zn}$ glasses all versus site separation (atom –atom distance)	133
Figure 5-14: Decreases in site separation and polaron radii versus total large size oxides for (a) $x\text{Ba}(40-x)\text{Si}$ glasses (b) $x\text{Ba}(10-x)\text{Al}$ glasses, and (c) $x\text{B}(15-x)\text{Zn}$ glasses.....	135
Figure 6-1: Hardness of glass blue line and glass ceramic red line (a) Indentation fracture toughness (b) Young's modulus (d) Brittleness and (e) Poisson's ratio of $x\text{Ba}(40-x)\text{Si}$ versus BaO/total network formers	145
Figure 6-2: Hardness (a) Indentation fracture toughness (b) Young's modulus (d) Brittleness and (e) Poisson's ratio of $x\text{Ba}(10-x)\text{Al}$ versus BaO/total network formers	147
Figure 6-3: Hardness of glass blue line and glass ceramic red line (a) Indentation fracture toughness (b) Young's modulus (d) Brittleness and (e) Poisson's ratio of $x\text{B}(15-x)\text{Zn}$ glasses versus ZnO/total network formers	149
Figure 6-4: Hardness of glass and glass ceramic (a) Indentation fracture toughness (b) Young's modulus (d) Brittleness and (e) Poisson's ratio of $x\text{Si}(20-x)\text{Zn}$ versus ZnO/total network formers	151
Figure 6-5: Hardness (a) Indentation fracture toughness (b) Young's modulus (d) Brittleness and (e) Poisson's ratio of $x\text{Si}(20-x)\text{La}(\text{Sr})$ versus La_2O_3 /total network formers.	152
Figure 6-6: Indentation fracture toughness versus Young's modulus (a) this study (b) this study compared with literature; Indentation fracture toughness versus hardness (c) this study and (d) this study compared with literature; Hardness versus Young's modulus (e) this study and (f) this study compared with literature.	154
Figure 6-7: (a) Brittleness versus density and (b) brittleness versus Poisson's ratio.	156
Figure 6-8: Indentation fracture toughness of (a) and hardness (b) of $x\text{B}(15-x)\text{Zn}$, $x\text{Si}(20-x)\text{Zn}$, $x\text{Ba}(40-x)\text{Si}$, $x\text{Ba}(10-x)\text{Al}$ glasses and for $x\text{Si}(20-x)\text{La}(\text{Sr})$ in (c) and (d) versus Poisson's ratio.	159
Figure 6-9: (a) Poisson's ratio versus atomic packing density, (b) E/H versus Poisson's ratio, showing the cracking mode for different oxide glasses;	160
Figure 6-10: (a) Poisson's ratio (b) brittleness of $x\text{B}(15-x)\text{Zn}$, $x\text{Si}(20-x)\text{Zn}$ $x\text{Ba}(40-x)\text{Si}$ and $x\text{Ba}(10-x)\text{Al}$ (c) and (d) for $x\text{Si}(20-x)\text{La}(\text{Sr})$ versus the ratio of Q^{p}/N species.	161
Figure 6-11: Indentation fracture toughness (a) hardness (b) of $x\text{B}(15-x)\text{Zn}$, $x\text{Si}(20-x)\text{Zn}$, $x\text{Ba}(10-x)\text{Al}$ and $x\text{Ba}(40-x)\text{Si}$ and for $x\text{Si}(20-x)\text{La}(\text{Sr})$ (c) K_{Ic} (d) hardness. (e) E of $x\text{B}(15-x)\text{Zn}$, $x\text{Si}(20-x)\text{Zn}$, $x\text{Ba}(10-x)\text{Al}$ and $x\text{Ba}(40-x)\text{Si}$ (f) E of $x\text{Si}(20-x)\text{La}(\text{Sr})$ versus averaged Q^{p}/N species	163

Figure 6-12: (a) E and (b) H versus T_g (c) hardness and (d) indentation fracture toughness versus density for $x\text{B}(15-x)\text{Zn}$, $x\text{Si}(20-x)\text{Zn}$, $x\text{Ba}(40-x)\text{Si}$ and $x\text{Ba}(10-x)\text{Al}$ glasses. (e) H and (f) indentation fracture toughness versus density for $x\text{Si}(20-x)\text{La}(\text{Sr})$ glasses..... 165

1. Introduction

Solid oxide fuel cells (SOFCs) are devices which convert chemical energy into electrical energy through chemical reactions with higher efficiency than conventional thermal energy conversion systems (Zhao and Malzbender 2013, Malzbender, Zhao et al. 2014). SOFCs have a self-reformation ability (see section 2.3.2 for more details) coupled with fuel flexibility (Ghosh, Kundu et al. 2008, Wang, Wang et al. 2009), such as the use of hydrocarbon and municipal waste (Mahato, Banerjee et al. 2015) and are environmentally friendly (Laorodphan, Namwong et al. 2009) and are therefore an option to help achieve CO₂ reduction targets (Ohara, Mukai et al. 2001). SOFCs operate at high temperatures (600-1000 °C) (Laorodphan, Namwong et al. 2009, Chang, Lin et al. 2010, Chang, Lin et al. 2011), in an oxidizing, reducing and humid environment (Wang, Lu et al. 2007). The required minimum service life for mobile and stationary applications are 5000 h and 50000 h respectively (Coillot, Méar et al. 2012). Recent reports indicates that more than 75000 h service can be exceeded for stationary applications (Rodríguez-López, Wei et al. 2017). There are two popular designs named according to the cell stacking arrangement; planar or tubular (Reis and Brow 2006, Laorodphan, Namwong et al. 2009, Chang, Lin et al. 2010, Chang, Lin et al. 2011, Zhao and Malzbender 2013, Malzbender, Zhao et al. 2014). Planar SOFCs are preferred over tubular ones due to a simpler manufacturing process and higher current outputs as planar SOFCs have a shorter current path (Reis and Brow 2006, Wang, Lu et al. 2007). The problem with the design of planar SOFCs is that it requires hermetic sealing to function (Chang, Lin et al. 2010, Chang, Lin et al. 2011) and the hermetic sealing of the electrodes, electrolytes and metallic interconnects remains a key challenge for pSOFCs (Sun, Xiao et al. 2010). Critical sealing positions in a pSOFCs are the inlets and outlets of both anode and cathode to prevent the fuel and oxidants mixing (Wang, Wang et al. 2009, Sasmal, Garai et al. 2014). To generate high voltages cells are stacked in series (Larsen and James 1998); a single cell consists of a dense electrolyte, porous anode and cathode made of nickel zirconia cermet and doped lanthanum manganite perovskite (Kaur, Pandey et al. 2014) as shown in fig (1-1). The commercialization of pSOFCs depends on the reliability of the sealants (Zhao and Malzbender 2013, Malzbender, Zhao et al. 2014), which must meet a set of requirements such as gas tightness, high temperature stability, chemical stability and compatibility, mechanical integrity, electrical insulation and thermal expansion tailored to match that of other components of the SOFCs (Hsiu-Tao Chang 2009, Wang, Wang et al. 2009). Glass

and glass-ceramics are the most commonly used sealing materials because glass based sealants are cheaper and much better than metallic sealants in terms of resistance to dual atmospheres and can be tailored compositionally to meet most of the sealing requirements with glass based sealants also having the advantage of better wetting to sealing interfaces (Zhao, Malzbender et al. 2011, Zhao and Malzbender 2013, Malzbender, Zhao et al. 2014). Seals used in the SOFCs are produced by tape casting or screen printing and can also be applied in form of a paste containing dispersed powder (Zhao and Malzbender 2013, Malzbender, Zhao et al. 2014).

Two important criteria for the selection of a sealant are the glass transition temperature (T_g) which must be below the operating temperatures of the SOFCs (Chang, Lin et al. 2009, Zhao and Malzbender 2013, Malzbender, Zhao et al. 2014), and the thermal expansion coefficient (TEC) which must closely match the TEC of other cell components to avoid thermal stresses due to mismatch (Chang, Lin et al. 2009). The T_g must not be higher than the operating temperature of the fuel cells as this will subject the other components of the fuel cells to thermal degradation or burnout of substances during sealing and because the glass will not soften below its T_g it is susceptible to cracking as a result of TEC mismatch which is more pronounced below the T_g (Fergus 2005, Kaur, Pandey et al. 2014). Other relevant thermal properties include the glass viscosity during sealing of about 10^6 PaS to avoid wicking and the softening temperature T_s (Lessing 2007). The softening point is viscosity dependent and depicts the flow characteristics of the glass (Fergus 2005). The viscosity at T_g and T_s are $10^{11.3}$ and 10^9 Pa S respectively and to provide effective hermetic sealing at the operating temperature the viscosity of sealing glasses must be $> 10^9$ Pa S (Mahapatra and Lu 2010). A brief highlight will be presented here about the types of different sealants their advantages and drawbacks as follows. Majority of the glass and glass ceramic compositions are alkali or alkaline earth containing aluminosilicates, borosilicates, borate and phosphate based glasses (Larsen, Poulsen et al. 1999, Tulyaganov, Reddy et al. 2013). Compositions based on alkali silicates are not suitable due to reaction of the alkalis with the SOFC components as they form volatile species (oxides) and also some stable hydroxides and carbonates leading to chromium poisoning (Fergus 2005, Ghosh, Sharma et al. 2008). A lot of researchers have focused on aluminosilicate glasses with high barium between 30-35mol% with the well-known consequences of deleterious $BaCrO_4$ formation especially with the chromium containing metallic interconnect and this phase have high TEC compared with other SOFC components and hence leading to seal separation (Yang, Stevenson et al. 2003). Glass

compositions with boron as the sole network former is prone to weight loss of about 20% in humid environment of the fuel cell and equally reacts with SOFC parts in both oxidizing and reducing conditions (Tulyaganov, Reddy et al. 2013). P_2O_5 based glasses also are not suitable for use as sealing glasses due their volatility at the fuel cell operating conditions(Larsen, Poulsen et al. 1999). There are a lot of studies on different glass and glass-ceramic systems for SOFCs applications, out of which silica and boron containing alkaline earth systems are identified as the most preferred and the reasons why they are promising are discussed in chapter 2 and in sections 2.7 for more details

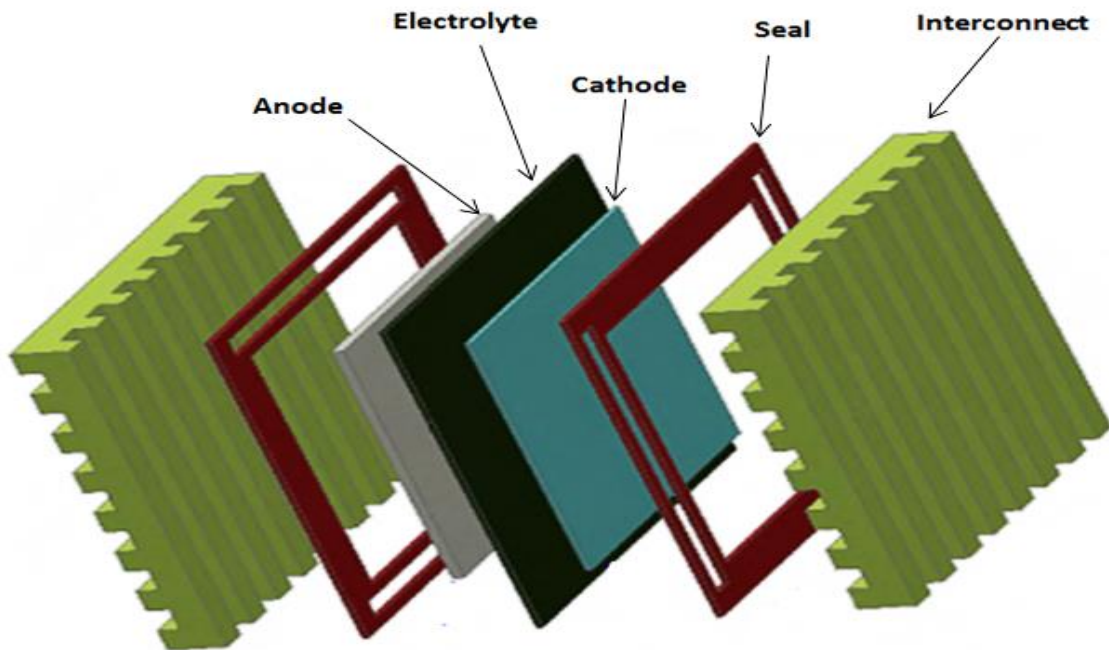


Figure 1-1 Schematic cell arrangement of SOFCs adopted from Mahapatra and Lu (2010)

In this thesis, after this Introduction chapter, a Literature Review chapter is presented in which thermal, mechanical and electrical properties of sealing glasses are examined in terms of the provided structure-property information from the literature. The experimental procedures chapter details sample preparation and measurement techniques use to assess thermal, mechanical

electrical properties such as differential thermal analysis (DTA), Vicker's hardness, indentation fracture toughness and elastic moduli as well as impedance spectroscopy.

The Results chapter presents the results obtained for six different glass series ($x\text{B}(15-x)\text{Zn}$, $x\text{Si}(20-x)\text{Zn}$, $x\text{Ba}(40-x)\text{Si}$, $x\text{Ba}(10-x)\text{Al}$, $x\text{Si}(20-x)\text{La}(\text{Ba})$ and $x\text{Si}(20-x)\text{La}(\text{Sr})$) that were produced in these experimental works; for detailed compositions see experimental procedure under item 3. All of these samples were characterised for structural properties and the mechanical properties of the glasses except $x\text{Si}(20-x)\text{La}(\text{Ba})$ glasses were obtained. And then follows the electrical properties of $x\text{B}(15-x)\text{Zn}$ and $x\text{Ba}(40-x)\text{Si}$ samples as both glass and glass ceramics, $x\text{Si}(20-x)\text{Zn}$ as glass-ceramics and $x\text{Ba}(10-x)\text{Al}$ as glasses.

The experimental findings of all the different glass series were assessed in detail, and any possible links between different properties are explored along with other literature data in the Results and Discussion chapter. Finally, Conclusions and Recommendations for Future Works are presented and appendixes of the raw data attached at the end of the thesis with comparisons to other data in the literature where necessary.

The objectives of the work described in this thesis are;

- Characterisation of the thermal properties of the samples relevant to SOFCs sealing applications typically the (T_g and TEC).
- Measurement of the electrical and other physical properties and how they relate to SOFCs applications.
- Assessment of the mechanical properties of produced glasses to gain insight into structural integrity especially at room temperature where the glass and glass ceramics are most brittle since stresses are only relieved at the operating temperatures above T_g .

2. Literature review

This chapter will present the required background to understand SOFCs and parameters such as the types of fuel cells and materials used for the construction of SOFCs, including the different components including the sealants which are the main focus of this study and the principle of operations and different designs for SOFCs. The available sealing technologies and the effect of compositions on key sealant properties mainly thermal, mechanical and electrical properties relevant to sealing glasses are also considered.

2.1 Fuel cells.

Present day fuel cells are derived from the work of Sir William Groves in 1839, although his cell setup did nothing more than to deflect a galvanometer it served as a starting point for the development of fuel cells (Yeager 1961). The most advanced fuel cell is the hydrogen-oxygen type (Yeager 1961, Garland, Papageorgopoulos et al. 2012). And up to date hydrogen is the most preferred fuel gas for the SOFCs due to its high efficiency compared to conventional fuel to power converters (Zhu and Deevi 2003, Haseli 2018). In a broader perspective fuel is considered to be any anodic reactant in a battery. Originally the term fuel cells was used for an electrochemical cell that used low-cost fuels but in recent times electrochemical cells that consumes high cost fuels have been included in the definition of fuel cell (Yeager 1961). A common feature of fuel cells is that they never store large amounts of the electrode reactants but rather the reactants are fed continuously into the system as they are consumed; therefore only a small quantity of reactant is present within the cell at a given time. Most fuel cells use pure oxygen or air as oxidizing agents, others oxidizers such as halogen gases are not usually used due to high cost and compared to oxygen they are not easy to handle (Yeager 1961).

Fuel cells can be likened to flash light battery cells with the difference that in battery cells the fuel and the oxidant are stored within the cell, while for fuel cells fuel is stored outside the setup and supplied to it when required and so fuel cells can simply be referred to as continuous feed primary batteries (Friauf 1961). The efficiencies of the different types of fuel cells are given in table 2.1 with SOFCs and Protonic ceramic fuel cells have efficiencies of between 45-60% at the operating temperature.

Types of fuel cell	electrolyte	Operating T	Fuel	Oxidant	Efficiency
Alkaline (AFC)	Potassium hydroxide (KOH)	50-200°C	Pure hydrogen or hydrazine	O ₂ /Air	50-55%
Direct methanol (DMFC)	Polymer	60-200°C	Liquid methanol	O ₂ /Air	40-55%
Phosphoric acid (PAFC)	Phosphoric acid	160-210°C	Hydrogen from hydrocarbons and alcohol	O ₂ /Air	40-50%
Sulfuric acid (SAFC)	Sulfuric acid	80-90°C	Alcohol or impure hydrogen	O ₂ /Air	40-50%
Proton exchange membrane (PEMFC)	Polymer, proton exchange membrane	50-80°C	Less pure hydrogen from hydrogen or methanol	O ₂ /Air	40-50%
Molten carbonate (MCFC)	Molten salt such as nitrate, sulphate, carbonates	630-650°C	Hydrogen, carbon monoxide, natural gas, propane, marine diesel	CO ₂ /O ₂ /Air	50-60%
Solid Oxide (SOFC)	Stabilized zirconia ceramic and doped perovskite	600-1000°C	Natural gas or propane	O ₂ /Air	45-60%

Protonic ceramic (PCFC)	Thin membrane of barium cerium oxide	600-700°C	hydrocarbons	O ₂ /Air	45-60%
-------------------------	--------------------------------------	-----------	--------------	---------------------	--------

Table 2.1: Summary of fuel cells and their properties (Stambouli and Traversa 2002)

2.2 Types of fuel cells.

Classifications of fuel cells are generally based on the type of electrolyte used as the medium for ionic conduction within the cell as summarised in table 2.1 above. The first five in the table are associated with low to medium operating temperature between 50-210°C and have relatively low efficiency 40-50% in terms of electrical generations especially when run on methanol or hydrocarbon and efficiency can reach 50% with pure hydrogen as the fuel. The remaining three types on the list table 2.1 operate at high temperatures between 600-1000°C and can utilize methane directly in the fuel cell and exhibit efficiency of 45-60% when natural gas is used as fuel and the ability for heat recovery. Out of the list of fuel cells proton exchange membrane fuel cell and solid oxide fuel cell have received growing interest from researchers as they are suitable for cars and mass transportation and in the case of SOFC for domestic applications (Stambouli and Traversa 2002, Mahato, Banerjee et al. 2015).

Based on their electrolyte type and the temperature of operation the following types of fuel cells will be briefly discussed and advantages or drawbacks will be highlighted.

- i) Proton exchange membrane fuel cell (PEMFC)
- ii) Alkaline fuel cells (AFC)
- iii) Molten Carbonate fuel cell (MCFC)
- iv) Solid oxide fuel cell (SOFC).

2.2.1 Proton exchange membrane fuel cell (PEMFC)

Proton exchange membrane fuel cells (PEMFCs) have a high power density and run at low temperatures (50-80°C) with a very quick start-up and shutdown. However, their use is restricted to research and demonstrations due to poor reliability and cost issues which have hindered commercialization (Wang, Chen et al. 2011). In PEMFCs the electrolyte is a solid polymer that

allows proton transfer. These ionic polymers only have the ability to transfer proton in the moist state and not in the dry conditions, and their ionic conductivity increases with increasing water content; their gel-like polymeric structures carry fixed positive and negative charges (Peighamardoust, Rowshanzamir et al. 2010). Protons migrate from the anode to the cathode via the dense proton exchange membrane and the catalytic oxidation of hydrogen produces the protons (Bose, Kuila et al. 2011).

2.2.2 Alkaline Fuel Cells (AFC)

AFCs are seen as an alternative to PEMFCs because they are cost effective as they need no expensive electrolytes or noble metal catalyst (Schulze and Gülzow 2004). AFCs operate on the basis of alkaline water electrolysis and are low temperature devices with high electrical efficiency. The major problem with AFCs is the intolerance of the alkaline electrolyte to CO₂ (Kohnke 2011). AFCs have high electrical efficiency and are easy to handle with good suitability for alternating loads (Gülzow 2004). The advantage of AFCs compared to polymer electrolyte fuel cells is that liquid fuels such as ammonia can be used (Gülzow 2004).

2.2.3 Molten Carbonate Fuel Cells (MCFC).

Molten carbonate is used as the electrolyte for this system and operates above 600 °C (Antolini 2011, Nguyen, Song et al. 2012). MCFCs have become more attractive for power generation due to their resistance to some fuel impurities and the ability to utilize the fuel impurity gases such as CO₂ and CO as a source of fuel particularly from a hot flue source (Nguyen, Song et al. 2012). The electrolyte is contained in a beta-alumina ceramic matrix. The other components MCFCs are a porous anode as the fuel electrode and a porous cathode as the oxidant electrode. The cell is operated at an atmospheric pressure between, 1-10N m². And the fuels used are H₂ and CO while the oxidants are O₂ and CO₂ (Antolini 2011).

2.2.4 Solid Oxide Fuel Cells (SOFCs)

Solid oxide fuel cells as explained in chapter one are electrochemical devices which convert the chemical energy stored in gaseous fuels such as CO or CH₄ directly into electrical energy, together with some heat generation by electrochemical combination of fuels with an oxidant from air. For optimal operation of SOFCs several materials' requirements must be met which include (i) acceptable electrical properties such as high oxygen-ionic conduction and low

electronic conduction in the electrolyte and mixed type conductivity for the electrodes (anode and cathode) (ii) chemical and structural stability during operation under oxidizing and reducing atmosphere (iii) low reactivity and inter diffusion of elements between components (iv) and TEC compatibility between components working together (Knauth and Tuller 2002). For the stationary applications a number of small size 1-25kW cells have been constructed and test run for few thousand hours by several organisations, however such runs have not been a complete success basically due to lack of robust glass seals (Singhal 2002).

2.2.4.1 Advantages of fuel cells

The use of fuel cells in power generation has some advantages over the conventional power generation systems. Fuel cells have the advantages of direct conversion of chemical energy into electrical energy and unlike conventional power generation systems intermediate combustion losses are avoided. Fuel cells thus have the potential for increased electrical efficiency. Noise pollution is minimal because of lack of moving parts in the fuel cells set up and low emissions of pollutants. They have the potential to be used in a range of applications since their efficiency is size independent. The major areas of applications to date are both mobile and stationary (domestic and industrial in which heat and electrical energies are required) (Minh 1993, Singhal 2002).

2.2.4.2 Advantages and challenges of SOFCs compared with other fuel cells

The different types of fuel cells presented in table 2.1 and section 2.2 and from the table the different fuel cells can be subdivided into low and high temperature fuel cells. Among all the different types of fuel cells SOFCs are most preferred due their cost effectiveness, fuel flexibility and high energy conversion efficiency coupled with heat recovery and combined power generation. SOFCs are used for residential and auxiliary power units and also in industrial energy supplies (Mahapatra and Lu 2010, Huang, Xie et al. 2012). Other specific advantages of SOFCs includes modular construction and lower emission of pollutants, the use of solid ceramic materials and the non-inclusion of liquids as electrolytes prevents corrosion and electrolyte management problems. The use of high operating temperatures (>600°C) enhance rapid reaction kinetics, enables reformation of hydrocarbon fuel (internal reforming) within the fuel cells rather than requiring an expensive external reformer (Singhal 2002). SOFCs generates high quality byproducts in form of heat for co-generation, thus these advantages suggest that SOFCs can be

simple and more efficient compared to other technologies. In addition SOFC being completely solid gives room for thin layer fabrication of its ceramic components and can be configured into desired shapes not possible in fuel cells that have liquid electrolytes (Minh 1993).

Despite the advantages enumerated above SOFCs have some drawbacks which need to be solved in order to get the full potential of the system. The most commonly used electrolyte in conventional SOFC is the yttria stabilized zirconia (YSZ) whose ion conduction efficiency is only achieved at very high temperatures $\geq 800^{\circ}\text{C}$; this very high temperature also impedes commercialisation of the SOFCs with particular concern about materials degradation and cost. Reducing the operating temperature offers the advantages of selecting wider range of cheaper materials for SOFCs construction (Huang, Xie et al. 2012). Another critical area that also hinders the commercialisation of pSOFCs has to do with lack of robust sealant, although a substantial working time ≥ 75000 h has been successfully surpassed, the issue of long term reliability and stability of the SOFCs materials and components still needs to be addressed (Rodríguez-López, Wei et al. 2017). To address the issue of hermetic sealing different sealing materials including metals have previously been used. Among all the sealing materials the choice of glass and glass ceramics as a sealants stand out to be most favourable of sealing materials for pSOFCs. However the brittle nature of glass and glass ceramics makes such seals susceptible to cracking as a result of stresses induced during thermal cycling. Studies using finite element indicates the presence of a high stress level of 43MPa under operating conditions which is enough to initiate cracks over time leading to a loss of gas tightness and stack performance efficiency (Rodríguez-López, Wei et al. 2017).

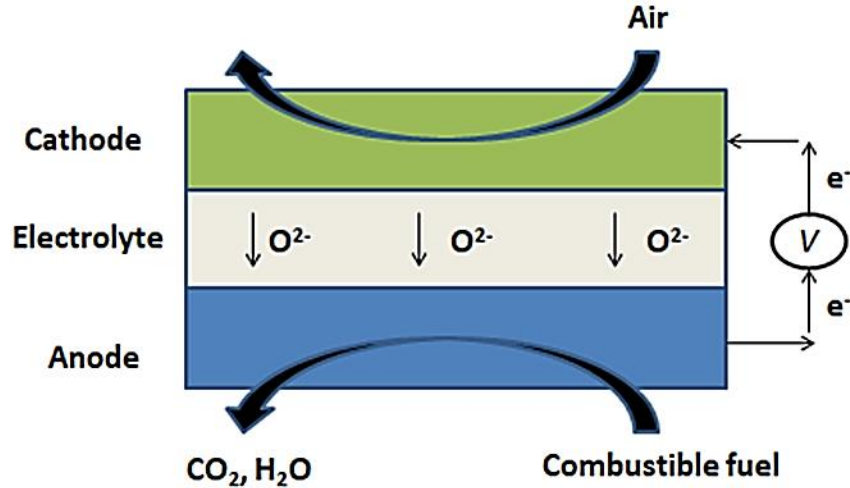


Figure 2-1: Schematic operation activities in a SOFCs unit

Fig 2-1 presents a schematic of the operation of a SOFC. The operating temperature for SOFCs depends on how high a temperature is required to achieve high ionic conduction in the electrolyte; for the most common electrolyte, YSZ, the operating temperature should be higher than 973K (McIntosh and Gorte 2004, Sun and Stimming 2007). SOFCs are also classified according to their operating temperature as low 500-700°C, intermediate 700-900°C and high temperature 900-1000°C (Timurkutluk, Timurkutluk et al. 2016).

During the operation of the SOFCs oxygen molecules in the cathode get reduced to anions by electrons flowing from the external circuit.



The oxygen anion migrates to the anode via oxygen vacancies in the electrolyte due to differences in potential and concentration and oxidise the fuel according to



Electrons released as a result of the reaction above moves through the external connection to the cathode to complete the circuit. The anode catalyses the oxidation reaction and remains ionically and electronically conductive (McIntosh and Gorte 2004, Sun and Stimming 2007).

SOFCs (see fig 2-2) have two basic stack designs – planar and tubular stacks with the former preferred over the later due to a simpler manufacturing process and a higher power density per volume. The challenge for planar SOFCs is that they require high temperature sealing to function while this is not requirement for tubular designs (Fergus 2005, Reis and Brow 2006, Wang, Lu et al. 2007). The state of the art design is a planar anode supported SOFC used for intermediate temperature and this design replaces high cost ceramic interconnects with low cost metallic ones (Ghosh, Kundu et al. 2008, Ghosh, Sharma et al. 2010, Luo, Lin et al. 2015). To date neither planar nor tubular designs have met the requirement for mobile applications because such applications require short start-up times and high performance in a limited space. Despite the high power density attainable in planar SOFCs they are not structurally able to withstand the high heating/cooling rates required in mobile applications and while the tubular design is thermally stable due to its circular symmetry it has a low power (Timurkutluk, Timurkutluk et al. 2016). Table (2.2) gives a summary of the advantages and disadvantages for both planar and tubular SOFCs designs.

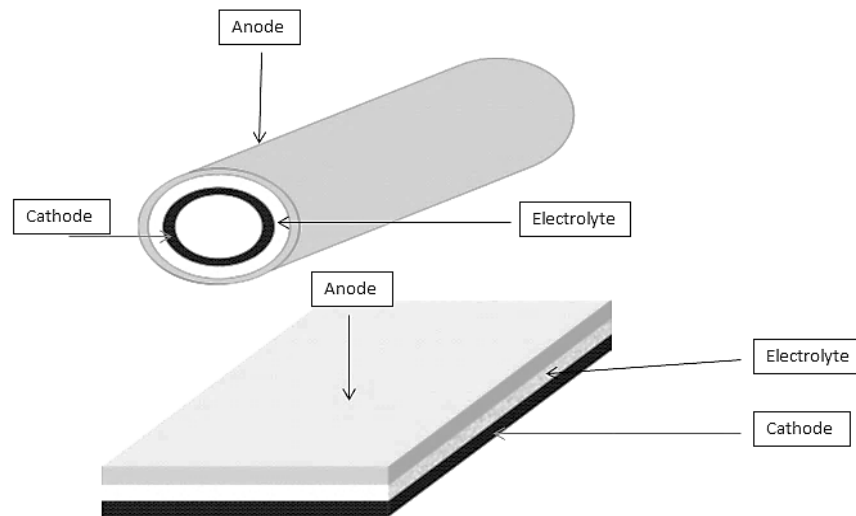


Figure 2-2:SOFCs designs tubular top and planar bottom adopted from ref. (Timurkutluk, Timurkutluk et al. 2016)

Property	Tubular	Planar
Power density	Low (0.20-0.25W/cm ²)	High (2W/cm ²)
Volumetric power density	Low	High
High temperature sealing	Easy	Difficult
Start-up and shut-down time	Fast	Slow
Interconnector fabrication	Difficult	Expensive
Fabrication cost	High	Low
Thermal cycle stability	High	Low

Table 2.2: Advantages and disadvantages of tubular and planar SOFC designs (Timurkutluk, Timurkutluk et al. 2016)

2.2.4.3 Tubular design.

The tubular shaped design has been developed by Siemens Westinghouse Power Corporation (SWPC) with a length of 1.8 m, a wall thickness about 2 mm, and an outside diameter >20 mm. The design operates at 900-1000 °C due to its high ohmic resistance; such temperatures are necessary in order to obtain an approximate power density of 200 mV/cm². Flat tubes and ribs are incorporated into the design to reduce the ohmic resistance (Singhal 2000).

2.2.4.4 Planar design

The planar design comes in different configurations, these include: the electrolyte supported, anode or cathode supported and interconnect supported as presented in Fig 2-3. The advantages or otherwise of these configurations are presented in table 2.3. Electrode supported cells have higher performance because the electrode supports a very thin electrolyte with low ohmic resistance. Under this category the anode supported type is the most common, however, a nickel based anode under goes what is called redox cycling where reduction of NiO→Ni and the oxidation of Ni→NiO occurs and this causes a volumetric change leading to cell damage over time. Electrolyte supported SOFCs are mechanically robust compared to electrode supported ones as thus they are less susceptible to failure. The interconnect-supported like the electrolyte supported is strong mechanically but its problem is that it limits the flow field in the design as cell support comes in as a requirement (Timurkutluk, Timurkutluk et al. 2016).

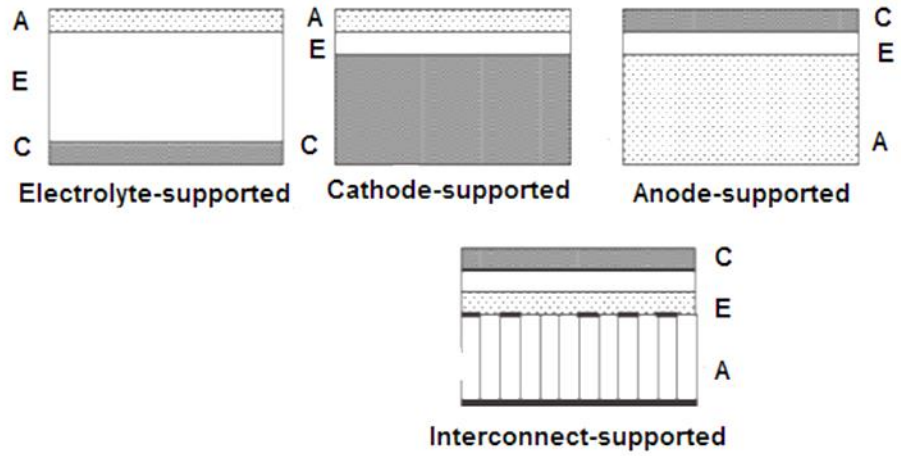


Figure 2-3: Types of cell configurations for Planar SOFCs adopted from ref. (Minh 2004)

Cell configuration	Advantages	Disadvantages
a) Self-supporting		
Electrolyte-supported	Relatively strong structural support from dense electrolyte, less susceptible to failure due to anode reoxidation (Ni/YSZ anode) and cathode reduction (LSM cathode)	Higher resistance due to low electrolyte conductivity, High temperature is required to overcome electrolyte ohmic losses.
Anode-supported	Highly conductive anode Lower operating temperature as thin electrolyte is used	Potential anode reoxidation, Mass transport limitation due to thick anodes
Cathode-supported	No oxidation issues but potential cathode reduction Lower operating temperature as thin electrolyte is used	Lower conductivity Mass transport limitation due to thick cathodes
b) External -supporting		
Interconnect-supported	Thin cell components for lower operating temperature Stronger structures from metallic interconnects	Interconnect oxidation Flow field design limitation due to cell support requirement
Porous substrate	Thin cell components for lower operating temperature Potential for use of non-cell material for support to improve properties	Increase complexity due to addition of new materials Potential electrical shorts with porous metallic substrate due to uneven surface

Table 2.3: Merits and Demerits of cell configurations (Minh 2004)

As noted depending on which part of the components is supporting the cell, there are electrolyte and the electrode supported concepts for the planar design (McIntosh and Gorte 2004, Blum, Meulenberg et al. 2005), see Fig 2-3 and table (2.3). The electrolyte type is usually supported on yttria stabilized zirconia (YSZ) with thickness 100-200mm and an area of 10 x 10 cm² or more in some cases. The operating temperature is as high as 850-1000 °C as a result of high resistance because the electrolyte is thicker than other components. On the other hand to reduce the electrolyte resistance its thickness is decreased and that of anode increased to support it. The anode which is made of composite YSZ, gadolinium doped ceria (GDC), or samarium doped ceria (SDC) with nickel oxide is chosen to support the thin electrolyte due to better electrical conductivity of its materials (Blum, Meulenberg et al. 2005).

2.3 Materials used in SOFCs

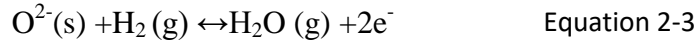
Selection of materials for the various components of a cell stack depend on their ability to withstand both oxidizing and reducing conditions (Singh 2007). Table 2.4 summarises the components of SOFCs and the factors affecting materials used.

2.3.1 Electrolyte

Several ceramic materials such as rare earth doped ceria and rare earth doped bismuth oxide are used as electrolytes but the most common is yttria stabilized zirconia (YSZ). The basic requirement of an electrolyte is to have good ionic conductivity to reduce cell impedance and secondly to avoid current leakage having little or no electronic conduction is important. Electrolytes in an SOFC operate on the principle of oxygen ion (O²⁻) conductivity and the choice is based on availability and cost. Oxygen ions (O²⁻) migrate from the cathode to the anode side through the electrolyte and react with the fuel. YSZ exhibits only ionic conduction; due to vacancies in its crystal structure O²⁻ ions travel from cathode to the anode side (Singhal 2000, Stambouli and Traversa 2002). Ceria is most compatible with cathode materials and has the highest conductivity but is less stable in low oxygen partial pressures. Strontium/magnesium doped lanthanum gallate (LSGM) has better conductivity compared to YSZ but is less compatible with the anode materials and is less easily prepared than YSZ (Fergus 2006). Hence YSZ is most widely used.

2.3.2 Anode

The anode must be stable in the reducing condition of the fuel and be electronically conductive; a high porosity in the anode of 20-40% enables the passage of reactants and product gases. Non-oxidizing metals are used as anode materials. The oxidation of the fuel takes place as follows



For SOFCs the anode is a composite made from one of these electrolyte materials YSZ, gadolinium doped ceria (GDC), or samarium doped ceria (SDC) in a powdered mixture with nickel oxide (Singhal 2000, Stambouli and Traversa 2002). NiO and YSZ are stable even at high temperatures, so they do not form solid solution but can be sintered to form a composite and can then be reduced to form a porous nickel-yttria stabilized zirconia cermet (Ni-YSZ) upon exposure to fuel gases. The function of the YSZ is to give structural support; the thermal expansion matches closely with that of YSZ electrolyte and helps in ionic conductivity of the anode (Zhu and Deevi 2003, Sun and Stimming 2007). In case hydrogen is not used directly as fuel for SOFCs fuel reformation which involves conversion of for example methane into hydrogen is required and that occurs in the (Ni-YSZ) anode via internal steam reforming as in equation 2-4 or through catalytic partial oxidation (Zhu and Deevi 2003) in equation 2-5 below.



The steam reformation reaction in equation 2-4 is associated with the gas shift reaction in equation 2-6



The above reactions also help reduce the problem of carbon deposition on the nickel particles of the anode which is known to deteriorate cell performance (Zhu and Deevi 2003).

2.3.3 Cathode

A number of factors are considered for the selection of cathode materials due to high operating temperature for SOFCs. Noble metals such as platinum, palladium, or silver can be used but they are excluded by high cost and lack of long term durability caused by volatilization of silver

(Minh 1993). The cathode operates in an oxidizing condition at 1000°C and takes part in an oxygen reduction process.



Requirements for a cathode include chemical stability coupled with electronic conductivity. Again the cathode must have some porosity to allow for the transport of product gases and reactants. A range of perovskite type structured materials containing lanthanum strontium ferrite, and lanthanum strontium cobaltite ferrite are used as cathode materials. (Singhal 2000, Stambouli and Traversa 2002).

2.3.4 Interconnects

The interconnectors provide electric contact to the cathode and protect it from the reducing condition of the fuel on the anode side. Due to this dual function the requirements on the interconnectors are the most severe compared to other cell components. These conditions include stability in dual atmospheres during cell operation; closely matched TECs to both those of the electrolyte and air electrode, low permeability for oxygen and serving as electrical contact the conductivity of the interconnector must be close to 100% electronic. Doped lanthanum chromite satisfies these conditions and is therefore used as an interconnect material (Singhal 2000).

SOFCs components	Materials used	Choice factor	Ref
Electrolyte	Ytria stabilized zirconia (YSZ)	Availability and cost	(Singhal 2000, Stambouli and Traversa 2002, Mahato, Banerjee et al. 2015)
	Cerium oxide doped with samarium (SDC)		(Singhal 2000, Stambouli and Traversa 2002, Mahato, Banerjee et al. 2015)
	Cerium oxide doped with gadolinium (GDC)		(Singhal 2000, Stambouli and Traversa 2002, Medvedev, Lyagaeva et al. 2016)
	Bismuth yttrium oxide (BYO)		(Singhal 2000, Stambouli and Traversa 2002)
Anode	Composite YSZ, GDC or SDC with nickel oxide		(Singhal 2000, Stambouli and Traversa 2002)
	NiO/YSZ	Suits YSZ electrolyte	(Singhal 2000, Stambouli and Traversa 2002)
Cathode	Perovskite lanthanum strontium manganite LaSrMnO ₃ (LSM)		(Singhal 2000, Stambouli and Traversa 2002, Medvedev, Lyagaeva et al. 2016)
	Lanthanum calcium manganite LaCaMnO ₃ (LCM)	TEC match with YSZ and good performance above 800 ° C	(Singhal 2000, Stambouli and Traversa 2002)
Interconnect	Doped lanthanum chromite	Severe requirements	(Singhal 2000)
Sealing materials	Glasses, glass ceramics	TEC match, gas tightness	

Table 2.4: Materials used in SOFCs and their reasons for selection

2.3.5 Sealing of SOFCs

Sealing is required especially for the electrolyte-electrode assembly, which is a very thin 10-15 μm , delicate, and brittle part of the SOFCs. The primary function of the seal is to physically separate and provide electrical insulation in the SOFCs stack. Many sealing concepts have been demonstrated by researchers (Chou, Stevenson et al. 2002). For example ferritic stainless steel with aluminium (FeCrAlY alloy) interconnects have been sealed to YSZ electrolyte by brazing. The use of Si-C-N polymer and development of mica and mica based compressive sealants has also been reported by (Chou, Stevenson et al. 2002, Singh 2012). Singh has developed a glass with the ability to self-heal cracks at the SOFC operating temperature. A composite glass/YSZ and alumina fibre where the fibre provides stress relief on the electrolyte-electrode geometry by being compliant has also been reported (Singh 2007, Singh 2012). There are three commonly used sealing technologies for SOFCs: i) rigidly bonded seals, ii) compressive seals and iii) compliant seals with each category having its specific advantages and limitations.

2.3.5.1 Rigidly bonded seals

Glass and glass ceramics dominate this type of bonding; as it is desirable to have the sealant's coefficient of thermal expansion match those of other components. This type of joint is brittle and non-deformable so they are susceptible to fracture. Sealants made from glass and glass-ceramics exhibit stability in both oxidizing and reducing atmospheres in SOFCs, in addition to other desirable properties like wettability with YSZ electrolyte, and the interconnect materials, they also provide good electrical insulation (Weil 2006). Some examples of glass systems used are alkaline earth silicates and borosilicates; the advantages of these seals over the other categories are their ability to flow above the glass transition temperature, easy manufacture and lower cost of their materials compared to noble metal seals or mica based seals. Their drawbacks include thermal and chemical instabilities and poor resistance to dynamic forces (Mahapatra and Lu 2010). The two most important criteria for sealing glasses are T_g and TEC, with the TEC ranging between $(9-13)\times 10^{-6} \text{ }^\circ\text{C}^{-1}$ for the sealing glasses used in fuel cells (Laorodphan, Namwong et al. 2009).

2.3.5.2 Compressive seals

Compressive seals are used as an alternative to glass and glass-ceramic seals. Because they are not rigidly bonded to the cell stack components they provide a free expansion and contraction

during thermal cycling. These non-bonding seals are made of silicate materials with a sheet or plate like-structure which act as a gasket and under high compressive loads hermetic sealing is attained. A typical example in this type of seal is the mica seal; mica belongs to the phyllosilicate minerals consisting of silicate tetrahedrons. Their chemical composition is represented by $KT_2\text{-}_3(X, Si)_4O_{10}(O, F, OH)_2$, where K stands for potassium, T can either be lithium, titanium or magnesium etc., and X is mostly aluminum but sometimes it may be boron or beryllium. Mica seals are known for their high quality (Q) factor, resistivity and capacitance stability and are extensively used for sealing electronic devices (Simner and Stevenson 2001, Chou, Stevenson et al. 2002).

2.3.5.3 Compliant bonded seals

TEC mismatch is not considered a major problem in these types of seals because they are compliant and deform plastically up to the operation temperature. Insulating materials must be used to prevent electrical shunting at the interface between the sealant and the other SOFCs parts because they are metal based sealing materials. Problems associated with compliant seals include cell bowing and irregularities in gas distribution. Noble metals are the material of choice for these seals due to their stability against corrosion. Some of their drawbacks are delamination due to poor wetting and TEC mismatch between oxide layers and interconnects (Weil 2006, Mahapatra and Lu 2010).

2.3.5.4 Composite seals

Glass and glass-ceramics form rigid seals and although they have shown the advantage of flexibility in properties through compositional modifications, they are inherently brittle and because of metastability uncontrolled crystallization may eventually occur, which causes seal damage. On the other hand brazed seals show good performance in the short term but during long term operations in dual atmospheres they tend to be chemically instable. A compressive mica seal has good thermal and electrical insulation properties, but its constituents cause electrode poisoning during operations and an unacceptable leakage rate is associated especially with the mica papers available in the market. Because of the above problems identified with the different sealing techniques, they cannot single handedly meet all the requirements for sealing, hence there is the need to examine an alternative composite seal by using filler additives such as, Al_2O_3 , or ZrO_2 (Zhang, Yan et al. 2013) and MgO (Nielsen, Solvang et al. 2007) with a view to

solving stack sealing problems by improving geometric integrity of the seal through controlling viscous flow (Zhang, Yan et al. 2013). The additive fillers increase reliability and thermal stability of the glass matrix by acting as reinforcement phase (Ye, Yan et al. 2012).

2. 4 Glass and glass-ceramic seals

2.4.1 Wetting and glass to metal seals

Glass to metal sealing is a traditional fusion technique in which glass is melted over the surface of the metals to be joined. The molten glass flows and wets the metal surface and reacts to form an interfacial layer that bonds them together (Donald 1993, Lei, Wang et al. 2012). In an ideal situation the glass will spread and wet all metal surfaces because its surface energy is low compared to that of the base metals. On the other hand spreading and wetting will be prevented if the interaction depends on van der Waal forces or intermolecular attraction forces which usually are lower strength and cannot overcome cohesive forces (Woldemar Anatol 1964).

Glass adhesion to solid surfaces tends to be stronger when chemical forces are involved. Unshielded atoms on the solid surface react with the glass and form compounds at the metal/glass boundary, and a transition layer will be formed if these compounds diffuse into the interface and adhere to the bulk materials (Leslie 1964).

High temperatures are required to achieve chemical bonding. During the process of bonding one of the phases changes to liquid at the sealing temperature through fusion or reaction to establish intimate contact with each other. Therefore, both wetting and spreading are important factors that determine sealing and are usually demonstrated or described by the sessile drop method.

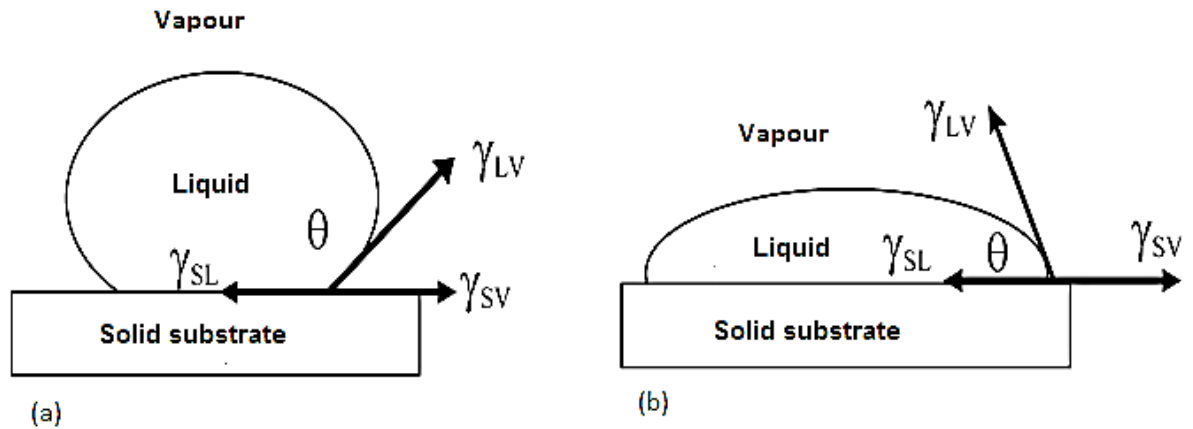


Figure 2-4: Contact angle θ (a) non-wetting (b) wetting adapted from ref (Donald 1993)

The formation of acute angles in a sessile drop experiment indicates wetting can occur and obtuse angle indicates non-wetting. Wetting usually occurs where the surface free energy of solid substrate becomes lowered by the liquid in contact. On the other hand if the surface free energy is increased after contact with the liquid then the situation is a non-wetting one. However, an interface still forms when the free energy of the system is decreased. Usually the solid substrate determines the shape of the sessile drop. A driving force of the form $\gamma_{sv} - \gamma_{sl}$ acts on the sessile drop periphery when γ_{sv} is lowered by the liquid as can be seen in the Young-Dupre equation.

$$\gamma_{sv} = \gamma_{sl} + \gamma_{lv} \cos\theta \quad \text{Equation 2-8}$$

The conditions for obtaining acute contact angle are $\gamma_{sv} > \gamma_{lv}$, or $\gamma_{sv} > \gamma_{sl} > \gamma_{lv}$ and for obtuse angles the condition is reversed as $\gamma_{sv} < \gamma_{lv}$, or $\gamma_{sv} < \gamma_{sl} < \gamma_{lv}$. Where γ_{lv} , γ_{sv} and γ_{sl} are the surface free energies of liquid/vapour, solid/vapour and solid/liquid interfaces and the use of surface free energy gives a better understanding in terms of thermodynamic relationship.

Dirty surfaces prevent good contact between sealing parts and favours non-wetting conditions. The barrier as a result of metastability in most systems can be overcome by high temperature activation to achieve wettability. Wettability also depends on whether the solid substrate is active or passive, i.e whether the substrate dissolves or not during sealing. For an active substrate which takes part in the wetting process the Young-Dupre equation can be transformed to include the contribution of free energy of reaction $\frac{\Delta G_R}{dA_s dt}$. This contribution is always practically larger than surface energy of liquid/vapour thus spreading occurs.

$$\gamma_{sv} - \left(\gamma_{sl} + \frac{\Delta G_R}{dA_s dt} \right) \geq \gamma_{lv} \cos \theta \quad \text{Equation 2-9}$$

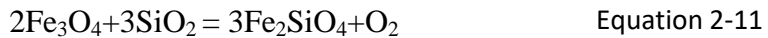
The spreading or liquid flow on wetting surface is expressed in equation below.

$$W_s = \gamma_{sv} + \gamma_{lv} - \gamma_{sl} \quad \text{Equation 2-10}$$

If the spreading on the wetting surface (W_s) is positive then there will be spreading as the driving force for wetting is larger than γ_{lv} . For a negative W_s the driving force is small, although an acute angle is formed but there will be no spreading (Pask 1991).

2.4.2 Bonding of glass to metal seals and coatings

It has been suggested that bonding between enamel and the metal surface is as a result of a mechanical process because a rough surface appears on the interface between the joined parts even though they were previously smooth before joining. The mechanism can be described in two ways. First as mechanical process in which formation of dendrites are involved and secondly as a chemical one in which some sort of electrolytic corrosion is involved in the bonding process (Donald 1993, Donald 2000). For example the oxides formed on the surface of a Kovar alloy substrate firstly dissolves in the molten glass in a chemical reaction process between the oxides and the SiO_2 in the glass:



Depending on the wetting time the oxide may or may not completely dissolve into the glass. This process can be referred to as chemical bonding since Fe diffuses into the glass and joins the substrate via the oxide to the glass. However, as the wetting time is extended the oxide dissolves itself in the glass and reacts with SiO_2 and then the glass now has direct contact with the surface and penetrates the intergranular oxides forming mechanical bonding with pinning effect between the glass and the substrate. Therefore in this case both chemical and mechanical bonding coexist in the wetting process (Luo and Shen 2009).

Most metals have oxides films on their surfaces which leave some traces when they rub a glass surface. While mercury wets glass only in the absence of oxygen other metals such as tin, indium and gallium adhere to glass through oxide deposits. The oxide layers prevent the

formation of gas bubbles at the glass/metal interface, and provide indirect contact between the interfaces. Hydrogen, carbon dioxide and pure nitrogen atmospheres all have effects on wetting between the molten glass and the metal substrate depending on the surface conditions, with both nitrogen and CO₂ enhancing wetting on an oxidised surface. There is a high affinity for oxidized surfaces by the molten glass because the solubility of the oxide films at the interface between glass and metals contributes significantly to adhesion.

There are number of factors influencing the aging and lifetime behavior of glass or glass-ceramic to metal seals. Interfacial reaction can cause residual stresses to build up leading to seal degradation as the interfacial reactions may forms undesirable product with different TECs compared to the bulk materials leading to cracks or separation. Undesirable reaction products are formed between Fe and Cr containing metallic alloys and nucleating agents such as phosphorus that may be present in some glass and glass-ceramics; they react to form iron or chromium phosphide which forms a coarse microstructure and act as stress concentration points degrading seal performance. The presence of water in the glass composition may lead to the formation of bubbles due to the presence of hydrogen as in the reaction between water and diffusing Cr species (Donald, Metcalfe et al. 2008).



Water can also react with Al, Ti, and Nb. These undesirable reactions can be controlled by using transition metal oxides such as nickel oxide that will react with Cr to form Cr₂O₃ instead of hydrogen as in equation 2-13 above.

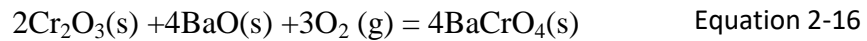


which results in the formation of fine microstructure with Ni precipitates. If CuO is added a thin oxide layer is formed with no precipitates.



Thickening of an interfacial reaction product layer can be a critical problem if the layer continues to increase during the operation life of the cell (Donald, Metcalfe et al. 2008).

Similar reactions can occur in glass based seals. For example the interface between barium calcium aluminosilicate glass-ceramics (BCAS) of composition 21.44SiO₂-6.66B₂O₃-5.35Al₂O₃-56.1BaO-7.19CaO was found to contain BaCrO₄ products leading to physical separation of the glass seal from stainless steel (Yang, Xia et al. 2013). The mechanism of BaCrO₄ formation is that chromia layer on the stainless steel dissolves into the glass-ceramic and forms a solid solution in the presence of chromite vapour which proceeds to form barium chromate and water as follows:



2.5 Glass formation

According to Shelby a glass is an amorphous solid completely lacking in long range order and exhibiting a glass transformation region. By this definition any material formed by melting, vapour deposition, sol-gel and neutron irradiation of crystalline materials can be generally called glass (Shelby 2005). Glass formers form the backbone of the glass structure and can make glass with normal laboratory techniques eg SiO₂, B₂O₃, GeO₂, P₂O₅, P₂O₃ etc. The modifiers do not form glass under ordinary conditions but are added into glass to modify their properties while intermediates can act as either network formers and modifiers and they include Al₂O₃, BeO, ZnO, TiO₂ etc (Sun 1947).

There exist similarities between glasses and their crystalline states in properties such as density, mechanical and thermal properties (Varshneya, 2006). However, unlike crystals, glasses are referred to as undercooled liquids because they do not have a definite and sharp melting point (Warren 1934). All glasses exhibit two main identical properties namely a lack of long range ordering in their structures) and a clearly visible glass transition range or T_g (Shelby 2005). As a result of this short range ordering and the non-existence of constraints to formation of periodicity in atomic arrangements as opposed to crystalline materials leads to a degree of inexactness in the orientation and location of next nearest neighbours within the glass (Salmon 2002).

Glasses as known are produced through different routes however; the most common both in laboratory and industrial scales is the melting and quenching. A basic question that needs clarification is to find out what criteria leads to glass formation for any given materials. the

answer to this inquiry comes from two theories of glass formation (i) structural and (ii) kinetic theories (Varshneya 2006).

2.5.1 The structural theory of glass formation

The first and simplest modern theory of glass formation was based on the proposal by Goldschmidt (1926) referred to as the radius ratio criterion. He suggested a general formulation (R_nO_m) that forms glasses easily when the ratio of their ionic radius of cation R and oxygen ion falls between 0.2 and 0.4. His argument here is that in this range tetrahedrally coordinated cations surrounded by four oxygens are obtained and form glasses during cooling; however, this argument is empirical and could not explain why merely four-fold coordinated cations are adequate to form glass (Shelby 2005). Approximately a decade later Zachariasen published a paper stating a number of rules which favours the ability of various cations to form glass (Zachariasen, 1932). Zachariasen's proposal became one of the most widely accepted and reported in the attempt to explain the structural theory of glass formation so far. The X-ray diffraction study of Warren and his students (1934) was in support of Zachariasen's model. However, Zachariasen's theory can only explain the required conditions of glass formation of pure glass formers rather than modified glass networks.

Zachariasen gave conditions for oxide glass formation as (i) the sample must contain a large amount of cations and are surrounded by oxygens in tetrahedral or trigonal arrangements. (ii) the tetrahedra and trigonal units are corner sharing (iii) and some oxygens link only two cations and not make additional bonds as reported by (Sun 1947). Also according to Sun oxides with high values of single bond strength have greater tendency for glass formation. Based on the single bond strength the oxides are classified into network formers (119-81kcal/mol; 497-334 kJ/mol), intermediates (73-60 kcal/mol; 305-251 kJ/mol), and network modifiers (60-10kcal/mol; 251-42 kJ/mol) (Sun 1947, Dimitrov and Komatsu 2012) and also according to electronegativity of the cations, where electronegativity is the power of an atom to attract a bonding pair of electrons (Matsunaga, Rogers et al. 2003). In the former case Sun argued that high bond strength hinders structural reorganisation of the melt thus preventing crystallisation during cooling. While in the later situation network formers which are semi-covalent and predominantly acidic such as SiO_2 , B_2O_3 and Al_2O_3 have high electronegativities between (2 to 3.5), and ionic and basic oxides such as Na_2O , BaO and MgO have very low electronegativities (1 to 1.2) and are

classified as modifiers. The basic and ionic oxides such as ZnO have intermediate electronegativity values and are classified as intermediates (Reddy, Nazeer Ahammed et al. 2001, Dimitrov and Komatsu 2012). Despite the wide acceptance of the Zachariasen-Warren rules there are criticisms of some of these rules governing glass formations. One of such critics is from Lebedev and his co-workers who queried what the word random means. Lebedev and co-workers believed that some degree of ordering is expected because of the chemical bonding and that the glass structure is not as random as thought by Zachariasen as evidence of short range ordering similar to their crystal structure exist. Therefore the subsequent discovery of glassy metals, heavy metal fluoride and semiconducting chalcogenide whose structure is oxygen free and thus suggests an overhaul of the so called 'randomly packed' structure (Varshneya 2006).

2.5.2 Kinetic theory of glass formation

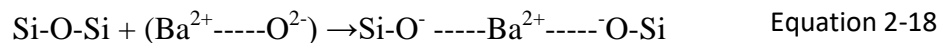
It is possible to avoid crystallisation in most liquids through fast cooling and form glass even in liquids that would crystallise in a normal cooling process. So the important question is not simply what materials forms glass but rather at what cooling rate a given substance turns into glassy state. To this effect it is established that almost all liquids (water and molten metals included) can form glasses if subjected to sufficiently high cooling rates to below their freezing points (Varshneya 2006). The initiation of nuclei and subsequent growth of the crystals leads to crystallisation whereas avoiding these processes through fast cooling rates leads to glass formation (Varshneya 2006). This processes are temperature dependent and it is worthy of note that crystallization does not occur above the liquidus temperature. Viscosity also plays an important role in the glass formation ability of a given melt for example in the case of oxide glass formers they are characterised by large viscosity at melting points and a rapidly rising viscosity with decreasing temperature during the cooling process (Uhlmann 1972).

2.6 Glass structure

In this thesis multi-component alumino-borosilicate glasses which contain (Si, B, and Al) as network formers are investigated. Since these glasses are silicate based with the incorporation of boron oxide and alumina, it is important to discuss the simple silicate structure after which the structural changes in glasses that contains all the network formers and modifiers will be presented.

2.6.1 Structure of silicate glasses

The silicate glass structure in its simplest form contains the SiO_2 as the network former. Modifiers are commonly alkali oxides such as Na_2O and alkaline earth oxides (CaO or BaO). The silicon forms SiO_4 tetrahedra with four oxygens covalently bonded to the central Si. These tetrahedra connect to each other by bridging oxygens (BOs) to form a network (Si-O-Si). (Varshneya 2006). The introduction of alkali or alkaline earth modifier cation into a silicate melt results in breaking one Si-O-Si bond per unit charge of the modifier cation creating a NBO ion at the SiO_4 tetrahedra and the silica remains four coordinated (see fig 2-5) (Shelby 2005, Varshneya 2006). Increasing the modifier content decreases the 3D network towards a sheet structure which breaks further to form rings and chains of SiO_4 interconnections (Wu and Stebbins 2009). Assuming a divalent modifier such as Ba^{2+} is added into the glass the depolymerisation may occur as follows



The electrostatic interactions between the modifier and NBOs are weaker than the bond between Si-O with a bridging atom (Wu and Stebbins 2009). In fig (2-6) and table 2.5 a description of the silicate connectivity with oxygen is presented and the nomenclature Q^n is used to report the degree of connectivity with oxygens. The small subscript n refers to the number of oxygens between 0-4. A silica tetrahedron with $n = 0$ is completely isolated and depolymerised and highest degree of connectivity is attained at $n = 4$.

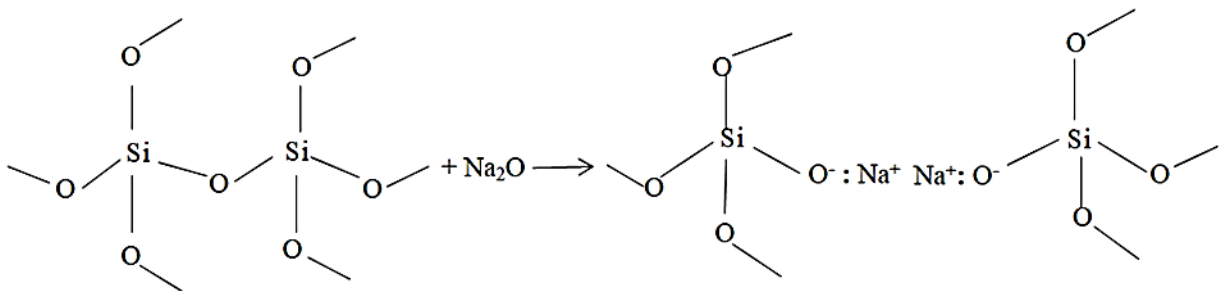


Figure 2-5: depolymerisation of silicate glass backbone by a modifier (Na_2O)

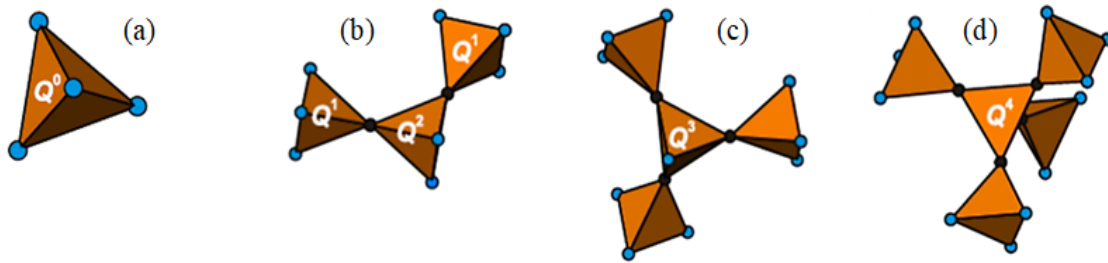


Figure 2-6: Typical Q^n species (a) completely isolated Q^0 ; (b) Q^2 linked to 2 Q^1 terminal tetrahedra units, (c) Q^3 linked with Q^1 terminals and (d) Q^4 linked to other tetrahedral units. (Black and blue atoms are bridging and non-bridging oxygens). Adopted and modified from (Edén 2011)

Q^n	Silicate group	nomenclature
Q^4	SiO_2	tectosilicate
Q^3	$\text{Si}(\text{O})_3\text{O}^-$	phyllosilicate
Q^2	$\text{Si}(\text{O})_2(\text{O}^-)_2$	metasilicate
Q^1	$\text{Si}(\text{O})(\text{O}^-)_3$	disilicate
Q^0	$\text{Si}(\text{O}^-)_4$	orthosilicate

Table 2.5: Q^n silicate groups and their nomenclature (Eden 2012)

2.6.2 Structure of borosilicate glasses

Boron oxide is a network former and can form a B_2O_3 glassy network. When additional elements and oxides are introduced into boron oxide then the structural rearrangement in the glass depends on factors such as melting temperature or pressure and the interaction of the different components in a given composition (Hubert and Faber 2014). Unlike silica tetrahedral structure which depolymerises with modifier, the initial addition of modifier into boric–oxide glass leads to the conversion of trigonal boron to tetrahedral boron which accommodates the added oxide. Few or no non-bridging oxygens (NBOs) are formed. As the amount of alkali/alkaline earth is increased the tetrahedral boron begins to convert back to asymmetric BO_3 (Wu and Stebbins 2009, Zhang, Yue et al. 2013). The BO_4 units participate in forming different cyclic units such as di, tri, tetra or pentaborate units. Each of the BO_4 units is connected with two other such units

and single oxygen from each unit connects with a metal ion and forms extended chains of BO_4 tetrahedron. As the amount of modifier increases the conversion of BO_4 back to BO_3 in form of pyro or ortho borate groups (Pascuta and Culea 2011). In a modifier free borate and silicate glass the structural units exist without mixing and as soon as a modifier is added then there will be overlap or mixing into each other and in this case boron may exist either in trigonal units such as in boroxol, pyroborate and metaborate or in tetrahedral form such as in diborate, triborate and pentaborate depending on the compositions. In borosilicates it is believed that the silicate and borate structures are mixed together (Hubert and Faber 2014). The effect of alumina addition on the borate and borosilicate is to decrease the amount of four fold coordinated boron as the formation of AlO_4 first is more favourable (Konijnendijk and Stevels 1976).

According to Varshneya (Varshneya 2006) modifier cations associated with a SiO_4 tetrahedron and create NBO or take part in the conversion of BO_3 trigonal to the BO_4 tetrahedra so that here the modifier behaves as a charge compensator to the negatively charge $[\text{BO}_4]^-$ units. (An example is given as one mole of Na_2O compensates for one mole of B_2O_3 , although according to Manara it is not always the case that exactly one Na^+ compensates the charge of one BO_4 units, other species may take part (Manara, Grandjean et al. 2009). The network modifiers preferentially convert BO_3 to BO_4 at low modifier to B_2O_3 ratio R (where $R < \sim 0.5$) but after reaching a critical point the modifiers then associate with SiO_4 and BO_4 units and create NBOs (Manara, Grandjean et al. 2009). Alkali oxide prefers to associate with boron forming BO_4^- until a critical composition is reached. The maximum fraction of BO_4^- is reported to be higher in alkali borosilicate compared to alkali borate and increases with silica content (Gohar, Doweidar et al. 1990). Gohar et al also reported an observation that NBOs increase with addition of alkalis at constant silica and varying B_2O_3 and NBOs also increase with fixed alkali and increasing silica indicating that the alkalis maintained modifier role and depolymerised the silica network. It is assumed that at a value of $R > 0.4$ the formation of BO_4^- occurs at the same time with the depolymerisation of the silica network. In $\text{CaO-Al}_2\text{O}_3\text{-B}_2\text{O}_3$ there is a competition for CaO by Al_2O_3 and B_2O_3 to form AlO_4 and BO_4 units (Doweidar, Moustafa et al. 2001) and AlO_4 is preferably formed before BO_4 due to higher single bond strength of the Al-O in AlO_4 compared to B-O bonds in BO_4 as reported by (Lu, Ni et al. 2006). As explained by Osaka et al that in alkaline earth aluminoborate the alumina is assumed to be in one of the following units or structure i) AlO_4 in tricluster unit or (AlB_3O_7) and this occurs when the amount of modifier is

less than that of alumina content. ii) charge compensated AlO_4^- and iii) AlO_6 in six coordination (Osaka, Oda et al. 1986). On the other hand triclusters of the form $(\text{BO}_3)_2\text{O}(\text{SiO}_3)$ are also reported for borosilicate glasses due the unavailability of transforming to coordination state higher than four or as a result of shortage of oxygen needed to form BO_4 could not be supplied by the modifier such as BaO. This sort of triclusters are seen when there is high amount of NBOs and so small percentage of oxygen may form triclusters with 3 network former neighbours (Zhao, Kroeker et al. 2000). Increase in alumina decreases the concentration of boron in BO_4 units and increases the number of BO_3 units (Doweidar, Moustafa et al. 2001).

2.6.3 Structure of aluminosilicate glasses

The structure of aluminosilicate glasses consist mainly of SiO_2 and Al_2O_3 tetrahedra where the silica is a network former and the alumina is an intermediate whose role changes between that of network former and network modifier depending on its amount in the glass compared to alkali and alkaline earth content. When the alumina content $[\text{Al}_2\text{O}_3] \leq [\text{MO}+\text{M}_2\text{O}]$ the Al^{3+} forms AlO_4^- tetrahedra. Generally aluminium ions are in four fold coordination in peralkaline compositions ($\text{Al}/\text{MO}<1$) and join the silicon–oxygen glass structure and on the other hand where the composition is peraluminous ($\text{Al}/\text{MO}>1$) aluminium forms a small amount of five-fold coordinated aluminium with negligible six fold coordinated aluminium also being present (Xiang, Du et al. 2013). Fivefold coordinated Al is present in compositions containing alkali and or divalent modifiers respectively (Wu and Stebbins 2009) and the amount of higher coordinated aluminium increases with increase in the peraluminous ratio where all the M^+ and M^{2+} ions play charge compensation roles. The formation of five-fold coordinated alumina is also favoured by higher cation field strength modifiers in aluminosilicate glasses. Cation field strength is a measure of how cations attract anions (defined as the ratio of the formal charge to the square of the mean first shell cation-oxygen bond distance or simply the ratio of charge divided by the radius). However, if the concentration of the modifier with high cation field strength is high this favours NBO formation (Ha and Garofalini 2017). Al^{3+} ions are usually found in the interstices of the network structure and surrounded by equivalent numbers of BOs and NBOs (Varshneya 2006). The AlO_4^- and SiO_2 tetrahedra join together to form a network containing Al-O-Si, Al-O-Al and Si-O-Si bonds. Modifiers are required in the vicinity of the AlO_4^- tetrahedra to charge compensate the negative charge in order to stabilize the network.

2.6.4 Modified rules for cation coordination and accepting NBOs in multi-oxide glasses

Category A rules capture the preferred coordination number for each cations Si^{4+} , $^{[3]}\text{B}^{3+}$ and Al^{3+} and category B rules summarised the tendencies of NBOs being found at different polyhedra.

Rule A1. Si^{4+} is always in tetrahedral coordination except when prepared under excess pressure, and then SiO_5 and SiO_6 polyhedra can be formed.

Rule A2. Al^{3+} is predominantly in tetrahedral coordination in aluminosilicate glasses if there are sufficient modifiers to charge balance all the AlO_4 units. However, even if all the AlO_4 can be charged balanced, AlO_5 and AlO_6 may be formed in the presence of high field strength modifiers eg trivalent ions. This complication of alumina co-existing in 4, 5 and 6 coordination applies for (Al, B) or (Al, P) based glasses, unless Si is present and is the dominant network former in these glasses.

Rule A3. B^{3+} may be present as $^{[3]}\text{B}^{3+}$ or $^{[4]}\text{B}^{3+}$ coordination in the glasses.

Rule B1. AlO_4^- and BO_4^- carry a single negative charge that requires balancing by a modifier cation.

Rule B2. AlO_4 and BO_4 occupy the most polymerised sites in the network and avoid NBOs, if both Al and B are present in the same glass; Al has the strongest ability to avoid NBO ions.

Rule B3. Si^{4+} exhibits the lowest preference for simple (ordered) BO/NBO distribution (Edén, Sundberg et al. 2011, Eden 2012).

The formation of NBOs and BO_4 in alkali and alkaline earth aluminoborosilicates proceeds according to the reaction $\text{Si}(\text{Q}_3) + ^{[3]}\text{B}^{3+} = \text{Si}(\text{Q}_4) + ^{[4]}\text{B}^{3+}$ where Q^3 and Q^4 are the BOs and in the reaction the equilibrium shifts to the right in the order of the cation field strength of the modifiers $\text{Mg}^{2+} > \text{Ca}^{2+} > \text{Sr}^{2+} > \text{Ba}^{2+} > \text{Li}^+ > \text{Na}^+ > \text{K}^+ > \text{Rb}^+ > \text{Cs}^+$ (Hubert and Faber 2014). For example it was reported for K, Na, Ba, Sr, Ca, and Mg aluminoborosilicates for a given Al/B ratio that increases in NBOs and decreases in $^{[4]}\text{B}^{3+}$ were caused by smaller and higher charged cations. Similarly Wu et al. reported the higher field strength of Ca^{2+} compared to Na^+ decreased the amount of BO_4 and increased NBOs in aluminoborosilicate glass (Wu and Stebbins 2009).

2.6.5 The roles of the oxides used in sealing glasses.

A focus of sealing glass research has been to reduce the operating temperature of SOFCs to the so-called intermediate value of 700-800 °C which will reduce the thermal degradation of the materials used for the construction of SOFCs. It is generally considered that a T_g between 600-750 °C is desirable for sealing glasses working around 800°C (Nonnet, Khedim et al. 2012). The selection of sealing glass compositions to address such challenges is based on the role each oxide is expected to play to arrive at the required properties for sealing applications as summarised in table 2.6 and discussed in detail below.

Oxides	Function	
SiO ₂	Network former	(Goel, Tulyaganov et al. 2009)
B ₂ O ₃	Network former, reduces T_g , T_s , viscosity and improves wettability	(Goel, Tulyaganov et al. 2009) (Schwickert, Sievering et al. 2002)
Al ₂ O ₃	Controls crystallization	(Goel, Tulyaganov et al. 2009) (Schwickert, Sievering et al. 2002)
BaO	Reduces T_g , T_s and raises TEC	(Goel, Tulyaganov et al. 2009, Mahapatra and Lu 2010)
SrO	Crystallization stimulant and modify T_g , T_s and TEC	(Goel, Tulyaganov et al. 2009, Mahapatra and Lu 2010)
La ₂ O ₃	Viscosity modifier and long term TEC stabilizer	(Goel, Tulyaganov et al. 2009) (Schwickert, Sievering et al. 2002)
ZnO	Reduces T_g , T_s and sealing temperature, improves flux and reducing agent	(Reis and Brow 2006) (Schwickert, Sievering et al. 2002)

Table 2.6: Summary of the oxide functions in glass

2.6.5.1 Effect of Silica

Silica is the main network former in many glasses including many sealing glasses. Silica based compositions are reported in the literature as having the potential to be used as sealants due to their better thermomechanical properties (Larsen and James 1998) which means their ability to withstand both thermal and mechanical strain generated during SOFC operation. The thermal strain develops due to TEC mismatch between the glass sealant and other SOFC components and

temperature gradient while the mechanical strain largely dependent on Young's modulus, shear modulus and Poisson's ratio of the seal glass and adjacent SOFC components (Mahapatra and Lu 2010). Silica is an insulator with a very low electrical conductivity arising from its tetrahedrally connected structure (Varshneya 2006). To date silica based sealing compositions are preferred to phosphate or high B_2O_3 glasses due to volatility and high temperature stability with low mechanical strength of the latter group of glasses (Wang, Lu et al. 2007), and also the softening point depends on the silica content in a given compositions considering its network forming behaviour and high melting temperature (Wang, Wang et al. 2009).

2.6.5.2 Effect of B_2O_3

Boron in sealing glasses leads to decreases in viscosity, gives better wettability on the steel surface by delaying crystallization (Borhan, Gromada et al. 2016). When large amounts of B_2O_3 substitute silica there will be a decrease in thermal properties because B-O bonds are less stronger than Si-O ones (Coillot, Méar et al. 2012), and so addition of B_2O_3 also decreases the crystallization tendency. Thermal properties such as TEC are reported to be dependent on B_2O_3/SiO_2 ratio in the composition (Sohn, Choi et al. 2004, Tulyaganov, Reddy et al. 2013). However the dependence of TEC on the B_2O_3/SiO_2 ratio is not always straightforward as the effect of B_2O_3 is affected by the presence of other oxides in a multi-component oxide glasses or compositions. A decrease in T_g , T_s and TEC with B_2O_3 addition has been observed for barium containing diopside glass. Volatilization under humid conditions is a common problem for glasses with high B_2O_3 content as volatile species are formed under these conditions (Zhang, Fahrenholtz et al. 2008). Boron also stabilizes the amorphous structure as it increases the activation energy for crystallization (Fergus 2005) and it also increases the activation energy for electrical conductivity (Tulyaganov, Reddy et al. 2013).

2.6.5.3 Effect of ZnO

ZnO is classified as intermediate oxide (Smedskjaer, Youngman et al. 2013) and has been widely considered for use in sealing glasses. A decrease in T_g and T_s has been reported for several invert glasses designed for SOFCs with ZnO and or B_2O_3 additions, leading to a decrease in the sealing temperature. Increase in ZnO also caused a decrease in TEC in these compositions (Reis and Brow 2006). ZnO is better compared to MgO and CaO in terms of enhancing sintering and crystallization process in pyroxene based glasses (Tulyaganov, Reddy et al. 2013). This enables

the formation of sintered and mechanically strong glass-ceramics. It has also been reported that ZnO behaves in a similar way to B₂O₃ with regards to thermal properties such as viscosity and TEC. Up to 10mol% ZnO decreases T_g by 50°C and decreases viscosity but slightly increases TEC in many alkaline earth aluminosilicate compositions. The decrease in the T_g and viscosity value and the slight increase in TEC indicates that here ZnO weakens the glass structure and is acting as a modifier. However the role of ZnO may change from a network modifier creating NBOs to a network former if present at levels greater than 8mol% (Tulyaganov, Reddy et al. 2013).

For a pyroxene based glass composition the activation energy for crystallization decreases with ZnO additions while the activation energy of conductivity both increases and decreases as reported by (Tulyaganov, Reddy et al. 2013). According to Cetinkaya et al, (Cetinkaya Colak, Akyuz et al. 2016) addition of ZnO in borate glasses may increase or decrease the activation energy for electrical conductivity (E_a) depending on the role of the ZnO. When zinc oxide acts as a network former NBOs are created and the glass structure expands and then the alkali metal moves easily leading to a decrease in activation energy. However, there is also reported increase in E_a when zinc oxide behaves as a network former by joining the glass network; in this case NBO density is lower and the structure is tighter (Borhan, Gromada et al. 2016).

Zinc oxide has better stability than B₂O₃ in wet hydrogen atmosphere (Goel, Tulyaganov et al. 2008, Tulyaganov, Reddy et al. 2013). Chemical durability and mechanical properties are enhanced with ZnO addition in silicates and borosilicates while in phosphate glasses lower softening points are observed. Zinc oxide also act as a nucleating agent in alkali silicate and aluminosilicate glasses when present in low amounts (Smedskjaer, Youngman et al. 2013). ZnO additions have been reported to decrease sealing temperature because ZnO decreases the T_g and T_s while maintaining good TEC match (Sasmal, Garai et al. 2014).

2.6.5.4 Effect of BaO

Barium oxide has also been extensively considered for sealing glasses as it increases TEC (Arora, Singh et al. 2011), when added to many compositions including diopside glass. Barium also causes a decrease in molar volume of the glass structure. BaO is also reported to increase polymerisation although depolymerisation follows after reaching critical BaO content in clinopyroxene glasses (Tulyaganov, Reddy et al. 2013). Although barium is claimed to form

some tetrahedral coordination by Tulyaganov et al, this is not very liable as the coordination of barium and strontium in typical silicate glasses is approximately 7 (Rai and Mountjoy 2014). However something very close to the suggestion by Tulyaganov is the report that strontium forms 4.4 to 5 coordination in borosilicate glasses although their actual data fit indicates 5.68 as coordination number for Sr-O (M  ar, Yot et al. 2007). BaO additions are also known to decrease T_g (Ghosh, Kundu et al. 2008). However, it has been argued that T_g and T_s are controlled by SiO_2/B_2O_3 ratio and not BaO content (Sohn, Choi et al. 2002). The activation energy for electrical conductivity may increase or decrease with BaO depending on the composition (Goel, Tulyaganov et al. 2007), and the lower field strength of BaO leads to a decrease in the activation energy for crystallization (Goel, Tulyaganov et al. 2009, Tulyaganov, Reddy et al. 2013).

2.6.5.5 Effect of La_2O_3

La_2O_3 has been reported to control or stabilize viscosity and TEC in silicate glasses and glass-ceramics and has been deliberately added to modify or change the thermal characteristics of glasses and glass-ceramics (Sohn, Choi et al. 2002, Goel, Tulyaganov et al. 2008, Tulyaganov, Reddy et al. 2013). La_2O_3 controls crystallization of borosilicate glass and enhances the bulk mechanical properties (Ghosh, Sharma et al. 2010). Additions of 1.3-2.6 mol% La_2O_3 to diopside glasses lead to reductions in T_g , T_s , TEC and the activation energy for crystallization while there was little variation in the activation energy for electrical conductivity (Tulyaganov, Reddy et al. 2013).

2.7 Previously studied sealing glasses

Glass and glass ceramics have been the focus of many researchers as they can be tailored to optimize their properties such as TEC and T_g by compositional modification (Tulyaganov, Reddy et al. 2013). In order to find optimal glass based sealant for fuel cells the three primary glass network formers SiO_2 , B_2O_3 , and P_2O_5 have been individually considered as potential sealants for SOFCs (Ghosh, Das Sharma et al. 2008). However all did go well with phosphate based glasses due to poor thermal stability at high operating temperature and therefore volatilize and react with the anode material Ni-YSZ which leads to the formation of nickel phosphide and zirconium-oxyphosphate respectively (Larsen and James 1998). Boron is also affected by the high temperature humidified environment and volatilize forming gaseous substances such as $B_2(OH)_2$ or $B_2(OH)_3$ (Zhang, Fahrenholtz et al. 2008). So silica based sealant have proven to be

the best for use as sealants in SOFCs however the major problem with these glasses and glass ceramics are their alkali content which compromised their insulation capacity as reported by (Larsen and James 1998, Ghosh, Sharma et al. 2008) and also cause chromium volatility with subsequent poisoning of the fuel cell cathode (Fergus 2005, Lessing 2007). As the search continues alkaline earth containing silicate glasses have also been investigated (Ley, Krumpelt et al. 1996, Mahapatra, Lu et al. 2008) notably these systems BaO/SrO-Al₂O₃-SiO₂, BaO/SrO-CaO-Al₂O₃-SiO₂ (Tulyaganov, Reddy et al. 2013) however alkaline earth alumino-borosilicate glass and glass ceramic is the most preferred as these group of glasses satisfy the thermal properties requirement for SOFCs (Fergus 2005, Ghosh, Sharma et al. 2008) and also have better electrical insulation than alkali containing glasses (Mahapatra and Lu 2010). Especially the following glasses and glass ceramic systems form the list of most favoured compositions BaO/SrO-CaO/MgO-Al₂O₃-SiO₂-B₂O₃ based glasses (Tulyaganov, Reddy et al. 2013).

In this paragraph some more specific alumino-borosilicate based glass and glass ceramic compositions investigated for SOFCs in the literature will be presented and discussed based on the advantages or otherwise of these compositions as observed by the respective authors. Ley and Krumpelt investigated this 24.56SrO-20.13La₂O₃-6.92Al₂O₃-40.29B₂O₃-8.11SiO₂ glass ceramic and reported that it has a TEC that is compatible with SOFCs components in the range $8-13 \times 10^{-6} \text{K}^{-1}$ but boron volatility over time is a problem as it contains up to 40 mol% B₂O₃ (Ley, Krumpelt et al. 1996). Lahl (Lahl, Singh et al. 2000) investigated the crystallization kinetics of 45AO-5Al₂O₃-45SiO₂-5B₂O₃ (A=Ba, Ca, Mg) with minor additives such as TiO₂, ZrO₂, CrO₃ and NiO as a sealant for pSOFCs and reported phase separation as the amount of alumina increased from 5 to 10mol% and also the formation of the detrimental phase cordierite (Mg₂Al₄Si₅O₁₈) which has a very low thermal expansion coefficient compared to the SOFCs components. Dieter and Dahlmann also studied the thermal stability and crystallization behaviour of magnesium containing glass-ceramics with composition (2-15)MgO-(<2)Al₂O₃-(45-60)BaO-(25-40)SiO₂-(5-15)B₂O₃(wt.%) and demonstrated the stability of the main crystalline phase barium silicate Ba₂Si₃O₈ after 1000 h heat treatment (Gödeke and Dahlmann 2011). Different series of glasses in the system barium aluminosilicate 18.2SiO₂-12.5B₂O₃-8.8Al₂O₃-46.5BaO-14La₂O₃ (wt.%) have been tested for properties such as T_g, TEC, dilatometric softening temperature T_d, crystallization process and electrical resistivity by Ghosh et al 2008 and Sun et al 2010. In addition the two authors reported a good bonding of the sealant

with YSZ electrolyte and metallic interconnects. The TEC of this sealant matched that of the electrolyte but there was mismatch of less than 10% with the Crofer 22APU metal interconnect (Ghosh, Kundu et al. 2008) where Crofer 22APU refers to ferritic stainless steel alloy (Park, Shin et al. 2018). Sun et al. (Sun, Xiao et al. 2010) investigated the effect of alumina on 33.3SiO₂-16.7B₂O₃-10Al₂O₃-40BaO glass and observed an increase in sealing and crystallization temperatures with alumina swapped for B₂O₃. A strontium silicate system 40SiO₂-51SrO-9ZnO-xM where M is a minor additives 2-4wt% of oxides such as B₂O₃, Al₂O₃, V₂O₅, Cr₂O₃ has been reported to meet the desired TEC ($9-11 \times 10^{-6} \text{ K}^{-1}$) and high softening temperature T_s relevant for SOFC applications (Tiwari, Dixit et al. 2011).

The interfacial bonding behaviour between glasses in the system 40SiO₂-20B₂O₃-30AO-10La₂O₃ (A=Sr, Ba) and the interconnect Crofer 22APU have been studied for chemical compatibility at 850°C up to 750 h, and the sealant has not shown any sign of delamination and had good a TEC match with Crofer 22APU (Kaur, Pandey et al. 2012). The adhesion and sealing properties of a B₂O₃ free system 47SiO₂-9Al₂O₃-26SrO-5La₂O₃-6ZnO-7TiO₂ joined to gadolinium doped ceria electrolyte and stainless steel SUS430 was evaluated for intermediate temperature SOFC applications. It was found that there was good adhesion between the sandwiched seal, electrolyte and the stainless steel after 200 h of heat treatment at 700 °C and there was good thermal stability and a very low leak rate of 0.0007-0.003 standard cubic centimetres per centimetres (sccm/cm at 0.5psi) (Wang, Hsu et al. 2012). The crystallization process in alkaline earth silicate system 42.2SiO₂-1.9B₂O₃-2.94Al₂O₃-19.23CaO-18.5SrO-13.23ZnO-2TiO₂ has also been studied using DTA and hot stage microscopy and the results indicates that smaller particle sizes <20µm crystallize fast to produce porous seals while larger particles >45µm crystallize slowly (Reis, Pascual et al. 2010). Other studies on the crystallization kinetics of 40SiO₂-20B₂O₃-30MgO/SrO-10A₂O₃ (A=Y, La, Al) were carried out at 800°C for times up to 10 h within which some of the samples crystallized to form celsian. The MgO containing glass had a high crystallization temperature than the SrO glass and this may be associated with the higher field strength of Mg²⁺ compared to Sr²⁺ cations. The TECs of these glasses are far less than those required for SOFC applications (Kumar, Arora et al. 2008). Table 2.7 details some additional compositions used for SOFCs in the literature. Although glass compositions with greater amounts of modifiers than total network formers are not recommended by some authors notably Mahapatra et al (Mahapatra and Lu 2010), invert glasses

and glass ceramics with low total sums of network formers (less than 45mol%) are reported for SOFC sealing. According Reis et al the invert glasses crystallised to form thermal stable phases with thermal expansion coefficients compatible with that of YSZ electrolyte and the glass ceramic also bonds strongly chromium containing steel alloy at temperature below 900°C. Invert glass are glasses in which modifiers break the network structure and create NBOs and so the molecular level structures is inverted and therefore have no continuous network glass forming tetrahedral units (Reis and Brow 2006).

Systems	Ref
56.1BaO-7.17CaO-5.39Al ₂ O ₃ -6.66B ₂ O ₃ -21.4SiO ₂	(Kaur, Pandey et al. 2012)
50BaO-7.8CaO-4.8A ₂ O ₃ -28.1SiO ₂ with B ₂ O ₃ , La ₂ O ₃ , ZnO additives	(Ghosh, Das Sharma et al. 2008)
30MgO/CaO-10La ₂ O ₃ -20B ₂ O ₃ -40SiO ₂	(Kaur, Pandey et al. 2012)
10SrO-15La ₂ O ₃ -15Al ₂ O ₃ -30B ₂ O ₃ -30SiO ₂	(Ojha, Rath et al. 2011)
30SrO-15La ₂ O ₃ -15Al ₂ O ₃ -10B ₂ O ₃ -30SiO ₂	(Ojha, Chongdar et al. 2011)
40SiO ₂ -30BaO-20ZnO-7.5B ₂ O ₃ -2.5Al ₂ O ₃	(Arora, Singh et al. 2011)
(0-40)BaO-(0-15)La ₂ O ₃ -(0-15)B ₂ O ₃ -(0-10)Al ₂ O ₃ -(0-40)SiO ₂	(Hsiu-Tao Chang 2009)
(30-35)SiO ₂ -(3-8) B ₂ O ₃ -(3-8)Al ₂ O ₃ -(30-35)SrO-(15-20)CaO-3A ₂ O ₃ (A= La, Y)	(Abdoli, Alizadeh et al. 2014)
42.2SiO ₂ -1.9B ₂ O ₃ -2.94Al ₂ O ₃ -19.23CaO-18.5SrO-13.23ZnO-2TiO ₂	(Reis, Pascual et al. 2010)
47SiO ₂ -9Al ₂ O ₃ -26SrO-5La ₂ O ₃ -6ZnO-7TiO ₂	(Wang, Hsu et al. 2012)
18.2SiO ₂ -12.5B ₂ O ₃ -8.8Al ₂ O ₃ -46.5BaO-14La ₂ O ₃	(Ghosh, Das Sharma et al. 2008)
(2-15)MgO-(<2)Al ₂ O ₃ -(45-60)BaO-(25-40)SiO ₂ -(5-15)B ₂ O ₃	(Gödeke and Dahlmann 2011)
45AO-5Al ₂ O ₃ -45SiO ₂ -5B ₂ O ₃ (A=Ba, Ca, Mg)	(Lahl, Singh et al. 2000)
24.56SrO-20.13La ₂ O ₃ -6.92Al ₂ O ₃ -40.29B ₂ O ₃ -8.11SiO ₂	(Ley, Krumpelt et al. 1996)

Table 2.7: Additional compositions used as sealants for SOFCs see section 2.7 and 2.7.2 for more details

2.7.1 Thermal stability requirements of sealing glasses

According to Kangguo et al two methods are usually followed to study the crystallization kinetics of glasses they are i) isothermal in which the glass sample is heated up to higher than its T_g and then kept at that temperature for some time and the glass crystallises at the fixed temperature and ii) non-isothermal is where the samples are heated at a fixed heating rate. Activation energy for crystallization can be determined from both isothermal and non-isothermal methods and it is an important kinetic parameter (Cheng 2001). The thermal stability of glasses is a measure of their ability to resist crystallization under the influence of the thermal energy. Generally the thermal stability is glass structure dependent and so if the thermal stability is low it means the glass structure favours crystallization. Again according to Kangguo et al a thermal stability criterion for glasses has been proposed as follows $k_{fl}(T) = \nu \exp[-E/RT \times (T_p - T_f)/T_f]$ (Cheng 1999) where T_f is inflection point temperature and T_p is the maximum peak temperature on the DTA curves. This criterion not only considers activation energy E and frequency factor ν but also includes the thermodynamic aspects $(T_p - T_f)/T_f$. The thermal stability of the glass series in this study have been determined simply by examining the difference between the crystallization peak point and that of onset glass transition temperature T_g to estimate the effect of the various substitutions in the glasses on its thermal stability as proposed by (Ghosh, Sharma et al. 2010, Ojha, Rath et al. 2015) to be $T_c - T_g$ the wider the difference between T_c and T_g the better the glass stability in terms of crystallization resistance. The heating rate is an important parameter to be taken into consideration in determining the thermal stability especially for sealing glasses. In the process of sealing lower heating rates enable removal of entrapped gasses so that insoluble gases like water vapour and air gradually escape from the joint when the glass viscosity is sufficiently low during long heat treatment ensuring a fine microstructure and hermeticity. On the other hand higher heating rates avoid concurrent crystallization. Hence the heating rate plays an important role in determining the microstructure and properties of the sealant where sintering with concurrent crystallization takes place (Smeacetto, Salvo et al. 2008). The heating rate recommended by SOFC manufacturers should be <5 °C/min to avoid thermal shock. However higher heating rates can be used to study their effects on the densification and crystallization of the glass. The advantage of increasing the heating rate is to delay crystallization and give room for complete densification because T_c shifts to a higher value. This is good for

sealing but the concern on the other hand is that as the T_g and T_s are shifted it leads to delay in obtaining the decrease in viscosity when the temperature is raised and this will affect satisfactory spreading of the glass during sealing. Therefore, the choice of an optimal heating rate is a compromise between delayed crystallization caused by increased heating rate and delayed decrease in viscosity drop caused by decreasing heating rate. For example an optimum value of T_c is obtained by higher heating rate of say (eg.10 °C/min) and optimum viscosity is obtained by lowest heating rate (1°C/min) so taking the suggestion of Khedim et al, as an example, an optimum choice of heating rate might be 3 °C/min because it produce the suitable glass sample morphology at a 900 °C sealing temperature (Khedim, Nonnet et al. 2012).

2.7.2 Mechanical properties of sealing glasses

Glasses are known to be brittle in nature and thus may fracture readily when subjected to thermal or mechanical stresses. For this reason the fracture toughness and thermal shock resistance are considered important properties because they can be useful in estimating the resistance of the glass to these stresses. The thermal shock resistance and fracture toughness of a glass are directly related to the Young's modulus of the glass (and other properties) which depends on its chemical composition (Inaba, Fujino et al. 1999). Crack initiation and propagation at the glass seal and other component interface happens as the thermomechanical stress exceeds either the tensile strength of the seal glass or the interfacial bonding strength. It is required that the seal withstands pressures between 14-35kPa induced by gas flow coupled with vibration and thermal cycling of more than 100 for stationary applications and 1000 for mobile applications (Mahapatra and Lu 2010) Understanding the mechanical properties at both room temperature (Malzbender and Zhao 2012, Zhao and Malzbender 2013) and at the (high) operating temperatures are therefore necessary (Malzbender and Zhao 2012, Zhao and Malzbender 2013).

The mechanical behaviour of sealing glasses have been studied by a few groups recently. For example, Zhao and Malzbender (Zhao and Malzbender 2013, Malzbender, Zhao et al. 2014) have carried out studies on fully and partially crystallized 36.7BaO-15.8CaO-46.8SiO₂ (BCS) compositions and reported an improvement in mechanical properties with crystallization and sintering. Similar compositions of the form (0-40)BaO-(0-15)La₂O₃-(0-15)B₂O₃-(0-10)Al₂O₃-(0-40)SiO₂ (BCAS) have been investigated at intermediate temperatures of 700 -750°C using four point bending and the fracture strength data were analysed using Weibull statistics (Chang, Lin

et al. 2009). In that study the extent of crystallization and the types of phases formed after sintering and aging were found to influence properties such as flexural strength compared to the cast bulk sample; for example the flexural strength and stiffness were improved below T_g due to formation of a barium lanthanum silicate phase ($Ba_3La_6(SiO_4)_6$). However above T_g both flexural strength and Young's modulus of the sintered glass ceramics were lower compared to the non-aged glass because stress relaxation was provided by the residual glass (Chang, Lin et al. 2009, Hsiu-Tao Chang 2009, Chang, Lin et al. 2010). Milhans and co-workers found that creep properties of BCAS glass-ceramics depended on crystalline volume fraction, the higher the percentage of crystalline phase the more creep resistant the glass-ceramic was (Milhans, Khaleel et al. 2010, Milhans, Li et al. 2011). However, the mechanical and creep properties of the BCAS sealants are not stable over long thermal cycles as they tend to crack.

Reinforcement of BaO–CaO–SiO₂ ternary system with addition of small amounts of Al₂O₃, B₂O₃, V₂O₅, ZnO to make a composite glass-ceramic with 0-30mol% alumina and YSZ improved the mechanical properties compared to the composition without reinforcement (Liu, Sun et al. 2008, Zhao, Malzbender et al. 2011). The composite contained particles and short fibres which deflected cracks and prevented propagation in the matrix, which in turn improved fracture toughness. The use of the fillers tends to enhance the long term stability of TEC especially at elevated temperatures (Choi and Bansal 2008, Zhao, Malzbender et al. 2011). After crystallization, micro-voids do develop in the glass and aging is known to change the mechanical properties of the amorphous phases by smearing the boundary joining them to crystalline phases. The difference in TEC between the crystalline and amorphous phase induces micro-voids which can degrade the Young's modulus of the sealant especially at room temperature. Although the presence of micro-cracks and micro-voids was found to degrade the Young's modulus of a glass-ceramic sealant composition 22.1SiO₂-7.3B₂O₃-5.4Al₂O₃-56.4BaO-8.8CaO at room temperature, reheating back to operation temperature caused self-healing of the cracks by residual glass and this potentially restore the mechanical properties to their undamaged level with the rise in temperature.

Apart from BCS and BCAS systems, the indentation fracture toughness behaviour of borosilicates with composition (30-35)SiO₂-(3-8) B₂O₃-(3-8)Al₂O₃-(30-35)SrO-(15-20)CaO-3A₂O₃ (A= La, Y) in mol%, has been studied by (Abdoli, Alizadeh et al. 2014). The lanthanum containing sealant was found to have a hardness and elastic modulus than the yttria one. (Abdoli,

Alizadeh et al. 2014). In another study the temperature dependence of Young's modulus and the effects of seal porosity on mechanical properties were reported for an alkali barium silicate composition. There was a linear decrease of Young's modulus as temperature goes from room temperature to about 400°C and porosity and the glass was judged to be unsuitable for sealing applications (Trejo, Lara-Curzio et al. 2012).

More general relationships between the mechanical properties of glasses and composition are discussed in section 2.8 below.

2.7.3 Electrical properties of sealing glasses

The electrical conductivity of glasses is dependent on chemical composition and the spatial arrangement in the glass structure (Eldin and El Alaily 1998). A modifier free glass has low conductivity. For example vitreous silica according to Kingery et al, SiO₂ glass generally has a resistivity $> 10^{14} \Omega \text{ cm}$ at above 200°C (Kingery 1961). With a small addition of sodium of 0.04ppm and at 300°C vitreous silica has a resistivity of about $10^{13} \Omega \text{ cm}$, with further addition of 20 ppm Na leads to a further decrease in resistance to about $5 \times 10^9 \Omega \text{ cm}$ and this reflects the sensitivity of impurities on the electrical properties (Eldin and El Alaily 1998). At room temperature borosilicate glasses are insulating and non-conductive with a specific resistance of 10^{11} to $10^{13} \Omega \text{ cm}$ (Lima, Monteiro et al. 2012). The conductivity of pure borosilicate (SiO₂-B₂O₃) is negligible but it does increase with the addition of modifiers such as Na₂O, or Li₂O and by increasing the concentration of alkali oxide to 50mol% the conductivity increased to as high as $3 \times 10^{-3} \text{ S/cm}$ (a resistivity of $333.33 \Omega \text{ cm}$) measured between 300 to 900 K in air as reported for nuclear waste glasses by Maji et al. (Maji, Jena et al. 2016).

Alkali ions in glasses are the current carriers and compared to divalent oxides they are more mobile and therefore the conduction characteristic depends on the amount and type of the alkali ions. The mobility of the alkali depends on its size, bonding between the ion and O²⁻ and the strength of the network. For example, Na containing glasses tend to have higher conductivities than K or Li containing glasses because Na⁺ has a smaller ionic size than K⁺ and a lower electrostatic field strength than Li⁺ (Wang, Hu et al. 2008). In general, the electrical conductivity of glasses is caused by the displacement of the modifiers cations by the influence of

the applied electrical field; the conductivity is dependent on the amount of charge carriers and their mobility as given by

$$\sigma = nq\mu \quad \text{Equation 2-19}$$

where n is the concentration of charge carriers, μ is the mobility of the carriers and q is the electrical charge of the carriers (Braunger, Escanhoela et al. 2012). Although electrical conductivity is directly dependent on the amount of charge carriers and their mobility, the mobility does not depend only on the valence and size but also on the compactness of the glass which changes with the amount of charge carriers. As it cannot easily be related to simple proportionality between the concentration of the charge carriers and the conductivity because the conductivity increases more sharply than the concentration. This is because apart from compactness of the glass structure which is very much affected by the modifier concentrations the conductivity is also very sensitive to impurities and especially to the presence of sodium ions, as mentioned above. On the other hand, the rapid increase in conductivity slows down after reaching 50mol% sodium oxide as this is associated with the changes in the glass structure such as in the size of the interatomic distances as reported by (Braunger, Escanhoela et al. 2012).

Sealing glasses for SOFCs must be electrically resistive with a resistivity of $>10^4 \Omega \text{ cm}$ at the operating temperature of 800°C (Lara, Pascual et al. 2006). The effect of network formers and modifiers on resistivity is better established than that of intermediate and additives as their behaviour varies with compositional changes. The effect of combined or mixed ions on resistivity is that both increases and decreases in resistivity have been observed. Increases in the ionic radii and valence of the modifier ions increases resistivity, and the electrical resistivity of alkaline earth containing sealing glasses for SOFCs are reported to be $>10^4 \Omega \text{ cm}$ (Mahapatra and Lu 2010). Phase evolution during crystallization of glass may cause increases in conductivity compared to the parent glass (Ravagnani, Keding et al. 2003, Lara, Pascual et al. 2006, Mahapatra and Lu 2010). If the phase formed contains alkali ions the conductivity decreases after crystallization; however, on the other hand if the residual glass contains more alkali ions then the conductivity increases after crystallization (Shelby 2005).

Densification reduces the void spaces available in the glasses and therefore hinders the mobility of alkali ions within the glass ceramics by steric constraints (Gomaa, Abo-Mosallam et

al. 2009), and as reported by Ingram et al, densification in crystalline samples increases the activation energy for electrical conductivity as a result of blockage of the preferred pathway for the moving species (Ingram 1989). The polarizability of the oxides in the glasses also plays an important role in the electrical properties. The network formers SiO_2 and B_2O_3 have small elastic shifts or responses to the electric field due to strengthened cross-links in the glass structure resulting in their small polarizability (Borhan, Gromada et al. 2016). The network former cation B^{3+} has a very low polarisability of 0.002 \AA^3 (Yue, Yu et al. 2009) compared that of Si^{4+} (0.0165 \AA^3) (Duffy 2002) but with a very large unit field strength and this will affect strongly the electron charge density of the nearby oxide ions. So increases in B_2O_3 results in low oxide ion polarisability (Yue, Yu et al. 2009). Alumina has intermediate single bond strength and relatively higher polarisability of 0.054 \AA^3 compared with both Si^{4+} and B^{3+} (Dimitrov and Komatsu 2012). In contrast, Ba^{2+} cations with small field strength possess very high polarisability (1.55 \AA^3) so aluminoborosilicate glasses with high boron or silica contents are expected to have low oxide polarisabilities (Duffy 2002).

Cation jumps into interstices and holes within the glass network have been used to explain the electrical conductivity of glasses. A number of interdependent factors are assumed to control the probability of cations jumping; these include the number and the charge of the mobile ions, the separation between the centres of interstices, the number of the interstices and the frequency of the mobile vibrations within the network spaces (Eldin and El Alaily 1998). The conductivity can be described as ionic or electronic depending on whether ionic charges or electrons contribute to the conduction process (Mahapatra and Lu 2010). According to Shelby most oxide glasses such as silicate, borates, germinates and most phosphates exhibit ionic conduction while chalcogenide and some phosphates are electronic conductors (Shelby 2005). Oxide glasses with large amounts of low mobility metal ions such as Ba^{2+} or transition metals such as Zn^{2+} show electronic type conduction and can be classified as highly resistive semiconductors (Moridi, Nouruzi et al. 1991). Further classification suggests that in alkaline and alkaline earth glasses ionic charges control the conductivity while electrons and holes dominates the process in transition metal containing glasses. However, the electrical resistivity of sealing glasses are affected by both types of conduction mechanisms (Mahapatra and Lu 2010).

Alkaline earths in borosilicate glasses are believed to be the charge carriers but it is not clear whether the mechanism of ionic movement is through a vacancy or interstitial process (Ghosh, Sharma et al. 2010); Anderson Stuart theory suggests a vacancy mechanism where cationic movement is primarily by jumping into nearby equivalent space, while the Elliot model can be interpreted as an interstitial mechanism because the jumping process itself must have been triggered by flow and arrival of other cations. Lara et al pointed out that in a homogeneous glass structure, an interstitial mechanism would be favoured because additional cations are not restricted to trigger ionic movement in all different directions. However, if the glass structure contains silica tetrahedral rings which form layers or alternate with other structures this may favour a vacancy conduction mechanism (Lara, Pascual et al. 2006).

In sodium borosilicates or sodium boro-aluminosilicate glasses, the migration of Na^+ cations is by a point defect mechanism in which the diffusivity of alkali causes electrical conduction. The mode of conduction below T_g is considered to be a collective jump mechanism by some researchers (Schober and Laird 1991), while others invoke a defect mechanism based on local density variations in these amorphous materials. The concept of a single ionic jump mechanism is well established in the literature for silicate-based oxide glasses (Souquet, Lévy et al. 1994).

The diffusion mechanism (Neyret, Lenoir et al. 2015) which was originally proposed for ionic crystals, says that cation displacement comes from migration of interstitial cation pairs. In silicate glasses, monovalent cations associate themselves with NBOs and this is referred to as the normal position. When given enough thermal activation the cation is forced to jump from its normal position to an interstitial site and this creates a vacancy by leaving the previous position it occupied. Normal sites are usually close together in oxide glasses whose alkali content is in excess of 10 at%. The departing or displaced cation does share NBOs with other cations. This means that two cations, one occupying a normal position and the other in a defect position or site, are sharing the same NBO and they form interstitial cation pairs similar to Frenkel defects in ionic crystals. Thermal activation is required and below T_g the mechanism of conduction is the single jump type (Neyret, Lenoir et al. 2015) whereas above T_g the conduction mechanism is the cooperative free volume type (Grandjean, Malki et al. 2007).

The frequency dependence of conductivity at high frequency of the glass-ceramics is generally related to hopping of charge carriers between different localised states as reported by Borhan et al. for barium aluminosilicate glass-ceramics with CaO, CoO, and B₂O₃ additives. This suggests an increase in hopping rate with frequency (Borhan, Gromada et al. 2016). Capacitance decreases with increasing frequency because at low frequency the permanent dipoles can align themselves along the field and contribute to the total polarisability of the dielectric. At higher frequencies, the change in electric field is very rapid and hence the dipoles cannot align themselves and therefore have negligible contribution to polarisability and hence the dielectric permittivity decreases with increasing frequency (Yue, Yu et al. 2009). It is important to consider atom to atom distances or average site spacings and polaron radii when discussing the mechanism(s) of conduction related to polaron hopping (an interaction between electrons and atoms). As reported by Moridi et al, (Moridi, Nouruzi et al. 1991), the electrical conductivity mechanism in barium borosilicate is due to small polaron hopping. A polaron is a quasi-particle studied in both ordered and disordered solids to understand electron-atom interactions in solid materials. So a small polaron is an electron that sits in a potential well due to ionic displacement it created and then is confined to a volume equal to a unit cell or less. It requires thermal energy in addition to electric field to move as hopping is required for conduction to take place. Conductivity in this process is low and increases with temperature. So the electrical conductivity can be discussed in relation to polaron and site separation which is the mean distance between similar atoms. This mechanism of electrical conduction is best described by the thermally activated polaron hopping theory. This theory states that electrons together with lattice deformation hop between transition metal ions from a lower to a higher oxidation state. In other words experimental data can be discussed by using Mott's and Holstein's theory which suggest that charge carriers move as hopping of polarons in the glass and glass ceramic between two metal ions (Kupracz, Lenarciak et al. 2017). The average site spacing R is given by (Moridi, Nouruzi et al. 1991).

$$R=(1/N)^{1/3} \quad \text{Equation 2-20}$$

where N is the concentrations of ions given by

$$N=\frac{\rho MN_A}{AW \times 100} \quad \text{Equation 2-21}$$

and ρ is density, M is the weight percent of oxide eg BaO in glass and N_A is Avogadro's number and A_w is the atomic weight of oxide under consideration eg BaO. The polaron radius (r_p) given by

$$r_p = \frac{1}{2} \left(\frac{\pi}{6N} \right)^{1/3} \quad \text{Equation 2-22}$$

The decrease in resistivity of the glass as temperature increases has been cited as evidence for the presence of an ionic conduction mechanism in the glass. If the amount of network modifiers is higher then significant expansion of the glass structure occurs because of the presence of the larger ions, thus these ions can migrate more freely and have lower activation energy for conduction (Eldin and El Alaily 1998). Below T_g the electrical resistivity follows Arrhenius behaviour (Mahapatra and Lu 2010).

$$\rho = \frac{T}{\lambda} \exp \left(\frac{E}{kT} \right) \quad \text{Equation 2-23}$$

Here E , λ , T , and k represent activation energy for ionic conductivity, pre-exponential factor, temperature and the Boltzmann constant, respectively. On the other hand, above T_g the decrease in electrical resistivity follows the Vogel-Tammann-Fulcher equation (Mahapatra and Lu 2010).

$$\rho = \frac{T}{\lambda} \exp \left(\frac{B}{T-T_1} \right) \quad \text{Equation 2-24}$$

where λ , B , and T_1 are specific constants. In electrical conductivity where VFT law applies, a sort of cooperative transport mechanism is reported to exist resulting in enhanced conductivity above T_g possibly due to network rearrangement enabling easier diffusion of the mobile species (Grandjean, Malki et al. 2007).

2.7.4 Dielectric constant of sealing glasses

The dielectric constant of a material provides information on electrostatic properties such as capacitance and energy storage capabilities. The complex dielectric constant consists of real and imaginary parts $\epsilon = \epsilon' + i\epsilon''$, where ϵ' is the real and ϵ'' is the imaginary part. The ratio of the imaginary part divided by the real part gives the loss tangent (Liu, Zhao et al. 2008).

$$\text{Loss tangent } \tan \delta = \epsilon''/\epsilon' \quad \text{Equation 2-25}$$

The loss tangent is related to the ratio of the energy dissipated per radian in a given materials (ϵ'') to the energy stored (ϵ') at the peak of polarization by the electric field (Darwish and Gomaa 2006). Dielectric loss is the phase difference due to energy loss within the sample at a given frequency, and the contribution to the dielectric loss is mainly associated with thermally activated relaxation of freely rotating dipoles where the thermal energy is the only type of relaxation and as temperature increases it is due to electrical conduction as a result of hopping motion of ions (Pal, Agarwal et al. 2009). The dielectric loss can be categorised into intrinsic and extrinsic loss. The intrinsic loss is crystal structure dependent and is a result of crystal lattice interactions with an applied external electric field, while extrinsic loss is related to microstructural features of the material such as defects, porosity, impurities and microcracks (Chovanec, Galusek et al. 2012).

The following primary processes are the cause of energy losses from dielectric materials: ion migration loss, ion vibration and deformation loss and electronic polarization losses. Among these losses, ion migration losses which includes dc conductivity loss, ion jump and dipole relaxation losses is the major factor affecting the use of ceramic materials because this type of loss increases at lower frequencies and also with increasing temperatures (Wang, Hu et al. 2008). The total polarization in a given sample is the sum of all the different contributions to polarization (Morsi, Ibrahim et al. 2016). Modifiers have a role in dielectric losses of glasses, the dielectric loss increases with the diffusivity in the glass structure. For example, the order for alkali elements is $\text{Li} > \text{Na} > \text{K}$. Mg^{2+} ions have higher dielectric loss due to their high mobility compared to Ca^{2+} ions and Zn^{2+} ions due its polarizable nature (Wang, Hu et al. 2008). Since the electrical resistivity for alkaline earth increases in the order $\text{Ba}^{2+} > \text{Sr}^{2+} > \text{Ca}^{2+} > \text{Mg}^{2+}$ it means the dielectric loss will be highest for Mg^{2+} and lowest for Ba^{2+} ions (Mahapatra and Lu 2010).

The dielectric constant is a result of the combined effect of the contributions to polarizability from electronic, ionic and dipole orientations. The dielectric constant increases as the total polarization rate increases. The contributions from electronic and ionic components (α_e and α_i) only are considered or taken into account at high frequencies. These contributions are dependent on ion radius and atomic weight. Hence, larger ionic radii give rise to a greater electronic contribution α_e and larger atomic weight favours low ionic contributions α_i . For

example K^+ and Na^+ containing glasses $62SiO_2-25B_2O_3-1.2Al_2O_3-5.4CaO-6.4A_2O$ ($A=Na$ or K) have similar dielectric constants because they have similar total polarizabilities. The K^+ is larger in size and has larger α_e than Na^+ while Na^+ has a lower weight and so has larger α_i compared to K^+ . The atomic weight of divalent ions contributes to dielectric constant. For example, Ca^{2+} compared to Mg^{2+} has higher atomic weight and therefore contributes smaller α_i hence a smaller dielectric constant. In the case of Zn^{2+} which has a larger atomic weight meaning lower ionic contributions, however, due to electron polarization of its 18 electron structure it has high α_e and so its dielectric contribution is similar to Mg^{2+} despite the difference in weight as reported in (Wang, Hu et al. 2008). Decreases in dielectric constant with increasing boron oxide content have been observed by Yue et al, as a result of the reduction in the number of polarons per unit volume (Yue, Yu et al. 2009). In addition, boron-rich glasses also exhibit a high tangent loss at higher frequency if for example the additions of boron against silica lead to oxygen bridges of the Si^{4+} ions being broken and therefore weakening the glass structure. Consequently, glass resistivity also decreases with boron swapped (on molar basis) for silica this is expected because addition of boron does not add mobile ions to the glass which can help move electric current (Borhan, Gromada et al. 2016).

The dielectric constant can be used to represent the ease with which electric dipoles are formed so a structure which is more loosely bound and with more irregular polyhedra is expected to have higher dielectric constant (Mccauley 2000). The frequency dependence of dielectric parameters is referred to as dispersion of the dielectric (Yue, Yu et al. 2009). Large amounts of alkali in glass decrease the dielectric constant likely due to alkali–alkali distance reduction as the concentration of the mobile ions increases and this enhances their interactions. This increased interaction of the mobile ions may lead to decreased interactions of the dipoles, hence a reduction in dielectric constant (Darwish and Gomaa 2006).

In a polycrystalline glass-ceramic, space charges may arise from the grain boundary conductivities of the different phases leading to a high dielectric constant at low frequency while at high frequency the dielectric constant is dominated by grains with a low dielectric constant. Decreasing dielectric and tan delta with frequency is a normal behaviour of dielectric materials with mobile charge carriers (ions and/or electrons) especially at room temperature. The decrease in the dielectric constant is as a result of the fact that the polarization does not occur

instantaneously with the electric field as charges have inertia. In other words, the decrease in dielectric constant is due to a delay in response to the applied alternating electric field. Most dielectric ceramics have high conductivities at higher temperatures (Prasad and Basu 2013). Conductivity increases with frequency due to hopping of charge carriers between localized states. In summary, the conductivity is increased with availability of charge particles while space charge formation increases the dielectric constant (Borhan, Gromada et al. 2016). The accumulation of this space charge at broken bonds or chains is the cause of increase in dielectric constant observed at lower frequencies (Darwish and Gomaa 2006)

2.8 Mechanical property structure relationships for glasses

In general the Young's modulus is proportional to the number of chemical bonds per unit volume and average bonding strength in the glass structure, while the hardness is related to elastic strength and to the complex behaviour of resisting mechanical deformation on the surface of the glasses (Hirao, Yoshimoto et al. 1991). Densification of glasses cause increases in Young's modulus and hardness due to elimination of free voids and increase in the number of bonds per unit volume of the glass structure.

There is a linear relationship between E and hardness as can be seen from equation (2-26) as reported by Yamane et al, (Yamane and Mackenzie 1974).

$$H_v = 0.051 \left(\frac{\alpha}{0.462 + 0.09C_g - C_g^2} \right)^{0.5} E \quad \text{Equation 2-26}$$

where α and C_g are mean single bond strength with respect to Si-O and packing density of the glass. Both E and hardness depend on bond strength and how closed packed atoms or ions are in the glasses, although hardness may involve some form of plastic deformation during indentation. Generally, both parameters are composition dependent for example boron in 4 fold coordination has stronger B-O bonds than in 3 fold coordination and therefore increases both E and hardness of the glass (Yoshida, Tanaka et al. 2001).

According to fracture mechanics the fracture toughness and Youngs modulus are related by

$$K_{Ic} = \left[\frac{2E\gamma_f}{1-\nu^2} \right]^{0.5} \quad \text{Equation 2-27}$$

where the quantities E , γ_f , and ν represent Young's modulus, surface energy of new created surfaces and Poisson's ratio respectively. The surface energy γ_f can be related to E by

$$\gamma_f = \left(\frac{E}{r_o}\right) \left(\frac{r}{\pi}\right)^2 \quad \text{Equation 2-28}$$

r_o is the average interatomic distance between atoms and r is a measure for the range of interatomic forces. From equations 2-27 and 2-28 above the following is derived

$$K_{Ic} = f(r_o, r, \nu)E \quad \text{Equation 2-29}$$

From the above relationship fracture toughness is proportional to Young's modulus and the proportionality constant is dependent on the separation between atoms, interatomic bond strength, and Poisson's ratio. The similarity in character of the glass network bonding gives a linear relationship between K_{Ic} and E (Hirao, Yoshimoto et al. 1991).

However, discrepancies do occur where E increase and fracture toughness decrease. Such discrepancies can be explained based on the fact that fracture toughness is not associated only with energy required to break or fracture bonds but also with energy dissipating process such as plastic deformation, crack branching and blunting occurring at the crack tip. For example borate glasses are known to exhibit large inelastic dissipation energies, the magnitude of which depends on the modifier content. Another way to explain difference between E and K_{Ic} is to consider the ease of plastic deformation. Fracture toughness increases for large plastic deformation. (Yoshida, Tanaka et al. 2001). A clear correlation between E and K_{Ic} in borosilicate glasses to a larger extent than aluminosilicate glasses have been observed by Eagan et al (Eagan and Swearingen 1978).

In trying to understand the elastic properties of silicate glasses qualitative bond strength related arguments has been proposed. For example Charles suggested that the weak bond between modifiers and NBOs decreases the rigidity of silicate glasses (DeGuire and Brown 1984). On the other hand Dietzel proposed that the interatomic bond strength increases elastic modulus and this was later supported by Loewenstein who proved that high field strength cations like Li^+ , Be^{2+} , Mg^{2+} lead to increase in Young's modulus of silicate glasses (DeGuire and Brown 1984). In the case of multi-oxide glasses the dependence of elastic moduli on composition is only partially consistent in relation to the simple bond strength prediction looking at equation 2-26

packing density also matters. For example from Charles reasoning most alkalis should decrease the Young's modulus when added to silica, whereas from Dietzel's point of view the elastic moduli should increase with modifier field strength. However, the modulus increases with Li_2O despite the fact the Li-O bond is electrostatically weaker compared with the shorter Si-O bond (DeGuire and Brown 1984). Mallinder and Proctor explain that if only compositional changes and not applied stress bring oxygens close together, then E should increase because moduli increases as modifier field strength increases. They also added that Li_2O decreases the volume (V_o) per gram atom of oxygen in alkali silicate and that V_o is inversely related to the Young's modulus. Thus adding large modifier such as BaO increases the volume and decreases Young's modulus of the glasses (DeGuire and Brown 1984).

The Poisson's ratio of a material gives a measure of the resistance of the material to volume change as well as to shape change (Greaves, Greer et al. 2011). Poisson's ratio is small for shear resistant but compressible materials such as cellular solids and can reach 0.5 for incompressible bodies such as rubber.

Glasses fall in between these two and have values from 0.1 to 0.4 and specifically for oxide glasses mainly in the 0.16 - 0.3 with highly polymerised silica rich glass having the lowest value of ν and the highest for glass networks consisting of chains and cluster units (Rouxel and Ji 2008). Changes in Poisson's ratio as well as fractal bond connectivity suggest changes in the network dimensionality of the glass (Abd El-Moneim, Youssof et al. 2006, Rouxel 2007). Open structures based on corner sharing tetrahedra of amorphous silica and germania are highly polymerised and this results in strong resistance to transverse contraction and hence they exhibit low ν of 0.15 and 0.19 respectively and the K_{Ic} of tetrahedrally coordinated $\nu\text{-SiO}_2$ is $0.7 \text{ MN m}^{-3/2}$ (Sehgal and Ito 1999). B_2O_3 glass with corner sharing triangular BO_3 units is characterised by Poisson's ratio of 0.26, an increase in ν suggest smaller extent of densification (Rouxel and Ji 2008). However, the brittleness defined as ratio of H/K_{Ic} and fracture toughness of $\nu\text{-B}_2\text{O}_3$ with values of $1.20 \mu\text{m}^{-1/2}$ and $1.44 \text{ MN m}^{-3/2}$ reported by Sehgal and Ito (Sehgal and Ito 1999). These improved properties may be due to the planar trigonal and boroxol group like structures of B_2O_3 providing plastic flow through sliding due to slip of the boroxol ring as the energy required for plastic deformation is decreased with boroxol rings (Hirao, Matsuoka et al. 1989).

The intrinsic strength of glasses has been estimated based on the assumption that the fracture of glass is controlled by the Si-O bond strength. The calculated force to break this bond in fused silica was 18 GPa. The strength of bulk glasses in practical applications is 100-1000 times lower than its theoretical strength due to presence of surface flaws which induces stresses in the glasses (Eagan and Swearekgen 1978). The strength of oxide glasses is better estimated by $E/10$ which suggests that oxide glasses can have strengths up to 7000 MPa. However, in practice this value rarely exceeds 100 MPa (Donald 1989). The strength of multi-component glasses consisting of network formers and modifiers maybe related to the elastic modulus, the silicon-oxygen bond density and the bond strength (Eagan and Swearekgen 1978).

Another factor limiting the use of oxide glass especially for structure bearing applications is the phenomenon of static fatigue which is a situation in which depending on the environment a material fails from small pre-existing defects due to continuously applied stress far less than that required for fracture. Crack propagation becomes catastrophic in this condition as soon as the crack size reaches a critical size. The mechanical strength of oxide glasses therefore is controlled by the environment and time (Adams and McMillan 1977, Donald 1989). Water present in the environment is the common corrosive medium attacking oxide glasses (Michalske and Freiman 1983, Donald 1989).

Recent work by both Sellappan *et al.* (Sellappan, Rouxel *et al.* 2013) and Tiegel *et al.* (Tiegel, Hosseinabadi *et al.* 2015) have shed more light on the mechanical response of glasses under sharp contact loading. The resistance to contact contact damage has been classified by the value of the Poissons ratio as resilient glass $0.15 < \nu < 0.20$, semi-resilient $0.20 < \nu < 0.25$ and easily damaged glasses $0.25 < \nu < 0.30$ respectively (Sellappan, Rouxel *et al.* 2013, Tiegel, Hosseinabadi *et al.* 2015). Resilient is a general name describing less brittle glass capable of absorbing sharp contact loads and resist cracking. The semi-resilient glasses resist cracking by absorbing loads up to 0.3N and they show characteristic 3 to 4 corner cracking at loading higher than 0.3 N and easily damaged glasses are the very brittle ones with larger poisons ratio (Sellappan, Rouxel *et al.* 2013). Connelly *et al.* reported an inverse correlation between K_{Ic} and E , however, from equation 2-29 a linear correlation would be expected (Connelly, Hand *et al.* 2011). However, as the composition varies the values of the fracture toughness and Young's modulus may also change just like the mixed alkali silicate glasses which exhibit some of the largest indentation

fracture toughness values but have relatively low Young's moduli (Sellappan, Rouxel et al. 2013).

Finally thermo-mechanical stresses are generated during SOFCs operation and are estimated based on three parameters as in the following equation.

$$\sigma = \Delta E \times \alpha \times \Delta T \quad \text{Equation 2-30}$$

where ΔE , α , ΔT are change in Young's modulus, TEC and temperature.

3 Experimental procedures

3.1 Glass melting

Here sample preparations including compositional batch formulation, glass melting and mechanical processing such as (cutting, grinding and polishing) and subsequent annealing are presented. Followed by characterisation techniques involved also discussed. 6 series of compositions were produced (see table 3.1) for initial molar batched amounts and compared with x-ray fluorescence (XRF) data in table 3.3. In each case batches were designed to produce 300 g of glass. SiO_2 , B_2O_3 , $\text{Al}(\text{OH})_3$, La_2O_3 , BaCO_3 , ZnO , and SrCO_3 were used as raw materials; sources and purities given in table 3.2. The batched powders were manually mixed thoroughly using a spatula until a fine uniform mixture was obtained. The well mixed batch was transferred to a zirconia stabilized platinum crucible and heated to 1200°C - 1450°C depending on the series in an electric furnace for up to 5 hours. After allowing one hour achieving a batch free melt a Pt stirrer was inserted into the melt, and the melt was stirred for the remaining 4 hours of melting to achieve homogenization. Finally the molten glass was cast into a pre-heated stainless steel mould to avoid thermal shock. After a short cooling time to enable sufficient solidification so that the glass could maintain its shape the mould was removed and the hot glass was transferred to an annealing furnace, where it was held at the annealing temperature, $\pm 50^\circ\text{C}$ of the T_g for each glass series for one hour and then cooled to room temperature at a rate of $1^\circ\text{C}/\text{min}$. The glass code as presented in table 3.1 represents the two oxides swapped for each other for each series for example $x\text{B}(15-x)\text{Zn}$ refers to boron swapped for zinc oxide however to explain a particular series within itself $x\text{B}(15-x)\text{Zn}$ will be simplified to $10\text{BZn}15$, $12.5\text{BZn}12.5$, $15\text{BZn}10$, $17.5\text{BZn}7.5$ and $20\text{BZn}5$ mol% etc and therefore to refer to the whole series they stand as $x\text{B}(15-x)\text{Zn}$, $x\text{Si}(20-x)\text{Zn}$ etc. in the case of LaSi series Ba and Sr in brackets indicates the only difference between two in terms of oxides one contains barium and the other strontium oxide and remaining oxides are the same not exactly in quantity but in type.

Glass Code	Compositions in mol%	Melting (°C)	Annealing (°C)
xB(15-x)Zn	10BaO-(15-x)ZnO-15La ₂ O ₃ -5Al ₂ O ₃ -(10+x)B ₂ O ₃ - 45SiO ₂ (X= 2.5, 5, 7.5, 10)	1350	650
xSi(20-x)Zn	10BaO-(20-x)ZnO-15La ₂ O ₃ -5Al ₂ O ₃ -10B ₂ O ₃ - (40+x)SiO ₂ (X= 2.5, 5, 7.5)	1350	650
xBa(40-x)Si	(15+x)BaO-5ZnO-15La ₂ O ₃ -5Al ₂ O ₃ -20B ₂ O ₃ - (40+x)SiO ₂ (X= 2.5, 5, 7.5, 10)	1330	650
xBa(10-x)Al	(10+x)BaO-5ZnO-20SrO-(10-x)Al ₂ O ₃ -20B ₂ O ₃ - 35SiO ₂ (X= 2, 3, 4, 5)	1250	600
xSi(20-x)La(Ba)	10BaO-15ZnO-(20-x)La ₂ O ₃ -5Al ₂ O ₃ -10B ₂ O ₃ - (40+x)SiO ₂ (X= 5, 10, 15)	1450	650
xSi(20-x)La(Sr)	15SrO-10ZnO-(20-x)La ₂ O ₃ -10Al ₂ O ₃ -15B ₂ O ₃ - (30+x)SiO ₂ (X= 5, 7.5, 10, 12.5, 15)	1430	650

Table 3.1: Nominal molar compositions for all series

Oxides	Raw chemicals	Purity	Supplier
SiO ₂	Silica, SiO ₂	99.8%	Glassworks services, Ltd Doncaster, UK
B ₂ O ₃	Boric acid, H ₃ BO ₃	99.5%	Sigma-Aldrich, UK
Al ₂ O ₃	Aluminium hydroxide, Al(OH) ₃	99.5%	Fisher chemical, UK
BaO	BaCO ₃	99%	Fisher chemical, UK
SrO	Strontium carbonate, SrCO ₃	99%	Fisher chemical, UK
ZnO	Zinc oxide, ZnO	99.8%	Fisher chemical, UK

Table 3.2: Raw materials used for glass batching

3.2 Density measurement

The density of powdered glass samples was measured using an AccuPyc II 1340 pycnometer gas displacement system. The system uses helium (99.995% pure) as its medium to measure volume of the glass powder by measuring the pressure change of the helium in a calibrated volume. If the

weight of the sample is known then the density is automatically worked out by the system. The measurement is done in two steps:

- 1) Purging helium into the chamber to clean the sample and the chamber of air and moisture and this is done by selecting 25 cycles of cell filling and expulsion using the helium gas.
- 2) The sample volume is measured by filling the sample cell with the gas medium to the required filling pressure. The final pressure (P_f) at equilibrium was recorded as the gas expands in the expansion cell. The volume of the sample was determined using:

$$V_s = V_{sc} - \frac{V_{ex\ c}}{(P_r/P_f) - 1} \quad \text{Equation 3-1}$$

where V_s is the volume of sample and V_{sc} is the volume of sample cell and $V_{ex\ c}$ is the volume of expansion cells all in cm^3 . The P_r and P_f are the run fill pressure and final pressures respectively. The Accupyc 1340 was accurate to approximately 0.03% of the reading plus 0.03% of nominal full-scale cell chamber volume.

3.3 XRD analysis

Powder X-ray diffraction (XRD) was used to verify if the samples were amorphous or contained some crystalline phases. Both crystalline and glass samples were crushed to fine particles less than $150\mu\text{m}$ in size and room temperature measurement was carried out using a Siemens D5000 XRD machine with $\text{Cu K}\alpha$ ($\lambda=1.54056\text{\AA}$) radiation. The radiation source was operated at 40 kV and 40 mA. The samples were scanned from $15-70^\circ 2\theta$ with a step size of 0.04 at a scan rate of 4.8 s per step.

The principle of operation for X-ray diffraction (see fig 3-1) is based on Bragg's law which states

$$2d\sin\theta = n\lambda \quad \text{Equation 3-2}$$

where n in the equation stands for the order of diffraction and d is the distance between parallel planes of atoms. The interplanar spacings d in the crystal structure of the sample give rise to a characteristic diffraction angle for any given wavelength of X-rays. No two crystal structures have the same diffraction pattern hence XRDs provide specific information about the crystal structure and so that each crystalline phase can be identified.

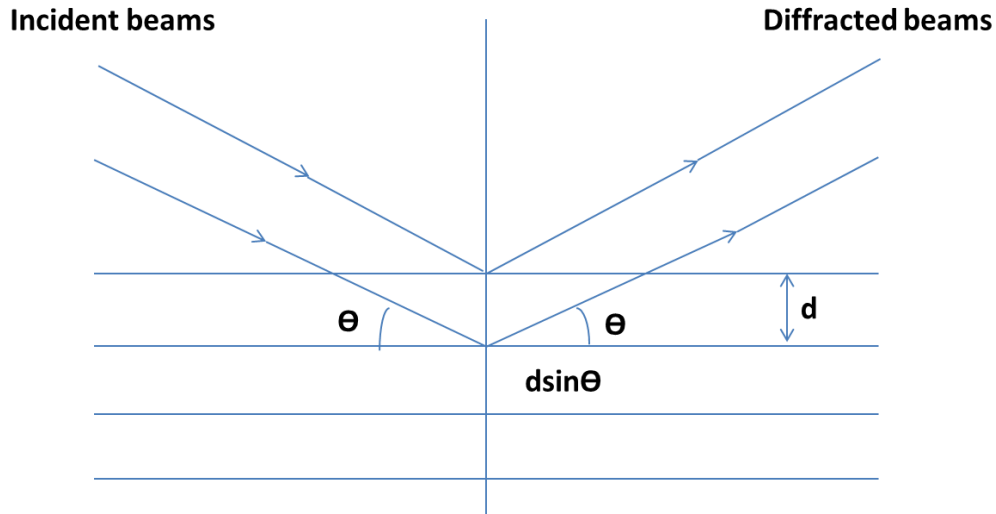


Figure 3 -1: Schematic diagram of X-ray diffraction in crystals

Sharp peaks appear on the XRD pattern of crystalline samples while for amorphous glass broad peaks are seen which can be correlated to silica and borate units. These peaks appear broad because of the disordered nature of atoms in the amorphous material such as glass. Superimposed crystalline peaks in the glass hump are a common feature of XRD pattern of glass composite materials. The XRD patterns of the crystalline phases were analyzed using the database ICDD PDF4+ software. Fig 3-1 is a schematic diagram of X-ray diffraction in crystals.

3.4 X-ray fluorescence (XRF)

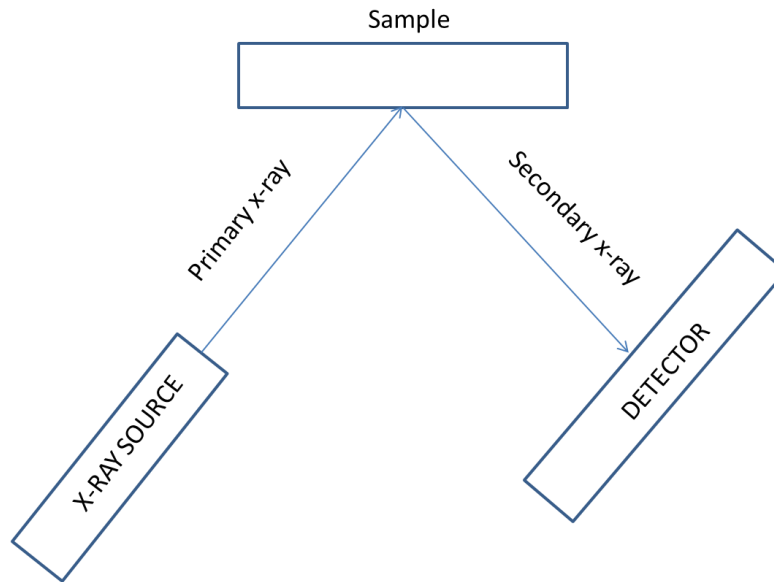


Figure 3-2: Schematic drawing of XRF functional structure

Generally all x-rays consist of two components an x-ray source and a detector and sometimes a filter inserted between the primary x-ray and sample to modify the x-ray. A stable atom consists of nucleus and electrons orbiting it, the electrons are on different levels and shells according to their energy levels. When a high energy from the primary source hit the sample it disturbs its stability and knocks out inner k-shell lower energy electron and creates a vacancy. Immediately after an electron from higher energy level for example L-shell drops to the K-shell and replace it and releases energy in doing so which is referred to as secondary x-ray. The energy released as secondary x-ray is characteristics of that particular element. XRF can be used for both qualitative and quantitative information. So the collected secondary x-ray by the detector is processed into a spectrum and the peak energy identifies the elements while the intensity gives the concentration of the element. To measure the elemental composition of the borosilicate glass samples in this study a bulk rectangular samples approximately 10×10×6 mm were used. After mounting the sample in a sample cup and then placed in the sample trays in the XRF machine and note the sample position. Click on measure tab and then analyse and thereafter open the sample changer sub-routine. Delete any existing program using the red “X” tool and then click on sample position and then add measurement and verify the position and make sure the position “type” is set to Routine. Then next set priority to normal and make sure the tab with cup is ticked and now

click add and then return to overview screen and click on your sample position followed by the measure button. After running for 20 minutes the elements are displayed in weight percent and then converted to oxide without normalization using the software on the system and from that boron was estimated by difference due to difficulty in measuring it as it's a light element.

Glass code	SiO ₂	B ₂ O ₃	Al ₂ O ₃	La ₂ O ₃	BaO	ZnO
10BZn15	46.16(45)	9.29(10)	5.08(5)	14.56(15)	9.68(10)	15.22(15)
12.5BZn12.5	47.33(45)	12.22(12.5)	4.96(5)	15.47(15)	9.29(10)	12.73(12.5)
15BZn10	47.18(45)	15.83(15)	5.09(5)	14.75(15)	8.98(10)	8.17(10)
17.5BZn7.5	47.95(45)	17.52(17.5)	4.77(5)	14.31(15)	8.57(10)	6.87(7.5)
20BZn5	47.97(45)	15.83(20)	5.11(5)	16.04(15)	9.86(10)	5.19(5)
Glass code	SiO ₂	B ₂ O ₃	Al ₂ O ₃	La ₂ O ₃	BaO	ZnO
40SiZn20	41.54(40)	9.01(10)	5.03(5)	14.19(15)	10.86(10)	19.37(20)
42.5SiZn17.5	44.87(42.5)	8.44(10)	5.01(5)	14.28(15)	10.17(10)	17.23(17.5)
45SiZn15	46.16(45)	9.29(10)	5.08(5)	14.57(15)	9.68(10)	15.22(15)
47.5SiZn12.5	47.95(47.5)	9.52(10)	4.77(5)	14.31(15)	9.57(10)	13.88(12.5)
Glass code	SiO ₂	B ₂ O ₃	Al ₂ O ₃	La ₂ O ₃	BaO	ZnO
15BaSi40	45.07(40)	16.92(20)	5.34(5)	13.97(15)	14.13(15)	4.57(5)
17.5BaSi37.5	39.58(37.5)	19.05(20)	6(5)	13.63(15)	17.21(17.5)	4.53(5)
20BaSi35	36.88(35)	20.7(20)	4.23(5)	13.62(15)	19.45(20)	5.06(5)
22.5BaSi32.5	32.93(32.5)	19.4(20)	4.51(5)	14.35(15)	22.68(22.5)	5.03(5)
25BaSi30	31.25(30)	19.85(20)	5.09(5)	13.15(15)	24.15(25)	5.51(5)
Glass code	SiO ₂	B ₂ O ₃	Al ₂ O ₃	SrO	BaO	ZnO
10BaAl10	35.09(35)	19.29(20)	9.44(10)	22.6(20)	9.36(10)	4.22(5)
12BaAl8	35.87(35)	17.33(20)	8.91(8)	19.18(20)	13.24(12)	5.47(5)
13BaAl7	35.82(35)	18.11(20)	8.37(7)	19.42(20)	14.17(13)	4.11(5)
14BaAl6	35.55(35)	17.79(20)	6.17(6)	20.75(20)	15.35(14)	4.45(5)
15BaAl5	34.55(35)	18.43(20)	4.81(5)	20.77(20)	16.22(15)	5.22(5)
Glass code	SiO ₂	B ₂ O ₃	Al ₂ O ₃	La ₂ O ₃	SrO	ZnO
35Si15La(Sr)	35.89(35)	15.09(15)	9.23(10)	15.08(15)	15.37(15)	9.34(10)
40Si10La(Sr)	41.43(40)	14.98(15)	9.68(10)	10.07(10)	15.07(15)	8.77(10)
42.5Si7.5La(Sr)	42.77(42.5)	14.55(15)	10.01(10)	8.33(7.5)	15.44(15)	8.9(10)
45Si5La(Sr)	46.61(45)	13.88(15)	10.21(10)	4.91(5)	15.21(15)	9.18(10)
40Si20La(Sr)	39.67(40)	14.55(15)	7.94(5)	19.28(20)	8.89(10)	9.67(10)
40Si15La(Sr)	40.76(40)	13.2(15)	7.02(5)	16.02(15)	13.24(15)	9.76(10)

Table 3.3: Bracketed figures represent initial molar batched quantities in mol% and unbracketed numbers are XRF analysed data which is semi quantitative and serve as a guide to compositional error

3.5 Thermal analysis

In order to study the thermal properties of the prepared samples a differential thermal analyser (Perkin Elmer TG/DT thermal analyser) was used. Properties such as T_g and T_c were determined. Small amounts of glass powder approximately $40\text{mg} \pm 0.2\mu\text{g}$ in a platinum crucible were heated from room temperature to $1000\text{ }^\circ\text{C}$ ($\pm 0.5\text{ }^\circ\text{C}$) at a heating rate of $10\text{ }^\circ\text{C}/\text{min}$ in air alongside alumina as an inert reference subjected to similar heating profile. The onset point of the first endothermic curve/relaxation peak was used to estimate the value of T_g . Crystallization temperature (T_c) is indicated by an exothermic peak. Glass powder samples ground to the same size as used for the XRD were used for the DTA. Fig 3-2 an example of a DTA graph for one of the samples in this study.

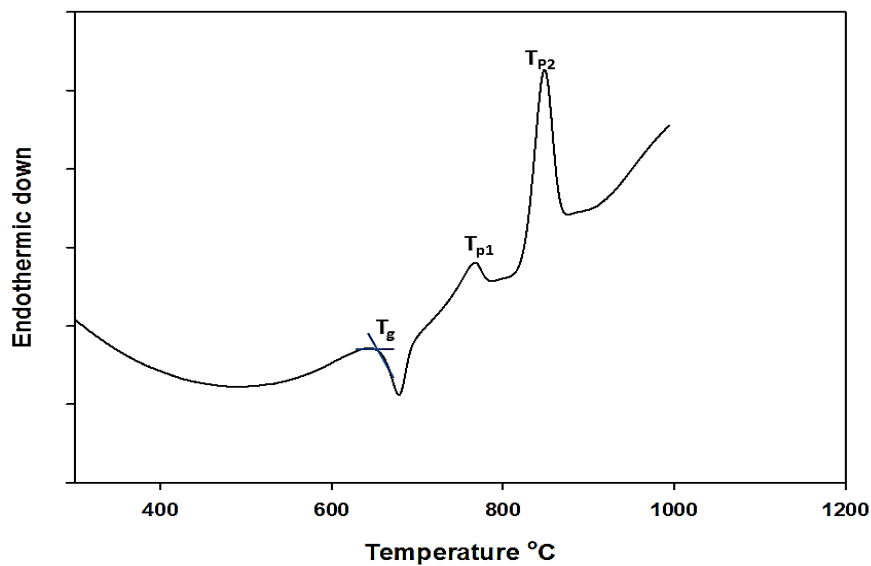


Figure 3-3: DTA graph showing an estimate of T_g (onset) and T_c (crystallization peak maximum)

The thermal expansion coefficients (TEC) were measured using thermo mechanical analyser TMA for all of the glass samples. The samples were sliced into rectangular shapes of size approximately $10 \times 6 \times 6\text{ mm}$ and heated from RT to $650\text{ }^\circ\text{C}$ at $1\text{ }^\circ\text{C}/\text{min}$. Samples were re-measured after crystallization of the samples at $800\text{ }^\circ\text{C}$ for 50 h to assess the effects of any induced crystal phases on the TEC.

3.6 FT-IR spectroscopy

Information about the bonding of the glasses was obtained using Fourier transform infrared spectroscopy (Perkin Elmer Frontier FTIR).

Infrared spectroscopy measures the absorption of infrared radiation by the chemical bonds in molecules of substances. The radiation absorbed by the chemical bonds in the molecules corresponds to the difference in energy of the bonds and are unique for every chemical bond in a molecule. Therefore, this FTIR gives structural information about a given material.

One of the key components of FTIR spectroscopy is the Michelson interferometer. The incoming light is split inside an interferometer; one beam goes to the internal fixed mirror and the other goes to the moving mirror. The split beams recombine after reflection inside the interferometer and undergo both constructive and destructive interference giving the interferogram which contains the spectral information. The intensity pattern is proportional to $\cos^2(2\pi d/\lambda)$ where d is the path difference between the mirrors caused by motion of the movable mirror and λ is the wavelength. Assuming the velocity of the moving mirror is constant c , then the path difference will be $d=2ct$ where t denotes time. After detection and storage of the data a Fourier transform is applied to the data to produce the conventional spectrum.

FTIR is complementary to Raman spectroscopy (see below) because the different vibration modes in the molecules could be Raman-active, IR-active or active for both. In addition both techniques are often used due to the advantage of simple analysis procedure. However there exist some differences in the two techniques (Rehman 2013) as in table 3.3

	Infrared	Raman
Physical effect	Absorption. Dipole moment changes in molecules can be analysed eg strong (ionic bonds like O-H, N-H, C=O).	Scattering. (observing the emissions of scattered light) and changes in the polarization of molecules eg strong (covalent bonds like C=C, C-S) etc.
Sample preparation	Involves sample preparations	Little or samples preparations
Materials or samples	Mainly organic compounds.	Different types of samples in both dry and wet.
Resolution	1-20 μm (beam splitter dependent).	0.05 - 8 μm (laser dependent)
Frequency range	4000-400 cm^{-1} in the mid IR and 30000 – 50 cm^{-1} at far and near IR.	4000-50 cm^{-1}
problems	Presence of water has strong signal effect.	Fluorescence is an issue as some glasses have high fluorescence.

Table 3.4: Comparison between FTIR and Raman spectroscopy (Rehman 2013)

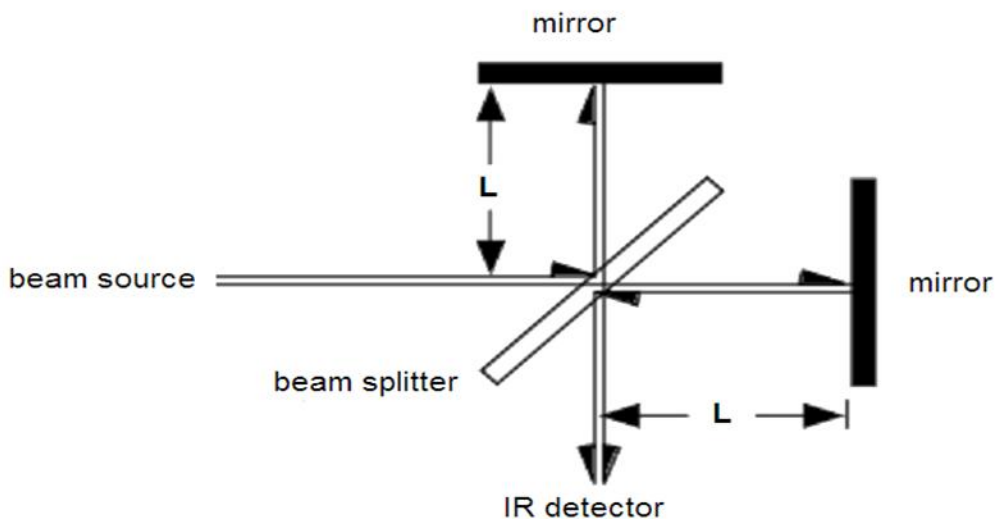


Figure 3-4: Michelson interferometer used in an IR spectrometer

Approximately 2 mg of each sample and 200 mg of KBr was mixed using agate mortar and pressed into pellets of 13 mm diameter using a hydraulic press (Specac[®]). Spectra in the range $400\text{-}4000\text{cm}^{-1}$ were immediately measured. Prior to measurement background scanning was undertaken. Both transmittance and absorbance data were collected after which peaks were assigned different bonds using data in the literature. There absorption bands on the FTIR spectra were assigned as follows. Generally, the presence of diffuse bands indicates the disorder in the silicate network because of wide distribution of Q^n units occurring in the silicate systems (Goel, Tulyaganov et al. 2010, Kumar, Rupali et al. 2011). Bands in the region $800\text{-}1200\text{ cm}^{-1}$ are related to stretching vibration of the SiO_4 unit with different bridging oxygens. Si-O-Si and Si-O-Al linkage bending vibrations and vibrations of bridging oxygen among trigonal boron atoms occurs in the regions $400\text{-}600\text{ cm}^{-1}$. While the Al-O and La-O bonds with the Al and La ions in four fold coordination exhibit stretching vibrations at $600\text{-}800\text{ cm}^{-1}$ (Aronne, Esposito et al. 1997, Goel, Tulyaganov et al. 2010, Kumar, Rupali et al. 2011). The band at wavenumbers around $1370\text{-}1440\text{ cm}^{-1}$ is related to B-O stretching vibrations of BO_3 units whereas BO_4 tetrahedron stretching vibration gives a band at 1000 cm^{-1} (Kumar, Pandey et al. 2010, Kumar, Rupali et al. 2011).

Wavenumber cm^{-1}	Type of bond	
400-500	ZnO ₄ tetrahedral bending vibration units (in zinc borate glasses)	(Cetinkaya Colak, Akyuz et al. 2016)
400-600	Si-O-Si linkages bending vibration	(Środa and Paluszkiewicz 2007, Kumar, Pandey et al. 2010, Kaur, Pandey et al. 2012)
460 462	SiO ₄ bending vibration	(Środa and Paluszkiewicz 2007, Kumar, Pandey et al. 2010, Kaur, Pandey et al. 2012, Cui, Hao et al. 2015)
460	460 is BO ₄ ⁻ group vibration	(Gohar, Doweidar et al. 1990)
470	Si-O-Si and O-Si-O bending modes involving bridging Oxygens (Q ⁴)	(Kumar, Pandey et al. 2010, Kaur, Pandey et al. 2012)
471	Si-O-Si asymmetric bending	(Sun, Xiao et al. 2010)
490	Zn-O peak difficult to observe due to severe vibronic structure between 400-500 and also due to poor resolutions	(Wang, Li et al. 2009)
496	Si-O-Si bending modes in SiO ₄ units	(Sasmal, Garai et al. 2014)
558 and 612	O-Si-O symmetric stretching vibration of SiO ₄ units	(Sasmal, Garai et al. 2014)
643	Vibration from pure La-O in LaO ₄ tetrahedral	(Sasmal, Garai et al. 2014)
650-800	La ³⁺ or Al ³⁺ ions stretching vibration in four fold coordination or bending vibration of bridging oxygen between BO ₃ atoms	(Kaur, Pandey et al. 2012, Sasmal, Garai et al. 2014) (Kumar, Pandey et al. 2010)
700-711	B-O or B-O-B bending vibration modes of BO ₃ units	(Sasmal, Garai et al. 2014, Cui, Hao et al. 2015, Cetinkaya Colak, Akyuz et al. 2016)
724	Bending of B-O-B in BO ₃ and also belongs to AlO ₄ group	(Sun, Xiao et al. 2010)
775 and 801	Six membered borate and boroxol rings with 2 or 1 BO ₄ units observed when B ₂ O ₃ is more	(Cui, Hao et al. 2015)

	than 5mol%	
841	Stretching vibration of B-O of BO ₄ units	(Sasmal, Garai et al. 2014)
923	$\bar{\text{O}}\text{-Si-O}^-$ stretching vibration with two NBOs	(Sasmal, Garai et al. 2014)
988	Si-O-Si asymmetric stretching	(Cui, Hao et al. 2015)
800 and 1200	B-O stretching in BO ₄ units in (Zinc borates)	(Cetinkaya Colak, Akyuz et al. 2016)
800-1300	Broad band indicates stretching vibration of SiO ₄	(Kumar, Pandey et al. 2010, Kaur, Pandey et al. 2012)
850-1100	Two band 925 and 1012 overlapped assigned to stretching to BO ₄ and the later to combine stretching of Si-O-Si and B-O-B network tetrahedral units	(Sun, Xiao et al. 2010)
939	B-O link of BO ₄ group	(Darwish and Gomaa 2006)
990-1200	Overlapping contribution from silicate and borate groups	(Darwish and Gomaa 2006)
1000	BO ₄ tetrahedron not observed due to overlap with SiO ₄ stretching in this region. (formation of SiO ₄ with NBO ions)	(Gohar, Doweidar et al. 1990, Kumar, Pandey et al. 2010, Kaur, Pandey et al. 2012)
1011-1030	Antisymmetric overlapping of BO ₄ and Si-O-Si	(Cui, Hao et al. 2015)
1087	Anti-symmetric stretching vibration of Si-O-Si of SiO ₄ unit	(Sasmal, Garai et al. 2014)
1220	The shoulder is stretching of boroxol ring	(Sun, Xiao et al. 2010)
1200, 1265, 1385	B-O vibrations related to tri BO ₃ and Tetraborate BO ₄ groups	(Sasmal, Garai et al. 2014)
1240 and 1355	Vibrations from borate structure consisting of BO ₃ units only such as Meta, Ortho, and Pyroborate	(Doweidar, Moustafa et al. 2001)
1265	bond stretching of B-O linked with B-O-B units	(Gohar, Doweidar et al. 1990)
1200-1600	B-O stretching vibration of BO ₃	(Darwish and Gomaa 2006,

		Cetinkaya Colak, Akyuz et al. 2016)
1402	Stretching of B-O of BO ₃ characteristics for BO ₃ group	(Sun, Xiao et al. 2010)
1403-1426	Anti-asymmetric stretching of BO ₃	(Cui, Hao et al. 2015)
1300-1500	B-O stretching vibration in BO ₃ (boroxol ring)	(Gohar, Doweidar et al. 1990, Środa and Paluszkiwicz 2007, Kumar, Pandey et al. 2010, Kaur, Pandey et al. 2012)
1600-1640	Weak band of H ₂ O molecular vibration	(Kumar, Pandey et al. 2010, Kaur, Pandey et al. 2012, Sasmal, Garai et al. 2014)
3500	O-H stretching	(Gohar, Doweidar et al. 1990)

Table 3.5: Summary of FTIR assignments

3.7 Raman spectroscopy

The structure of the produced glasses was also characterized by Raman spectroscopy using a Renishaw inVia Raman Microscope). This machine equipped with CCD detector has a spectral resolution of 2 cm⁻¹ and exposure time of 10 s. Glass samples were ground into powder <63μm and scanned by a green laser (514.5 nm, 20 mW) from 50 to 2000 cm⁻¹.

In Raman spectroscopy when a laser beam strikes vibrating molecules, it can excite the atoms or the molecules and shift them to different states. The difference in energy between the original state and the new state of the molecules or atoms produces a shift in the subsequent emitted photon. The excitation moves the molecules to a higher or lower frequency compared to the original state; the former is called Stokes Raman scattering and the latter anti-Stokes Raman scattering. These Raman shifts can be used to distinguish the structures of compositions and molecules. The use of Raman spectroscopy helps to determine the local environment, structure and the dynamics for a glassy material. Raman and IR spectroscopies are complementary to each other. The difference between them is that IR spectra arise from changes in dipole moment while Raman spectra come from changes in polarizability. Raman spectroscopy has the benefit of determining some transitions that cannot be seen in an IR spectrum. In IR spectra the

characteristics of a given sample are determined using absorbance or transmittance spectra. In Raman spectra the y-axis is usually arbitrary and not in absorbance or transmission units as found in IR because it simply represents the amount of scattered photons received by the detector at a given frequency. For example, the peak heights in Raman spectra are not dependent on sample thickness but rather on the power of the incident laser so if the power is varied the intensity of the Raman spectrum also varies. Fig 3-4 is a schematic sketch of the Raman spectroscopy.

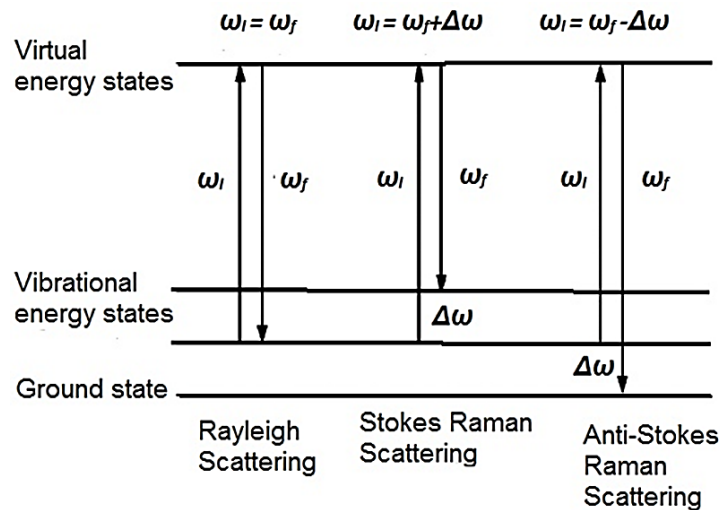


Figure 3-5: Schematic diagram of Raman spectroscopy showing Rayleigh, Stokes and anti-Stokes scattering

The Raman spectra for amorphous materials contain broad bands due to the variation of local environment in a glass. If the sample is crystalline the Raman shift is well-defined and sharp peaks are seen in the spectrum. Characteristic peaks were assigned to specific bonds.

Raman peaks are commonly classified into three broad regions, $400-800\text{cm}^{-1}$, $800-1200\text{cm}^{-1}$ and $1300-1600\text{cm}^{-1}$. In the first two broad bands both SiO_2 and B_2O_3 structures exist while the last band contains B_2O_3 structures only. Below 400cm^{-1} is a mixed and complex vibration of silicate network and modifier cations (Mahapatra, Lu et al. 2009) and the Zn-O vibration of the ZnO_4 unit is found in this region (Yadav and Singh 2015).

The deconvolutions of the Raman data were performed with wire 3.4 software and Gaussian fitting using the solver routine in Excel in the region 800-1200cm⁻¹ which is the region for the Si-O stretching vibrations. Before fitting the curves to the spectra the data is corrected for temperature and frequency dependent scattering intensities using the Long (1977) correction method (Mysen, Finger et al. 1982). First the background were subtracted by selecting the multiple spline curve option in the wire 3.4 software and the multiplied by Long correction factor (Long 1977) and finally the corrected spectra is normalized. After which the deconvoluted spectra were fitted with Gaussian bands.

The Raman assignments used in the current work are based on the literature values presented in table 3.6. The additions of modifiers into the glass structure cause some changes to the Raman spectra even though the modifiers are not Raman sensitive but they have notable effect on the Si-O, B-O and Al-O bonds. The effects of the modifiers can be observed in both the shift in frequency position of the Raman band and the increase or decrease of the peak intensity.

Wave number cm ⁻¹	symbol	Compound name
800-850	Q ⁰	Isolated SiO ₄ (Colomban 2003) or orthosilicate (Mahapatra, Lu et al. 2009)
900-950	Q ¹	Pyrosilicate or metasilicate (Mahapatra, Lu et al. 2009) Si ₂ O ₇ groups(Colomban 2003)
1050-1100	Q ²	Silicate chain(Colomban 2003) or disilicate(Mahapatra, Lu et al. 2009)
1100	Q ³	Sheet like region(Colomban 2003)
1150-1250	Q ⁴	SiO ₂ and tectosilicate(Colomban 2003)

Table 3.6: Identified Qⁿ species (Colomban 2003, Mahapatra, Lu et al. 2009)

Wave number cm ⁻¹	Type of bond	
220	Zn-O bending vibration of the ZnO ₄ unit	(Yadav and Singh 2015)
250	ZnO ₄ units bending modes	(Yadav and Singh 2015)
300-850	Si-O-Si mixed stretching and bending vibrations	(Mahapatra, Lu et al. 2009, Manara, Grandjean et al. 2009)
500	Si-O-Si bending vibration or BO ₄ tetrahedra characteristics	(Brow, Tallant et al. 1996, Manara, Grandjean et al. 2009)
550-850	Ring breathing modes of borates, metaborates and borosilicate rings.	(Manara, Grandjean et al. 2009)
614	Danburite	(Manara, Grandjean et al. 2009)
630	Breathing mode of borosilicate rings	(Manara, Grandjean et al. 2009)
635	3 coordinated boron	(Brow, Tallant et al. 1996)
670	Tetraborate group signature	(Manara, Grandjean et al. 2009)
755	Rings and chains metaborates	(Brow, Tallant et al. 1996)
750-780	Ring structures containing BO ₄ units e.g. di, tri, and Tetraborate	(Brow, Tallant et al. 1996)
770-808	4 and 3 coordinated boron in Diborate and boroxol rings	(Manara, Grandjean et al. 2009, Kaur, Pandey et al. 2012)
796-800	Si-O-Si symmetric stretching or vibration of ring structures	(Kaur, Pandey et al. 2012)
840 and 1230	Pyroborates	(Brow, Tallant et al. 1996)
850	Orthosilicate with O BOs	(McMillan 1984, Mahapatra, Lu et al. 2009, Yadav and Singh 2015)
900-920	stretching of Si-O with 3 NBOs Q ¹ (Pyrosilicate)	(McMillan 1984, Mahapatra, Lu et al. 2009, Manara, Grandjean et al. 2009, Yadav and Singh 2015)
930	Orthoborates	(Brow, Tallant et al. 1996)
950-980	stretching of Si-O with 2 NBOs Q ² (metasilicate)	(McMillan 1984, Mahapatra, Lu et al. 2009, Manara, Grandjean et al. 2009, Yadav and Singh 2015)

1000-1050	Stretching mode of Si-O ^o BO	(Manara, Grandjean et al. 2009)
1060-1070	Asymmetric stretching of Si-O-Si	(Kaur, Pandey et al. 2012)
1090	Diborate	(Brow, Tallant et al. 1996)
1050-1100	stretching of Si-O with 1 NBO Q ³ (disilicate)	(McMillan 1984, Mahapatra, Lu et al. 2009, Manara, Grandjean et al. 2009, Yadav and Singh 2015)
1120-1190	Fully polymerized Q ⁴	(Manara, Grandjean et al. 2009)
1200	Symmetric stretching of ¹³ B ³⁺ units in lithium lead borate glasses	(Yadav and Singh 2015)
1216-1260	Pyro-borate groups in borate glasses	(Yadav and Singh 2015)
1300-1600	B-O ⁻ (O ⁻ denotes NBOs) with chain and ring metaborates	(Mahapatra, Lu et al. 2009)
1200	Symmetric stretching of ¹³ B ³⁺ units in lithium lead borate glasses	(Yadav and Singh 2015)
1200	B-O stretching of pyroborate	(Kaky, Lakshminarayana et al. 2017)
1216-1260	Pyro-borate groups in borate glasses	(Yadav and Singh 2015)
1200-1300	B-O bonds stretching vibration of pyroborate	(Kaky, Lakshminarayana et al. 2017)
1250-1500	B-O chain stretching of metaborate group	(Manara, Grandjean et al. 2009, Kaur, Pandey et al. 2012)
1300-1600	B-O bonds stretching vibration of BO ₃ units	(Kaky, Lakshminarayana et al. 2017)
1410	BO ₃ units bonding BO ₄ units	(Manara, Grandjean et al. 2009)
1480	BO ₃ unit bonding BO ₃ units	(Brow, Tallant et al. 1996, Manara, Grandjean et al. 2009)
1320	Loose BO ₃ units	(Manara, Grandjean et al. 2009, Santha, Shamsudeen et al. 2011)
1515	BO ₃ units in boroxol rings	(Gohar, Doweidar et al. 1990, Manara, Grandjean et al. 2009)
1510-1570	B-O stretching mode involving one NBO of	(Yadav and Singh 2015)

[BO ₃] triangular and molecular oxygen		
1385-1397	Stretching vibration of B-O ⁻ bond in BO ₄ units from different borate groups	(Yadav and Singh 2015)

Table 3.7: Assignment of Raman peaks

3.8 Indentation measurements

To carry out mechanical testing glass samples were cut into 20×20×10 mm sections using a Secotom cutting machine with water-cooled diamond blade. The broad faces of the samples were then successively ground and polished using SiC 400/600/800/1200 grits under running water and 6/3/1µm diamond pastes. Cleaning and drying of the samples follows immediately before annealing at T_g to remove residual stresses developed during cutting, grinding and polishing. After annealing a Durascan micro/macro Vickers hardness tester with extended load range up to 10 kg was used to measure the indentation hardness from the indent size and indentation fracture toughness was calculated from the crack length measured.

To measure the hardness using Vickers indentation, the polished surfaces were indented with the standard load of 9.81 N for 15 seconds. The number of indentations made on each composition was between 13 and 15. Fig 3-5 is an example of indentation image taken by Durascan during Vickers hardness test. Vicker's hardness can be calculated using

$$H_v = 1.8555 \left(\frac{P}{d^2} \right) \quad \text{Equation 3-3}$$

where P is indentation load and d is average diagonal length of the indents.

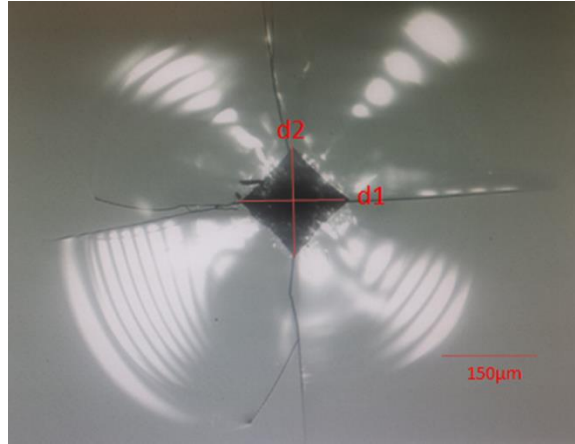


Figure 3-6: Photograph of a Vicker's hardness indent where d_1 and d_2 are the diagonals of the indent

The indentation fracture toughnesses of five out of the six series of the glasses were measured immediately after making the indent for 5 indentation loads namely 0.3, 0.5, 1, 2.5 and 5 kg. In each case the length of the median-radial cracks ($2c$) originating from the corners of the indents was measured (see figure 3-5). The indentation fracture toughness was then calculated using

$$K_{Ic} = \frac{0.0824P}{c^{3/2}} \quad \text{Equation 3-4}$$

where P is the applied load in (N) and c is half crack length and 0.0824 was proposed by Evans and Charles (1976). Ponton and Rawling (1989) reported that more consistent indentation fracture toughness values can be obtained by using this constant 0.0824.

Brittleness was then calculated using:

$$B = \frac{H_v}{K_{Ic}} \quad \text{Equation 3-5}$$

An estimate of surface energy was calculated from the measured fracture toughness and the modulus using:

$$\gamma = \frac{K_{lc}^2(1-\nu^2)}{2E} \quad \text{Equation 3-6}$$

3.9 Acoustic measurement of elastic moduli

Elastic moduli of the glasses samples were measured using the ultrasonic pulse echo technique. Both the longitudinal (V_L) and the transverse (V_T) ultrasonic wave velocities were measured using an Olympus Epoch 6000. 20 MHz longitudinal and 5 MHz transverse transducers were used. To facilitate proper contact of the transducer onto the surface of the samples and to aid transmission of sound waves glycerol and a coupling gel were used.

The ultrasonic pulse-echo technique is commonly used to determine elastic moduli of materials. The ultrasonic vibration travels in solid media in the form of a wave, and in order to transmit sound waves the material is required to be an elastic medium. This is a non-destructive testing method which conventionally uses longitudinal and transverse waves. The ultrasonic equipment sends high frequency waves through transducers into the test samples, and then the time of flight (t) is determined (Olympus technical notes, 2006).

The wave velocity (v) for the test sample was calculated as follows.

$$V = \frac{2l}{t} \quad \text{Equation 3-7}$$

where l stands for the thickness of sample. The shear modulus, G , was obtained using

$$G = \rho V_T^2 \quad \text{Equation 3-8}$$

where ρ is density, and V_T is longitudinal velocity. The Young's modulus, E , was obtained using

$$E = \rho V_T^2 \frac{(3V_L^2 - 4V_T^2)}{(V_L^2 - V_T^2)} \quad \text{Equation 3-9}$$

Poisson's ratio (ν) and the bulk modulus (K) were also calculated from the longitudinal and transverse wave velocities to reduce the cumulative error.

$$v = \frac{(V_L^2 - 2V_T^2)}{2(V_L^2 - V_T^2)} \quad \text{Equation 3-10}$$

and

$$K = \rho \frac{3V_L^2 - 4V_T^2}{3} \quad \text{Equation 3-11}$$

3.10 Impedance spectroscopy

The electrical properties of the glass and glass-ceramic samples were obtained from ac impedance spectroscopy using an Agilent E4980A impedance analyser (Agilent Technologies Inc., CA). For each sample the impedance was measured in the 20 to 10⁶ Hz frequency range with an applied voltage of 100 mV using the impedance analyser. Before heating the samples inside the horizontal tube furnace gold paste was fired at 800°C for 2 h on the two opposite surfaces to form electrodes. Room temperature measurements followed by high temperature ones from 500 to 25°C below the T_g with a 20°C interval, to ensure thermal stabilization after each reading, were taken. All the measurements were made in air. All impedance data were normalized by the geometric factor (thickness/surface area) of each sample. At temperatures below 100°C a high impedance is observed beyond equipment limit while very close to T_g additional contributions to the conductivity due to, for example, viscous motion of the glass structure were observed. Both the parent glasses and glass ceramics obtained by isothermal heat treatment were measured for electrical conductivity. Since the sample preparation involves gold electrode firing at 800°C for 2h it is most likely that the parent glass is no longer amorphous as glasses are known to be metastable some element of crystallization would be expected. And therefore electrical conductivity of the parent glasses may have been influenced by the heating process however this does not have any effect on the applications intended because the glass would undergo constant isothermal heating during operation for thousands of hours. In addition the impedance measurement of the parent glasses in appendix 1 (b) indicated single component electrical data as both the Z'' and M'' have peaks positions corresponding to similar frequency.

Data taken from impedance spectroscopy are analysed using the following complex formalism; impedance Z*, electric modulus M*, admittance Y*, and permittivity ε* as taken from (Jiadong, Ming et al. 2014).

$$M^* = j\omega C_0 Z^* \quad \text{Equation 3-12}$$

$$\varepsilon^* = (M^*)^{-1}$$

$$Y^* = (Z^*)^{-1} \quad \text{Equation 3-14}$$

$$Y^* = j\omega C_0 \varepsilon^* \quad \text{Equation 3-15}$$

Where $\omega = 2\pi f$ is angular frequency of measurement and C_0 is the capacitance of vacuum space.

From Arrhenius law the activation energy for electrical conductivity is obtained from the slope of the straight line see fig 5-1 (a) and (b). The Arrhenius law is given as follows

$$\sigma_{ac} = A \exp \left[\frac{-E_a}{k_B} \right] \quad \text{Equation 3-16}$$

4. Results 1: Physical, thermal and structural analysis

4.1. Physical, thermal and structural analysis for $x\text{Ba}(40-x)\text{Si}$ series

In the $x\text{Ba}(40-x)\text{Si}$ series an increase in density and an increase then decrease then increase in molar volume was observed with BaO additions (see fig 4-1), due to the higher molecular weight of barium 153.3g/mol and high ionic radius of Ba^{2+} (1.49Å) which expands the glass structure and decreases the glass compactness (Wang, Wang et al. 2009, Kaur, Pandey et al. 2012, Bootjomchai, Laopaiboon et al. 2014). The observed unusual behaviour where both density and molar volume increase in the same direction have been previously reported for $\text{RO-Al}_2\text{O}_3\text{-B}_2\text{O}_3$ ($\text{RO} = \text{Mg} > \text{Ca} > \text{Sr}$) containing glasses (Abd El-Moneim, Youssouf et al. 2006). The molar volume of $x\text{Ba}(40-x)\text{Si}$ increased and then decreased at a BaO/SiO_2 ratio of 0.57 and then increased again. This type of anomalous drop in molar volume have been reported by Bourgel et al, and is associated with the tendency of the network to densify its structure in barium borosilicate glasses at $25 < X < 48$ mol% of BaO (Bourgel, Malki et al. 2009).

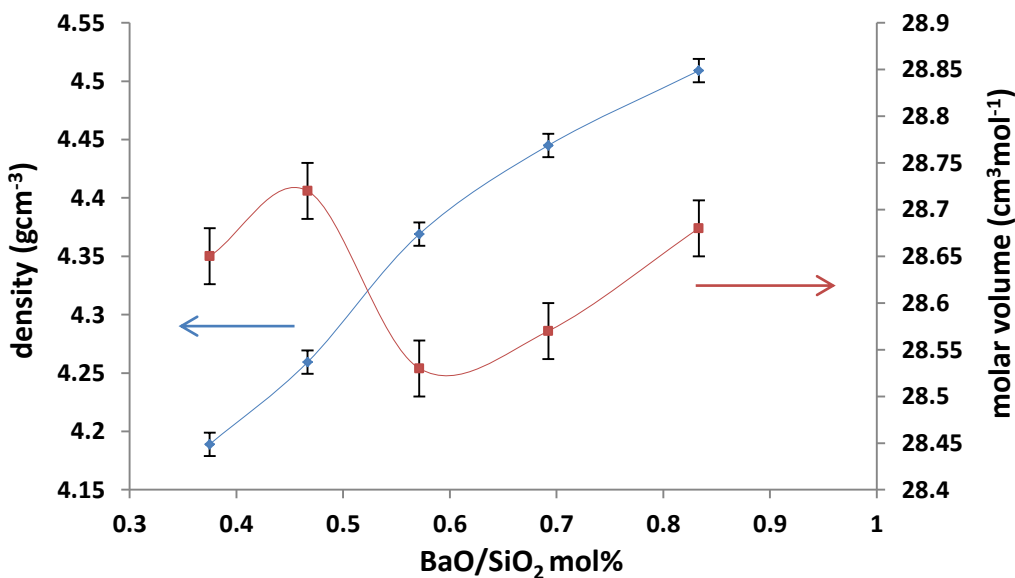


Figure 4-1: Density and molar volume versus Ba/Si ratio in $x\text{Ba}(40-x)\text{Si}$ glasses. For detailed compositions please see table 3.1

The XRD traces of $x\text{Ba}(40-x)\text{Si}$ glass and glass-ceramic samples are presented in fig 4-2 (a) and (b). The absence of sharp peaks in the glass samples suggest that there are no crystalline phases, and the broad hump at low angles around 28° indicates amorphous nature and as well as long range structural disorder in these glasses. In order to understand the crystallization kinetics and thermal stability of $x\text{Ba}(40-x)\text{Si}$ glasses were isothermally heat treated at 800°C for 50 h after which the crystalline samples were evaluated to identify the phases in the samples with respect to temperature and heating duration. The XRD of the crystalline samples in fig 4-2 (b) reveals the formation of lanthanum silicate boron oxide ($\text{La}_3(\text{Si}_2\text{O}_4)_2\text{BO}_2$) PDF no (04-010-1343). The intensities of the dominant peaks around 30° seem to decrease with increasing BaO and the peak heights are smallest for 25mol% BaO because decreasing silica removes one major constituent of the phase. As reported by (Tréguët, Caurant et al. 2017) 7 out of 10 phases in the $\text{SiO}_2\text{-B}_2\text{O}_3\text{-La}_2\text{O}_3$ ternary contains silica as part of the phases formed; the three phases observed in this study all contained silica. The lanthanum borosilicate single phase shown in fig 4-2 (b) is also reported by Shvanskii et al and claimed that it was the first La-borosilicate to be synthesized and its structure solved see (Shvanskii, Leonyuk et al. 2000). Lanthanum and neodymium are reported to be able to form single crystal phase in soda lime borosilicate glasses and the amount of the phase is heat treatment dependent (Nicoleau, Angeli et al. 2016). The effect of crystallization as shown by the TEC curve of the glasses in fig 4-2 (c) indicates that the TEC up to the onset of the T_g is decreased after crystallization possibly due to the differences between the residual glass and the parent glass as well as the crystalline phase itself.

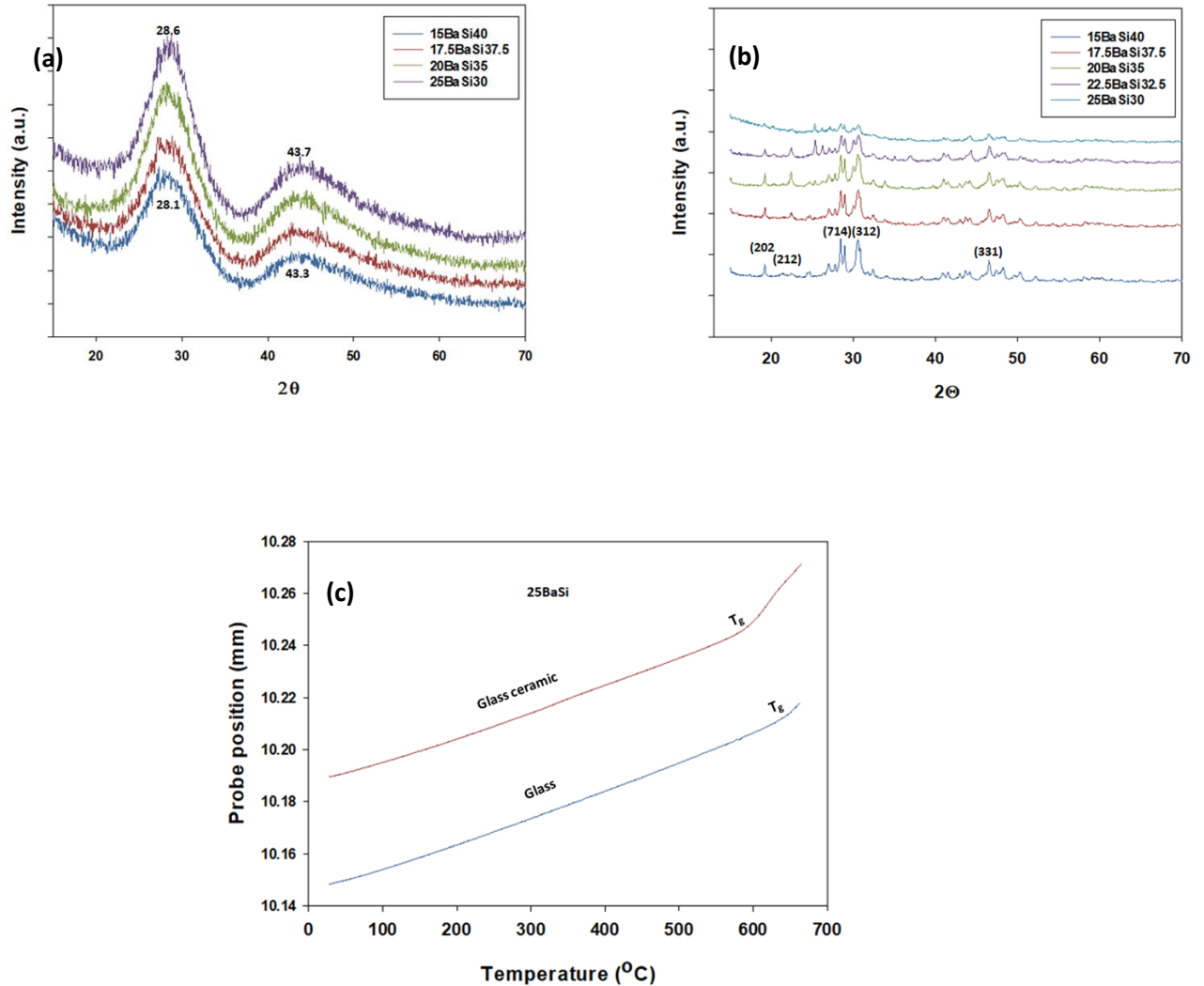


Figure 4-2:(a) XRD patterns of $x\text{Ba}(40-x)\text{Si}$ glass; (b) XRD patterns of $x\text{Ba}(40-x)\text{Si}$ samples crystallised at $800\text{ }^\circ\text{C}$ for $x\text{Ba}(40-x)\text{Si}$ with increasing Ba/Si ratio (c) representative examples of the TEC for glass and glass obtained from TMA for 25BaSi30 exhibiting the differences in TEC and T_g positions in the two samples

The influence of BaO incorporation on thermal properties of $x\text{Ba}(40-x)\text{Si}$ samples is shown in fig 4-3 (a) and (b). There seems to be a typical change of the DTA curves as BaO is added to the glasses. The glasses are stable up to temperatures above T_g before the emergence of crystallization peaks during the measurement. There is a decrease in T_g of about $18\text{ }^\circ\text{C}$ from 662 to $644\text{ }^\circ\text{C}$ as BaO was increased at the expense of SiO_2 in these glasses, a similar behaviour to this is reported by (Mishra, Mishra et al. 2009). T_g decreases with BaO addition because it

creates NBOs in the glass as mentioned by (Ghosh, Sharma et al. 2010). The decrease in T_g may suggest that the energy needed for structural relaxation of the glass network is also reduced. There are two crystallization peak temperatures in these glasses which may be an indication of phase separation as reported by Lahl et al, (Lahl, Singh et al. 2000), or the presence of two different crystalline phases in the glass see (Staff, Fernie et al. 2016).

An example expansion trace for both the glass and glass-ceramic is given in fig 4-2(c) where the residual glass in the glass-ceramic shows a slight decrease in the T_g position compared to the base glass. The thermal expansion (TEC) of barium containing glasses $x\text{Ba}(40-x)\text{Si}$ fig 4-3(b) increases linearly with BaO content similar to what has been reported by (Laorodphan, Namwong et al. 2009). This is because of the high ionic radius of barium (Kaur, Pandey et al. 2014) and due to lower cation field strengths which create NBOs in the network (Hubert and Faber 2014) and make the glass structure looser (Zhang, Yue et al. 2013). There is not much difference between the TEC of the glass (blue line) and glass-ceramics (red line) of $x\text{Ba}(40-x)\text{Si}$ samples except for the samples with a) a BaO/SiO₂ ratio around 0.7 where the TEC for the glass ceramic is much higher and b) a BaO/SiO₂ ratio around 0.83 where it is slightly higher than that of the glass samples. The decrease in T_g and increase in TEC with BaO addition suggest that BaO take network modifier positions and has dominant effect on the network rigidity. The T_g in fig 4-3(c) shows a continues decrease with increasing BaO which is known to depolymerise the silica network. According to Mahapatra et el the T_g and T_s of sealing glasses increased with increasing field strength of the modifier therefore unlike the BaO the addition of SrO, CaO and Mg could increase the T_g and T_s (Mahapatra and Lu 2010).

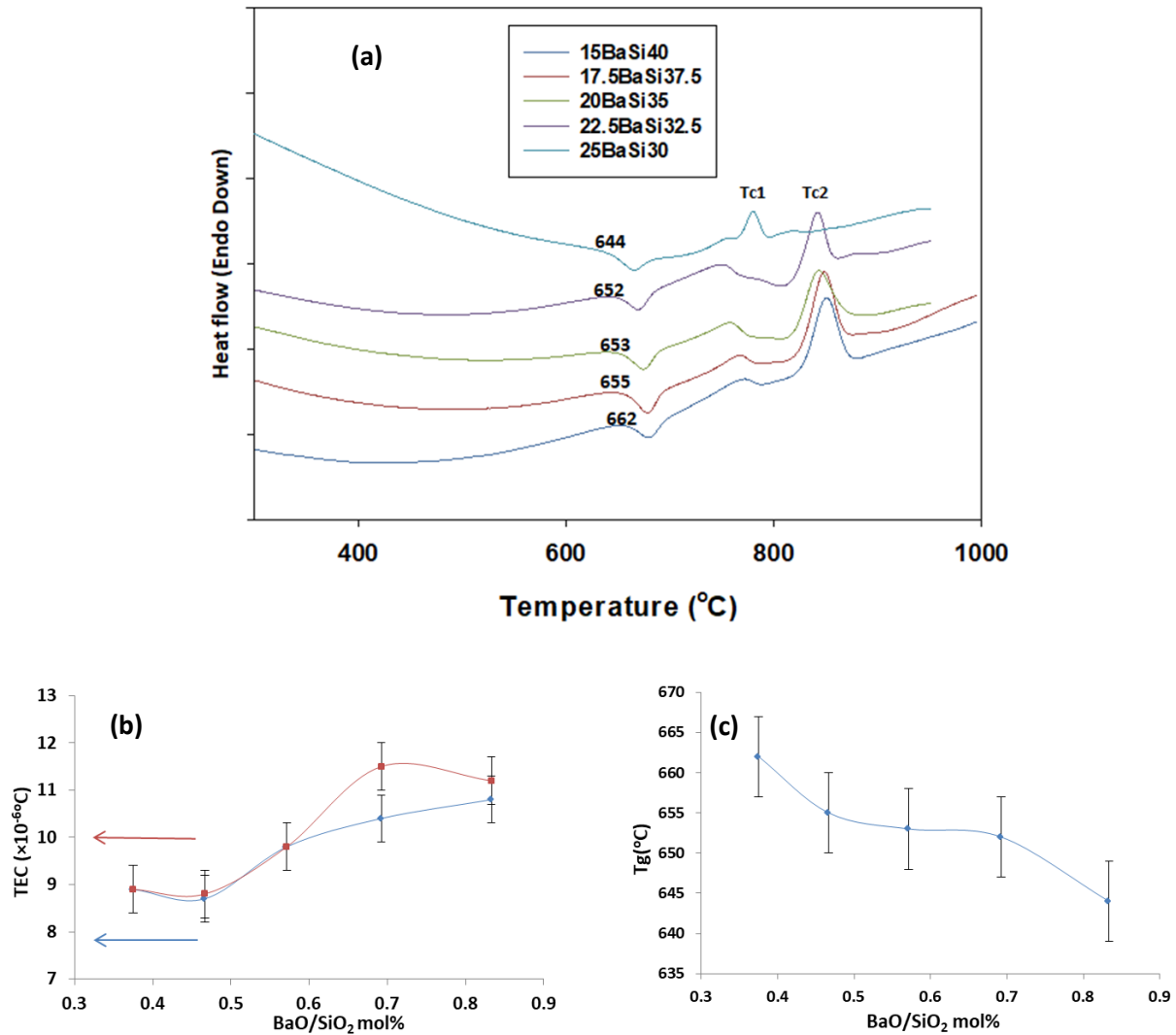


Figure 4-3: DTA curves, (b) TEC of glass (blue line) and glass ceramic (red line) (c) T_g of xBa(40-x)Si glass and glass ceramics versus BaO/SiO₂ ratio.

The systematic variations in the Raman and FTIR spectra of xBa(40-x)Si glasses with increasing BaO are presented in fig 4-4(a) and (b). There are about seven visible regions in the Raman spectra and five in the FTIR spectra. All the bands broad and small have been labeled and assigned to different vibrations obtained from the literature as outlined in tables (3.4) and (3.6). The intermediate region 800-1200cm⁻¹ from both techniques reveals the depolymerising effect of

increasing BaO on the SiOSi stretching vibrations with the peaks being shifted to lower wavenumbers and a shoulder appearing around 870 cm^{-1} assigned to Q^0 in the Raman spectra. This behaviour has been reported for both BaO and CaO substitution (see (Yadav and Singh 2015)) and a decrease in the peak intensity of this region can be seen more clearly in the FTIR spectra. For the Raman spectra the top end of the peaks becomes sharper and increase in intensity as it shifts to lower positions which suggest that BO_4 increases with addition of BaO as reported by (Kaur, Singh et al. 2012). Peaks assigned to the B-O stretching motion in BO_3 and BO_4 are located between 1250 to 1600cm^{-1} (see tables 3.4 and 3.6 for details), can be seen in both Raman and FTIR and these peaks shifted to lower wavenumbers in the Raman spectra with increase in intensity of the 1200cm^{-1} peak assigned to stretching vibration of BO_4 according to Cetinkaya et al in zinc borate glasses (Cetinkaya Colak, Akyuz et al. 2016) and corresponding decrease of the 1400cm^{-1} peak assigned to stretching of B-O of BO_3 characteristics for BO_3 group as BaO increases.

The FTIR peaks intensities follow the same pattern as the Raman ones but the peaks in FTIR moved to slightly higher wavenumbers. The reduction in intensity of the 1400 cm^{-1} peak indicates depolymerisation which means that BO_3 in the borate groups and NBOs in the glass structure are reducing according to (Kaur, Singh et al. 2012). The peaks between 600 and 800 cm^{-1} splits into two weak bands in the Raman spectra only; the first weak band is at $648\text{-}624\text{ cm}^{-1}$ and increased in intensity and shifted to lower wavenumbers with increasing BaO may be associated with obstructed bending vibration of ring type metaborates groups or the breathing mode of danburite-like rings (Yadav and Singh 2015). The other weak band $709\text{ -}717\text{ cm}^{-1}$ has been identified in FTIR spectra as symmetric stretches in Si-O-(Si, Al) in aluminosilicates (Środa and Paluszkiwicz 2008) and can also be assigned to B-O or B-O-B bending vibration modes of BO_3 units in borosilicate glasses (Sasmal, Garai et al. 2014). This band has moved to higher wavenumbers with increasing BaO but the decrease in intensity suggests that the BO_3 group is decreasing with possible conversion into the danburite like structure $[B_2Si_2O_8]^{2-}$ since the peak intensity around 624 cm^{-1} has increased (Parkinson, Holland et al. 2008). As also explained by Manara this band around 630 cm^{-1} could be the breathing mode of danburite like ring structure including two tetrahedra of both SiO_4 and BO_4 and charged balanced by Na_2O instead of CaO (Manara, Grandjean et al. 2009). Medium range order structures such as danburite have been reported for borosilicate glasses using Raman spectroscopy (Parkinson, Holland et al. 2008). The

peak between 400 and 600 cm^{-1} is also seen in both Raman and FTIR with a decrease in intensity and disappearance in the Raman spectra with increasing BaO while in the FTIR it slightly shifts to higher wavenumbers; similar behaviour has been reported by (Kaur, Singh et al. 2012). In general a decrease in intensity and width of these bands is associated with decrease in the bond angles of the SiOSi linkages which determines the frequency of this bending vibration (Kline, Tangstad et al. 2015, Hehlen, Neuville et al. 2017). The lowest wavenumber peak around 250 cm^{-1} in the Raman spectra may be assigned to the bending mode of ZnO_4 , however; according to Cetinkaya et al, the 400 to 550 cm^{-1} band in FTIR has also been assigned to the ZnO_4 tetrahedra in borate glasses (Cetinkaya Colak, Akyuz et al. 2016) which suggests that the presence of ZnO_4 unit is indicated by the data from both techniques.

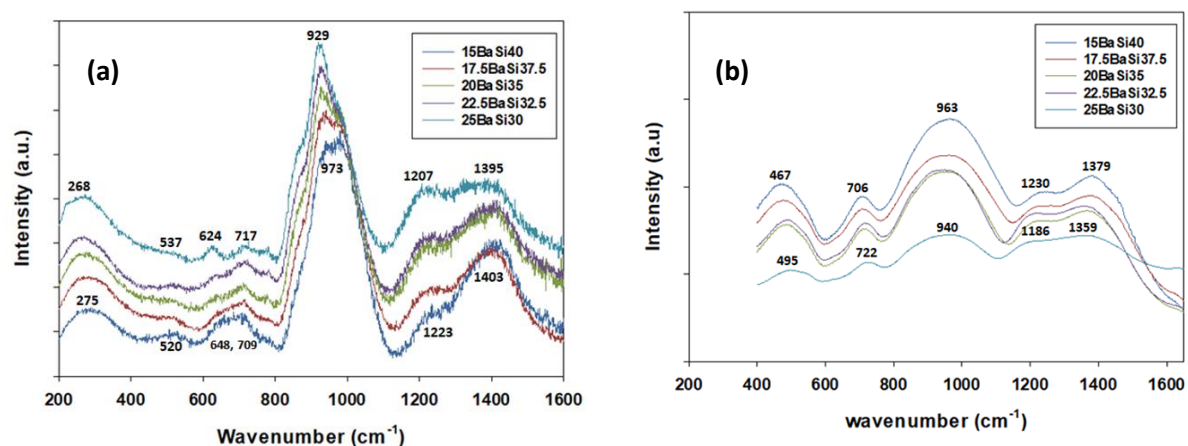


Figure 4-4: (a) Raman and (b) FTIR spectra for $x\text{Ba}(40-x)\text{Si}$ glasses

The deconvolution method described in section 3.6 was applied to the mid frequency region 800 to 1200 cm^{-1} which covers the Si-O stretching vibrations and the high frequency region between 1250 and 1500 cm^{-1} which is due to the presence of BO_n structural units. Deconvolution of the Si-O stretching regions reveals the presence of four Gaussian bands (Q^n species) and three Gaussian bands for boron species. Fig 4-5(a) and (b) gives a representative of the deconvoluted Raman spectra for the silicate and borate groups where the silicate units are represented by the Q^n notations and the borate units by loose $^{[3]}\text{B}^{3+}$, $^{[3]}\text{B}^{3+}$ in boroxol ring structure, and $^{[4]}\text{B}^{3+}$. The deconvoluted spectra for all other series are presented in appendix 6 and 7 while appendix 4 and 5 gives the values of the estimated area% of both the silicate and borate units. Fig 4-6(a) shows how the Q^n species (as determined from the peak area) changes with BaO addition see appendix 4 and 5 for all series. It can be seen that as BaO is added to the

$x\text{Ba}(40-x)\text{Si}$ series glasses Q^0 and Q^1 increased and Q^2 and Q^3 decreased. In fig 4-6(b) shows that the BO_4 increased which agrees with the literature (Zhang, Yue et al. 2013) and a reduction in the percentage of both loose BO_3 and BO_3 in boroxol rings can be observed. The Si-O stretching peaks shifts to lower positions from 963 to 940 cm^{-1} and 955 to 929 cm^{-1} in FTIR and Raman respectively. The plot of the variation of the ratio $(Q^4+Q^3)/(Q^1+Q^2)$, which can provide some insight into the polymerization, also shifts to lower position with BaO addition (see fig 4-6(c) and (d)) indicating increasing depolymerisation of the SiOSi network.

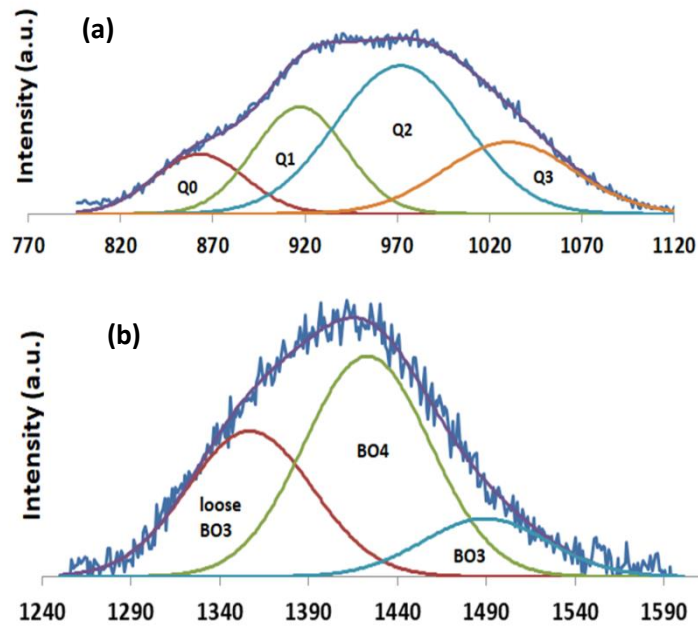


Figure 4-5: Deconvolution of (a) the silica unit (800-1200 cm^{-1}) and (b) borate group (1250-1600 cm^{-1})

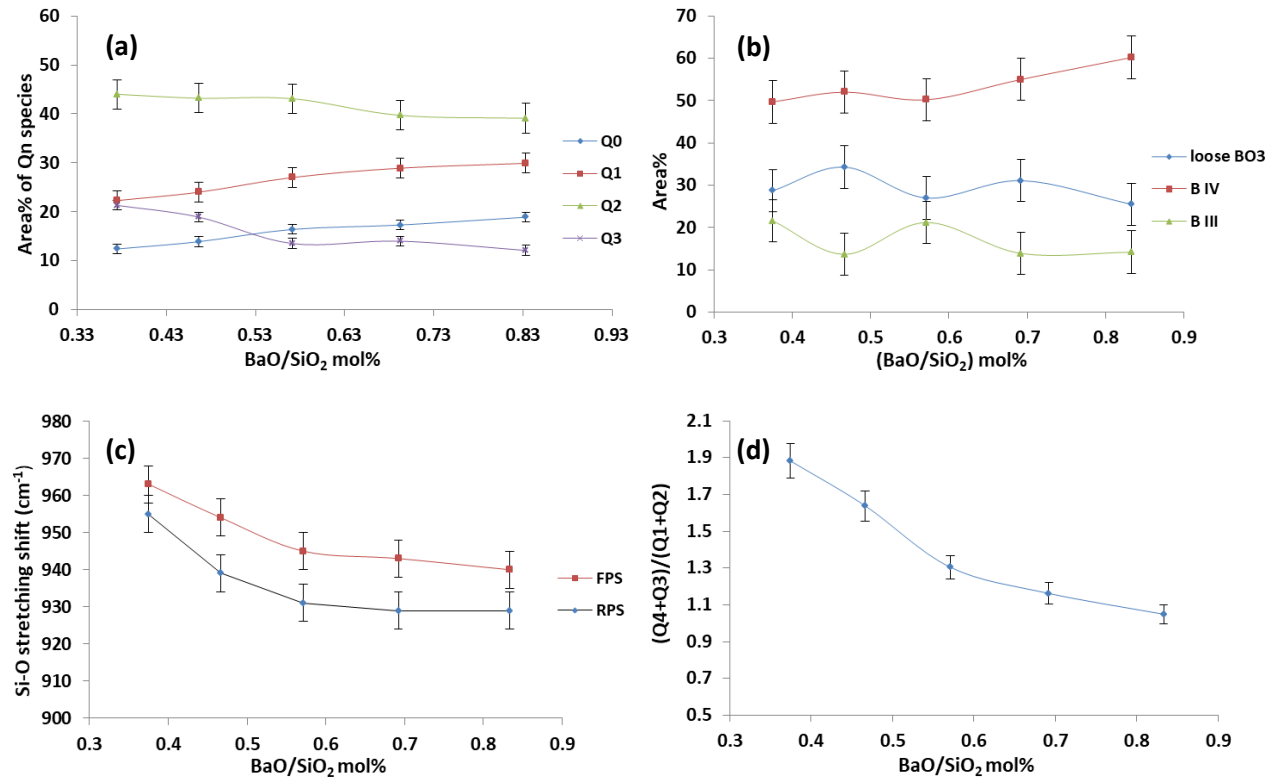


Figure 4-6: Area% of (a) Qⁿ species and, (b) Boron species. (c) Raman and FTIR peak shift (RPS,FPS) of Si-O stretching unit and (d) polymerisation index for xBa(40-x)Si glasses.

4.2 Physical, thermal and structural analysis of xBa(10-x)Al glasses.

In this series BaO was swapped on molar basis with alumina which means the ratio of the cations is 1:2 however alumina is expected to be in AlO₄ coordination since there is enough modifier in this glass to charge balance all the alumina and the excess goes to depolymerise silica and convert some BO₃ to BO₄ units. The effect of increasing BaO on the molar volume is different to that seen in xBa(40-x)Si glasses in that the molar volume of xBa(10-x)Al glasses decreased and the density increased as Ba/Al ratio increased (see fig 4-7 (a)). Thus in the xBa(10-x)Al case the change in molar volume mirrors the change in density in the expected fashion (compare fig 4.1 and 4.7(a)).

The XRD plot (fig 4-7(b)) is similar to that for xBa(40-x)Si (fig 4-2) in terms of peak position. There is a very small shift in the silica peak position and there is a clearly visible shift to the right of the borate peak position. This could suggest that both silicate and borate structures

of the $x\text{Ba}(10-x)\text{Al}$ glasses are slightly distorted by the BaO addition. The T_g in $x\text{Ba}(10-x)\text{Al}$ decreases $44\text{ }^\circ\text{C}$ in a non-monotonic fashion from 627°C to 583°C with increasing BaO and reducing alumina. There is only one clearly visible crystallization peak in these glasses (see fig 4-8(a)). As the amount of alumina is not more than 10mol% in these glass it will play a network former role hence the increase in T_g towards the higher alumina ratio as reported by (Arora, Singh et al. 2011) and the reduction in TEC (Lin, Cheng et al. 2012). T_g and TEC exhibit an increase and decrease in going from 10BaAl10 to 15BaAl5 mol% (see fig 4-8(b)) and 12BaAl8 exhibits two endothermic peaks suggesting two T_g in this glass which could reflect the presence of liquid-liquid phase separation as reported in (Häßler and Rüssel 2017). The TEC reaches a maximum for this particular glass sample, 12BaAl8, possibly due to the differences in the thermal expansion of the two phases.

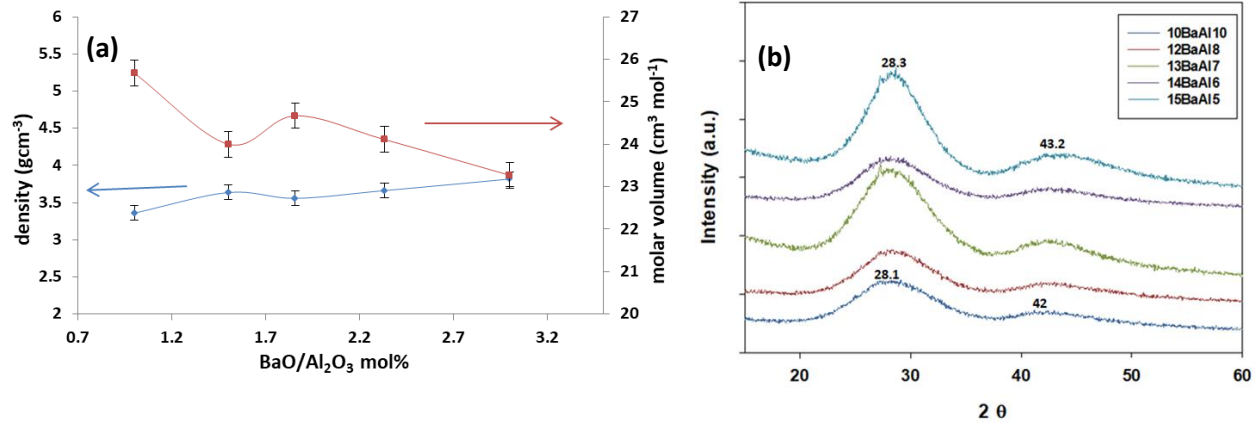


Figure 4-7: (a) molar volume and (b) XRD patterns for xBa(10-x)Al glasses.

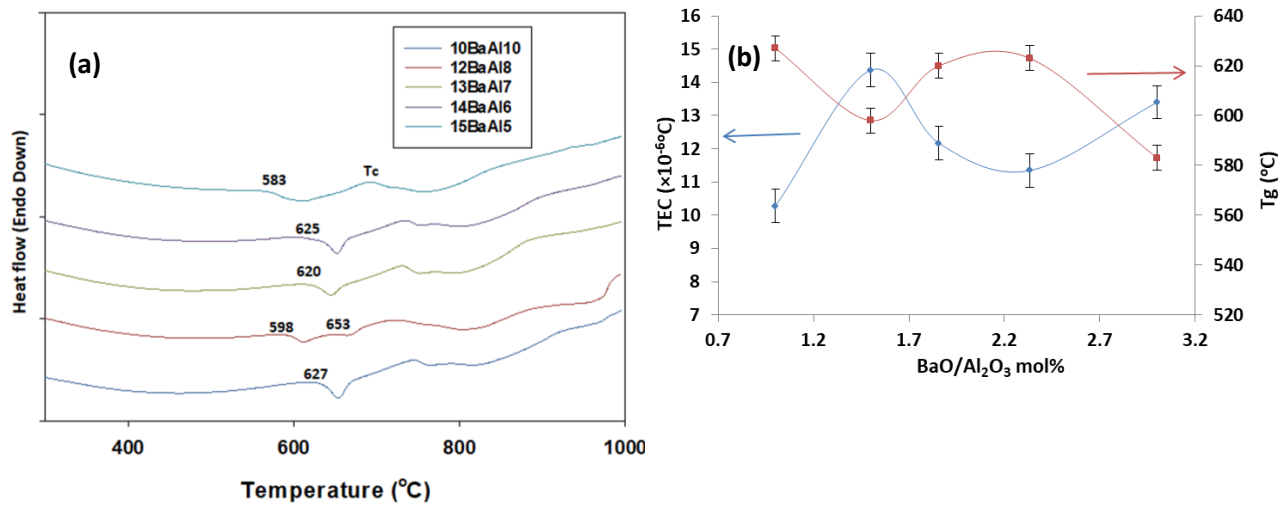


Figure 4-8: (a) DTA curves, (b) TEC and T_g of xBa(10-x)Al glasses

Fig 4-9 (a) and (b) show the Raman and FTIR spectra of xBa(10-x)Al glasses; the Raman spectra show 6 absorption bands without the band around 200 cm⁻¹ and the FTIR spectra 5 bands (see tables 3.4 and 3.6 for the different peaks assignment). As the amount of BaO increases and alumina decreases depolymerisation of the glass is indicated by both Raman and FTIR spectra as

the peak at 800-1200 cm^{-1} has moved to lower wavenumbers. The FTIR intensity of the sample 12BaAl8, which has two T_g s, is lower than that of other samples due to phase separation. The intensity of the borate peak around 1200 cm^{-1} in 12BaAl8 is very low. The peak around 1200 cm^{-1} assigned to stretching vibration of BO_4 according to Cetinkaya et al slightly increases and the BO_3 units bonding BO_4 units around 1430 cm^{-1} according to Manara et al or the anti-symmetric stretching of BO_3 units according to (Cui, Hao et al. 2015) also increases as BaO is increased. However these peaks appeared at slightly different positions to the other series as can be observed. The peak around 1200 cm^{-1} slightly appeared at lower wavenumber and the peak around 1430 cm^{-1} at a higher wavenumber and this could possibly be due to differences in Si-O-Si bond angle shift among the different glass series as reported by (Kline, Tangstad et al. 2015). Due to high amount of alumina in these glasses a lot of modifier is consumed in charge balancing AlO^{4-} and the rest is shared between silica depolymerisation and conversion of BO_3 to BO_4 units hence the reason for the increase in the borate units at 774, 1200 and 1430 cm^{-1} with BaO addition. This would suggest that swapping BaO with silica in $\text{xBa}(40-\text{x})\text{Si}$ has greater depolymerisation effect on the borate network compared to exchanging for alumina in $\text{xBa}(10-\text{x})\text{Al}$. The peak around 774 cm^{-1} broadens in width and shifts to lower wavenumbers 737 cm^{-1} indicating that the B-O-B bending in BO_3 unit is increasing and the six membered boroxol ring with 2 or 1 BO_4 usually observed if boron content is $> 5\text{mol}\%$ also the band around 1400 cm^{-1} unit increases see report by (Cui, Hao et al. 2015, Cetinkaya Colak, Akyuz et al. 2016). There is also a shift in the peak around 703-637 cm^{-1} to lower wavenumbers. Unlike in $\text{xBa}(40-\text{x})\text{Si}$ series this peak assigned to danburite did not show an increase in the 703 cm^{-1} peak.

The peak at 517 cm^{-1} decreases in intensity and moves to slightly lower positions possibly due to an increase in bond angles. Furthermore, in the deconvoluted silicate unit the area% of Q^2 and Q^3 in fig 4-10(a) is higher than those of Q^1 and Q^0 indicating that the silica network is less depolymerised in the $\text{xBa}(10-\text{x})\text{Al}$ series glasses compared to $\text{xBa}(40-\text{x})\text{Si}$ series ones. Meanwhile the deconvoluted borate peak in fig 4-10 (b) indicates an increase in the area% of BO_4 and slight increase in the BO_3 in boroxol rings around the ratio 1.85 and then a decrease. Meanwhile the loose BO_3 is behaving in opposite way to the BO_3 in boroxol rings and shows a minimum at the same ratio of Ba/Al 1.85 and show maximum at 2.33 and decreases afterwards. See appendix 4 and 5 for all the area% of both silicate and borate units for all series. The Si-O stretching peak positions in Fig 4-10 (c) decreased with increasing BaO with a small increase at

13BaAl7 mol% after which they continue to decrease. The degree of polymerisation (see Fig 4-10 (d)) shows that there is a slight decrease at initial BaO addition and a significant drop afterwards in the polymerisation degree at 1.85 ratio where at the same ratio also a decrease in loose BO_3 and increase in boroxol ring was observed see fig 4-10(b) above. The polymerisation degree first decreases and then increases with BaO additions.

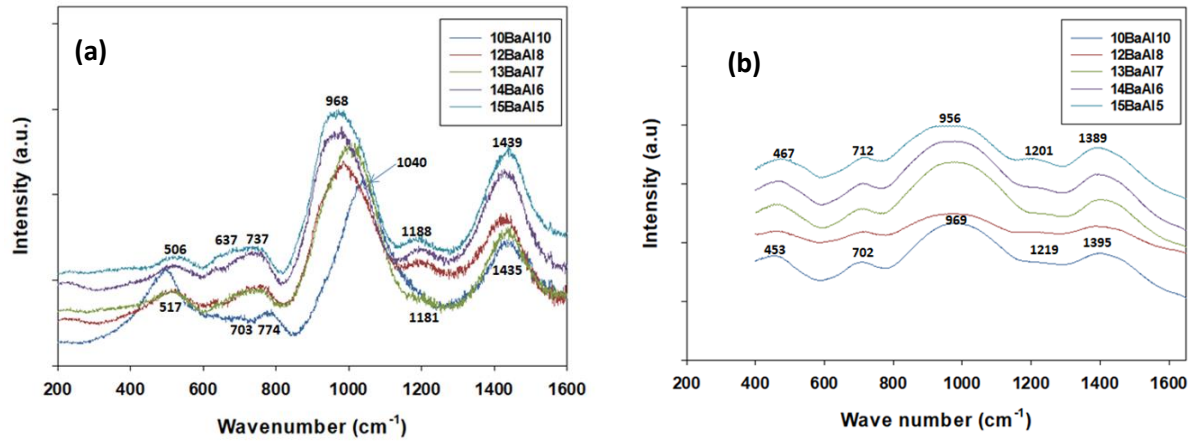


Figure 4-9: (a) Raman and (b) FTIR spectra for $x\text{Ba}(10-x)\text{Al}$ glasses.

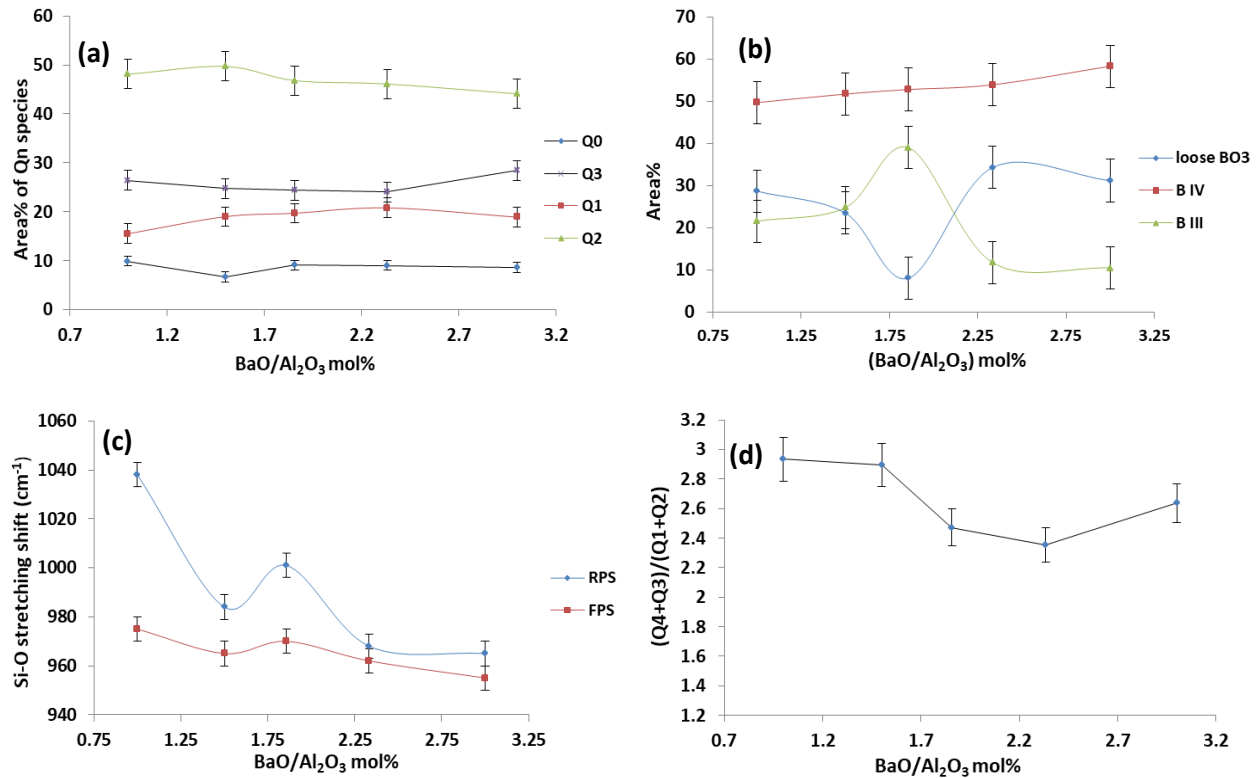


Figure 4-10: Area% of (a) Si Q^n species and, (b) boron species (c) Raman and FTIR peak shift (RPS, FPS) of Si-O stretching unit and (d) polymerisation index for $x\text{Ba}(10-x)\text{Al}$ glasses.

4. 3 Physical, thermal and structural analysis of $x\text{B}(15-x)\text{Zn}$ glasses.

In $x\text{B}(15-x)\text{Zn}$ glasses there is a steady increase in density and decrease in molar volume as the ratio of $\text{ZnO}/\text{B}_2\text{O}_3$ increases (Fig 4-11). This is because the molecular weight of ZnO is greater than that of boron oxide and the reduction in molar volume is due to ZnO occupying interstitial free spaces within the glass structure.

XRD of $x\text{B}(15-x)\text{Zn}$ samples (fig 4-12(a)) shows that $5x\text{B}(15-x)\text{Zn}$ crystallised on pouring to form single phase lanthanum disilicate ($\text{La}_2(\text{Si}_2\text{O}_7)$) PDF card number (01-082-0729) while the other samples remained as glasses. The addition of boron oxide modifies the short range order (SRO) of the glass to give two strong amorphous intensities with fairly constant broadening of these humps and slightly shifted to lower 2θ angles. however, silica do show

strong XRD peak at 2 theta angle 20-30° while in borate glasses shows maxima around 30° and due to short range in atomic ordering the humps appeared broad unlike crystalline samples where the hump turns narrower. As reported by Lopes et al, two broad peaks in alkali borosilicate around 28° and 43° 2 theta is a characteristics of borate glasses with high amount of alkaline earth and B₂O₃ summed up to 90mol% (Lopes, Soares et al. 2014). As shown in (fig 4-12(b)) the heat treatment of xB(15-x)Zn at 800°C for 50 h leads to the formation of single phase lanthanum silicate boron oxide (La₃ (Si₂O₄)₂ BO₂) (PDF no 04-010-1343). The peak at around 30° remained dominant with no shoulder but the one at 28° has a shoulder which increases with boron addition.

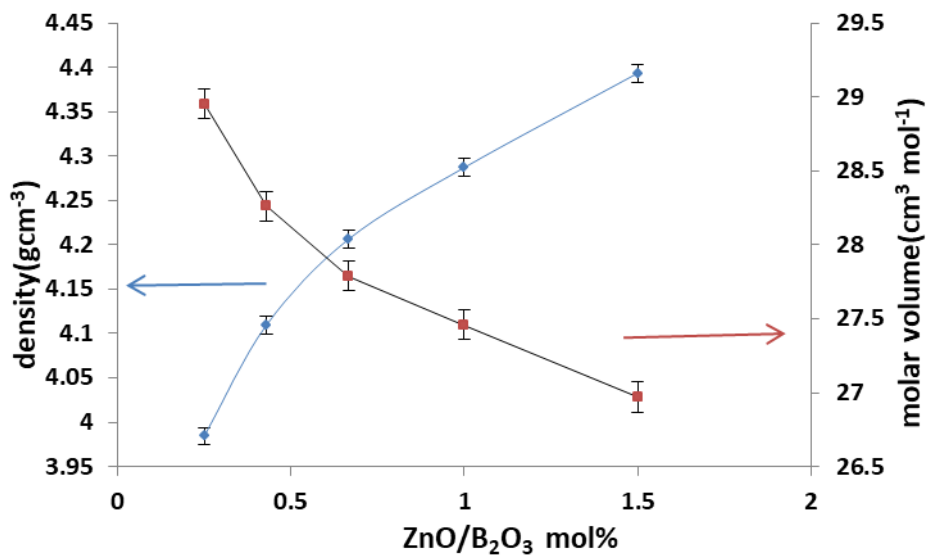


Figure 4-11: Density and molar volume change versus ZnO/B₂O₃ ratio of xB(15-x)Zn

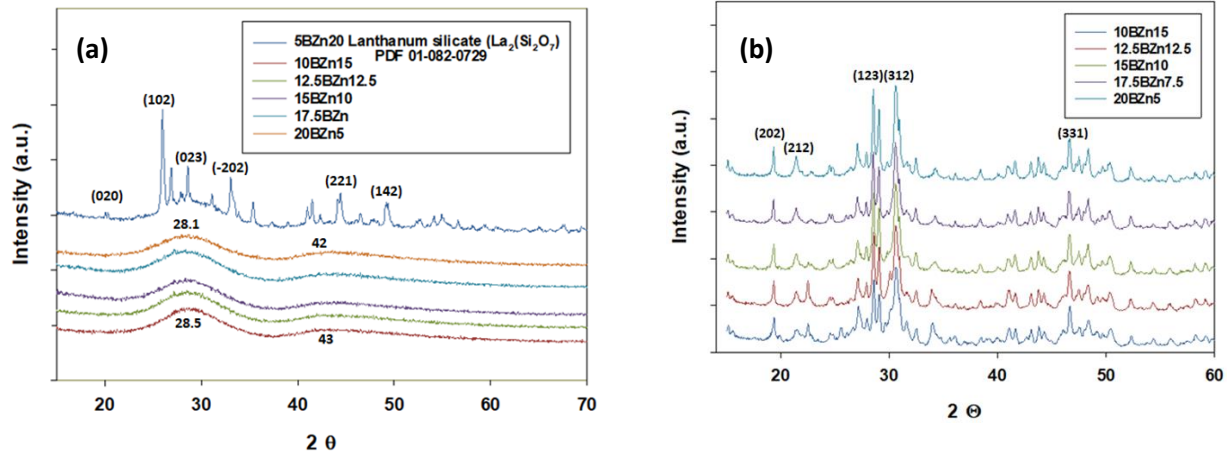


Figure 4-12: XRD pattern of $x\text{B}(15-x)\text{Zn}$ (a) Glass and single phase crystalline during pouring (b) single phase crystalline at 800°C for 50hr for $x\text{B}(15-x)\text{Zn}$ glasses.

The DTA curves of $x\text{B}(15-x)\text{Zn}$ samples (fig 4-13(a)) have similar features to those of BaS i exhibiting T_g and two crystallization peaks T_{c1} and T_{c2} with the second peak dominant over the first peak. T_g decreased slightly of 7°C across these glasses as boron oxide increased and zinc oxide decreased. Both boron oxide and zinc oxide have been reported as reducing T_g and T_s and consequently leading to a reduction in sealing temperature for fuel cells as reported by (Reis and Brow 2006, Zhang and Zou 2012). The TEC of $x\text{B}(15-x)\text{Zn}$ is reported for temperature between $300\text{-}600^\circ\text{C}$ in both glasses (blue line) and glass-ceramics (red line) (fig4-13(b)). The addition of ZnO increased the TEC from $8.3 \times 10^{-6} \text{ }^\circ\text{C}^{-1}$ at 5mol% ZnO to $8.8 \times 10^{-6} \text{ }^\circ\text{C}^{-1}$ at 15mol% ZnO however there was a slight decrease to $7.9 \times 10^{-6} \text{ }^\circ\text{C}^{-1}$ at 7.5mol% ZnO. After crystallization the TEC decreased slightly compared with the parent glass, except for when $\text{ZnO}/\text{B}_2\text{O}_3 = 1$ where TEC reached a maximum. The slight decrease in TEC of these glasses after heat treatment indicates that they should have long term thermal stability when used as a sealant for SOFCs as reported by (Puig, Ansart et al. 2016). In fig 4-13(c) the T_g increased as the amount of ZnO is increased and the amount of B_2O_3 is reduced.

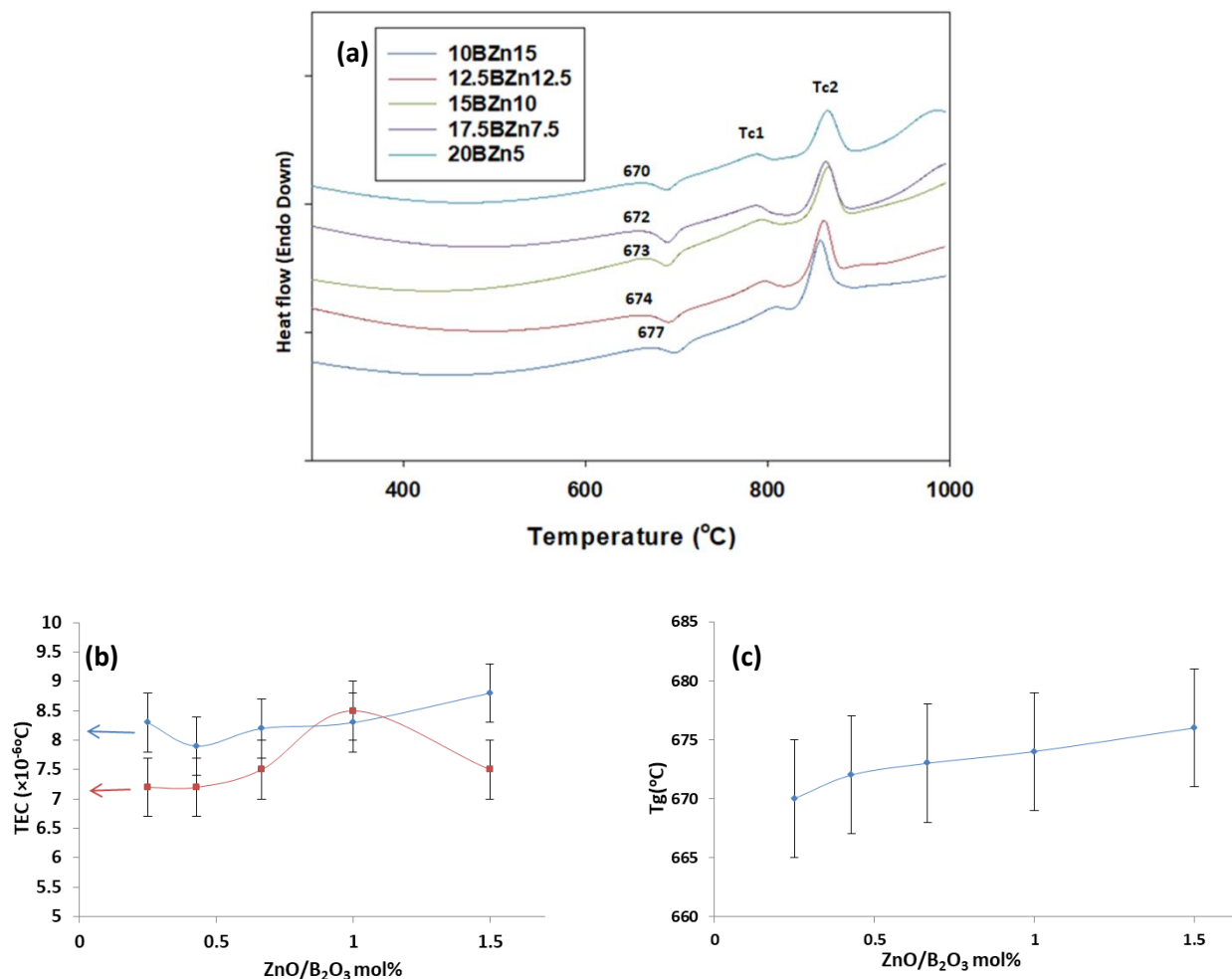


Figure 4-13: (a) DTA curves, (b) TEC of glass (blue line) and glass ceramic (red line) (c) T_g of $x\text{B}(15-x)\text{Zn}$ glass and glass ceramics.

As with the $x\text{Ba}(10-x)\text{Al}$ series the Raman and FTIR spectra of the $x\text{B}(15-x)\text{Zn}$ series glasses (fig 4-14 (a) and (b)) have 6 and 5 absorption bands in the Raman and FTIR spectra respectively (see table 3.4 and 3.6 for details of the general assignment of the peaks). The mid frequency range $800\text{-}1200\text{ cm}^{-1}$ suggests increasing polymerisation of the glass with increasing B_2O_3 as the peak positions move to higher wavenumbers in both Raman and FTIR. This indicates that the addition of boron oxide and reduction of zinc oxide seems to enhanced the polymerisation of the silica network as seen with soda lime borosilicate (Angeli, Boscarino et al. 2001). This is also further supported by the work of Wu et al, who found that a higher boron oxide content in sodium calcium borosilicate decreased the amount of NBOs (Wu and Stebbins 2009) which may

suggest enhanced structural rigidity. Looking at the higher wavenumbers the borate peaks in both techniques show an increased intensity in the region around 1400 cm^{-1} indicating an increase in the stretching vibration BO_3 units bonding BO_4 units. The shift to higher wavenumbers indicates that boron oxide additions enhance the formation of the BO_3 groups. The peak around 1220 cm^{-1} shows a slight decrease in intensity and in the FTIR spectra moves to higher wavenumbers which is an indication of a decrease in the boroxol rings and hence a corresponding increase in connectivity.

The band at $450\text{-}550\text{ cm}^{-1}$, which did not vary in intensity, has shifted to lower frequencies with increasing boron oxide additions, indicating that it is easier for bending vibrations of the Si-O-Si linkages to occur as observed by (Hao, Zan et al. 2012) and suggested increase in NBO as the possible cause; the shift to lower wavenumbers can also be associated with an increase in Si-O-Si bond angles as reported by (Kline, Tangstad et al. 2015). The band around 700 cm^{-1} also shifts to lower wavenumbers and again did not change its intensity similar to the one observed by (Hao, Zan et al. 2012) indicating that the lower wavenumber bending vibration of the B-O-B linkages in BO_3 units is fairly constant across the compositions studied. The only additional band in the Raman spectra is the $233\text{-}260\text{ cm}^{-1}$ band which is assigned to Zn-O bending vibrations in ZnO_4 tetrahedra; this band shifts to higher wavenumbers with increasing boron oxide content. Fig 4-15 (a) shows that the fraction of the Q^0 and Q^3 increased and Q^1 slightly drops at a ZnO/ B_2O_3 ratio of 0.45 after which it remains fairly constant and there is indication of a decreasing trend for the Q^2 . There is little variation of the BO_4 units at the lower ZnO/ B_2O_3 ratios but above a ZnO/ B_2O_3 ratio of 0.65 the number decreases. See appendix 4 and 5 for all the area% of both silicate and borate units for all series. Fig 4-15(c) shows that the Si-O stretching peak position decreases with ZnO and fig 4-15(d) that the polymerisation degree in $x\text{B}(15-x)\text{Zn}$ glasses initially increases as ZnO increases from 5 to 7.5mol% and then steadily decreases with increasing ZnO contents. This supports the earlier explanation that boron oxide additions enhanced the structure while ZnO slightly depolymerises the network. An initial increase in connectivity is not surprising as ZnO can act as network former or a network modifier.

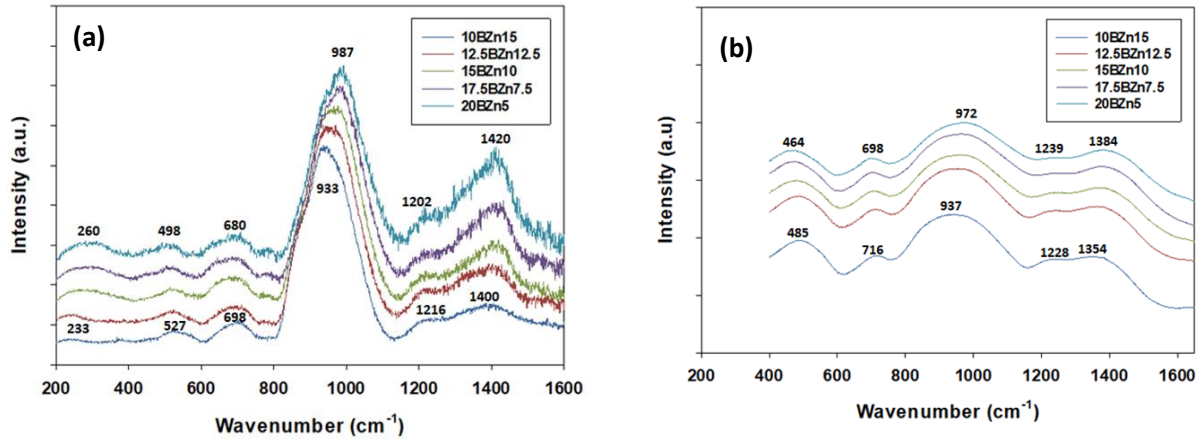


Figure 4-14: (a) Raman (b) FTIR spectra for $x\text{B}(15-x)\text{Zn}$ glasses

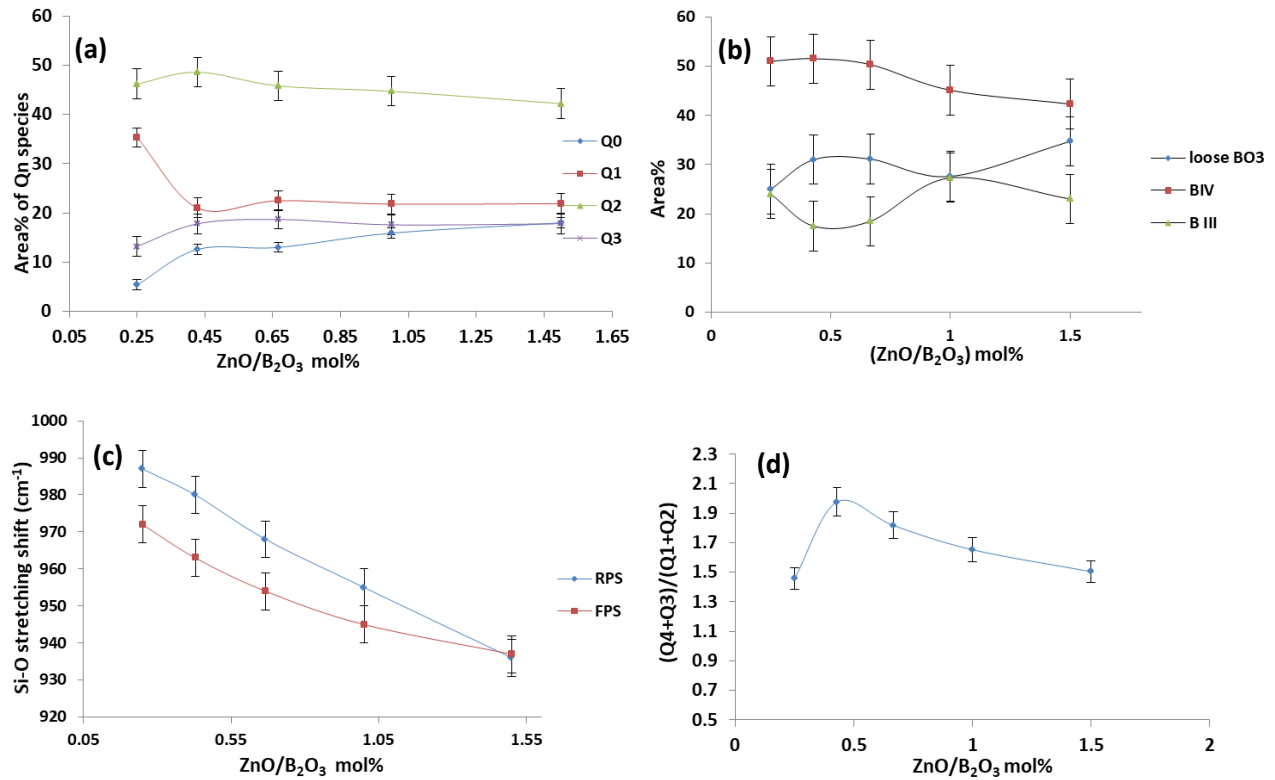


Figure 4-15: Fraction of (a) Qⁿ species and, (b) boron species, (c) Raman and FTIR peak shift (RPS, FPS) of Si-O stretching unit and (d) polymerisation index for xB(15-x)Zn glasses.

4. 4 Physical, thermal and structural analysis of xSi(20-x)Zn glasses

The effect of ZnO being swapped with SiO₂ on molar volume and density is presented in fig 4-16. Increasing the amount of ZnO against SiO₂ lead to an increase in density and a slight increasing trend in molar volume up to a ZnO/SiO₂ ratio of 0.4 and then a significant decrease afterwards. The behaviour of molar volume is not the same as in xB(15-x)Zn series when ZnO was swapped with B₂O₃ (fig4-11). This may be that ZnO in xB(15-x)Zn zinc may have joined the network according to (Smedskjaer, Youngman et al. 2013), while addition of ZnO increasing molar volume in xSi(20-x)Zn may suggest zinc oxide is mainly a modifier and increased inter atomic distance and create more NBOs and decreased glass compactness similar to reports by (Mohd Sabri Mohd, Mohd Hafiz Mohd et al. 2012). Although there is a drop in molar volume of xSi(20-x)Zn at the highest amount of ZnO 20mol% as can be seen in fig 4-16 possibly ZnO may have rejoin the network. Structurally T_g is seen to increase in xB(15-x)Zn fig 4-13 (c) and decrease in xSi(20-x)Zn fig 4-18 (c) as ZnO increases which further may support that the role of ZnO in the two series are not exactly the same. XRD indicates that xSi(20-x)Zn samples are

amorphous due to the absence of sharp peaks (fig4-17(a)). However just like in $x\text{B}(15-x)\text{Zn}$ and $x\text{Ba}(40-x)\text{Si}$ after isothermal heat treatment at 800°C for 50 h the formation of lanthanum silicate boron oxide ($\text{La}_3(\text{Si}_2\text{O}_4)_2\text{BO}_2$) (PDF no 04-010-1343) occurred.

The DTA curves of $x\text{Si}(20-x)\text{Zn}$ in fig 4-18(a) show that there is an increase of 18°C from 666 to 684°C in T_g as silica increases and ZnO reduces. Fig 4-18(b) shows that the TEC decreases slightly at the first ZnO addition at 0.34 ratios of the ZnO/SiO₂ and subsequently increased with increasing ZnO in both the $x\text{Si}(20-x)\text{Zn}$ glasses and glass-ceramics. The TEC of the glass ceramics (red data) are slightly lower than the parent glasses (blue data) which indicates good thermal stability as explained in section 4.3 for $x\text{B}(15-x)\text{Zn}$. Fig 4-18(c) also shows that the T_g steadily decreased as the amount of ZnO increased which suggests network depolymerisation.

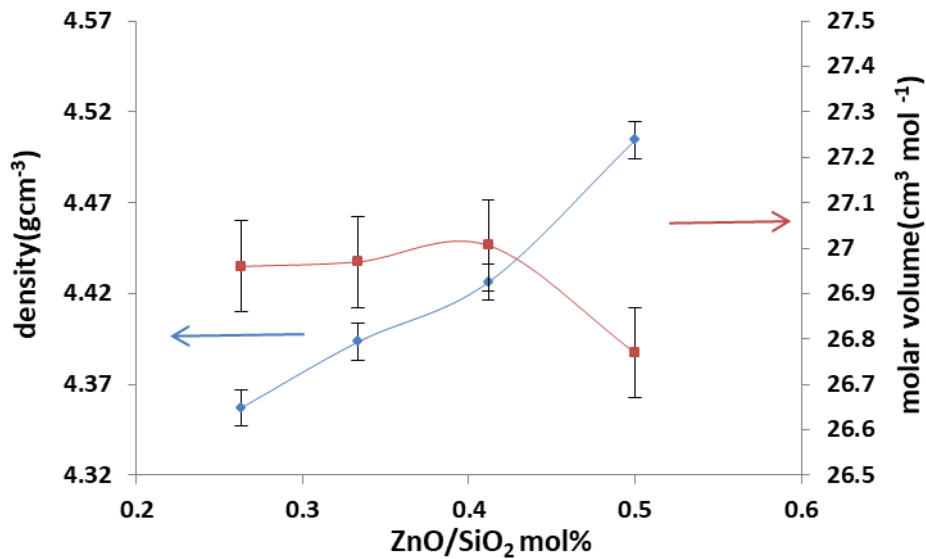


Figure 4-16: Density and molar volume versus ZnO/SiO₂ ratio of $x\text{Si}(20-x)\text{Zn}$ glasses

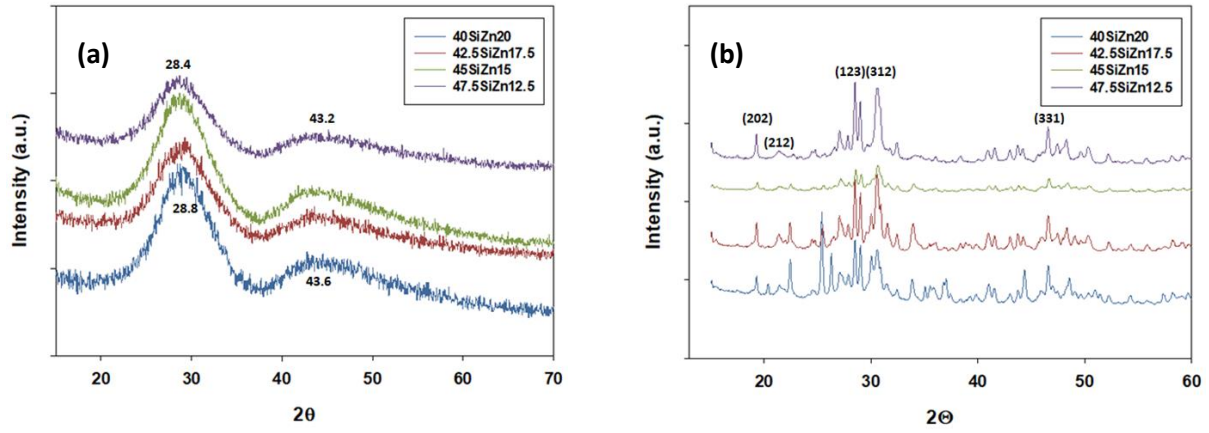


Figure 4-17: XRD patterns of $x\text{Si}(20-x)\text{Zn}$ (a) glasses and (b) glass ceramics

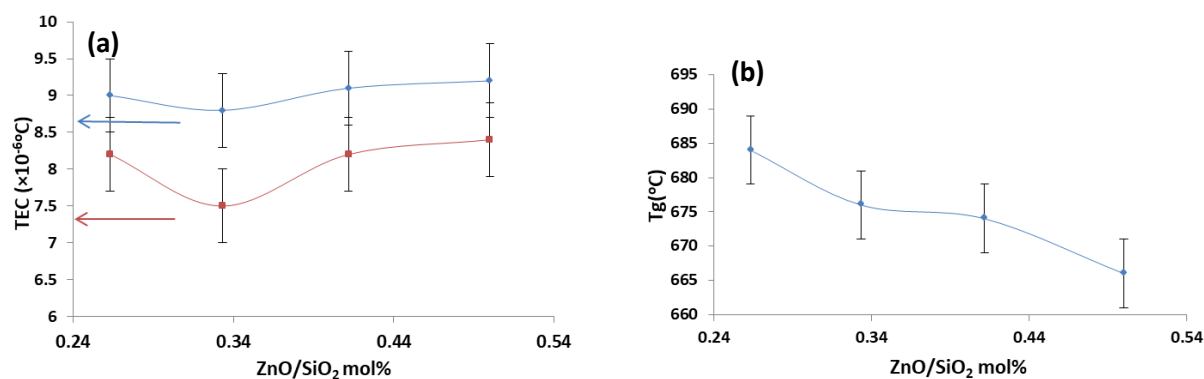
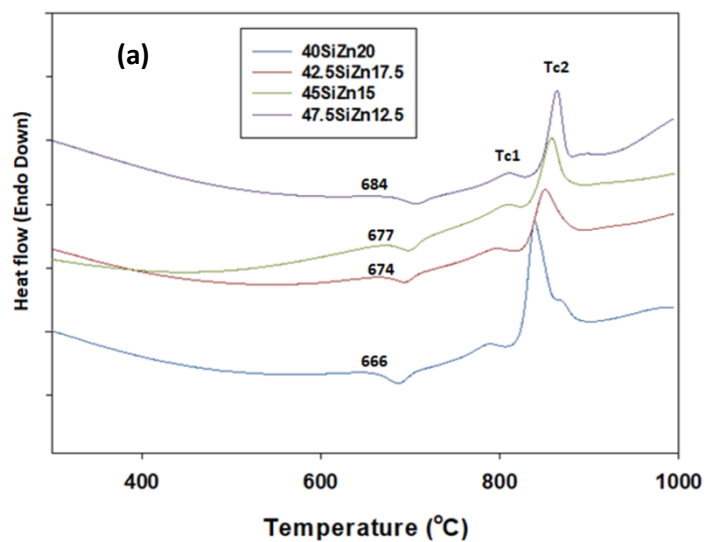


Figure 4-18: (a) DTA curves, (b) TEC of glass (blue data) and glass ceramic (red data) (c) T_g of $x\text{Si}(20-x)\text{Zn}$ glasses and glass ceramics.

The Raman and FTIR spectra of $x\text{Si}(20-x)\text{Zn}$ (fig 4-19(a) and (b)) are similar to those of $x\text{B}(15-x)\text{Zn}$ in (fig 4-14). There are visible structural changes in the mid frequency range due to increasing boron oxide in $x\text{B}(15-x)\text{Zn}$ and silica in $x\text{Si}(20-x)\text{Zn}$ glass series respectively which leads to increasing polymerisation of the silicate network as indicated by a shift to higher wavenumbers of the Si-O stretching unit and the gradual disappearance of the shoulder around 870 cm^{-1} assigned to Q^0 and subsequent shift of the Q^1 peak to higher wavenumbers. There is a slight increase in intensity and shift to higher wavenumbers in both peaks around 1200 and 1400 cm^{-1} . For the explanation of the other peaks see section 4.3.

Deconvolution of the silica and borate peaks in $x\text{Si}(20-x)\text{Zn}$ further supports the structural depolymerisation trend with increasing ZnO. As can be seen in fig 4-20 (a) there is a clearly visible decrease in the amount of Q^3 and Q^2 while Q^0 and Q^1 steadily increase. The amount of Q^2 is considerably higher than the amount of the other Q^n species. In fig 4-20(b) the amount of BO_4 is seen to be higher than the amount of loose BO_3 which decreases while the amount of BO_3 in boroxol ring increases. Depolymerisation is evidenced in both the deconvolution of the silicate and the borate units as ZnO/SiO₂ ratio increased. See appendix 4 and 5 for all the area% of both silicate and borate units for all series. The Si-O stretching peak position shift in fig 4-20(c) decreases in both Raman and FTIR data and the degree of polymerisation in fig 4-20(d) also steadily decreases again indicating that ZnO plays a modifying role and depolymerises the glass structure.

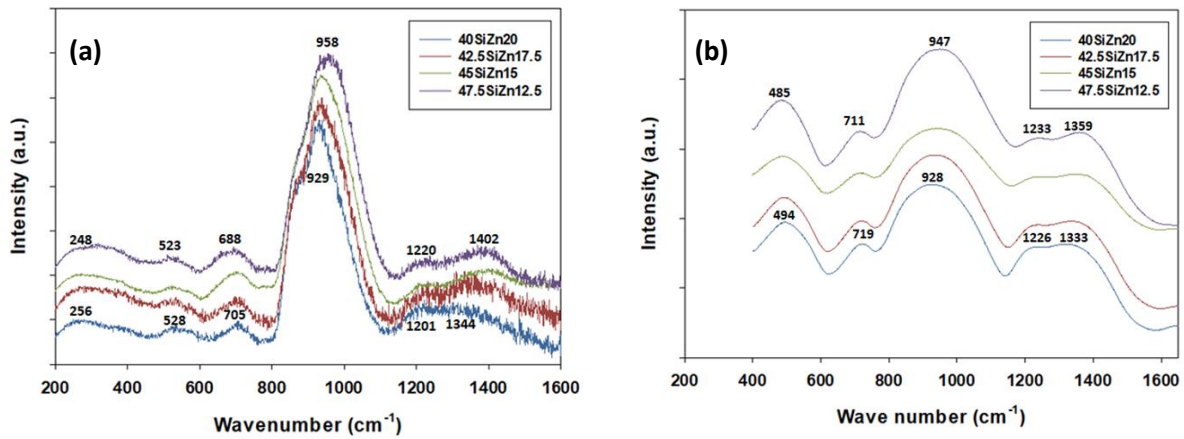


Figure 4-19: (a) Raman and (b) FTIR Spectra of $x\text{Si}(20-x)\text{Zn}$ glasses.

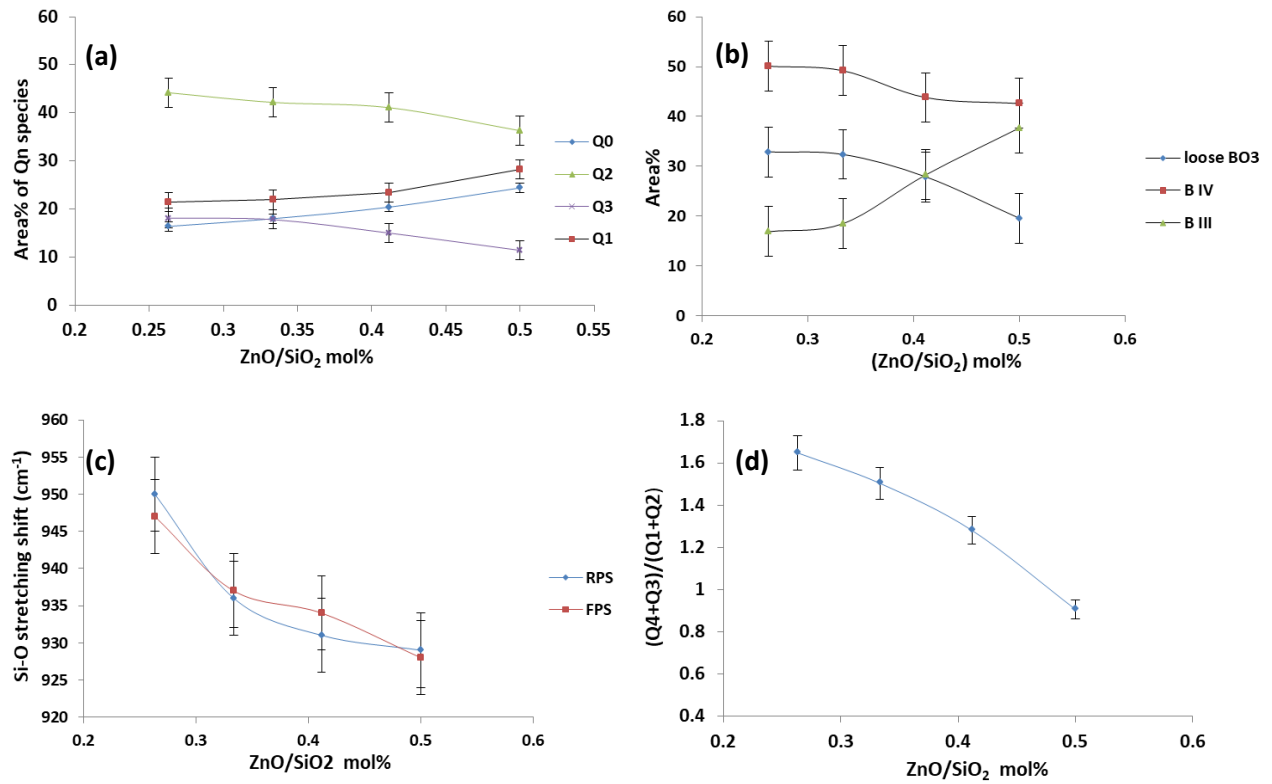


Figure 4-20: Fraction of (a) Qⁿ species and, (b) boron species, (c) Raman and FTIR peak shift of Si-O stretching unit and (d) polymerisation index of xSi(20-x)Zn glasses

4.5 Physical, thermal and structural analysis of xSi(20-x)La(Ba) and xSi(20-x)La(Sr) glasses

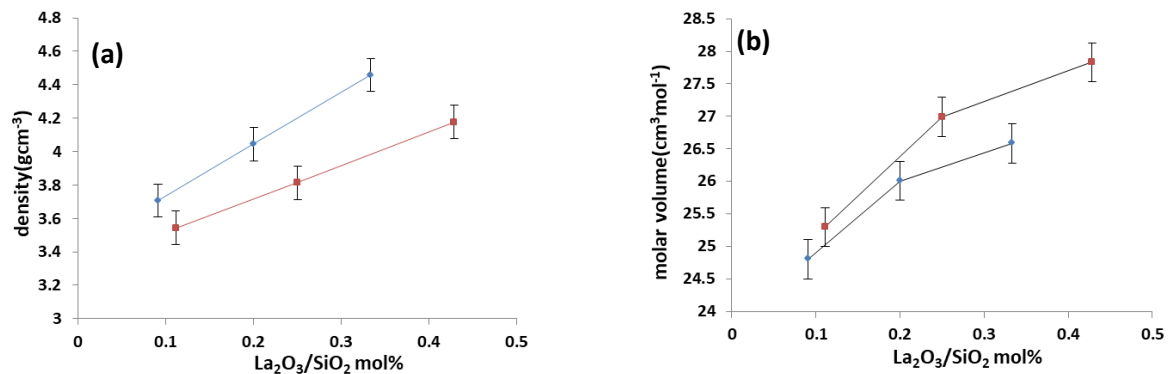


Figure 4-21: (a) Density and (b) molar volume of xSi(20-x)La(Ba) blue line and xSi(20-x)La(Sr) red line glasses versus La₂O₃/SiO₂ ratio.

in these two series swapping silica with lanthanum on molar basis introduces higher La_2O_3 into the glass than removing silica therefore the effect of the high lanthanum on physical properties will be discussed below. In fig 4-21 (a) and (b) shows that both the density and molar volume of $x\text{Si}(20-x)\text{La}(\text{Ba})$ and $x\text{Si}(20-x)\text{La}(\text{Sr})$ glasses increase with increasing $\text{La}_2\text{O}_3/\text{SiO}_2$. This is due to high molecular weight of lanthanum oxide (325.81gmol^{-1}) compared to that of silica (60.08gmol^{-1}). According to (Smiljanic, Grujic et al. 2016) with increasing La_2O_3 in $\text{La}_2\text{O}_3\text{-SrO-B}_2\text{O}_3$ glass there is an increase in oxygen content leading to increase in molar volume. The slightly higher density of $x\text{Si}(20-x)\text{La}(\text{Ba})$ compared with $x\text{Si}(20-x)\text{La}(\text{Sr})$ in fig 4-21(a) may be due the presence of Ba which is heavier than Sr; the opposite behaviour can be seen in the molar volume because Ba is larger than Sr so it occupies more space in the glass structure see fig 4-21(b). As noted in section 4.1 usually molar volume and density change inversely, however with these glasses both molar volume and density increased as the amount of lanthanum oxide increased. This sort of behaviour on lanthanum oxide addition has been reported by (Ojha, Rath et al. 2011) and was also observed for $x\text{Ba}(40-x)\text{Si}$ glasses discussed earlier (see section 4.1.1). An increase in molar volume indicates expansion of the glass network due to substitution of silica by lanthanum oxide. NMR studies show that increasing lanthanum causes an increased disorder in the borosilicate structure resulting in wider spacing and bond angle distribution due to the larger ionic radius of lanthanum (Ojha, Rath et al. 2015).

$x\text{Si}(20-x)\text{La}(\text{Ba})$ with a silica content of 55mol% phase separated into glass and contained un-dissolved quartz SiO_2 PDF: no (01-085-1054) (see fig 4-22(a)). Other $x\text{Si}(20-x)\text{La}(\text{Ba})$ and $x\text{Si}(20-x)\text{La}(\text{Sr})$ samples shown in fig 4-22(a) and (b) were amorphous. In both series the XRD peak positions move to slightly higher 2θ angles with increasing SiO_2 . Swapping silica with lanthanum on molar basis adds more lanthanum oxide into the glass than silica and therefore the crystallization of samples containing 20mol% lanthanum in $20\text{LaSi}40(\text{Ba})$ and $20\text{LaSi}30(\text{Sr})$ mol% on pouring to form apatite type lanthanum silicates ($\text{La}_{9.33}\text{Si}_6\text{O}_{26}$) PDF 00-049-0443 (see fig 4-23) is not surprising as the ratio of lanthanum to silica is approximately 1:1 which according to (Hosseini, Shvareva et al. 2013) leads to the formation of apatite type lanthanum silicate structure. On a general note as reported by (Nicoleau, Angeli et al. 2016) due to their low solubility in the glass matrix some elements such as the lanthanides can lead to the formation of crystalline phases in borosilicates during cooling. As noted above ten crystalline phases containing La_2O_3 exist in the $\text{SiO}_2\text{-B}_2\text{O}_3\text{-La}_2\text{O}_3$ ternary system: four of these are

(LaBSiO_5 , $\text{La}_3\text{Si}_2\text{BO}_{10}$, $\text{La}_{9.66}\text{Si}_5\text{BO}_{26}$, and $\text{La}_{10}\text{Si}_4\text{B}_2\text{O}_{26}$), three are B_2O_3 - La_2O_3 binary phases (La_3BO_6 , LaBO_3 , and LaB_3O_6) and another three are SiO_2 - La_2O_3 binary phases (La_2SiO_5 , $\text{La}_{9.33}\text{Si}_6\text{O}_{26}$, and $\text{La}_2\text{Si}_2\text{O}_7$) (Trégouët, Caurant et al. 2017). Out these ten different phases only three have been observed in this study. Two of the phases formed are based on the SiO_2 - La_2O_3 binary and one on the SiO_2 - B_2O_3 - La_2O_3 ternary, however no phase from the B_2O_3 - La_2O_3 binary has been observed. The significance of these phases is that in the glass-ceramics heat treated at 800°C a stable lanthanum borosilicate phase is formed which suggests that boron volatility may be mitigated and this could help avoid cathode poisoning which is a common problem in which boron in the sealing glass attacks the lanthanum in the cathode leading to formation of LaBO_3 and in addition glass-ceramic with this phase has a slightly lower TEC which is also a good sign of thermal stability.

The Raman spectra of these samples is presented in fig 4-23(b); similar structures have also been reported by (Kharlamova, Pavlova et al. 2011) for many apatite type structures. The sharp peak in the Raman spectra in fig 4-23(b) near 850 cm^{-1} is attributed to Q^0 silicate tetrahedra as reported by (Kidari, Dussossoy et al. 2012). The strong band in the region 800 - 1050cm^{-1} is characteristic of Si-O vibrations in a regular isolated tetrahedron (Kharlamova, Pavlova et al. 2011). The Raman peaks 384, 518, 850 and 916 are assigned to apatite type lanthanum silicate (Rodríguez-Reyna, Fuentes et al. 2006). In fig 4-23 (c) the Raman spectra are similar for the thermally treated samples indicating the formation of lanthanum silicate boron oxide ($\text{La}_3(\text{Si}_2\text{O}_4)_2\text{BO}_2$) (PDF no 04-010-1343), as seen by XRD (see fig 4-2 (b), 4-12 (b) and 4-17(b)).

In general the IR spectra of apatite type silicates are typical of orthosilicate structures with some isolated SiO_4 tetrahedral units. The DTA curves of glasses series $x\text{Si}(20-x)\text{La}(\text{Ba})$ and $x\text{Si}(20-x)\text{La}(\text{Sr})$ (fig 4-24) indicates that T_g increases with lanthanum oxide addition. A similar trend has been reported by (Ganvir and Gedam 2017). The DTA curve for both $x\text{Si}(20-x)\text{La}(\text{Ba})_4$ and $x\text{Si}(20-x)\text{La}(\text{Sr})_4$ samples reflects the phase separation in the two samples as can be seen in the XRD in fig 4-22(a).

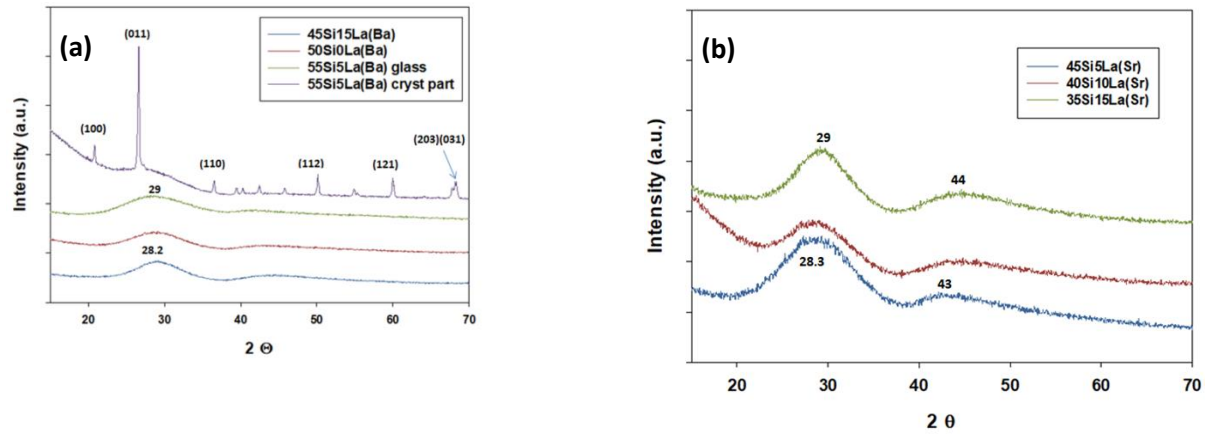


Figure 4-22: XRD patterns of un-dissolved quartz SiO_2 PDF: no (01-085-1054) for crystalline part of $x\text{Si}(20-x)\text{La}(\text{Ba})_4$ with other amorphous samples (a) and (b) Amorphous $x\text{Si}(20-x)\text{La}(\text{Sr})$ series with increasing La/Si ratio

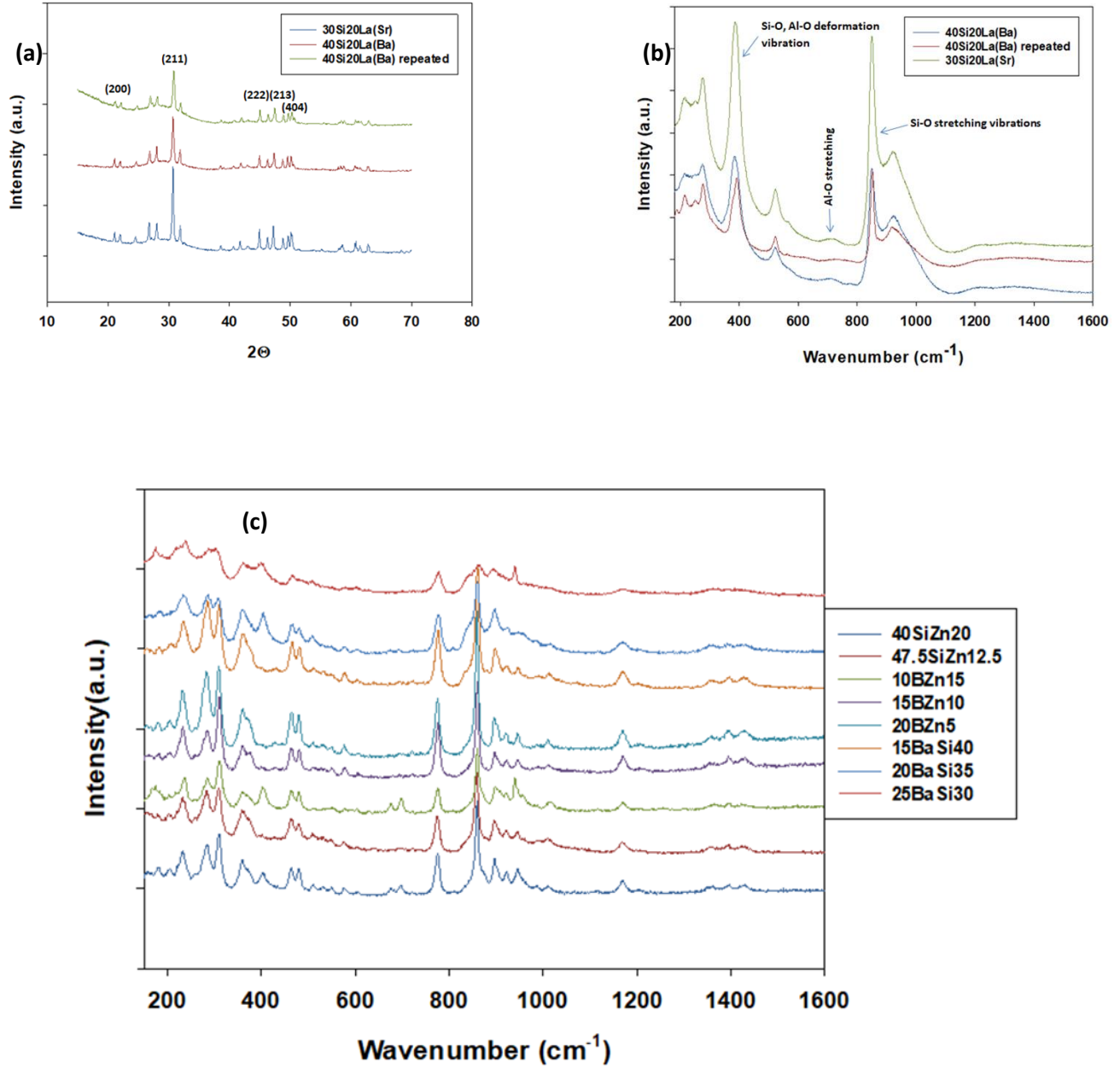


Figure 4-23: XRD patterns of apatite type lanthanum silicates ($\text{La}_{9.33}\text{Si}_6\text{O}_{26}$) PDF 00-049-0443 and (b) Raman spectra of the same phase for 20LaSi40(Ba) and 20LaSi30(Sr) mol% with La/Si ratio 1:2 and 1:1.5 respectively. (c) Raman spectra of thermally treated $x\text{Ba}(40-x)\text{Si}$, $x\text{B}(15-x)\text{Zn}$ and $x\text{Si}(20-x)\text{Zn}$ glasses showing the presence of lanthanum silicate boron oxide ($\text{La}_3(\text{Si}_2\text{O}_4)_2\text{BO}_2$)

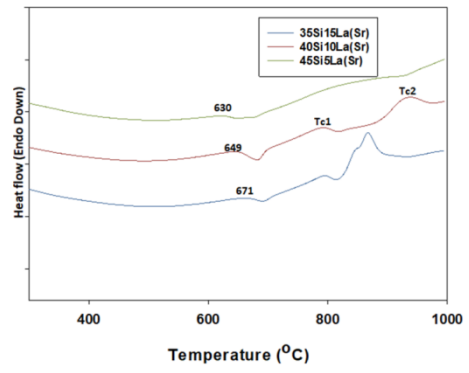
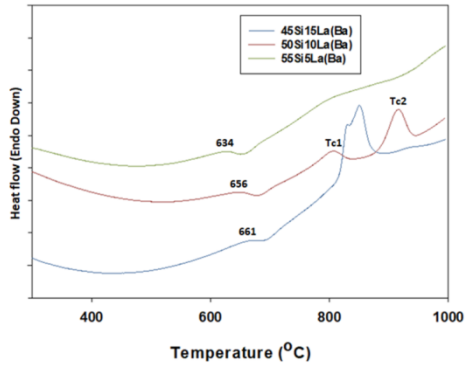


Figure 4-24: DTA curves (a) $x\text{Si}(20-x)\text{La}(\text{Ba})$ and (b) $x\text{Si}(20-x)\text{La}(\text{Sr})$

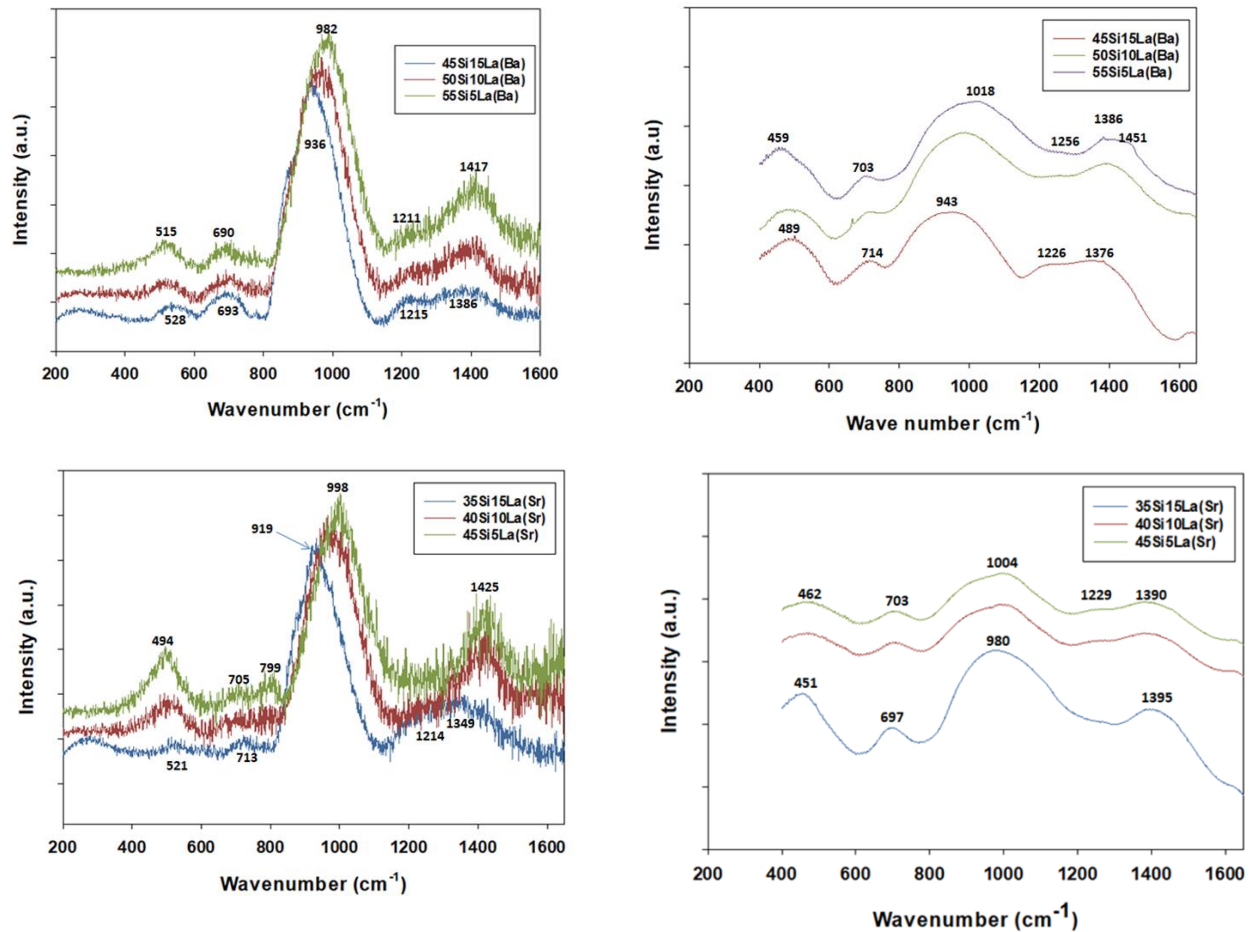


Figure 4-25: Raman (b) FTIR spectra of $x\text{Si}(20-x)\text{La}(\text{Ba})$ glasses; (c) Raman and (d) FTIR spectra of $x\text{Si}(20-x)\text{La}(\text{Sr})$ glasses

The Raman and FTIR spectra of $x\text{Si}(20-x)\text{La}(\text{Ba})$ glasses are shown in fig 4-25 (a) and (b). As the amount of SiO_2 increases and that of lanthanum oxide decreases both spectra indicate increased polymerisation with the SiOSi band shifting to higher wavenumbers and its intensity remaining fairly constant. The width of this peak slightly increased from $x\text{Si}(20-x)\text{La}(\text{Ba})_2$ to $x\text{Si}(20-x)\text{La}(\text{Ba})_4$. The intensities of the Raman peak around 1200 cm^{-1} decrease while Raman peak at 1380 cm^{-1} increases in intensity in the Raman spectra and the FTIR peak splits into two peaks at 1386 and 1451 cm^{-1} and these peaks shifted to higher position wavenumbers with increasing SiO_2 . The latter feature indicates polymerisation of the borate unit as it forms BO_3 units around 1386 cm^{-1} as reported by (Ardelean and Toderaş 2006) and 1451 cm^{-1} assigned to charged trigonal BO_2O^- linked to tetrahedral BO_4 see (El Hayek, Ferey et al.). The peaks at 450

and 700 cm^{-1} both shifted to lower wavenumbers and their intensities remained unchanged, except for the lower wavenumber around $450\text{-}500\text{ cm}^{-1}$ of $x\text{Si}(20-x)\text{La}(\text{Ba})_4$ which increased in intensity and a slight decrease in width of the band 459 cm^{-1} in the FTIR spectra. The shift to lower wavenumber may be due to increase in bond angles of Si-O-Si as stated earlier and fairly constant intensity suggest that the bending vibrations of the B-O-B linkages to BO_3 units around 700 cm^{-1} do not change much while the SiOSi bending around 500 cm^{-1} slightly increased.

The Raman and FTIR spectra of $x\text{Si}(20-x)\text{La}(\text{Sr})$ glasses (fig 4-25(c) and (d) respectively) have similar features to the spectra of $x\text{Si}(20-x)\text{La}(\text{Ba})$ glasses and hence the above discussion applies to $x\text{Si}(20-x)\text{La}(\text{Sr})$. However, the notable difference is that the higher wavenumber FTIR peak at around 1400 cm^{-1} in $x\text{Si}(20-x)\text{La}(\text{Sr})$ did not split into two which is unlike the case of $x\text{Si}(20-x)\text{La}(\text{Ba})$.

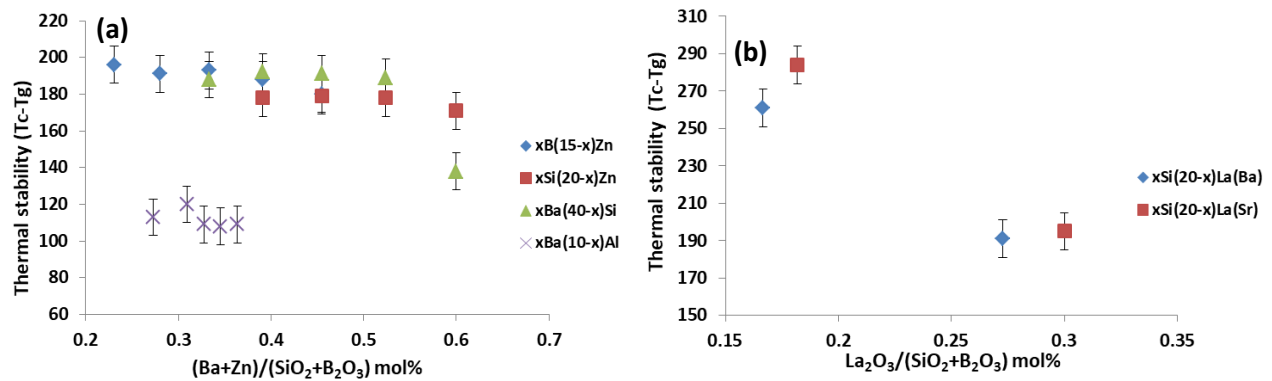


Figure 4-26: Thermal stability plotted against (a) total divalent modifiers/total network formers and (b) total trivalent modifiers/total network formers for all glass series.

Fig 4-26 shows that an increase in the ratio of the sum of modifiers BaO and ZnO to the sum of network forming oxides leads to a small decrease in thermal stability of $x\text{B}(15-x)\text{Zn}$, $x\text{Si}(20-x)\text{Zn}$, $x\text{Ba}(40-x)\text{Si}$ and $x\text{Ba}(10-x)\text{Al}$ samples indicating that addition of these oxides have no much effect on the thermal stability in these glasses except that there is a wide gap between the thermal stability of $x\text{Ba}(10-x)\text{Al}$ series and the other 3 series $x\text{B}(15-x)\text{Zn}$, $x\text{Si}(20-x)\text{Zn}$ and $x\text{Ba}(40-x)\text{Si}$ this is possibly due to using different crystallization peak positions as T_{c1} is considered for $x\text{Ba}(10-x)\text{Al}$ series because it has only one clearly visible T_c peak and T_{c2} for the

other series and in addition the highest amount of modifier in $x\text{Ba}(10-x)\text{Al}$ between 30 to 35mol% ($\text{SrO}+\text{BaO}$) and lower silica content of fixed 35mol% and fairly high boron content of fixed 20% may also contribute to the lower thermal stability obtained from the differences between the T_c - T_g . However, increasing the ratio of the sum of the modifiers to the sum of network formers in $x\text{Ba}(40-x)\text{Si}$ suggests a slight increase in thermal stability until the 25mol% BaO sample where a notable decrease in thermal stability is seen. On the other hand increases in the amount of La^{3+} in $x\text{Si}(20-x)\text{La}(\text{Ba})$ and $x\text{Si}(20-x)\text{La}(\text{Sr})$ glasses lead to decrease in thermal stability and this is a sign that these glasses would favour easy crystallization as reported (Ojha, Rath et al. 2015).

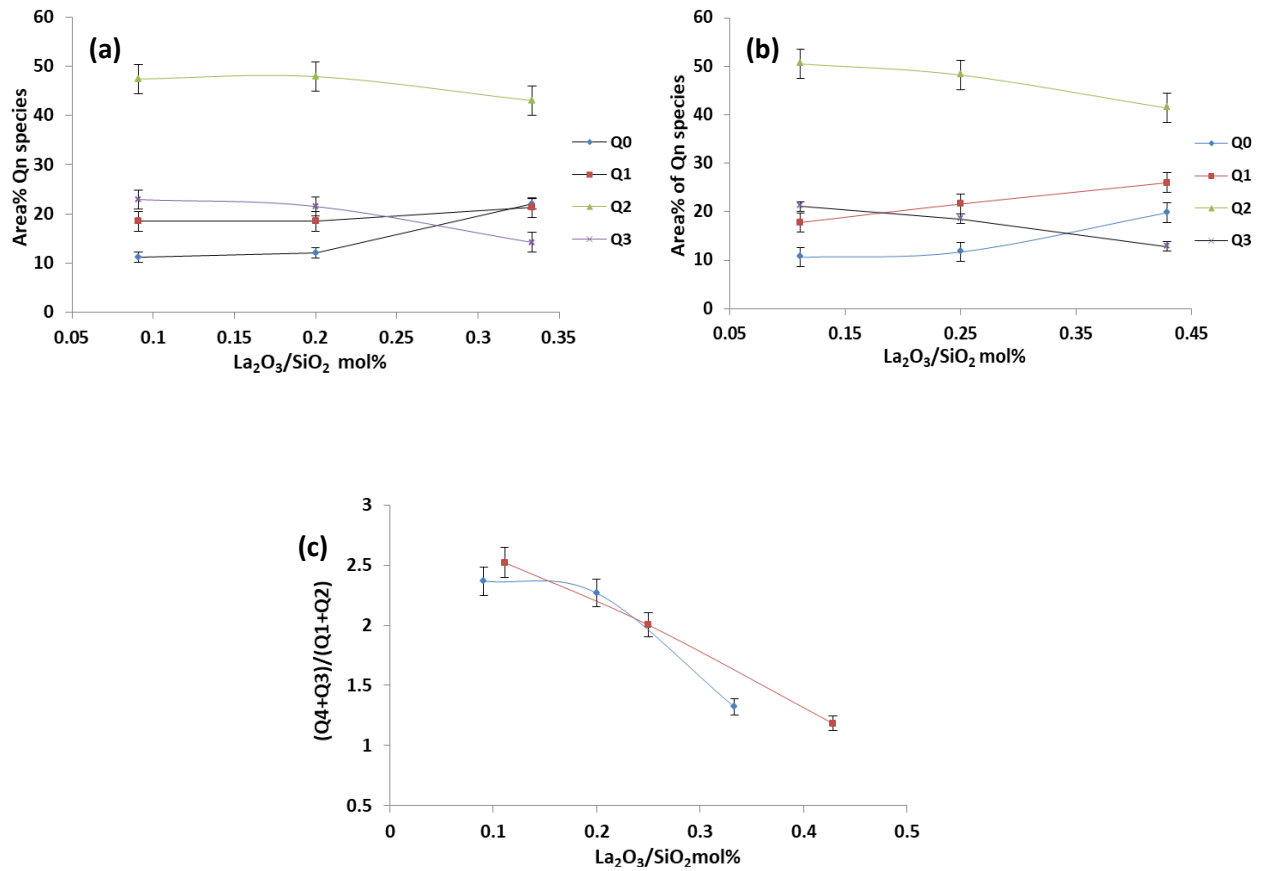


Figure 4-27: Fraction of Q^n species (a) $x\text{Si}(20-x)\text{La}(\text{Ba})$, (b) $x\text{Si}(20-x)\text{La}(\text{Sr})$ and (c) polymerisation index for both $x\text{Si}(20-x)\text{La}(\text{Ba})$ blue line and $x\text{Si}(20-x)\text{La}(\text{Sr})$ glasses in red line

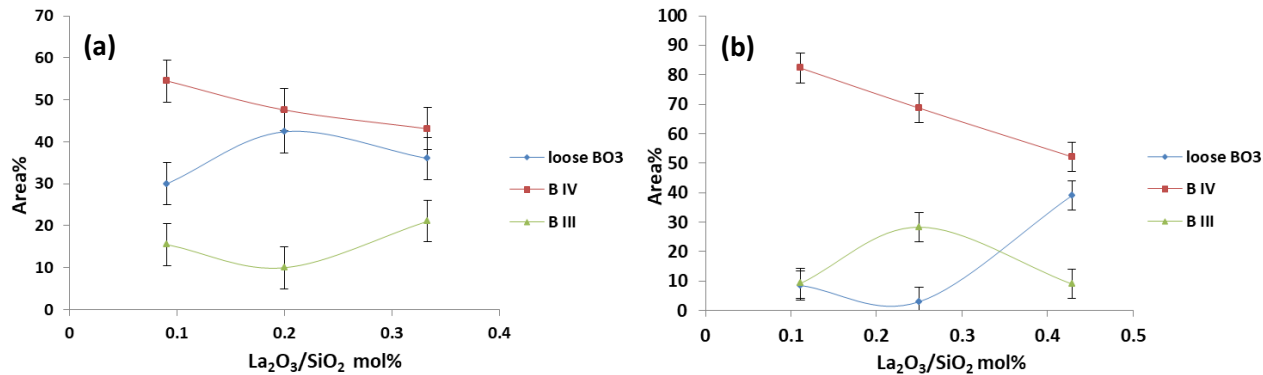


Figure 4-28: Area% of boron species (a) xSi(20-x)La(Ba) and (b) xSi(20-x)La(Sr) glasses.

Fig 4-27 (a) and (b) shows that as the amount of La₂O₃ increased in both series, a steady decrease in the area% of Q² and Q³ while Q¹ and Q⁰ increased. Although the amount of silica is higher in xSi(20-x)La(Ba), looking at the plots the amount of Q¹ and Q⁰ increases in a monotonic fashion in the xSi(20-x)La(Sr) glasses compared to xSi(20-x)La(Ba) glasses where a drastic increase is seen after a La₂O₃/SiO₂ ratio of 0.2. The behaviour of the degree of polymerisation (fig 4-27 (c)) also exhibits a monotonic decrease for xSi(20-x)La(Sr) glasses but little change for the xSi(20-x)La(Ba) glasses until a La₂O₃/SiO₂ ratio of 0.2. Fig 4-28(a) and (b) indicate that increasing the amount of La₂O₃ leads to a decrease in BO₄ fraction with the fraction of BO₄ in xSi(20-x)La(Sr) being higher than that in xSi(20-x)La(Ba) probably due higher field strength of SrO as compared to BaO (Zhang, Yue et al. 2013). Another clear difference is in the increase in loose BO₃ and the decrease in the BO₃ in boroxol rings for xSi(20-x)La(Ba) with increasing La₂O₃ ; the opposite is observed for the xSi(20-x)La(Sr) series.

4. 6 Summary and conclusion of results

1. Most of the as made samples are amorphous as indicated by the XRD patterns which have 2 clearly visible humps belonging to the silicate and the borate units.
2. The XRD and Raman of the isothermally heated series xBa(40-x)Si, xB(15-x)Zn, and xSi(20-x)Zn indicate the formation of lanthanum boron silicate phase.
3. Although 10 separate crystalline phases are known in the B₂O₃-La₂O₃, SiO₂-La₂O₃ binary and SiO₂-B₂O₃-La₂O₃ ternary systems only 3 were observed in this study.

4. All glass series studied exhibit decreasing T_g and T_c with modifier addition except for additions of lanthanum oxide in $x\text{Si}(20-x)\text{La}(\text{Ba})$ and $x\text{Si}(20-x)\text{La}(\text{Sr})$ which increased T_g . For a sealing glass the lowest possible T_g is preferred over a high T_g because thermal stresses develop below T_g .
5. The T_g s of the $x\text{Ba}(40-x)\text{Si}$ and $x\text{Ba}(10-x)\text{Al}$ series fall between 580 to 662°C which suggests they could be used for intermediate temperature SOFC applications.
6. The TECs of 20BaSi35, 22.5BaSi32.5, and 25BaSi30 mol% glass and glass-ceramic samples and all $x\text{Ba}(10-x)\text{Al}$ glasses meet the optimal values required for sealing glasses. A slight decrease in TEC after heat treatment is a sign of long term thermal stability as the TEC of the glass ceramics exhibit slightly lower values compared to their parent glasses. The highest TEC is observed in 12BaAl8 possibly due to liquid in liquid phase separation, as that sample has two T_g s.
7. The TECs for all of the $x\text{B}(15-x)\text{Zn}$, $x\text{Si}(20-x)\text{Zn}$, $x\text{Ba}(40-x)\text{Si}$, $x\text{Ba}(10-x)\text{Al}$, and $x\text{Si}(20-x)\text{La}(\text{Sr})$ glass and glass-ceramic samples measured between RT-300 °C are not appropriate for sealing to SOFCs but they are compatible for use in sealing to Ti-6Al-4V used in electrical feed through connectors.
8. Thermal stability as assessed by T_c-T_g decreases with modifier content and overall the $x\text{Ba}(10-x)\text{Al}$ series has the lowest thermal stability possibly because of different T_c peak positions were used and or due the presence of high modifier >30mol% across the series. The other glasses studied all have similar thermal stabilities.
9. The formation of thermally stable phase containing boron after heat treatment is a sign of improved thermal stability and this could mitigate boron volatility and also the formation of phase without barium and strontium is advantageous, if at all it will remain the same phase after sealing to SOFCs components.

5 Results II: Electrical properties

This section discusses the electrical properties of the glasses and glass ceramics produced in this study. $x\text{Ba}(40-x)\text{Si}$ in which BaO swapped for SiO_2 and $x\text{B}(15-x)\text{Zn}$ where B_2O_3 swapped for ZnO are considered in both glass and glass-ceramic forms; while in $x\text{Ba}(10-x)\text{Al}$ BaO was swapped for Al_2O_3 and is in the glass form only and $x\text{Si}(20-x)\text{Zn}$ series in which SiO_2 swapped for ZnO in glass-ceramic form only. In the case of $x\text{Ba}(10-x)\text{Al}$ it was difficult to obtain their crystalline counterparts because they adhered to the ceramic surface in the furnace when heat treated at 800°C for 50 h. Meanwhile in the case of $x\text{Si}(20-x)\text{Zn}$ the samples crystallised readily and therefore it was not possible to fire the gold electrodes for electrical measurements onto the glasses without crystallization and so for this series electrical conductivity was measured only for crystalline samples. The electrical properties will be looked at differently series by series and after that a generic presentation will follow.

5.1 Electrical properties of xBa(40-x)Si glasses and glass ceramics

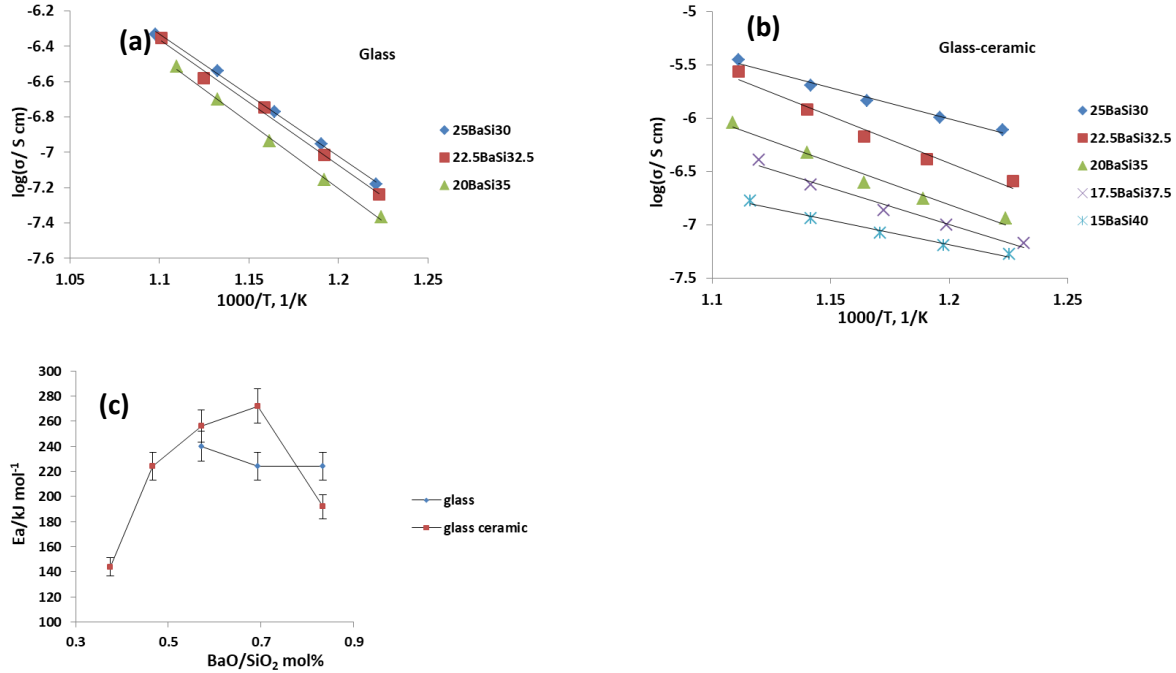


Figure 5-1: Variation of conductivity with temperature and composition for (a) xBa(40-x)Si glasses (b) xBa(40-x)Si glass ceramics and (c) variation of activation energy for electrical conductivity (E_a) versus BaO/SiO₂ for xBa(40-x)Si glasses blue line and glass ceramic red line

In fig 5-1 (a) and (b) an increase in conductivity with temperature and BaO addition can be observed for xBa(40-x)Si samples, and particularly more clearly in the glass-ceramic form fig 5-1(b). In figure 5-1 the presence of one slope running through an entire set of measurements is evidence for a single conduction mechanism in these glasses (Pal, Agarwal et al. 2009). The activation energies for electrical conduction in fig 5-1(c) exhibit different behaviour in glass and glass-ceramic forms. In glass, E_a decreases with increasing BaO and decreasing SiO₂ content which is expected as silica goes down and being depolymerised by the BaO addition, more free spaces are created for charge carries to move or hop under thermal activation. On the other hand, E_a of the xBa(40-x)Si glass ceramic suggests an increase with increasing BaO/SiO₂ ratio until it reached a maximum value of 272 kJ/mol at a ratio of 0.7 after which it decreased. Such an increase in E_a of the crystalline samples may be due to obstruction of ion free movement in the glass ceramic due to the presence of phase boundaries, and also due to densification which

reduces the void spaces available in the glasses and therefore hinders the mobility of alkali ions within the glass ceramics by steric constraints (Ingram 1989, Gomaa, Abo-Mosallam et al. 2009).

The drop in E_a of 25BaSi30 mol% may not be unconnected with the smaller extent of crystallization compared to other samples in the series, see the XRD in fig 4-2 (b). According to Anderson and Stuart, the E_a required for ionic conduction is dependent on two terms (i) the binding energy of the cationic charger carriers and (ii) the structural network strain energy. A fraction of the charge carriers with the aid of thermal activation can overcome potential barriers and jump to neighbouring sites and as the thermal energy increases the probability of the charge carriers to overcome the potential barriers increases (Braunger, Escanhoela et al. 2012). In line with this statement by Braunger et al, conductivity also increases with temperature as in fig 5-1 (a) and (b).

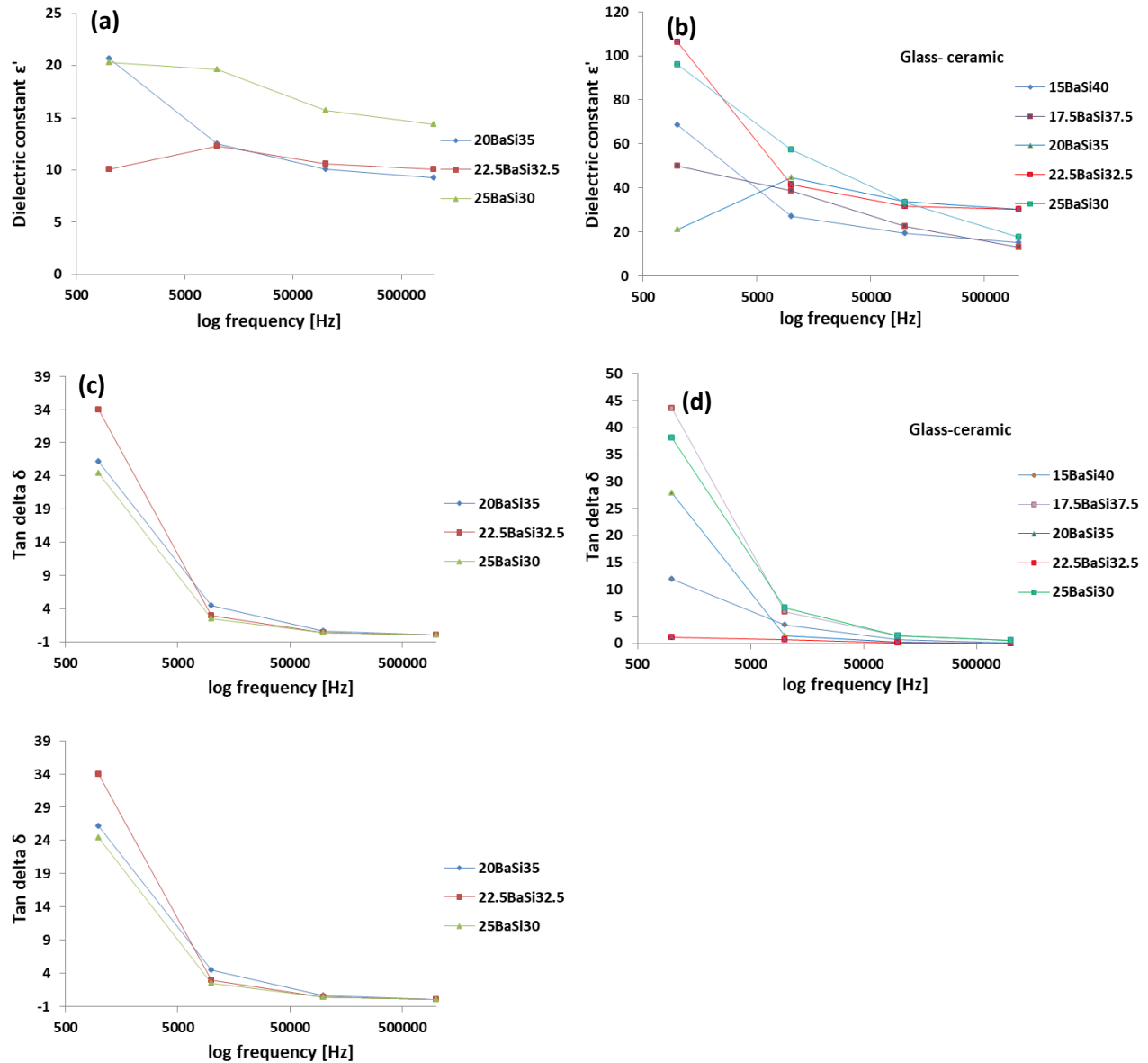


Figure 5-2: Frequency dependence of the dielectric constant of (a) $x\text{Ba}(40-x)\text{Si}$ glasses (b) $x\text{Ba}(40-x)\text{Si}$ glass ceramics and frequency dependence of the tangent loss of (c) $x\text{Ba}(40-x)\text{Si}$ glasses (d) $x\text{Ba}(40-x)\text{Si}$ glass ceramics. Measurement conditions $600\pm 3^\circ\text{C}$ and between 1 kHz to 1MHz. (Lines are guide to the eye).

The addition of BaO to $x\text{Ba}(40-x)\text{Si}$ glasses tends to lead to an increase in dielectric constant in both glasses (fig 5-2(a)) and glass-ceramics (fig 5-2(b)) within the series and there is

a decreasing trend in dielectric constant with increasing frequency. Decrease in dielectric constant and dielectric loss as frequency increases is associated with dielectric relaxation because the speed of dipole rotation at higher frequency cannot match the shift in the applied AC and so their rotation lags behind those of the applied field. Therefore, the dielectric constant decreases and approaches a nearly constant value as reported by (Li, Ra et al. 2009).

The tangent loss for the $x\text{Ba}(40-x)\text{Si}$ series ((fig 5-2(c) and (d)) also for the same reason mentioned above decreased and maintained a constant value as frequency increased. So the dielectric loss is high at 1 kHz in both glasses and glass-ceramics and decreases at higher frequencies; from 100 kHz to 1 MHz the tangent loss is between 0 and 5 for both $x\text{Ba}(40-x)\text{Si}$ glass and glass-ceramics.

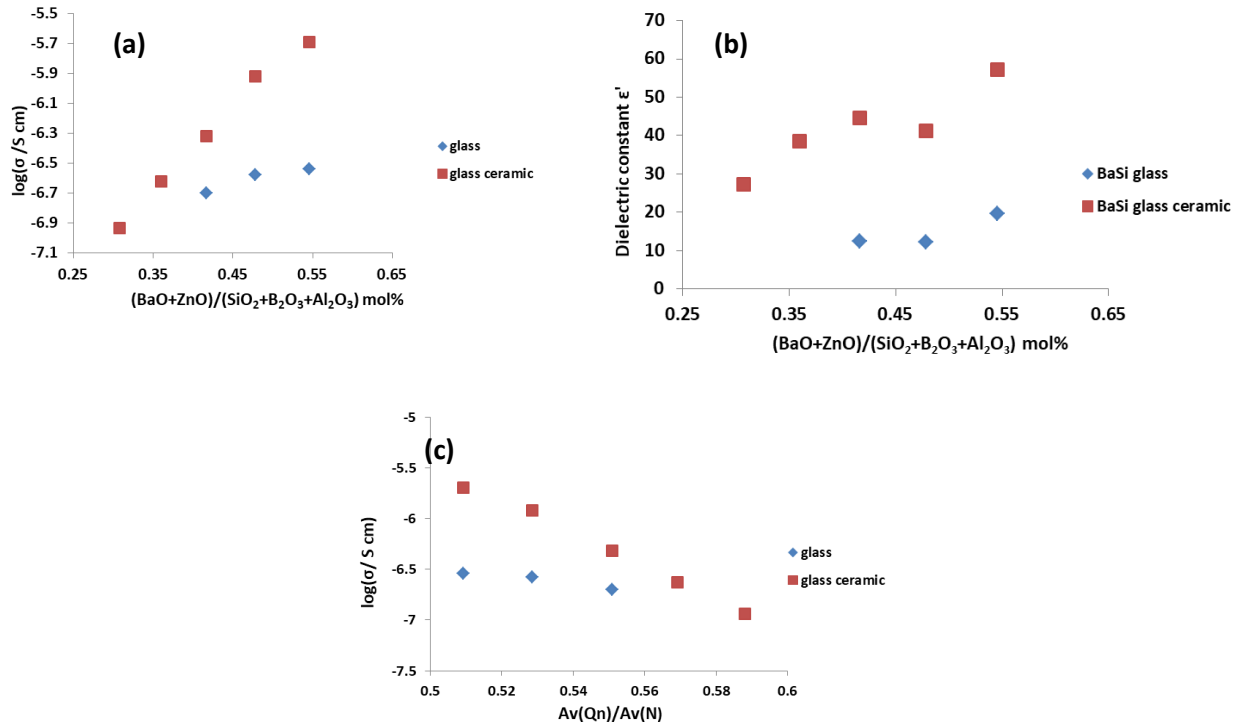


Figure 5-3: Conductivity (a) and dielectric constant (b) of $x\text{Ba}(40-x)\text{Si}$ glass and glass-ceramics versus total divalent modifier/total network formers. (c) Conductivity versus average Q^n/N of $x\text{Ba}(40-x)\text{Si}$ series. Measurement conditions $600\pm 3^\circ\text{C}$ and between 1 kHz to 1MHz

Since the applications of these sealing glasses will be at temperatures above their T_g the conductivity and dielectric constants as a function of composition were measured at temperatures around 600°C. The comparison between the conductivity of the glass and glass-ceramics of $x\text{Ba}(40-x)\text{Si}$ in fig 5-3(a) indicates that the glass ceramics are more conductive than their parent glasses. This is because the crystalline phase in these samples is more conductive than the residual glasses. There are two possibilities to consider as explained by Shelby; (i) if any given crystalline grains or phases in a glass composition contains alkali earth ions then there will be decrease in the conductivity because the alkali ions will be immobilised or (ii) if the residual glass contains more alkali ions then conductivity of the residual glass increases. However, this suggestion by Shelby is not applicable to this study because the impedance measurements suggest that the grains are more conductive than the grain boundaries which are the residual glass in the glass-ceramics (see Appendix 1a). In fig 5-3(b) the comparison between the dielectric constants of glass and glass ceramics within a series for $x\text{Ba}(40-x)\text{Si}$ also shows that the dielectric constant increases with increasing total divalent modifier/total network formers in both glasses and glass-ceramics and that the dielectric constants are generally higher for the glass-ceramics compared to the parent glasses. The increase in dielectric constant as BaO is added is due to the fact that the polarizability of Ba^{2+} ion is higher than that of Si^{4+} ion in $x\text{Ba}(40-x)\text{Si}$ series as reported in section (2.7.3). The effect of the increase in polymerisation on the electrical conductivity in fig 5-3(c) indicates that conductivity steadily decreases as the glass connectivity increases; the average Q^n/N where Q^n is the average of all the Q species and N is that of boron in 3 and 4 coordinations was calculated from the deconvolution of the Raman spectra of the parent glasses and the data from the glass ceramics were included in the plot to see the general effect of the increase in polymerisation on the electrical conduction. This clearly indicates that as the glass rigidity increases the available pathways for conduction are decreased reducing the conductivity in both glass and glass ceramics of the $x\text{Ba}(40-x)\text{Si}$ series.

5.2 Electrical properties of xBa(10-x)Al glasses

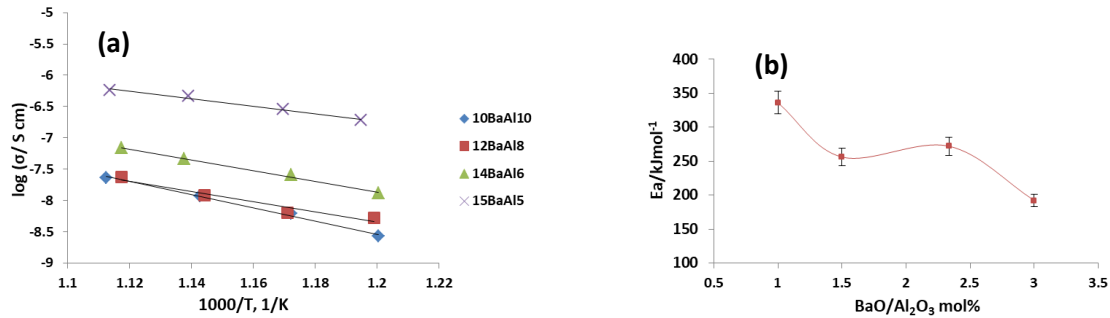


Figure 5-4: Variation of conductivity with temperature and compositions for xBa(10-x)Al glasses (b) activation energies (E_a) for conductivity for xBa(10-x)Al glasses as a function of increasing BaO/Al₂O₃ ratio

In fig 5-4(a) it is shown that the conductivity of xBa(10-x)Al glasses like that of xBa(40-x)Si glasses increases with temperature and increasing BaO content. The activation energy for conductivity (fig 5-4(b)) decreases with BaO addition just as explained above for the xBa(40-x)Si glass in section 5.1. However, between a BaO/Al₂O₃ ratio of 1.5 and 2.5 there is a small increase in E_a from 256 to 272 kJ/mol . This small rise in E_a can be correlated to a corresponding increase in T_g of that sample (see fig 4-8(b)) which suggests an increase in network connectivity as the cause for the slight increase in activation energy.

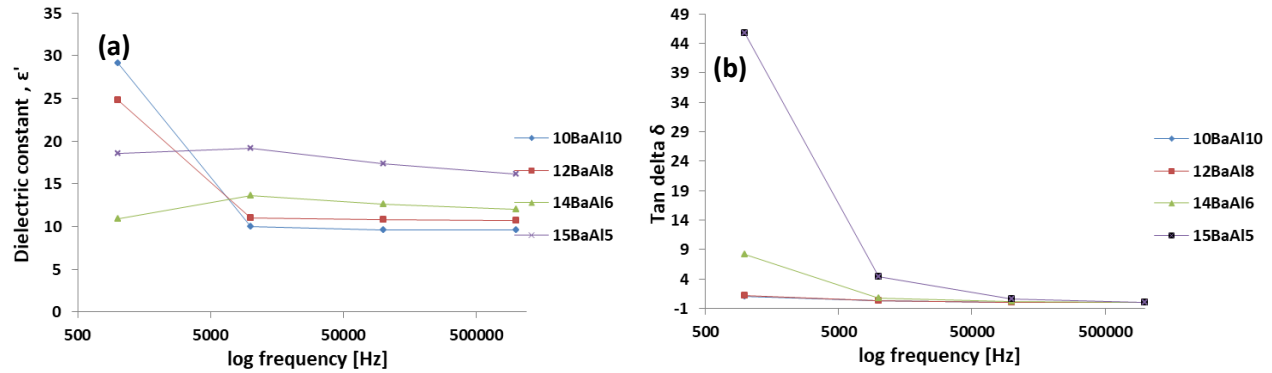


Figure 5-5: Frequency dependence for xBa(10-x)Al glasses of (a) the dielectric constant (b) tangent loss. Measurement conditions $600 \pm 3^\circ\text{C}$ and between 1 kHz to 1MHz.

In fig 5-5 (a) and (b) the dielectric constant and tangent loss exhibit similar behaviour to xBa(40-x)Si glass and glass ceramic and therefore the frequency dependence can be explained in the same way and is associated with the dielectric relaxation and the increase within the series of xBa(10-x)Al due to polarizability of BaO which is high than that of Al_2O_3 . The frequency dependent decrease in dielectric constant of xBa(10-x)Al series (fig 5-5(a)) shows there is a large decrease between 1 kHz and 10 kHz for xBa(10-x)Al1 and xBa(10-x)Al2; however, such a drop is not seen in xBa(10-x)Al3 and xBa(10-x)Al4 but rather a gentle initial increase in dielectric constant is observed as the frequency increased and then decreased afterwards. As space charge accumulation is known to exist at lower frequency and the fact that xBa(10-x)Al is measured in glass form may suggest low accumulation in some of the samples possibly due to more homogeneity. The slight initial increase is similar to xBa(40-x)Si in fig 5-2(a). Fig 5-5(b) shows that the tangent loss for xBa(10-x)Al1 to xBa(10-x)Al3 also varies between 0 and 5 with increasing frequency. However, there is a single data point that exhibits higher tangent loss at 1 kHz in xBa(10-x)Al4 glass possibly due to accumulation of space charge at the electrode interface.

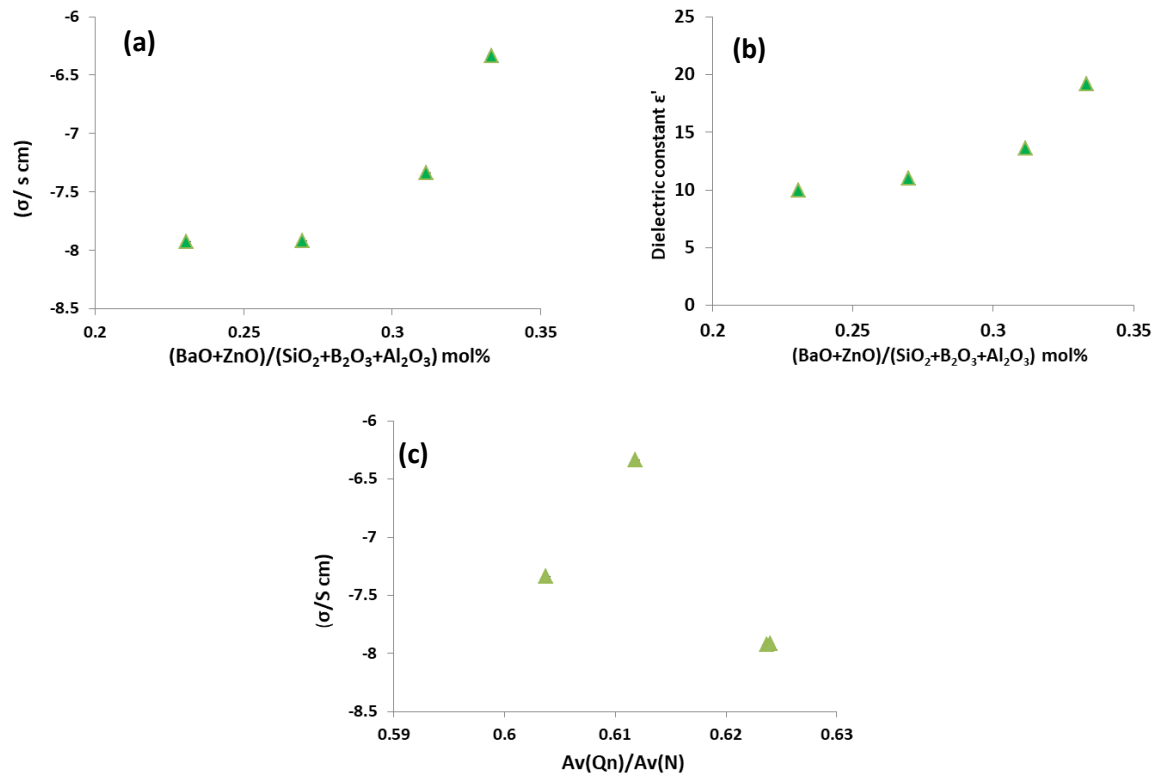


Figure 5-6: (a) Conductivity and (b) dielectric constant of $x\text{Ba}(10-x)\text{Al}$ glasses versus total divalent modifiers/total network formers. (c) Conductivity versus average Q^n/N for $x\text{Ba}(10-x)\text{Al}$ glasses. Measurement conditions $600 \pm 3^\circ\text{C}$ and between 1 kHz to 1MHz

The electrical conductivity and the dielectric constant of $x\text{Ba}(10-x)\text{Al}$ as a function of composition (fig 5-6(a) and (b)) shows there is an increasing trend as BaO is added against alumina. Although very little initial increase in conductivity is observed between 10BaAl10 and 12BaAl8 mol%; however, above a total divalent/total network former ratio of 0.3 the conductivity rapidly increases. Structural evidence from the Raman polymerisation index of these glasses (fig 4-10(d)) reveals there is very little change in polymerisation between samples 10BaAl10 and 12BaAl8 hence the reason for their similar conductivity. The dielectric constant in fig 5-6 (b) exhibited a clearly increasing trend with an increasing ratio of total divalent modifiers/total network formers ratio; however, the initial increase is not very large just as seen with the conductivity. In fig 5-6(c) the conductivity plotted against average total sum of Q species divided by that of borate species N given by Q^n/N exhibits a maximum at a ratio of 0.61

for 15BaAl5 mol%. As already stated above, it is shown in fig 4-10(d) that samples 10BaAl10 and 12BaAl8 mol% have similar polymerisation indices and therefore have similar conductivities which overlap in fig 5-6 (c) at a ratio of 0.624.

5.3 Electrical properties of $x\text{B}(15-x)\text{Zn}$ glasses and glass ceramics

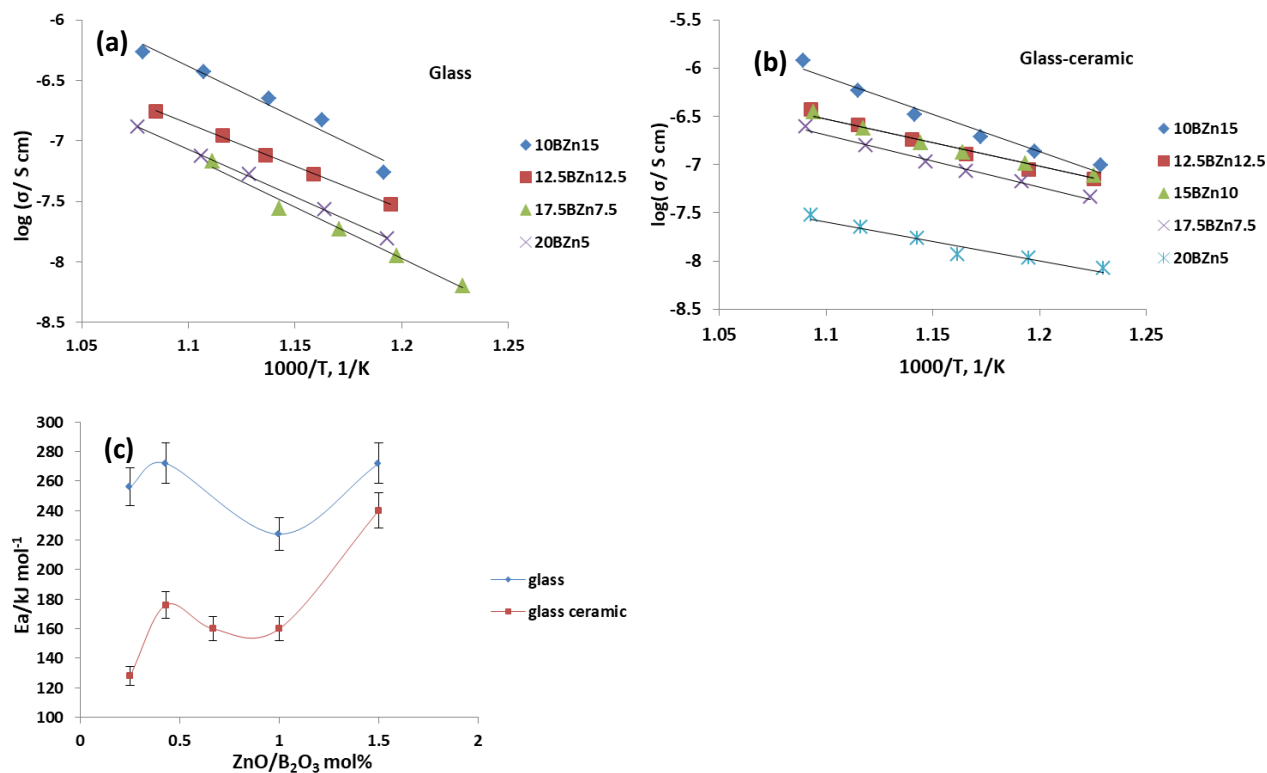


Fig 5-7 Variation of conductivity with temperature and compositions for (a) $x\text{B}(15-x)\text{Zn}$ glasses (b) $x\text{B}(15-x)\text{Zn}$ glass-ceramics. Activation energies (E_a) for conductivity for (c) $x\text{B}(15-x)\text{Zn}$ glasses and (d) $x\text{B}(15-x)\text{Zn}$ glass-ceramics as a function of increasing $\text{ZnO}/\text{B}_2\text{O}_3$ ratio.

Fig 5-7(a) and (b) shows that the electrical conductivity of both $x\text{B}(15-x)\text{Zn}$ glasses and glass-ceramics increases as a function of increasing temperature and show a decrease with increasing boron oxide content against ZnO. This is because boron oxide is a network former which leads to increased polymerisation of the glass structure as can be seen in the FTIR and Raman results (section 4.1.3) and so decreases the mobility of the ZnO charge balancing modifiers. In fig 5-7 (a) the conductivity of 20 $x\text{B}(15-x)\text{Zn}$ is lower than 17.5 $x\text{B}(15-x)\text{Zn}$ because of the

increase in polymerisation index of that sample (also see fig 5-9(a)). The increasing trend in activation energy as ZnO is added in this series suggests the difficulty in electrical conduction in these very resistive glasses see fig 5-7(c). The behaviour of the activation energy (E_a) is similar both $x\text{B}(15-x)\text{Zn}$ glasses and glass-ceramics, although in general the E_a values of the glass ceramics are lower than the parent glass, presumably due to increased conductivity of the lanthanum borosilicate crystalline single phase. As mentioned previously for $x\text{Ba}(40-x)\text{Si}$ glass-ceramics, the increasing trend in E_a for crystalline samples is caused by obstructions to conduction pathways caused by densification and presence of phase boundaries in the glass-ceramic and this implies higher energy is required to move charge carriers in the glass ceramics. However, the increase of E_a in $x\text{B}(15-x)\text{Zn}$ glass with increasing ZnO may suggest the incorporation of ZnO into the glass structure as ZnO could be in a network former role thereby raising the energy needed for conduction.

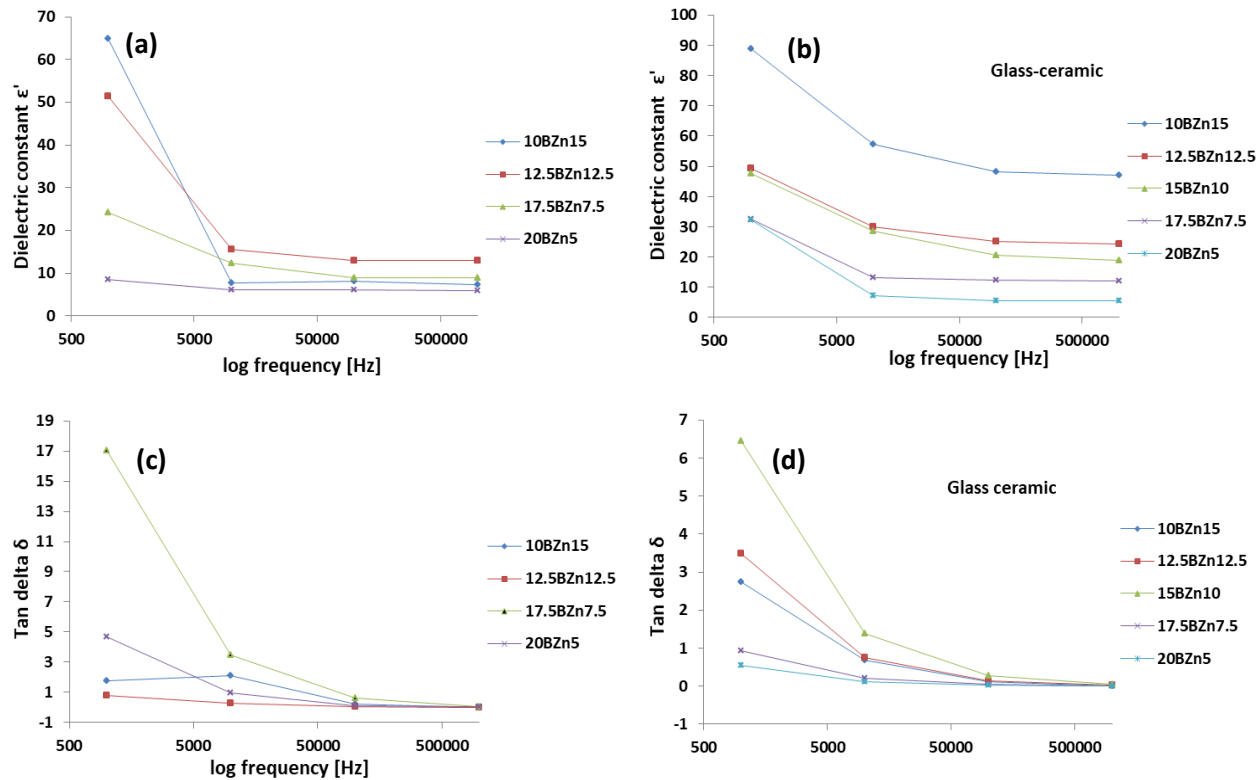


Figure 5-7: Frequency dependence of the dielectric constant of $x\text{B}(15-x)\text{Zn}$ (a) glasses and (b) glass-ceramics. Frequency dependence of the tangent loss of $x\text{B}(15-x)\text{Zn}$ (c) glasses and (d) glass-ceramics. Measurement conditions $600\pm 3^\circ\text{C}$ and between 1 kHz to 1MHz

Fig 5-8(a) and (b) shows that the dielectric constant and fig 5-8(c) and (d) the tangent loss of both $x\text{B}(15-x)\text{Zn}$ glasses and glass-ceramics decreases with increasing frequency in the same way as previous sections. The frequency dependent behaviour of both the dielectric constant and tangent loss is the same irrespective of the compositional differences. This indicates that the combined effect of polarization as frequency increased is similar in all series. The compositional effect within the series can also be observed as the amount of boron oxide is increased against ZnO across the $x\text{B}(15-x)\text{Zn}$ series. The dielectric constant is also seen to decrease due to the low polarizability of boron oxide compared to zinc oxide. Just as in $x\text{Ba}(40-x)\text{Si}$, the crystalline $x\text{B}(15-x)\text{Zn}$ samples have higher dielectric constants than the parent glasses. Fig 5-8(c) and (d) shows the tangent loss of $x\text{B}(15-x)\text{Zn}$ samples decreases with increasing frequency. Apart from the frequency dependence, the tangent loss in $x\text{B}(15-x)\text{Zn}$ samples did not show any particular compositional dependence. A similar lack of compositional dependence has also been observed

by Kupracz et al, for manganese borosilicate glasses (Kupracz, Lenarciak et al. 2017). The tangent loss across the series for both glasses and glass-ceramics shows variation between 0 and 5 with the exception of a single data point at 1 kHz for both 17.5 xB(15-x)Zn glass and 15xB(15-x)Zn glass-ceramics which are particularly higher. As discussed earlier this could be due to electrode polarization or some sort of inhomogeneities in the samples.

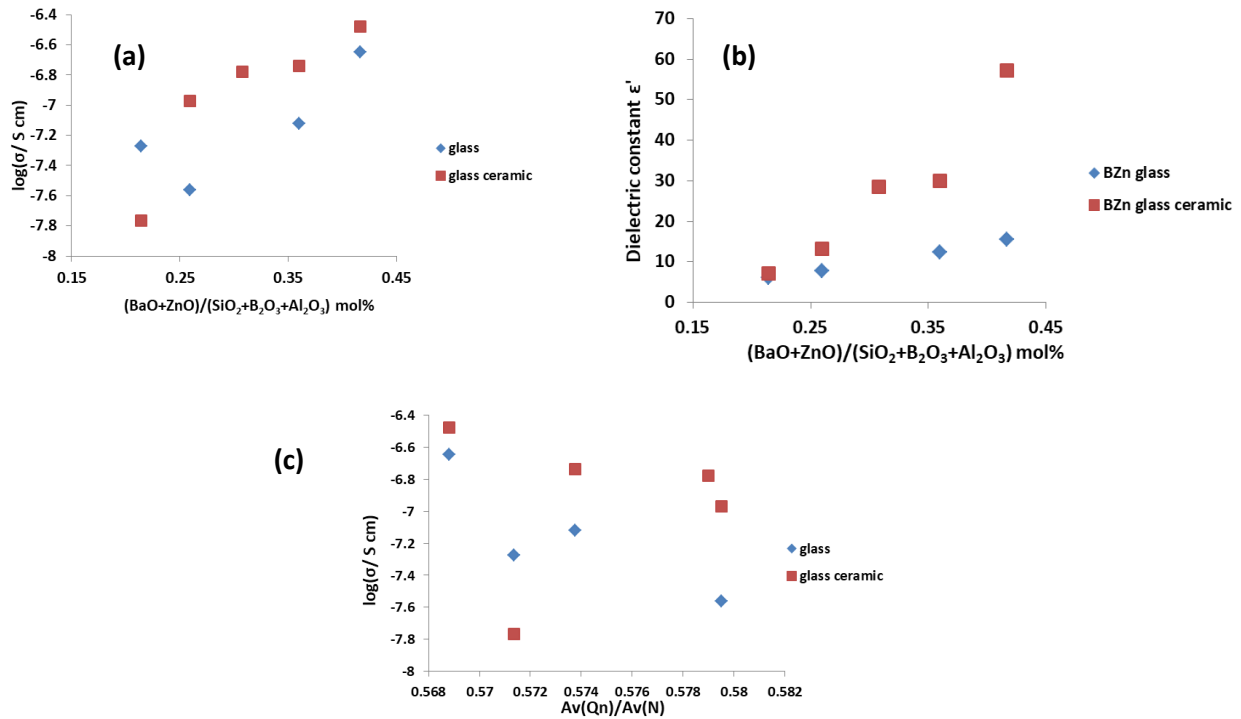


Figure 5-8: (a) Conductivity and (b) dielectric constant of xB(15-x)Zn glasses and glass-ceramics versus total divalent modifier/total network formers. (c) Conductivity versus average Q^n/N for xB(15-x)Zn series. Measurement conditions $600\pm 3^\circ\text{C}$ and between 1 kHz to 1MHz.

Fig 5-9(a) and (b) indicates that both the conductivity and dielectric constant of xB(15-x)Zn glass-ceramics are higher than those of the corresponding parent glasses and both increased with increasing amounts of ZnO. The drop in conductivity at a total divalent oxide/ sum of network formers ratio of 0.25 may be connected with the increase in polymerisation index of that sample as can be seen in fig 4-15(d). Fig 5-9(c) shows there is a decrease in conductivity with increasing connectivity as shown by increasing average Q^n/N ratio. However, after reaching a 20mol% boron oxide content in 20xB(15-x)Zn the Q^n/N ratio drastically reduced to the position 0.571

probably due to the effect of the boron anomaly. The results from the calculation of the polymerisation index indicates that the $20xB(15-x)Zn$ sample has the lowest value which suggests that $20xB(15-x)Zn$ has undergone a boron anomaly and also has the lowest conductivity because as it has the highest boron oxide content and smallest amount of ZnO which are more mobile compared to boron.

5.4 Electrical properties of $xSi(20-x)Zn$ glass ceramics

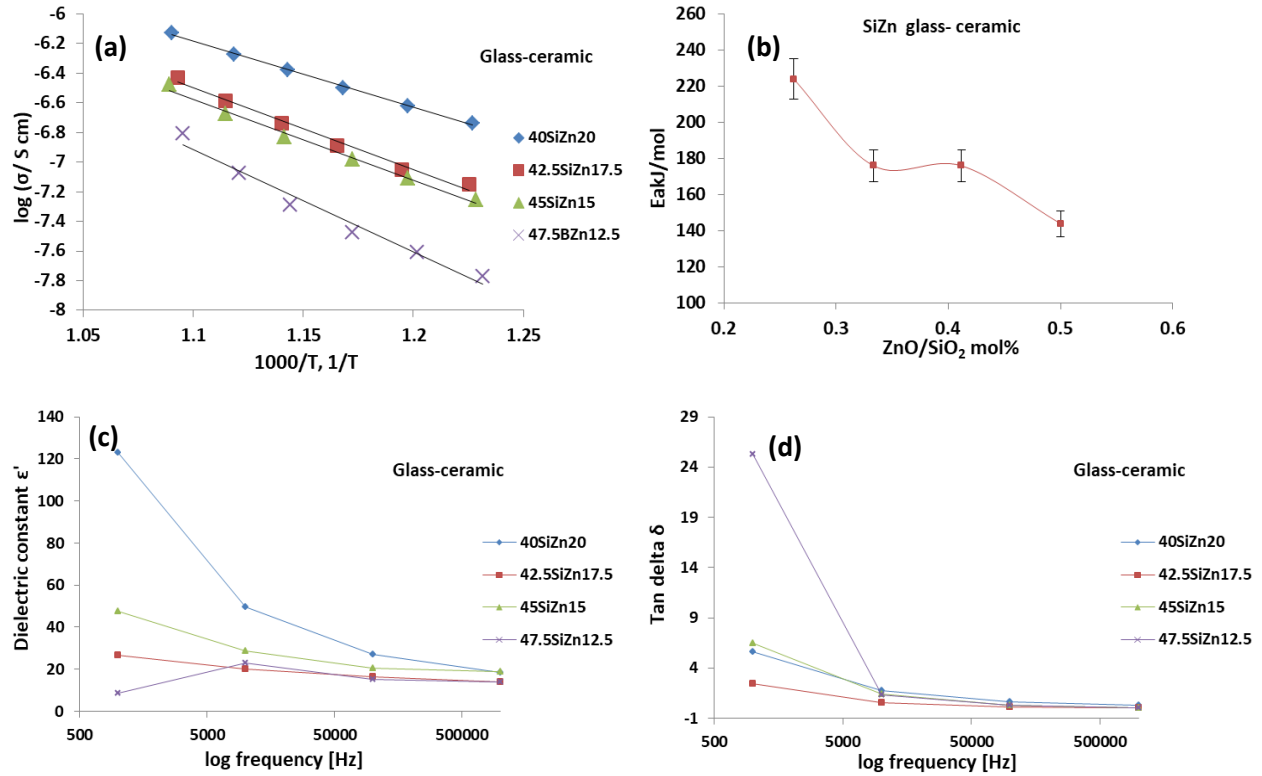


Figure 5-9: (a) Variation of conductivity with temperature and composition of $xSi(20-x)Zn$ glass ceramics; (b) variation of activation energies (E_a) as a function of increasing ZnO and frequency dependence of (c) dielectric constant and (d) tangent loss . Measurement conditions $600\pm 3^\circ\text{C}$ and between 1 kHz to 1MHz.

Fig 5-10(a) shows that the conductivity of $xSi(20-x)Zn$ glass ceramics, just like that of $xB(15-x)Zn$ glass ceramics increased with increasing temperature and ZnO content. The conductivities of 42.5SiZn17.5 and 45SiZn15 mol% (fig 5-10(a)) are not very different and likewise their activation energies for conductivity are similar (fig 5-10(b)). However, the E_a for conductivity

for $x\text{Si}(20-x)\text{Zn}$ glass-ceramics behaved differently to that of $x\text{B}(15-x)\text{Zn}$ glass-ceramics as it shows a decreasing trend with increasing modifier ZnO against silica across the series (see fig 5-10(b)). This can be interpreted with respect to an increase in polymerisation as boron oxide replaces zinc oxide in the $x\text{B}(15-x)\text{Zn}$ series as can be seen in fig 4-14(a), which may suggest that ZnO charge balanced boron oxide while in $x\text{Si}(20-x)\text{Zn}$ the ZnO acts as a modifier. Fig 5-10(c) shows the dielectric constant and (d) tangent loss also exhibit similar decreasing trends to all the series with increasing frequency. Just like in $x\text{B}(15-x)\text{Zn}$, the higher polarizability of Zn^{2+} compared to Si^{4+} in $x\text{Si}(20-x)\text{Zn}$ led to an increase in dielectric constant. The decrease in tangent loss is not very different within the series especially for frequencies above 1 kHz.

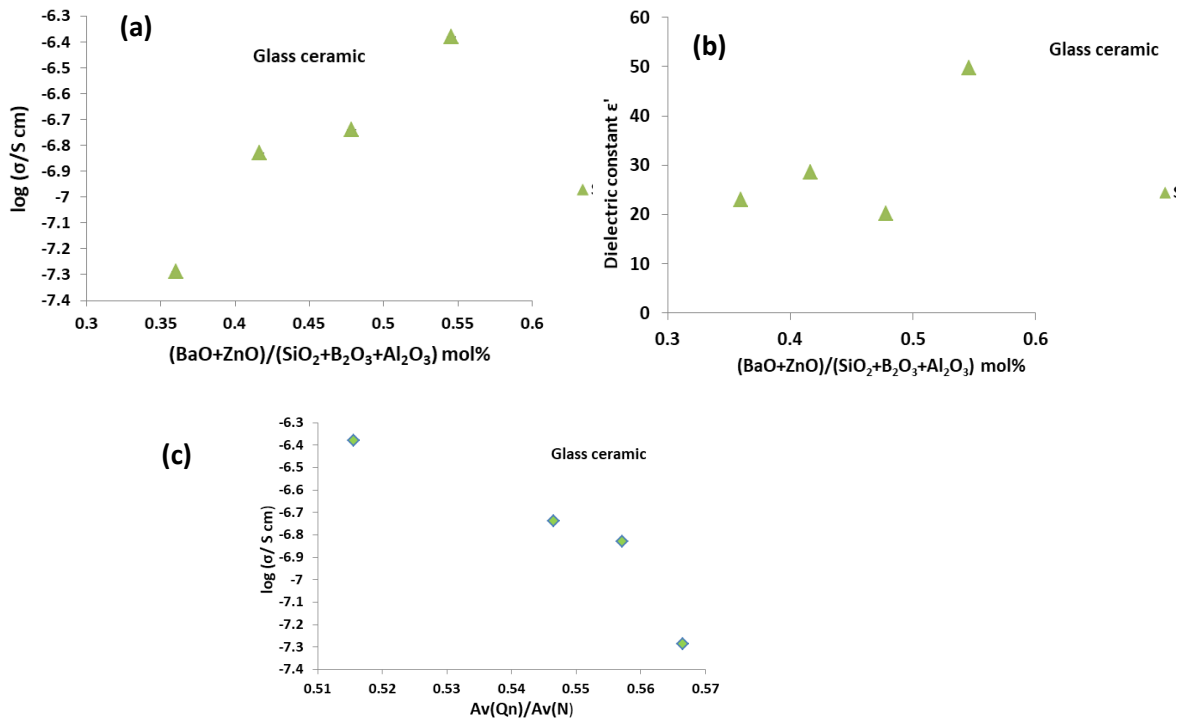


Figure 5-10: (a) Conductivity and (b) dielectric constant of $x\text{Si}(20-x)\text{Zn}$ glass ceramics versus total divalent modifier/total network formers. (c) Conductivity versus average Q^n/N of $x\text{Si}(20-x)\text{Zn}$ series. Measurement conditions $600\pm 3^\circ\text{C}$ and between 1 KHz to 1MHz

Fig 5-11(a) and (b) shows the conductivity and dielectric constant of $x\text{Si}(20-x)\text{Zn}$ increases as the amount of total divalent modifier oxides/total network modifiers increases in the glass-ceramics. There is a small drop in conductivity and a very significant drop in dielectric constant at a ratio 0.47 of the total divalent oxide/total network formers. The drop at this point particularly in dielectric constant is also shown by the $x\text{Ba}(40-x)\text{Si}$ series in both glass and glass ceramics. However, there is no clear structural evidence to support this behaviour and their conductivities did not follow the same pattern. Besides the dielectric constant values are also different for the two data sets as $22.5x\text{Ba}(40-x)\text{Si}$ has a dielectric constant of 41 whereas it is 20 for $x\text{Si}(20-x)\text{Zn}_2$.

5.5 General temperature and frequency dependent behaviour of glass and glass ceramics

Looking at fig 5-12 (a) and (b) the electrical conductivities in glass and glass ceramic in this study represented by $25\text{BaSi}30$ mol% show similar temperature and frequency dependence behaviour with the frequency dependence of the glass ceramics being more pronounced with less noise. This behaviour is similar in all glass and glass-ceramic samples measured in this study. The increase in conductivity with temperature is due to the increase in thermal energy available to move conducting particles (Pal, Agarwal et al. 2009, Braunger, Escanhoela et al. 2012). The conductivity associated with the plateau increases and covers wider frequency as temperature increases, see fig 5-12(a) and (b). According to Pal et al, this is because mobile ions gain more thermal energy and cross the conduction barrier(s) more easily (Pal, Agarwal et al. 2009).

The absence of a low frequency turn down in the conductivity data after the plateau regions shown in fig 5-12(a) and (b) leads to the conclusion that the impedance measurements show no evidence for any ionic conduction mechanisms in these glasses and glass-ceramics and that the predominant conduction mechanism must be electronic. Similarly in fig 5-12 (c) and (d) the dielectric constant of the glasses and glass-ceramics also increases with temperature and exhibit frequency dependency in both glass and glass-ceramics with the glass ceramic dielectric constant more rapidly decreasing with frequency compared with that of the parent glass. Generally dielectric constant and loss factor increase with temperature due to increased dipolar rotation and molecular mobility as the network structure becomes relaxed with increase in

temperature (Li, Ra et al. 2009). The decrease in both dielectric constant and dielectric loss is a combined effect of multi component polarization which includes space charge, dipolar, ionic and electronic contributions. The first, space charge polarization is due to blockage of mobile charges and occurs at frequency around or below 10^3 Hz. Dipolar is the second type of polarization which has to do with the orientation of molecules by the applied field and occurs in the frequency range of 10^{10} Hz and followed by ionic polarization which is a displacement of cations relative to anions at 10^{13} Hz and the last contribution is the electronic polarization which is a small displacement of electrons relative to atomic nucleus occurs in all materials at higher frequency of about 10^{16} Hz . So the total polarization of the dielectric measurement comes from the sum of these four contributions to polarization as reported in (Morsi, Ibrahim et al. 2016).

From Figure 5-12 (c), the flat plateau in permittivity above $\sim 10^5$ Hz indicates the contribution of ionic and electronic polarizability to the permittivity value of ~ 20 that is associated with the glass matrix. Due to the more conducting nature of the glass ceramics this plateau is not observed in the corresponding permittivity plots, fig 5-12 (d) as it has moved to much higher frequencies. Instead, the plots are dominated (with decreasing frequency) by thin layer (possibly grain boundaries) and space charge effects that give rise to a plateau value of ~ 100 and a low frequency incline, respectively. The negative values of tan delta below 10kHz for most temperatures indicates the presence of inductive effect at low frequency and this may be related to an electrode effect rather than the high conductivity.

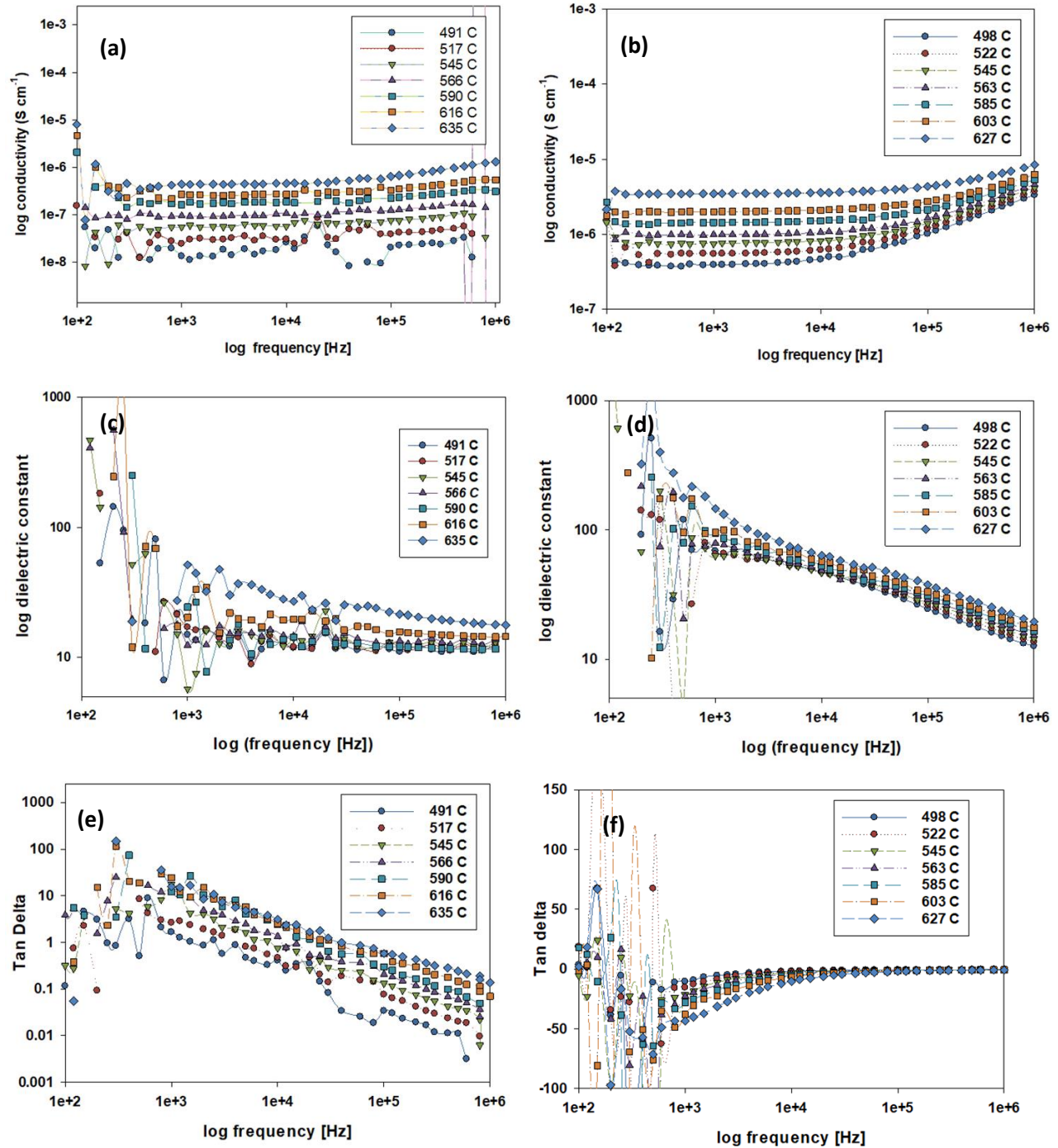


Figure 5-11: The temperature and frequency dependence of electrical conductivity of 25BaSi30 mol% (a) glass and (b) glass-ceramic. Dielectric constant (c) glass (d) glass-ceramic, Tangent loss (e) glass and (f) glass-ceramic.

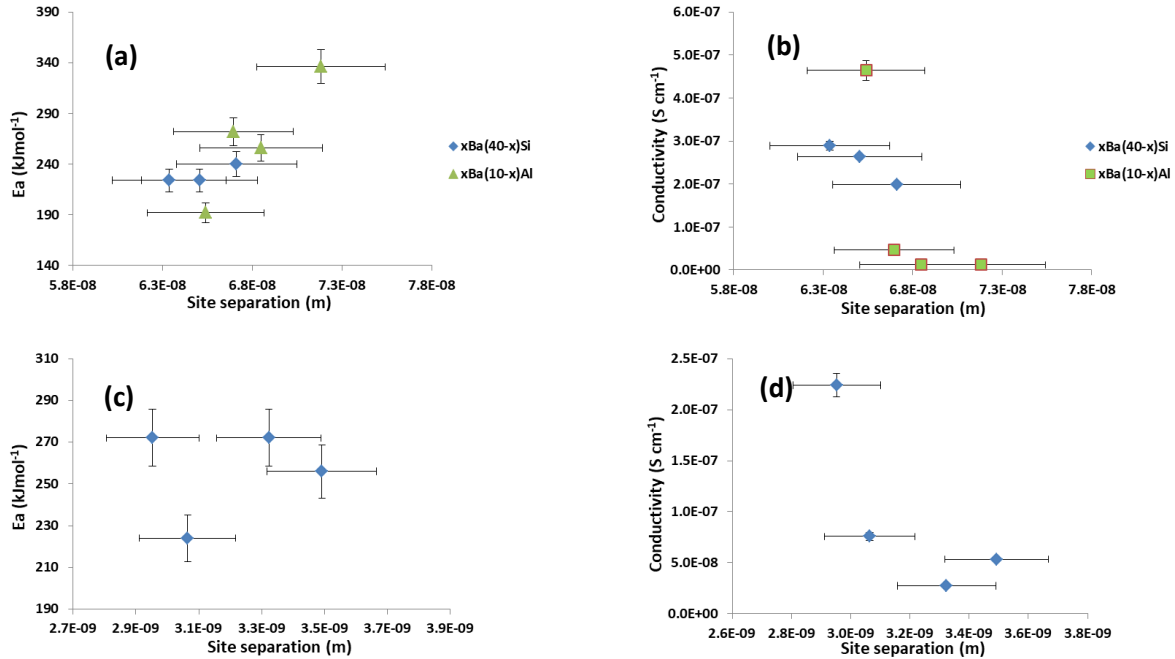


Figure 5-12: (a) Activation energy and (b) conductivity of $x\text{Ba}(40-x)\text{Si}$, $x\text{Ba}(10-x)\text{Al}$ glasses, and (c) Activation energy of $x\text{B}(15-x)\text{Zn}$ and (d) conductivity of $x\text{B}(15-x)\text{Zn}$ glasses all versus site separation (atom –atom distance)

According to Moridi et al, the electrical conduction mechanism in barium borosilicate is due to small polaron hopping (Moridi, Nouruzi et al. 1991). Although most of the studies report that polaron hopping is mainly associated with transition metals whose oxidation states change from low to high (see, for example Kupracz et al). All the glasses in this study contain ZnO however; it is not known to change its oxidation state and therefore is expected to remain as Zn^{2+} . The presence of low mobility of cations such as Zn and Ba in oxide glasses leads to electronic conduction where electrons move from one site to another by a thermally activated hopping mechanism (Moridi, Nouruzi et al. 1991). These low mobility ions tend to distort the surrounding lattice. Because of this lattice displacement the electrons form a bound state with the potential well giving rise to polaron behaviour. It can be seen in fig 5-13(a) the conduction activation energy for the $x\text{Ba}(40-x)\text{Si}$ and $x\text{Ba}(10-x)\text{Al}$ glass series increased with increasing distance between similar atoms (modifiers) which means higher energy is required by the charge

carriers (polarons) to hop between two sites. On the other hand, the conductivity is highly dependent on the mean distance between two atoms and it decreases as the atom to atom site separation increases (fig 5-13(b)). However for the $x\text{B}(15-x)\text{Zn}$ series in fig 5-13(c) the activation energy fluctuates with increasing site separation but the conductivity decreases with increasing site separation similar to the $x\text{Ba}(40-x)\text{Si}$ and $x\text{Ba}(10-x)\text{Al}$ series.

In fig 5-14 the calculated polaron radius is smaller than the site separation (see equation (2-17 and 2-19)) between modifier cations but it is large enough to influence nearby sites, which can be evidence to support conductivity being a result of small polaron hopping (Kupracz, Lenarciak et al. 2017). The polaron radius must be larger than the radius of the atom upon which electron is localized and must also be less than the site separation of the ions. There is steady decrease in the values of both the atomic site separation and polaron radius with increasing amounts of modifier atoms in the glasses. The small polaron radii indicate that polarons are basically localised. A localised state refers to a small polaron whose distortion cloud does not overlap. In contrast, an extended state refers to a large polaron radius (Kupracz, Szreder et al. 2014). When in a localised state, polarons are trapped in a site and can only move to neighbouring sites through thermally activated hopping process(es) as reported by (Schirmer, Imlau et al. 2009).

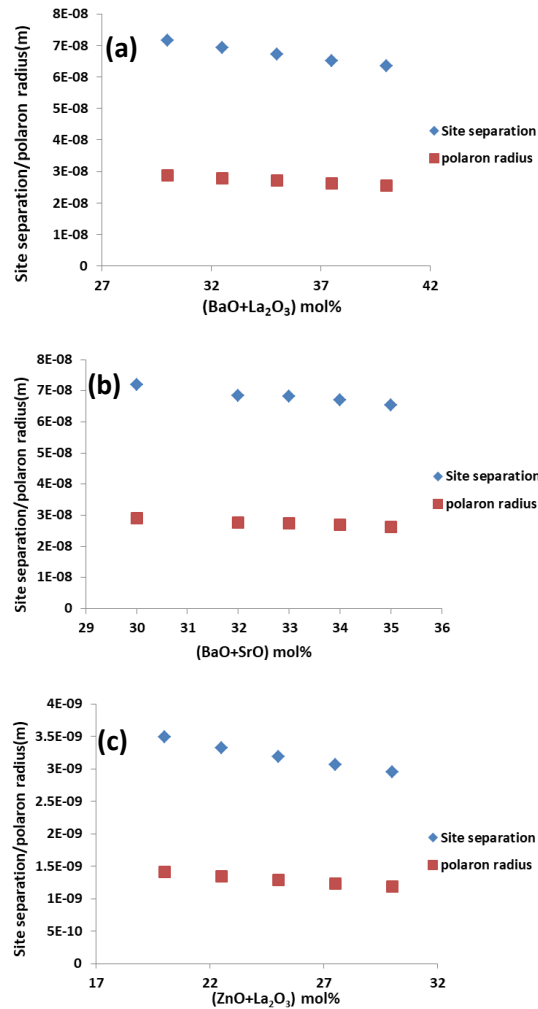


Figure 5-13: Decreases in site separation and polaron radii versus total large size oxides for (a) $x\text{Ba}(40-x)\text{Si}$ glasses (b) $x\text{Ba}(10-x)\text{Al}$ glasses, and (c) $x\text{B}(15-x)\text{Zn}$ glasses.

5.6 Discussions of results

The electrical conductivity in the BaSi series where BaO was swapped for silica (fig 5-1(a) and (b)) increased in both glass and glass-ceramics with BaO addition. This indicates that BaO in these glasses is acting in a modifier role which is supported by both the Raman and FTIR spectra and by deconvolution of the Raman spectra see fig 4-4 (a) and (b). The increase in conductivity with BaO addition is due to high polarisability of Ba^{2+} compared with Si^{4+} (see section 2.7.3).

The decrease in E_a for conductivity in BaSi glass fig 5-1(c) indicates that as BaO is added it reduced the energy needed for electrical conduction. However, on the other hand the increase in E_a for BaSi glass-ceramics (fig 5-1(d)) with increasing BaO content suggests that after crystallization blockage of the preferred pathway for conduction has occurred hence increased the energy required to move charge carriers in the glass-ceramic structure, where the impedance measurements suggest the presence of different phases or heterogeneities with different conductivities (see appendix 1a).

This information can be obtained from the combined impedance and electric modulus spectroscopic plots ($Z''(f)$ and $M''(f)$) which represent grain boundary resistivity (Z'') and the more conductive grains (M'') in the glass ceramics. This data suggests that the grains are more conductive than the grain boundaries and the occurrence of $Z''(f)$ and $M''(f)$ Debye-like peak maxima at different frequencies in appendix 1a indicates that they belong to different electroactive regions as reported by (Jiadong, Ming et al. 2014). Although conductivity increased due to the presence of crystalline samples fig 5-1(b) the activation energies in fig 5-1(d) are generally lower than those of the parent glasses except at BaO/SiO₂ ratios of 0.57 and 0.69. In particular, the drop in E_a for Ba25 Si30 mol% glass ceramic is as a result of high residual glass as this particular sample did not crystallise well compared to the other samples in the same series (see XRD in fig 4-2 (b)).

The dielectric constants of BaSi glasses and glass-ceramics decrease with increasing frequency due to the contribution of multi-component polarization such as electronic, ionic, dipolar or orientation and space charge effects (Pal, Agarwal et al. 2009, Morsi, Ibrahim et al. 2016) see also section 5.5 above for more details. The decrease in the dielectric constant is as a result of the fact that the polarization does not occur instantaneously with the electric field as the charges have inertia (Prasad and Basu 2013). Furthermore, the decrease in dielectric constant and tangent loss with increasing frequency is observed in these samples and then continue to decrease to a constant value at high frequencies. This variation according to Maxwell-Wagner model is because hopping between different metal ions cannot aligned with alternating field due to the existence of inhomogeneities, defects and secondary phases (Borhan, Gromada et al. 2016).

At lower frequency the accumulation of space charge at broken bonds or chains is the cause of increase in dielectric constant as reported by (Darwish and Gomaa 2006). Other factors

contributing to the dielectric constants of the glass-ceramics include combined effects of intrinsic and extrinsic factors such as porosity, compositional homogeneity, lattice vibration modes and grain size. The dominance of any of these factors is dependent on composition and sintering temperature of the glass-ceramics (Borhan, Gromada et al. 2016).

As both dielectric constant and tangent loss are converging towards an almost constant point it is difficult to see compositional dependence of these two parameters (see fig 5-2(c) and (d)). However in fig 5-3(a) and (b) an increasing trend in both conductivity and dielectric constant can be observed within the series as BaO is increased, due to the fact that the polarizability of Ba^{2+} ions is higher than that of Si^{4+} ions. On the other hand, the ratio of $Av(Q^n)/Av(N)$, which gives a measure of the degree of polymerization, shows a decreasing trend for the conductivity as the glass structure connectivity increases. This can be explained on the basis that an increase in the glass structural connectivity slows down the movement of charge carriers. However conductivity does not depend only on structural connectivity but also on factors such as the nature and the concentration of charge carriers (Braunger, Escanhoela et al. 2012) also explained in section (2.7.3)

In the second series BaAl where BaO was swapped for alumina the conductivity (fig 5-4(a)) and E_a (fig 5-4(b)) followed a similar trend to that for BaSi glasses (fig 5-1(a) and (c)) and therefore the above explanation for the behaviour of BaSi samples applies to BaAl samples. However, it is worth mentioning here that an increase in conductivity, dielectric constant and tangent loss is because the polarizability of Ba^{2+} is higher than Al^{3+} in BaAl series as reported in section 2.7.3. Since alumina additions are reported to have decreased dielectric constant because they decrease the amount of NBOs in glass which have high polarity (Lim, Kim et al. 2006); however, the alumina content is decreased and so it can be said that the effect of increasing BaO is the main reason for the rise in the dielectric constant of the BaAl series. It is possible that the higher activation energy is as a result of lattice/matrix effects (associated with ion movement) while the increased conductivities is due to the electronic conduction as reported by (Morsi, Ibrahim et al. 2016). There is no evidence from the impedance measurements to prove ionic conduction is the dominant conduction mechanism, however, localized ion movements may be possible and ionic conduction may be a minor contribution to the overall conductivity. In addition, the higher activation energy of BaAl series compared with BaSi may suggest the possibility of the mixed alkali effect in BaAl series although the conductivity increased as BaO

increased; however, the conductivity is less than that of BaSi which has smaller total modifier content. In all BaAl samples a fixed 20mol% of SrO is present whereas BaO was varied between 10 to 15 mol%. Despite the fact that the BaAl series has the highest amount of modifiers (BaO+SrO) these glasses have lower conductivities compared to glasses in other series except for BaAl5 mol% where the conductivity is high and showed a maximum at 35mol% SrO+BaO; this may suggest the presence of mixed alkali effects as can be seen in fig 5-6 (a). The dielectric constant fig 5-6 (b) as expected also exhibited a similar increasing trend as that of the electrical conductivity increased with total divalent oxide/total network formers increased. The reason for the increase in dielectric constant is similar to that given in the BaSi section above. The one difference is in the behaviour of BaAl series with increasing polymerisation as represented by the average Q^n/N . The BaAl series shows an initial increase in conductivity until a maximum point and then a decrease with further increases in the polymerisation index.

The BZn series (fig 5-7) and SiZn series (fig 5-8) look similar as ZnO is the only oxide that varied in both series. Although SiZn was only measured in glass-ceramic form the conductivity behaviour is similar to that for BZn glass which increases with increasing ZnO due to the high polarizability of Zn^{2+} compared to Si^{4+} and B^{3+} . Comparing the E_a of BZn glass and glass-ceramics reveals a slightly increasing trend as the ZnO content increases (fig 5-7(c)). This behaviour for E_a is different to that for SiZn which shows a decreasing trend as ZnO increased. This may not be unconnected with the fact that ZnO may be a network former in BZn and a modifier in the SiZn series. In addition, the behaviour of the dielectric constant and tangent loss as zinc oxide increased in BZn and SiZn in glass and glass-ceramics are similar to those seen with increasing BaO in BaSi and BaAl as both Zn^{2+} and Ba^{2+} have high polarizability compared to what they replaced (Si^{4+} , B^{3+} and Al^{3+} in the respective glass compositions). Generally, conductivities and dielectric constants for BZn in fig 5-9 (a) and (b) plotted against composition show that the parent glass has a lower value compared to the corresponding glass-ceramic and in all cases the conductivities and dielectric increase with an increasing amount of divalent modifiers. This behaviour is the same for SiZn glass ceramics in fig 5-11(a) and (b) except that in SiZn there is a clearly visible drop in dielectric constant at the ratio 0.47 of the divalent/sum of network formers. There is also a similarity between BZn and SiZn as their conductivities all decreased with an increase in the averaged Q^n/N see fig 5-9(c) and 5-11 (c) for comparison. Regardless of the compositional differences between the series considered in this study, the value

of the electrical resistivity in both glasses and glass ceramics are all above the threshold given in the literature as a requirement for sealing glasses; see table 7.1 and 7.2 for the values of electrical conductivities and activation energy for conduction.

samples (mol%)	Electrical conductivity σ / S cm ⁻¹ at (600°C)±3°C		In Ω cm at (600°C)±3°C		SOFC s requirements	Ref
	glass	Glass ceramic	glass	Glass ceramic		
10xB(15-x)Zn15	2.24×10 ⁻⁷	3.31×10 ⁻⁷	4.46×10 ⁶	3.03×10 ⁶	Should be >10 ⁴ Ω cm	(Lara, Pascual et al. 2006),(Mahapatra and Lu 2010),(Ghosh, Sharma et al. 2010), (Chen, Zou et al. 2013),(Reddy, Tulyaganov et al. 2014, Qi, Lihua et al. 2015),(Tulyaganov, Reddy et al. 2013), (Chen, Zou et al. 2013)
12.5xB(15-x)Zn12.5	7.57×10 ⁻⁸	1.82×10 ⁻⁷	1.32×10 ⁷	5.49×10 ⁶		
15xB(15-x)Zn10	noisy	1.66×10 ⁻⁷	noisy	6.02×10 ⁶		
17.5xB(15-x)Zn7.5	2.75×10 ⁻⁸	1.07×10 ⁻⁷	3.64×10 ⁷	9.37×10 ⁶		
20xB(15-x)Zn5	5.33×10 ⁻⁸	1.72×10 ⁻⁸	1.87×10 ⁷	5.82×10 ⁷		
40xSi(20-x)Zn20	No glass measured	4.17×10 ⁻⁷	No glass measured	2.40×10 ⁶		
42.5xSi(20-x)Zn17.5		1.82×10 ⁻⁷		5.49×10 ⁶		
45xSi(20-x)Zn15		1.48×10 ⁻⁷		6.76×10 ⁶		
47.5xSi(20-x)Zn12.5		5.17×10 ⁻⁸		1.94×10 ⁷		
15BaSi40	noisy	1.16×10 ⁻⁷	noisy	8.64×10 ⁶		
17.5BaSi37.5	noisy	2.37×10 ⁻⁷	noisy	4.21×10 ⁶		
20BaSi35	1.98×10 ⁻⁷	4.78×10 ⁻⁷	5.04×10 ⁶	2.09×10 ⁶		
22.5BaSi32.5	2.64×10 ⁻⁷	1.20×10 ⁻⁶	3.79×10 ⁶	8.32×10 ⁵		
25BaSi30	2.89×10 ⁻⁷	2.03×10 ⁻⁶	3.46×10 ⁶	4.93×10 ⁵		
10BaAl10	1.19×10 ⁻⁸	No glass ceramic	8.39×10 ⁷			
12BaAl8	1.21×10 ⁻⁸	measured	8.26×10 ⁷			

13BaAl7			
14BaAl6	4.60×10^{-8}	2.17×10^7	
15BaAl5	4.64×10^{-7}	2.16×10^6	

Table 7.1: Electrical conductivity/resistivity of glasses and glass ceramics in this study and the requirement for SOFC application from the literature

Activation energy for electrical conduction (kJmol^{-1}), error ± 3		
samples(mol %)	glass	glass ceramic
10BZn15	272	240
12.5BZn12.5	224	160
15BZn10		160
17.5BZn7.5	272	176
20BZn5	256	128
40SiZn20		144
42.5SiZn17.5		176
45SiZn15		176
47.5SiZn12.5		224
15BaSi40		144
17.5BaSi37.5		224
20BaSi35	240	256
22.5BaSi32.5	224	272
25BaSi30	224	192
10BaAl10	336	
12BaAl8	256	
13BaAl7		
14BaAl6	272	
15BaAl5	192	

Table 7.2: Activation energy for electrical conduction for glasses and glass ceramics produced in this study

Samples types	Electrical conductivity σ / S cm ⁻¹	Activation energy (Ea) kJ mol ⁻¹	refs
Glass ceramic(GC)	Maximum 4×10^{-7}	144-218	(Goel, Tulyaganov et al. 2010)
GC	$5.6 - 6.3 \times 10^{-9}$	137-149kJ mol ⁻¹	(Lara, Pascual et al. 2006)
GC	$2.2 \times 10^{-7} - 4.5 \times 10^{-8}$	NA	(Ghosh, Sharma et al. 2010)
GC	$1.6 \times 10^{-7} - 6.9 \times 10^{-9}$	NA	(Chen, Zou et al. 2013)
GC	$2.15 \times 10^{-7} - 7.55 \times 10^{-8}$	NA	(Liu, Huang et al. 2016)
glass	9.8×10^{-8}	NA	(Liu, Huang et al. 2016)
GC	$2.0 \times 10^{-8} - 8.5 \times 10^{-7}$	NA	(Zhang, Yang et al. 2015)
GC	$2.2 - 4.66 \times 10^{-7}$	176-195	(Kupracz, Szreder et al. 2014)
GC	$>10^{-6}$	169-183	(Reddy, Tulyaganov et al. 2014)

Table 7.3: Electrical properties values for other glasses and glass ceramics in the literature

5.7 Summary and Conclusions

1. The results of the impedance spectroscopy confirms the excellent insulating properties of all samples tested at around 600°C despite an increase in conductivity caused by the alkaline earth additions in all the glass samples and higher conductivity of the crystalline phases in glass-ceramics. Therefore, these glasses meet the electrical insulation requirements for use as sealant in SOFCs.
2. The electrical conductivity, dielectric constant and tangent loss all exhibit frequency and temperature dependences either in glasses or glass-ceramics. There is an increase in all these parameters with temperature and in the case of frequency the dielectric constant and tangent loss are higher at lower frequency and decreased with increasing frequency; this is different to conductivity which varies linearly at low to intermediate frequencies and then increases with frequency at higher values.
3. Conductivity decreases with increasing connectivity given by the average ratio of Q^n/N of the Q species and borate species, where N is the sum of N_3 and N_4 for all samples in the parent glasses and a similar pattern was observed for the glass-ceramics.
4. Conductivity and dielectric constant also increased with increasing amounts of doubly charged modifiers.
5. Conductivity and dielectric constants are higher in the glass-ceramics compared to the parent glasses suggesting that the lanthanum borosilicate crystalline single phase is more conductive than the residual glass, see Appendix 1a for the impedance plot.
6. The activation energy for electrical conductivity generally shows a decreasing trend in BZn, BaSi and BaAl in their glass forms; however, in the glass-ceramics E_a of BZn and BaSi increased. E_a for the SiZn glass-ceramics follows a similar trend to the glass samples of BZn, BaSi and BaAl.
7. Incorporation of modifiers leads to a decrease in the size of both site separation and polaron radii in the BZn, BaSi and BaAl glass series.
8. The increase in the atom–atom site separation correlates with an increase in E_a and a decrease in conductivity of BaSi and BaAl series.
9. Conductivity was discussed in terms of a hopping mechanism similar to small polaronic hopping in oxide glasses having transition metals and low mobility ions such as Ba^{2+} .

10. The impedance results reveal the possibility of electrode polarisation arising from space charge accumulation between electrode and glass samples leading to higher dielectric constant values at low frequency.

6 Results III: Mechanical properties

6.1 Mechanical properties of xBa(40-x)Si glasses

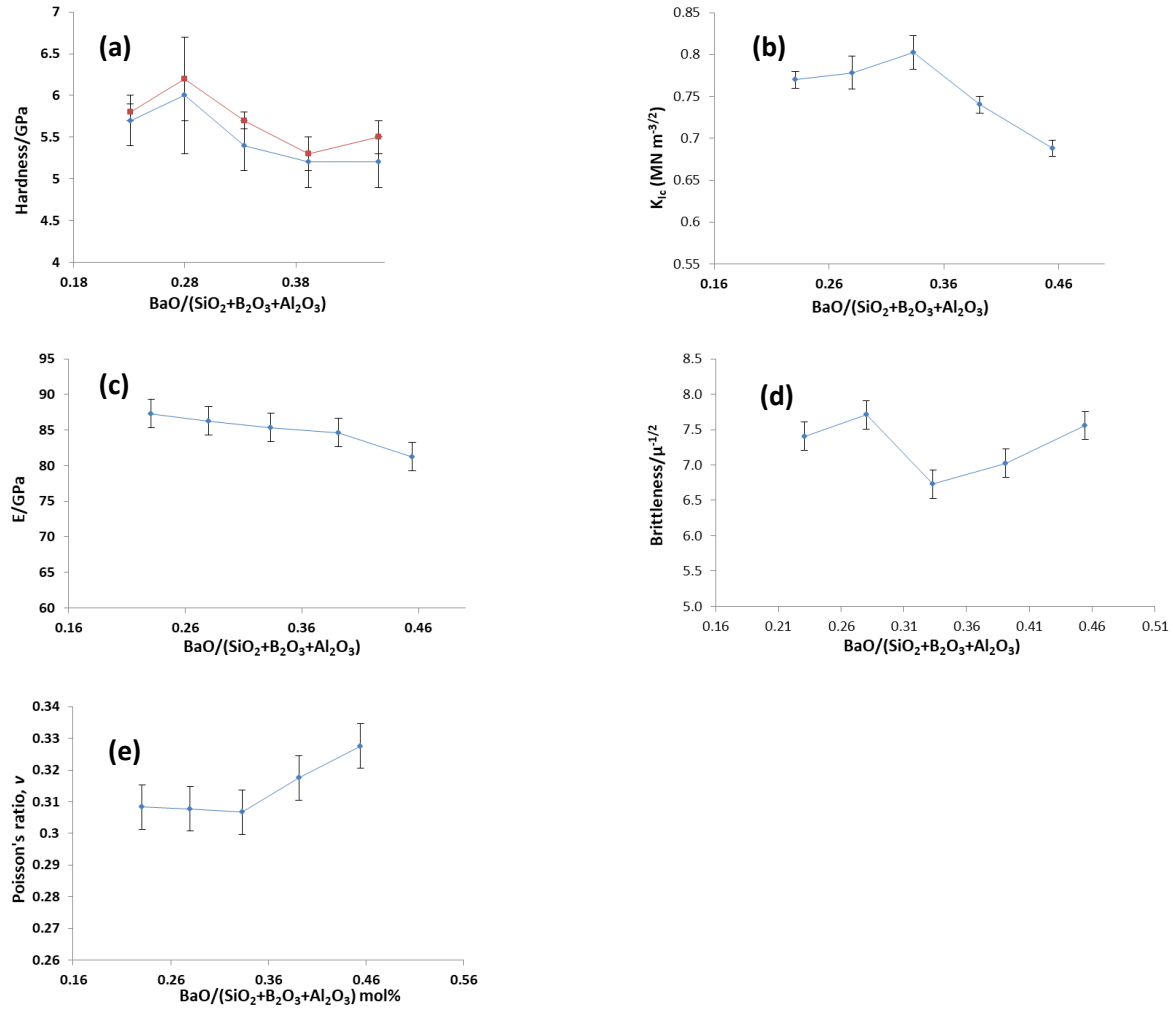


Figure 6-1: Hardness of glass blue line and glass ceramic red line (a) Indentation fracture toughness (b) Young's modulus (d) Brittleness and (e) Poisson's ratio of xBa(40-x)Si versus BaO/total network formers

The addition of BaO in to xBa(40-x)Si leads to a decrease in hardness and Young's modulus (fig 6-1(a) and (c)) while indentation fracture toughness (fig 6-1(b)) exhibits an initial increase and then decreased at a ratio of BaO/total network formers of ~ 0.3 in these glasses. The hardness is

slightly higher for the glass ceramics after crystallization compared with the parent glasses. The reason for the decrease in hardness and modulus is because BaO, which has a low field strength is less attracted to the network anions and thus is less well bonded into the glass. BaO containing glasses were reported by Hand and Tadjiev to have lower hardness (Hand and Tadjiev 2010). There is no structural evidence to support the initial rise in indentation fracture toughness seen in fig 6-1(b) as the polymerisation index (fig 4-6(d)) indicates decreases with BaO additions. This would suggest that the behaviour of the indentation fracture toughness is dependent on other factors including energy dissipation process such as plastic deformation, crack branching and blunting occurring at the crack tip and not associated only with energy required to fracture bonds as explain by Yoshida et al, for Vickers indentation of sodium borosilicate glasses (Yoshida, Tanaka et al. 2001). A similar effect on mechanical properties of lanthanum borosilicate glass by all the alkaline earths modifiers depending on their field strength was given in the order ($Mg^{2+} > Ca^{2+} > Sr^{2+} > Ba^{2+}$) was reported by (Kaur, Pandey et al. 2012) and found Mg^{2+} with the highest field strength improves mechanical properties and that Ba^{2+} having the lowest field strength just like in this study has decreasing effect with the lowest hardness and fracture toughness in the glasses reported.

Brittleness in $xBa(40-x)Si$ fig 6-1 (d) exhibits a similar trend to the molar volume fig 4-1 with similar drop at the same compositional ratio 0.33, where brittleness decreased by $1\mu m^{-1/2}$ and then increases linearly with increasing BaO. See appendix 3 for plot of brittleness versus molar volume of $xBa(40-x)Si$ exhibiting linear correlation an indication that brittleness scales with molar volume in this series. Brittleness although less often reported is a good parameter to estimate the susceptibility of a material to external mechanical loads; lower brittleness tends to correspond to higher fracture toughness as $B = H/K_{Ic}$. Poisson's ratio in fig 6-1(e) increases roughly linearly with BaO addition in $xBa(40-x)Si$ glass which can be explained on the basis of structural depolymerisation induced by the BaO which acts as a modifier (see figs 4-6(d) and 4-10(d)) on the degree of polymerisation calculated using the Manara method. Poisson's ratio exhibits inverse correlations with the indentation fracture toughness in $xBa(40-x)Si$ series as presented in fig 6-8

6.2 Mechanical properties of xBa(10-x)Al glasses

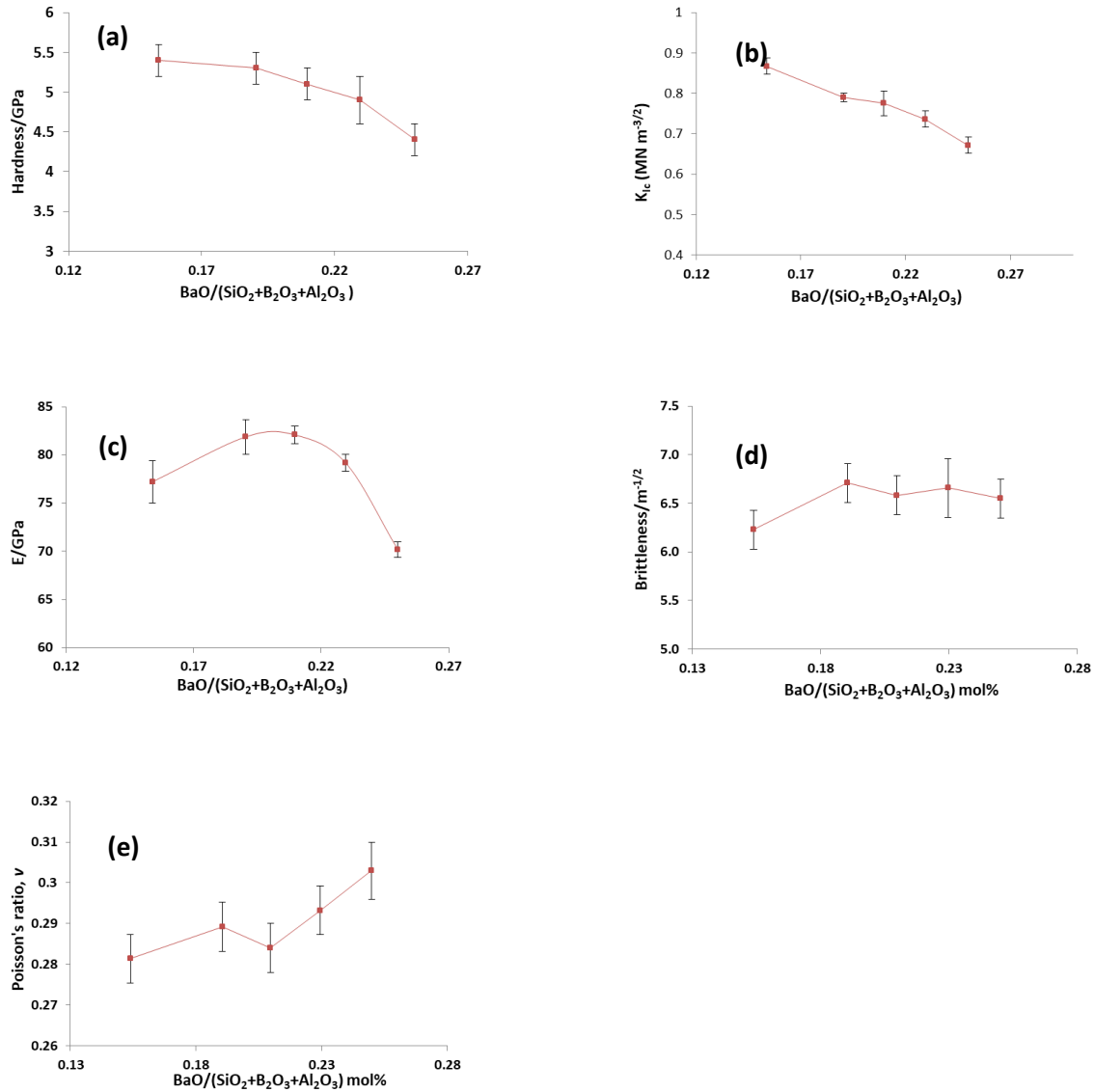


Figure 6-2: Hardness (a) Indentation fracture toughness (b) Young's modulus (d) Brittleness and (e) Poisson's ratio of xBa(10-x)Al versus BaO/total network formers

The effect of BaO addition in xBa(10-x)Al is similar to xBa(40-x)Si and therefore a decreasing trend is seen in hardness (fig 6-2(a)) and unlike xBa(40-x)Si the indentation fracture toughness in xBa(10-x)Al (fig 6-2(b)) exhibit a linear decrease without the initial increase shown by xBa(40-x)Si. However the behaviour of the Young's modulus fig 6-2(c) is different to that of H and K_{IC} as initial increase was observed until 0.2 ratio of the BaO/sum of network formers and thereafter

decreased. The brittleness of $x\text{Ba}(10-x)\text{Al}$ series initially increased with BaO additions but after a BaO/total network formers of 0.2 the brittleness became constant with further BaO additions. The Poisson's ratio of $x\text{Ba}(10-x)\text{Al}$ series behaves similar to $x\text{Ba}(40-x)\text{Si}$ and therefore shows an increasing trend as BaO increased and the ratio of BaO/total network formers decreased. Comparing the Poisson's ratio with the indentation fracture toughness suggests an inverse correlation just like that seen in the $x\text{Ba}(40-x)\text{Si}$ series see fig 6-8 for a plot of brittleness versus Poisson's ratio.

6.3 Mechanical properties of xB(15-x)Zn glasses

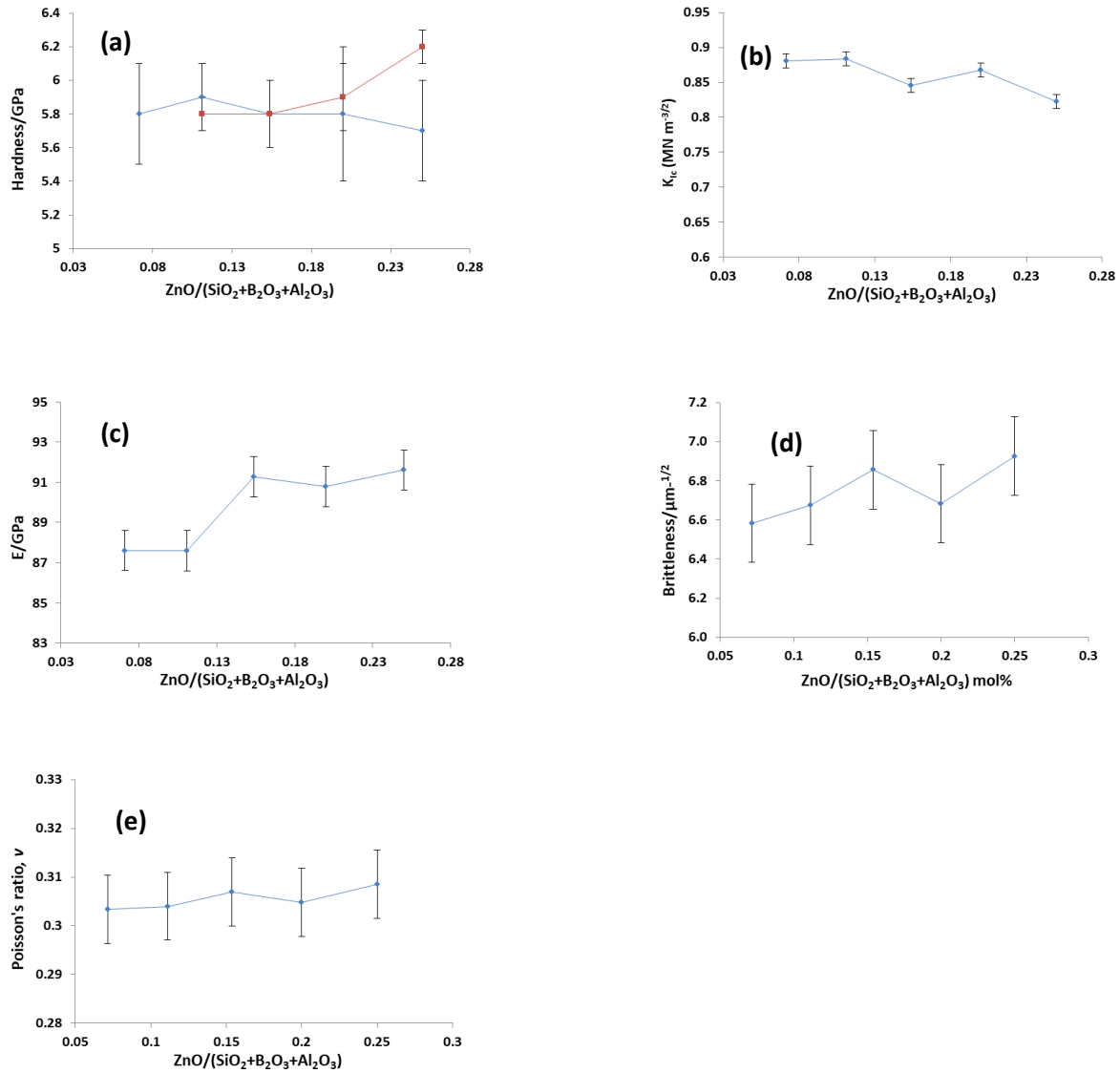


Figure 6-3: Hardness of glass blue line and glass ceramic red line (a) Indentation fracture toughness (b) Young's modulus (d) Brittleness and (e) Poisson's ratio of xB(15-x)Zn glasses versus ZnO/total network formers

The effect of swapping ZnO with boron in xB(15-x)Zn has little effect on hardness within the measurement error (fig 6-3(a)) where the hardness shows a decreasing trend with ZnO addition. However in the glass ceramic the hardness exhibit increasing trend this behaviour is opposite to

the parent glass which exhibit a slightly decreasing trend. The indentation fracture toughness fig 6-3 (b) also tends to decrease with increasing ZnO content. There is a small but notable increase in Young's modulus in the $x\text{B}(15-x)\text{Zn}$ series with ZnO additions, this increase in E in $x\text{B}(15-x)\text{Zn}$ might be associated with boron anomaly since ZnO was swapped for boron oxide in this series; changing from BO_3 trigonal units to more rigid BO_4^- tetrahedra is reported to increase E values by.

The brittleness of $x\text{B}(15-x)\text{Zn}$ (fig 6-3(d)) and the Poisson's ratio increase slightly with ZnO additions. This may suggest that ZnO is acting as a modifier (see sections 4.1.3 and 4.1.4) disrupting the silicate network and hence ν increases. It can be seen that in fig 6-3 (d) there is an increasing trend in brittleness with ZnO addition.

6.4 Mechanical properties of xSi(20-x)Zn glasses

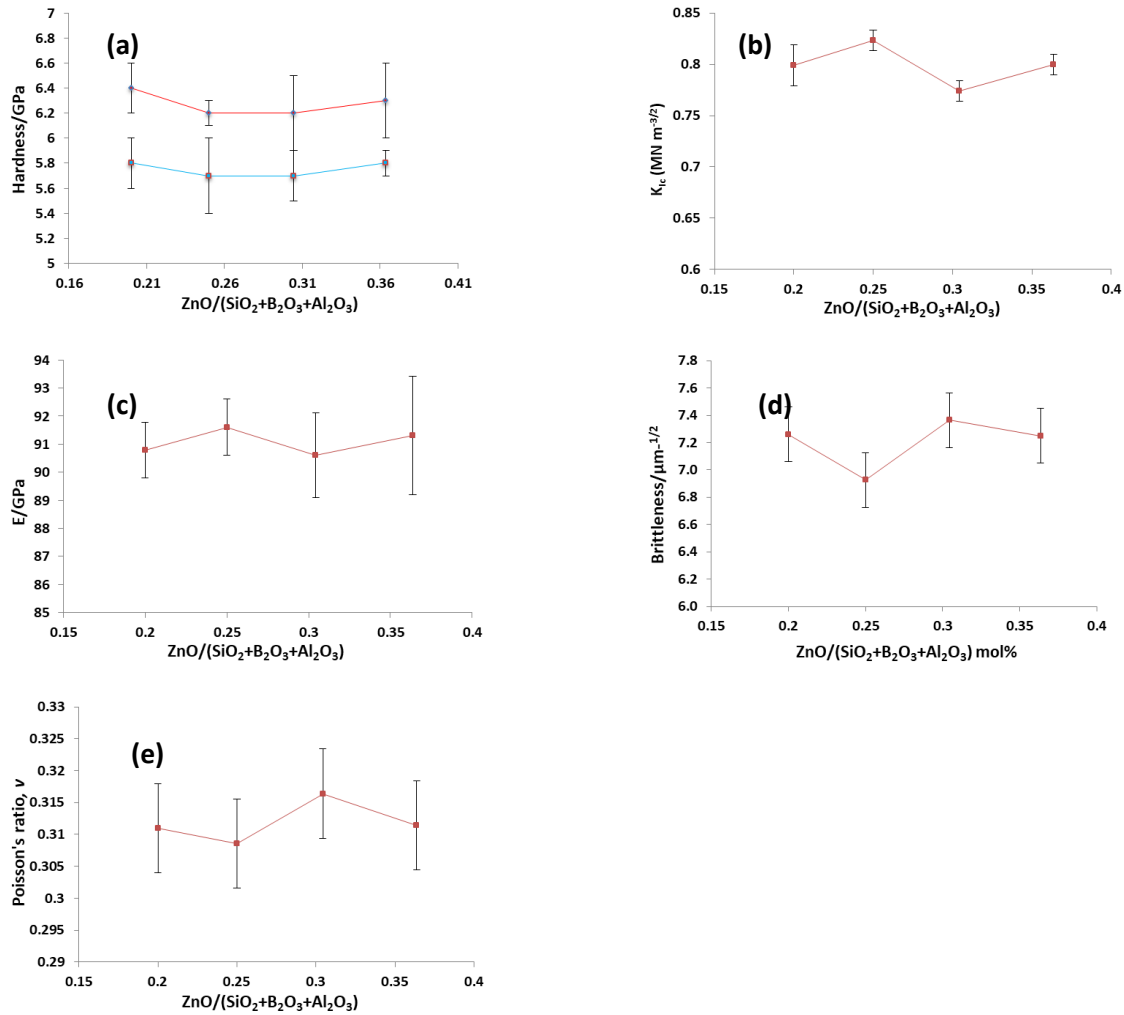


Figure 6-4: Hardness of glass and glass ceramic (a) Indentation fracture toughness (b) Young's modulus (d) Brittleness and (e) Poisson's ratio of xSi(20-x)Zn versus ZnO/total network formers

The effect of swapping ZnO with silica in xSi(20-x)Zn has little effect on hardness fig 6-4 (a), Young's modulus fig 6-4(c) and Poisson's ratio fig 6-4 (e) within the measurement error. This may suggest that these parameters did not show any compositional dependence as they all appear to be on a straight line as ZnO content is increased. But looking at fig 6-4 (a) shows an increased hardness in the glass ceramic over the parent glasses. It is worthy of note that the Poisson's ratio show inverse correlations with K_{Ic} as can be seen in fig 6-4(b), (d) and (e). also see fig 6-8 (a) for plot of K_{Ic} versus brittleness.

6.5 Mechanical properties of xSi(20-x)La(Sr) glasses

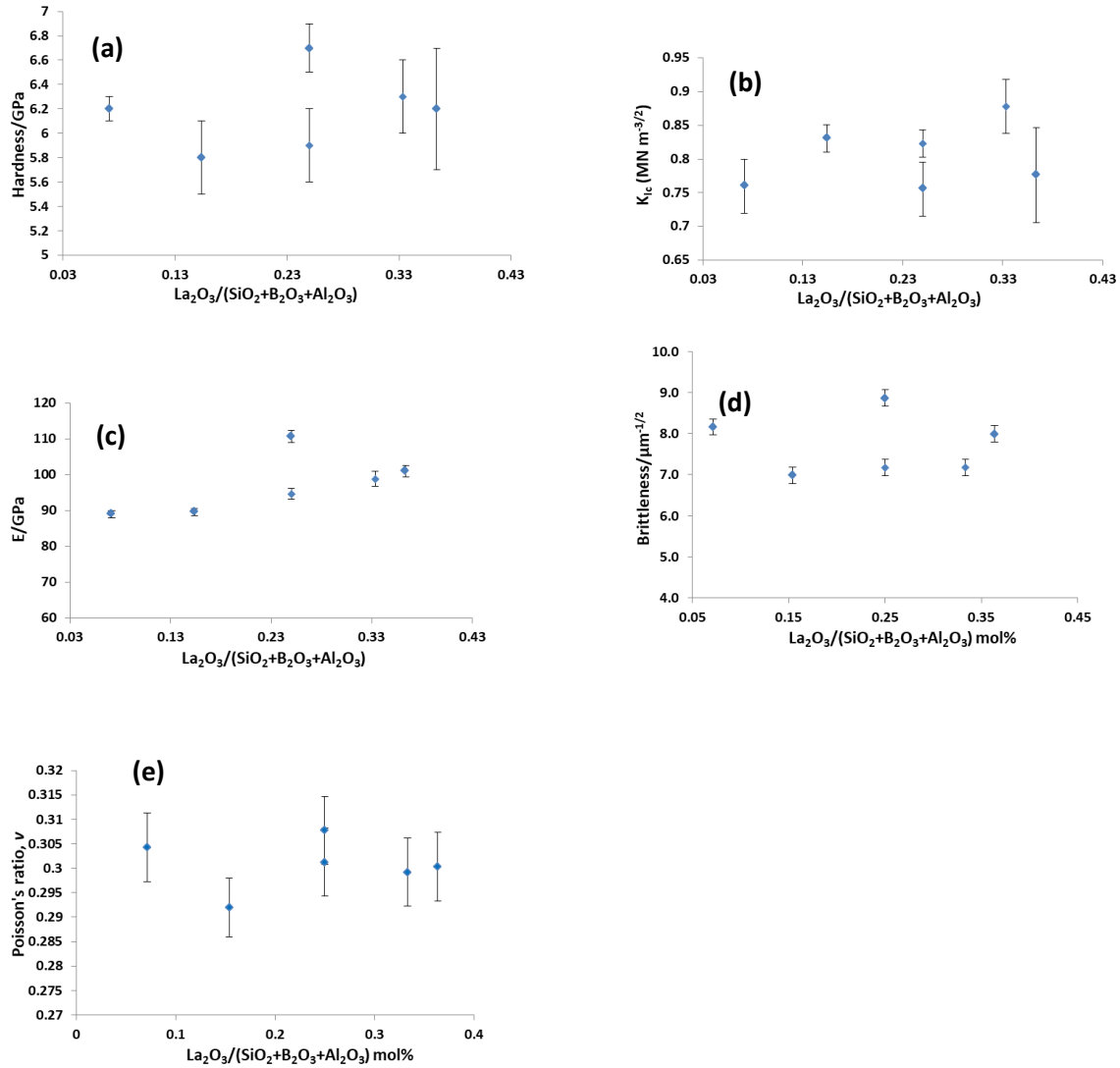


Figure 6-5: Hardness (a) Indentation fracture toughness (b) Young's modulus (d) Brittleness and (e) Poisson's ratio of xSi(20-x)La(Sr) versus La₂O₃/total network formers.

Swapping silica and lanthanum in this series on molar basis introduces higher La₂O₃ into the glass than removing silica therefore the effect of the high lanthanum on mechanical properties will be discussed below. The replacement of silica by lanthanum oxide in xSi(20-x)La(Sr) fig 6-5 indicates some zig zag format however the H fig 6-5 (a) shows an increasing trend with La₂O₃ while the indentation fracture toughness fig 6-5 (b) mirrors the H and a clearly linear correlation

can be seen between H and K_{Ic} see fig 6-6 (b) for plot of H versus K_{Ic} . The hardness data decreases and then increases with increasing lanthanum content. This sort of behaviour where the hardness increases and decreases at certain lanthanum contents has been reported by (Sasmal, Garai et al. 2014) for lanthanum containing barium free borosilicate glass. Lanthanum is reported to enhance mechanical properties as it is known to increase the rigidity of the glass network (Ghosh, Sharma et al. 2010) due to its high field strength (Sasmal, Garai et al. 2014). The Young's modulus in fig 6-5(c) generally depicts an increasing trend as La_2O_3 increases obviously due to the reasons just mentioned above. In general rare earth oxides such as La_2O_3 tend to depolymerise the silicate network and may also increase the hardness of the glass due to their high field strength as reported by Angeli et al, (Angeli, Charpentier et al. 2013), this is because the rare earth could act as an intermediate performing a modifier role depolymerising the network and also could resemble a network former role just like SiO_2 and B_2O_3 by stabilization of the anionic species due to high field strength of La_2O_3 , although La_2O_3 is not a network former but generally structural rigidity increased with increasing La_2O_3 due to its high field strength and thus ensuring mechanical integrity of the glasses.

The brittleness and the Poisson's ratio fig 6-5 (d) and (e) indicates similar pattern as can be seen as both decrease and increase together. On a general note H , E and K_{Ic} all increase as the amount of La_2O_3 increases while ν and brittleness exhibit a decreasing trend with La_2O_3 addition.

6.6 Generalised correlations between mechanical properties of glasses

Although the indentation fracture toughness (IFT) method is not completely reliable as it does not give reliable K_{Ic} values and in addition crack initiation and subsequent propagation in (IFT) is not the same with the sequence of cracks as in the case of the standardised methods such as chevron notch used for K_{Ic} measurement (Quinn and Bradt 2007) however it is less time consuming than conventional fracture toughness testing. Thus it can be used as a quick estimate for the fracture toughness values of oxide glasses but there is a need to compare data obtained from IFT with the standard chevron notch technique to test its reliability. Considering the Griffith-Irwin (equation 2-27) fracture toughness is a function of the Young's modulus and fracture surface energy of glasses. Looking at fig 6-6(a), the fracture toughness of all the glasses in this study generally increase with increasing Young's moduli. this study is compared with others from the literature fig 6-6(b) and suggest that E and K_{Ic} exhibit linear dependence except

for data from Malzbender 2011 which depicts vertical relationship. However, it could be concluded that the correlation could be generalised for oxide glasses.

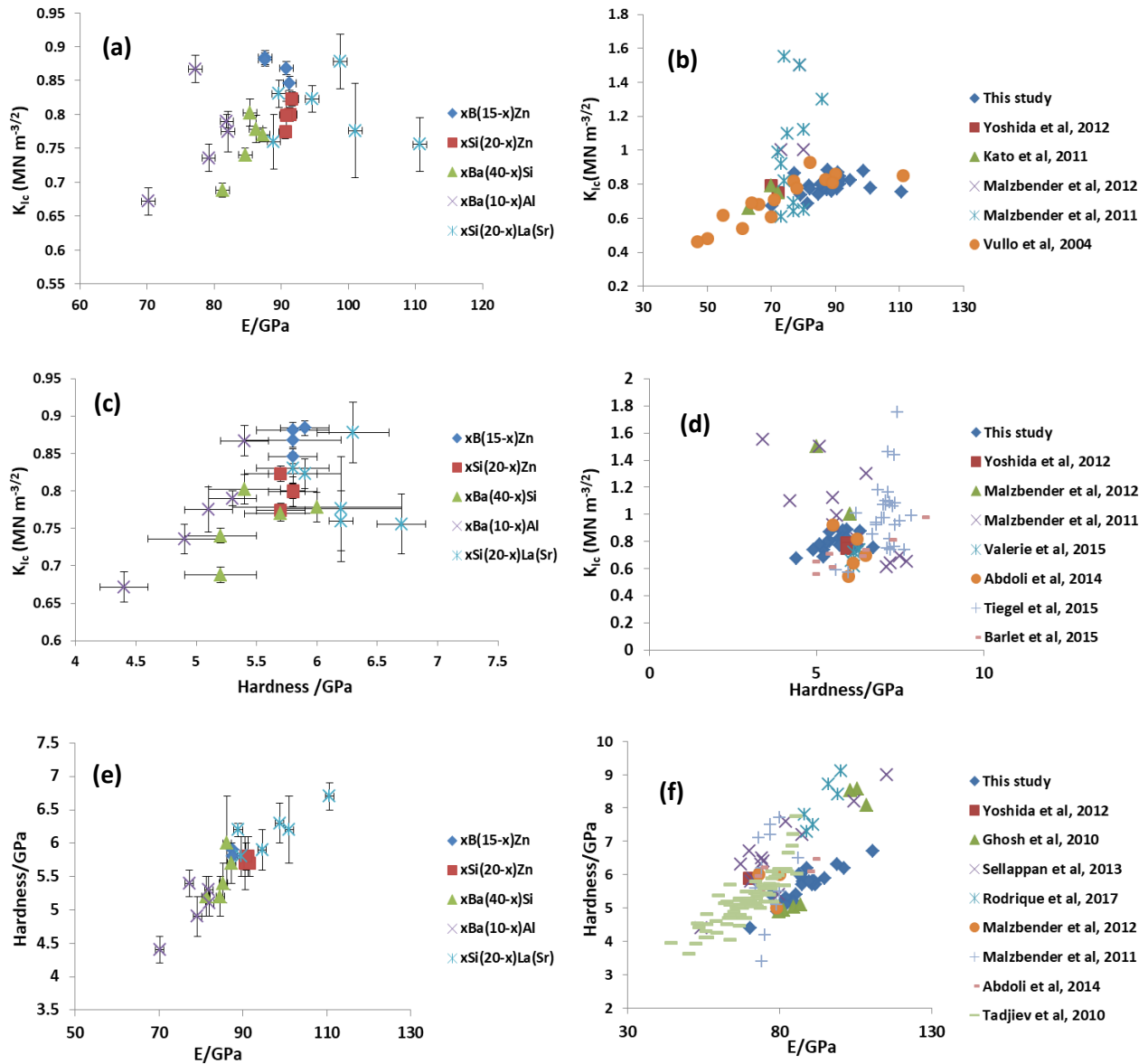


Figure 6-6: Indentation fracture toughness versus Young's modulus (a) this study (b) this study compared with literature; Indentation fracture toughness versus hardness (c) this study and (d) this study compared with literature; Hardness versus Young's modulus (e) this study and (f) this study compared with literature.

6.7 Indentation fracture toughness and hardness

The plot in fig 6-6(c) of indentation fracture toughness versus hardness in this study reveals different correlations for different glass series. In both $x\text{Ba}(40-x)\text{Si}$ and $x\text{Ba}(10-x)\text{Al}$ glasses a roughly linear relationship between hardness and fracture toughness is evident. For $x\text{B}(15-x)\text{Zn}$ and $x\text{Si}(20-x)\text{Zn}$ hardness does not vary much but there is a greater variation in fracture toughness so that the data points lie in a roughly vertical line. For $x\text{Si}(20-x)\text{La}(\text{Sr})$ there is no simple relationship between toughness and hardness. Although hardness and indentation fracture toughness are estimated using the size of indent a and the length of radial cracks c (Mohajerani and Zwanziger 2012), there is no one simple correlation as compositions vary especially considering the fact that K_{Ic} is not always composition dependent. The resistance of glass to cracking during indentation is controlled by 3 processes which include plastic or shear flow, densification and elastic deformation (Tiegel, Hosseinabadi et al. 2015). And as also reported by (Kato, Yamazaki et al. 2010) no clear correlation between crack resistance (defined as the load required to initiate radial cracks) and hardness although they suggested a relationship between crack resistance and densification that samples which exhibit larger densification around the indent have better crack resistance. In the same way the comparison of this study with others from the literature see fig 6-6 (d) also depicts scattered relationship between K_{Ic} and H .

6.8 Young's modulus and hardness

Larger radii, lower field strength cations are less strongly attracted to the surrounding structural silicate units, and therefore addition of this type of cation decreases stiffness and hardness of silicate glasses and so the R-O bond strength in alkaline earth containing glasses determine the hardness in such glasses. On the other hand the increase in hardness with alkalis (M^+) is due to strengthening of the Si-O bonds with increasing radii of the alkali ions which is as a result of the weakening of the M-O bonds. Moreover, as noted by (Smedskjaer, Jensen et al. 2010) that the correlation between NBO/T and hardness cannot be generalised to all silicate systems as seen in basaltic glass where both increase and decrease in hardness with NBO/T occur.

In terms of linear correlation between the hardness and Young's modulus of the glasses in this study it is found that the ordering trend suggest that an increase in both H and E follows the order $x\text{Si}(20-x)\text{La}(\text{Sr}) > x\text{Si}(20-x)\text{Zn} > x\text{B}(15-x)\text{Zn} > x\text{Ba}(40-x)\text{Si} > x\text{Ba}(10-x)\text{Al}$ (see fig 6-6(e)). According to equation (2-26) the hardness of glass is dependent on 3 variables, the average bond

strength α , E and C_g ; the variation in the C_g value is small so it has little net effect. However, modifier oxides with large single bond strengths increase hardness and Young's modulus in the order La-O>Zn-O>Ba-O>Sr-O (Dimitrov and Komatsu 2012) as can be seen in fig 6-1(e) above. The Young's moduli of all the glasses are higher than or comparable to most normal borosilicate glasses with 60 to 85GPa (Vullo and Davis 2004, Ghosh, Sharma et al. 2010) and the hardnesses are also higher than and comparable to many sealing glasses in the literature (Rodríguez-López, Wei et al. 2017). A comparison between this study and others from the literature also indicated a linear correlations between H and E which would suggest that this behaviour could be generalised for oxide glasses.

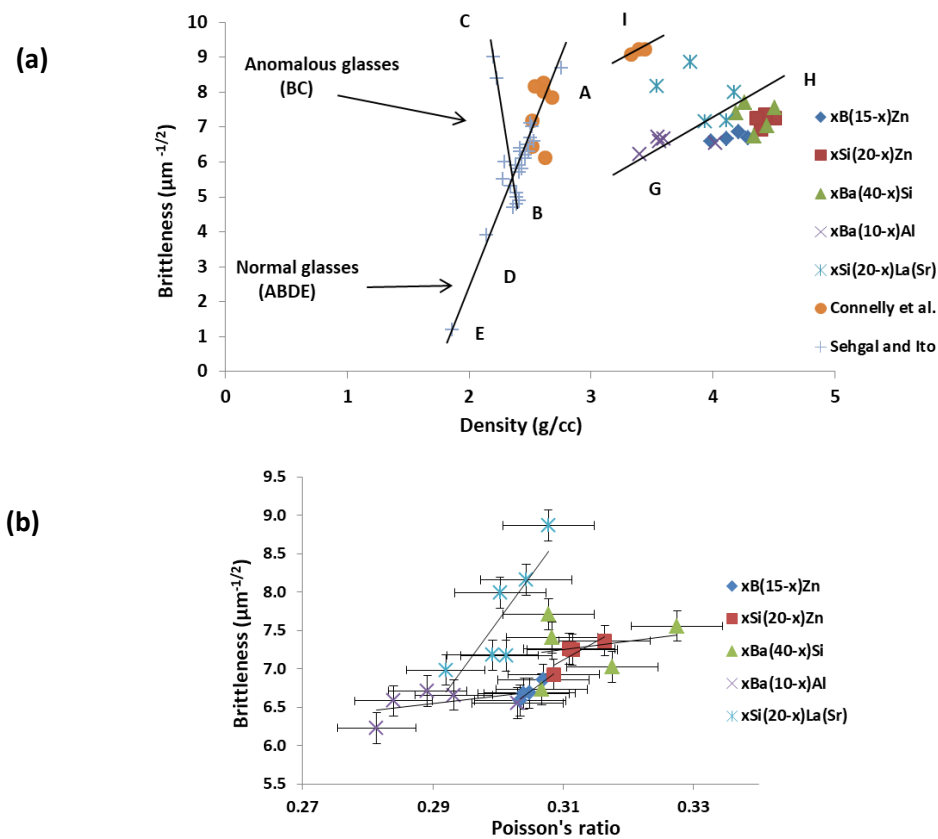


Figure 6-7: (a) Brittleness versus density and (b) brittleness versus Poisson's ratio.

6.9 Brittleness and density

Although there are only limited variations in the brittleness ($6.2 - 7.7 \mu\text{m}^{-1/2}$) for the glasses in this study probably due to similarity in the compositions, a brittleness versus density plot is shown in fig 6-7 (a) together with the Sehgal and Ito data for comparison; Sehgal and Ito 1999 observed a linear increase of brittleness with density for so called normal glasses which do not exhibit densification under indentation (line A-E in fig 6-7 (a)). So-called anomalous glasses which densify under indentation, exhibit a different trend (line BC). It was reported by (Connelly, Hand et al. 2011) that some nuclear waste glass data falls around the general trend reported by Sehgal and Ito while higher density glasses do not fall on the trend line identified by Sehgal and Ito and so they suggested that the Sehgal and Ito plot cannot simply be generalised. In the same way in this study although brittleness tended to increase with increasing density in general the data not fall along the Sehgal and Ito line.

A closer look at the data indicates that glass with densities greater than 3gcm^{-3} data lie along line G-H (this study) and I (Connelly et al 2011), shows deviation from the Sehgal and Ito graph probably reflecting the fact that significant increases in density are often achieved through the addition of relatively large and lower field strength species, which would be expected to result in weaker bonds that would tend to reduce brittleness. This study also observed that the densest sample with 25mol% BaO is not the most brittle sample just as was observed by (Connelly, Hand et al. 2011).

6.10 Relationships between fracture toughness, hardness, brittleness and Poisson's ratio

The Poisson's ratio of glass is reported to be an important parameter in determination of the mechanical properties of oxide glasses. Brittleness of oxide and non-oxide glasses is mostly affected by variation in the Poisson's ratio. Glass network rigidity and packing density controls the Poisson's ratio as reported by (Rouxel 2007).

$x\text{B}(15-x)\text{Zn}$, $x\text{Si}(20-x)\text{Zn}$, $x\text{Ba}(40-x)\text{Si}$ and $x\text{Ba}(10-x)\text{Al}$ (fig 6-8(a)) and $x\text{Si}(20-x)\text{La}(\text{Sr})$ (fig 6-8(c)) all exhibit a decrease in fracture toughness as the Poisson's ratio increases; this type of inverse correlation has been reported by (Barlet, Delaye et al. 2015) for sodium borosilicate glasses. It is well known that the addition of modifiers into the glass structure leads to

depolymerisation by creating NBOs which decrease the fracture toughness and increase the Poisson's ratio. This is further supported by Tiegel, et al who indicate that indentation fracture toughness tends to scale with network connectivity i.e glasses with a higher silica content which have lower Poisson's ratios (Tiegel, Hosseinabadi et al. 2015). It should be noted that the ability to densify under indenter and to resist cracking is a feature of so-called resilient glasses (Rouxel, Sellappan et al. 2014). Isochoric shear flow is the deformation mechanism feature for semi-resilient glasses with increase in packing density. In general hardness and Poisson's ratio fig 6-8 (b) are inversely related for all but one series of glasses in this study although different glass series follow different trend lines. A decrease in hardness with Poisson's ratio has been reported by (Barlet, Delaye et al. 2015) they suggested that when ν is low the glass structure becomes more connected and hence hardness becomes high. However, for $x\text{Si}(20-x)\text{La}(\text{Sr})$ glasses fig 6-8 (d) a different behaviour is apparently observed although the variation in Poisson's ratio is quite small. The behaviour of the $x\text{Si}(20-x)\text{La}(\text{Sr})$ glass series may be due to the addition of the lanthanum oxide which increases the hardness and the Poisson's ratio because La_2O_3 is reported to increase glass rigidity. The ν of the glasses in this study is high (0.28-0.32) and falls within a similar range to bulk metallic glasses (Lewandowski, Wang et al. 2005).

Increases in the amount of NBOs and depolymerisation of the silicate network by modifier additions lead to increase in brittleness and Poisson's ratio of all the glasses in this study see fig 6-1 to 6-4 (d) and (e) except for $x\text{Si}(20-x)\text{La}(\text{Sr})$ fig 6-5 (d) and (e) where addition of La_2O_3 seems to decrease brittleness and Poisson's ratio; similar behaviour can be found in (Pönitzsch, Nofz et al. 2016).

The Poisson's ratio of 0.28 to 0.32 and the fractal bond connectivity gives some insight on the dimensionality of the glasses. Fractal bond connectivity supply information about elastic behaviour of glasses in relation to their network structures (Saunders, Metcalfe et al. 1996). And the value of the dimensionality (d) ranging between 1.6 to 2 implies they are 2D structures similar to pure B_2O_3 with d equals to 1.85 as reported by (Abd El-Moneim, Youssof et al. 2006). It is worthy of note that the Poisson's ratio varies in a very narrow range this can be associated with the insensitivity of Poisson's ratio to compositional changes; and can also be related to the near constancy of ratio shear and longitudinal moduli (S/L) in these glasses. It has been reported for alkaline earth aluminoborate glasses that a near constancy of the S/L ratio is as a result of

increase in B_4 units with addition of alkaline earth modifier which affects both longitudinal and transverse strain in the same way (Abd El-Moneim, Youssof et al. 2006).

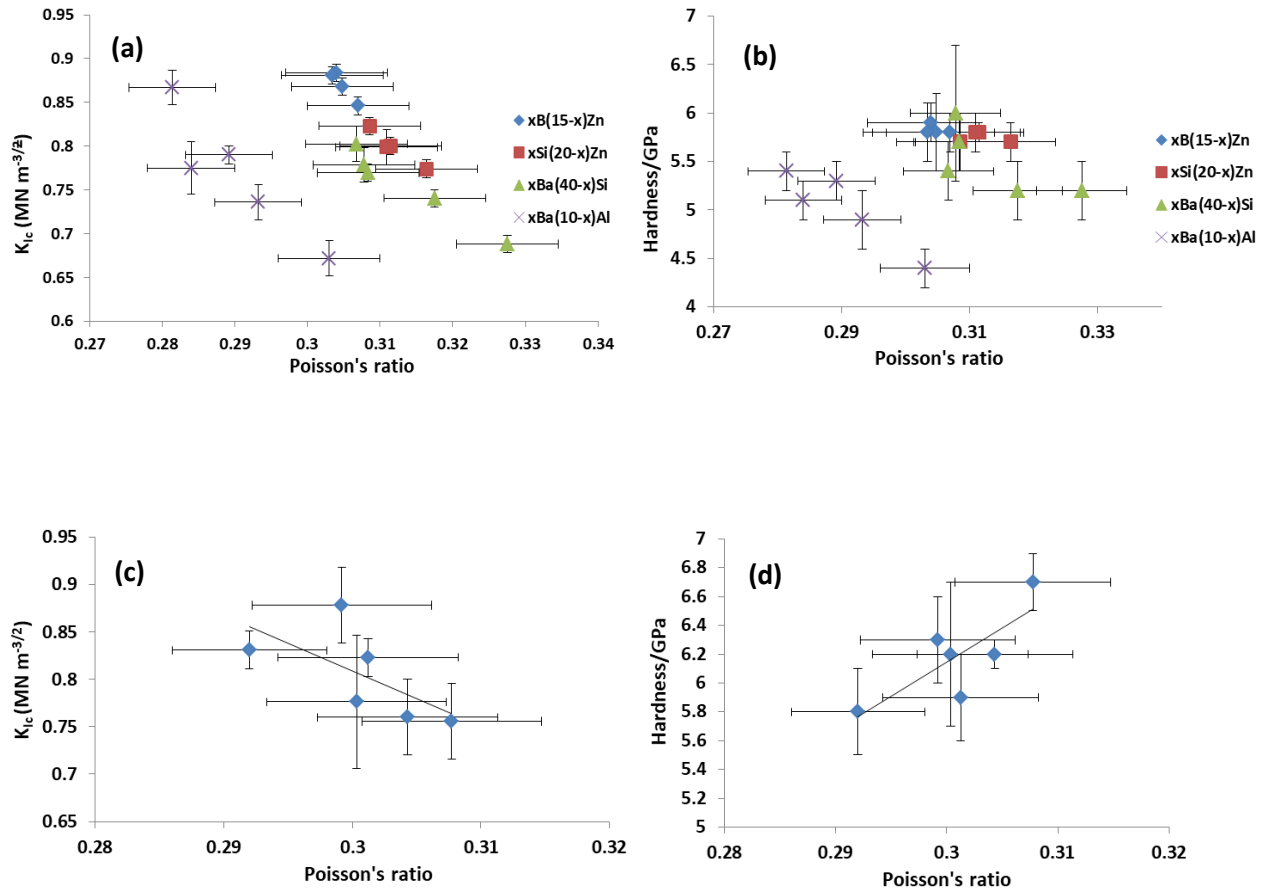


Figure 6-8: Indentation fracture toughness of (a) and hardness (b) of xB(15-x)Zn, xSi(20-x)Zn, xBa(40-x)Si, xBa(10-x)Al glasses and for xSi(20-x)La(Sr) in (c) and (d) versus Poisson's ratio.

Plotting Poisson's ratio versus packing density for the glasses studied here fig 6-9 (a) shows that they lie near but not on the empirical sigmoidal curve proposed by Rouxel, although there was notable spread in the original data used by Rouxel. The atomic packing density increases in the following order xBa(10-x)Al < xSi(20-x)La(Sr) < (xB(15-x)Zn, xSi(20-x)Zn) < xBa(40-x)Si. The relatively high Poisson's ratio of the glasses in this study implies that most of the bonds are ionic compared with for example SiO₂ which is predominantly covalent (Hwa and Chao 2005). Increase in Poisson's ratio is indicative of the fact that the cross-link density is decreased by the

increasing number of NBOs with increasing modifier content (Bootjomchai, Laopaiboon et al. 2014). Poissons ratio decreases as the E/G ratio decreases with respect to increase in cross-link density (Higazy and Bridge 1985) However the near constancy of the E/G values in this study suggest why the Poisson's ratio exhibit very little variations across the different series

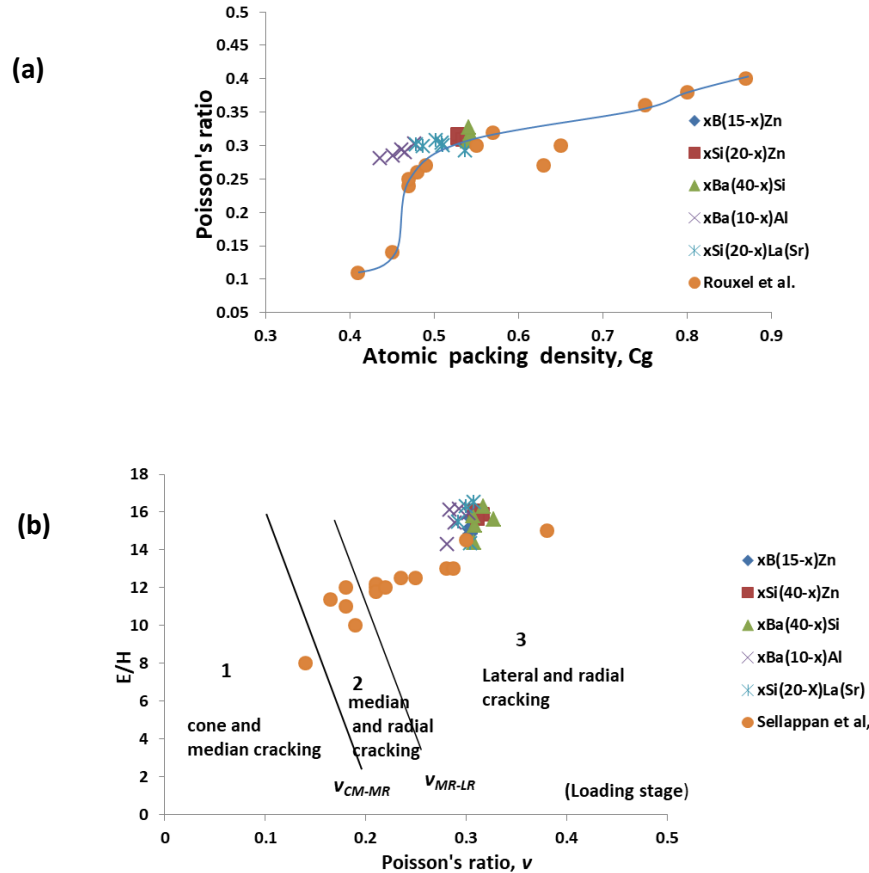


Figure 6-9: (a) Poisson's ratio versus atomic packing density, (b) E/H versus Poisson's ratio, showing the cracking mode for different oxide glasses;

As shown in fig 6-9 (b) the data in this study falls in the region identified by Sellappan et al, where lateral and radial cracking zone under indentation is observed as in this study (see region labelled 3) and the whole plot shows the limits of different micro cracking regimes as a function of ν against E/H ratio. The values of E/H and ν in this study lie between 14-16 and 0.28-0.31 and this relationship can establish some logical reasons regarding the compositional control of cracking behaviour in oxide glasses. In the diagram fig 6-9 (b) resilient glasses with lower ν are on the left hand side of the plot i.e ν_{CM-MR} edge, (where CM and MR is cone median and median

radial) cracking. For semi resilient glasses with ν between 0.2 to 0.25 the cracking pattern is the median and radial type while in the case of easily damaged glasses $\nu > 0.25$ lateral and radial cracking dominates and our data in this study falls under this category. In fact according to Rouxel higher values of E/H and ν indicates large stress development and leads to lower resistance to formation of radial median cracks (Rouxel 2015).

6.11 Correlations between mechanical properties and glass network structures

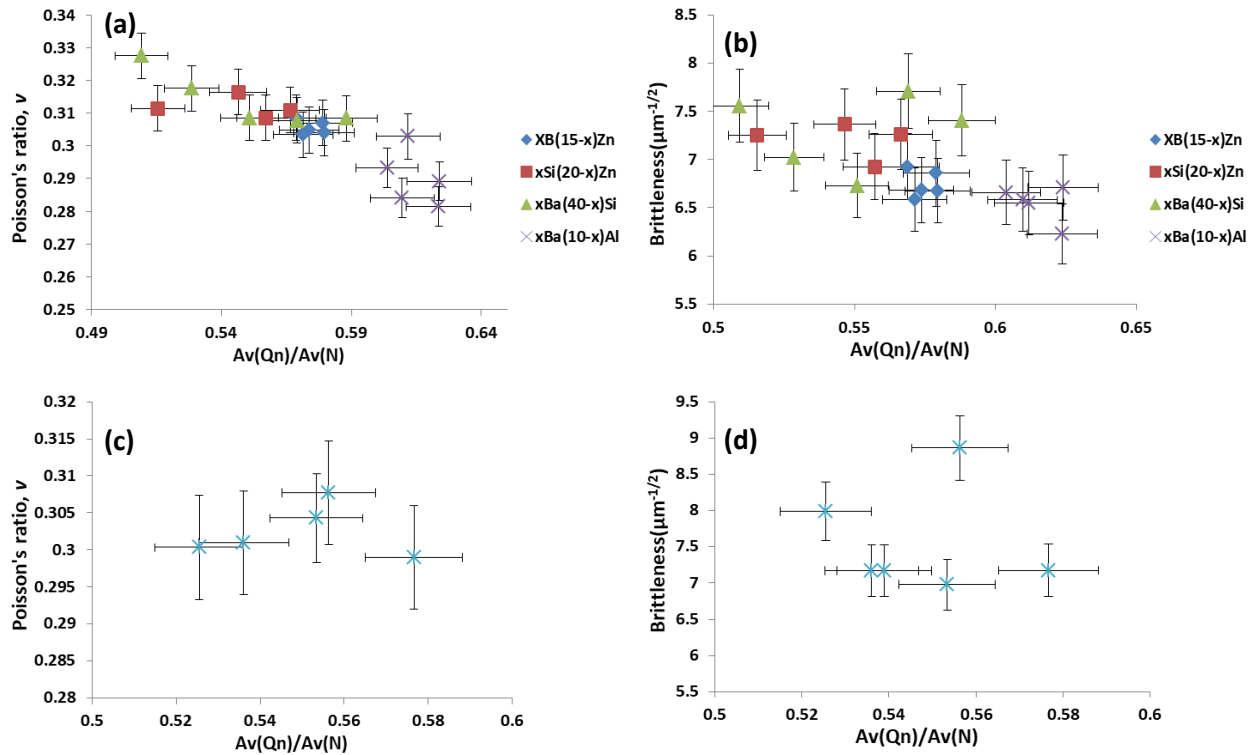


Figure 6-10: (a) Poisson's ratio (b) brittleness of $x\text{B}(15-x)\text{Zn}$, $x\text{Si}(20-x)\text{Zn}$, $x\text{Ba}(40-x)\text{Si}$ and $x\text{Ba}(10-x)\text{Al}$ (c) and (d) for $x\text{Si}(20-x)\text{La}(\text{Sr})$ versus the ratio of Q^n/N species.

Figs 6-10(a) and (b) show that both the Poisson's ratio and brittleness of $x\text{B}(15-x)\text{Zn}$, $x\text{Si}(20-x)\text{Zn}$, $x\text{Ba}(40-x)\text{Si}$ and $x\text{Ba}(10-x)\text{Al}$ glasses all decreased with increasing polymerisation as shown by the ratio of the average Q^n to N value where Q^n refers to averaged sum of the silicate species and N is the averaged sum of $^{[3]}\text{B}^{3+}$ and $^{[4]}\text{B}^{3+}$ in the glass. The exception, as ever is the $x\text{Si}(20-x)\text{La}(\text{Sr})$ series. In fig 6-11 (a), (b) and (c) both the indentation fracture toughness and

hardness indicates an increasing trend with increasing average Q^n/N ; again the data for the H of $x\text{Si}(20-x)\text{La}(\text{Sr})$ does not exhibit a clear trend. E values of $x\text{Ba}(40-x)\text{Si}$ and $x\text{Ba}(10-x)\text{Al}$ seems to increase with the increasing average Q^n/N while $x\text{B}(15-x)\text{Zn}$ and $x\text{Si}(20-x)\text{Zn}$ have fairly constant E (see fig 6-11 (e)). However the E in $x\text{Si}(20-x)\text{La}(\text{Sr})$ decreased with increasing average Q^n/N in fig 6-11(f)

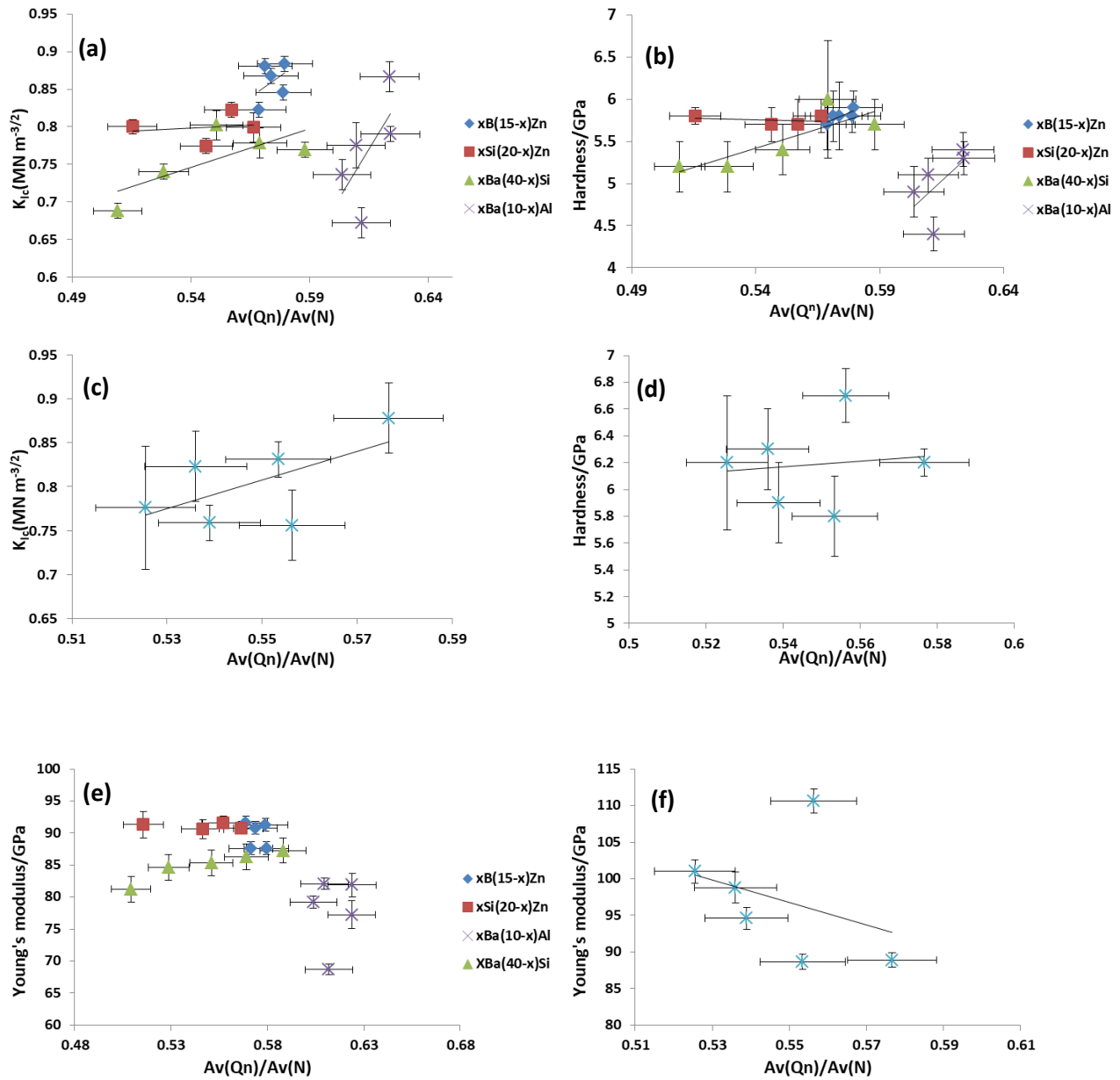


Figure 6-11: Indentation fracture toughness (a) hardness (b) of $x\text{B}(15-x)\text{Zn}$, $x\text{Si}(20-x)\text{Zn}$, $x\text{Ba}(10-x)\text{Al}$ and $x\text{Ba}(40-x)\text{Si}$ and for $x\text{Si}(20-x)\text{La}(\text{Sr})$ (c) K_{Ic} (d) hardness. (e) E of $x\text{B}(15-x)\text{Zn}$, $x\text{Si}(20-x)\text{Zn}$, $x\text{Ba}(10-x)\text{Al}$ and $x\text{Ba}(40-x)\text{Si}$ (f) E of $x\text{Si}(20-x)\text{La}(\text{Sr})$ versus averaged Q^n/N species

A correlation between E and H and T_g fig 6-12 (a) and (b) indicates as expected that E and H tend to scale with T_g reflecting the fact that all these properties tend to scale with structural rigidity of the glasses. Hardness and indentation fracture toughness (Fig 6-12(c) and (d)) both decrease with increasing density of $x\text{B}(15-x)\text{Zn}$, $x\text{Si}(20-x)\text{Zn}$, $x\text{Ba}(40-x)\text{Si}$ and $x\text{Ba}(10-x)\text{Al}$

glasses in this study. This may be connected with the effect of the modifiers in these glasses which will tend to occupy void space while reducing connectivity. As shown in fig 6-12 (e) and (f) slight increasing trends in hardness and density however indentation fracture toughness exhibit a more clear increase with density for $x\text{Si}(20-x)\text{La}(\text{Sr})$ glasses. The increase in fracture toughness, hardness and density is due to higher molecular weight of La_2O_3 and coupled with high field strength.

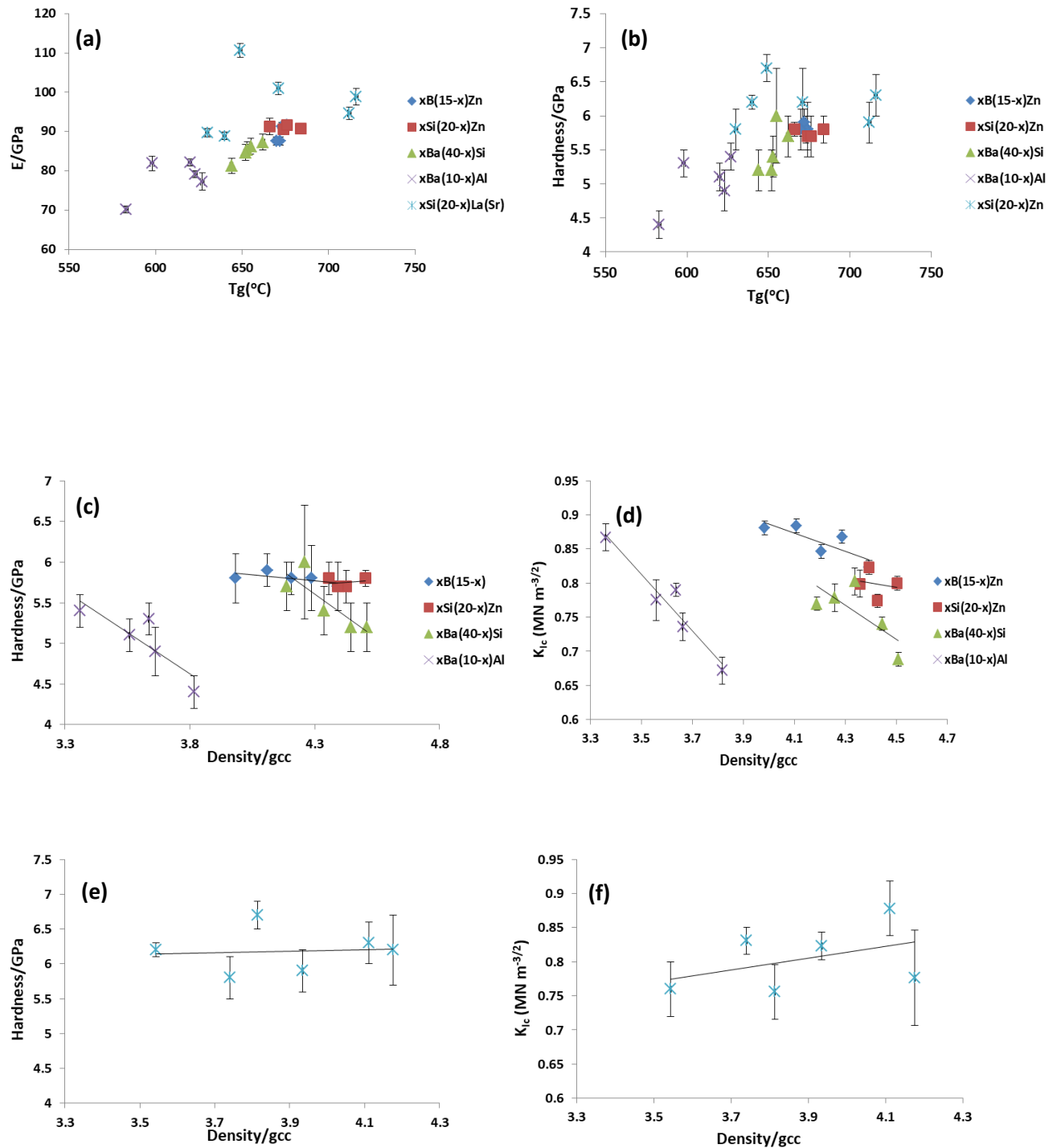


Figure 6-12: (a) E and (b) H versus T_g (c) hardness and (d) indentation fracture toughness versus density for $x\text{B}(15-x)\text{Zn}$, $x\text{Si}(20-x)\text{Zn}$, $x\text{Ba}(40-x)\text{Si}$ and $x\text{Ba}(10-x)\text{Al}$ glasses. (e) H and (f) indentation fracture toughness versus density for $x\text{Si}(20-x)\text{La}(\text{Sr})$ glasses.

6.12 Summary and Conclusions

Although the mechanical properties of sealing glasses are not given a particular target sealing glasses must be able to maintain sufficient mechanical strength to ensure adhesion and gas tightness during sealing and operation at high temperatures (Liu, Lin et al. 2015).

- 1) The values of E , H and indentation fracture toughness in this study are comparable to those reported in the literature.
- 2) La_2O_3 increases H and E and K_{Ic} whereas the doubly charged modifiers decreased the mechanical properties.
- 3) The values of Poisson's ratio and brittleness increase with alkaline earth additions a sign of depolymerisation within the glass structures however La_2O_3 does the opposite due to high field strength.
- 4) Indentation fracture toughness exhibit inverse correlation with ν in all the series.
- 5) Hardness and fracture toughness correlate positively with Young's modulus and each other for all the glass series studied.
- 6) H and indentation fracture toughness also inversely correlate with increases in density in $x\text{B}(15-x)\text{Zn}$, $x\text{Si}(20-x)\text{Zn}$, $x\text{Ba}(40-x)\text{Si}$ and $x\text{Ba}(10-x)\text{Al}$ glasses. While a slightly linear trend in $x\text{Si}(20-x)\text{La}(\text{Sr})$
- 7) Brittleness and density plot did not fall on the Sehgal and Ito plot of the so called normal and anomalous glasses confirming the lack of generality of this plot.
- 8) The ν and brittleness of $x\text{B}(15-x)\text{Zn}$, $x\text{Si}(20-x)\text{Zn}$, $x\text{Ba}(40-x)\text{Si}$ and $x\text{Ba}(10-x)\text{Al}$ inversely correlates with increasing average Q^n/N ratio, however brittleness and ν exhibit linear correlation see fig 6-7 (b) and 6-9(a) and (b).
- 9) Indentation fracture toughness of $x\text{Ba}(10-x)\text{Al}$, $x\text{Ba}(40-x)\text{Si}$, $x\text{B}(15-x)\text{Zn}$ and $x\text{Si}(20-x)\text{La}(\text{Sr})$ increased with the increasing average Q^n/N while $x\text{Si}(20-x)\text{Zn}$ series exhibit scatter. The H of $x\text{Ba}(40-x)\text{Si}$ and $x\text{Ba}(10-x)\text{Al}$ equally increased with the increasing average Q^n/N while H of $x\text{Si}(20-x)\text{Zn}$ $x\text{B}(15-x)\text{Zn}$ is fairly constant and the H of $x\text{Si}(20-x)\text{La}(\text{Sr})$ is scattered across the series. E values of $x\text{Ba}(40-x)\text{Si}$ and $x\text{Ba}(10-x)\text{Al}$ seems to increase with the increasing average Q^n/N while $x\text{B}(15-x)\text{Zn}$ and $x\text{Si}(20-x)\text{Zn}$ have fairly constant E and in the case of $x\text{Si}(20-x)\text{La}(\text{Sr})$ E depicts a decreasing trend with the increasing average Q^n/N ratio

- 10) Increasing boron oxide from 10 to 20mol% against zinc oxide in $x\text{B}(15-x)\text{Zn}$ lead to highest indentation fracture toughness, in this series and surprisingly the K_{Ic} values are higher than those glasses containing a fixed 20mol% boron oxide such as $x\text{Ba}(40-x)\text{Si}$ and $x\text{Ba}(10-x)\text{Al}$. Boron oxide is known to increase the fracture toughness of borosilicate glasses but the effect is most clearly seen when boron oxide is swapped with other oxides more than being fixed in the composition.
- 11) The E moduli of all the glasses are higher than or comparable to most normal borosilicate glasses with 60 to 85GPa (Ghosh, Sharma et al. 2010(Vullo and Davis 2004)) and the hardness are higher than or comparable to many sealing glasses in the literature (Rodríguez-López, Wei et al. 2017). See table 7.1 for comparison.

7. Discussion

The glasses and glass-ceramics in this study were investigated to understand the effects of composition on their physical, thermal, electrical and mechanical properties and the potential of using these glasses as SOFC sealing materials. Having considered the different series separately the following discussion compares the series in more detail.

7.1 $x\text{Ba}(40-x)\text{Si}$, $x\text{Ba}(10-x)\text{Al}$, $x\text{B}(15-x)\text{Zn}$, $x\text{Si}(20-x)\text{Zn}$, and $x\text{Si}(20-x)\text{La}(\text{Sr})$ glass and glass-ceramics

In the $x\text{Ba}(40-x)\text{Si}$ and $x\text{Ba}(10-x)\text{Al}$ series additions of BaO led to depolymerisation of the silicate part of the glass network but increased polymerisation of the borate part of the glass network (conversion of BO_3 to BO_4) as indicated by both FTIR and Raman (see figs 4-4, 4-6, 4-9 and 4-10). However, although additions of ZnO to the $x\text{B}(15-x)\text{Zn}$ and $x\text{Si}(20-x)\text{Zn}$ series led to depolymerisation of the silicate network (see figs 4-14 and 4-19), in this case BO_3 to BO_4 conversion did not occur. The differences between the effects of ZnO and BaO on the borate unit can probably be related to the amphoteric nature of Zn^{2+} and thus the role of ZnO is different from that of the alkaline earths despite having similar charges and a similar size to Mg^{2+} in particular according to reports by (Smedskjaer, Youngman et al. 2013). As BaO is added some additional free oxygen is equally added to the glass structure which help converts BO_3 to BO_4 (Lu, Ni et al. 2006) unlike ZnO which may end up in ZnO_4 tetrahedra competing for charge balance with BO_4 and AlO_4 and thus reducing the effective modifier concentration (Smedskjaer, Youngman et al. 2013).

Density increased in all of these series as BaO and ZnO were increased. Meanwhile molar volume increased with increasing BaO in $x\text{Ba}(40-x)\text{Si}$ but decreased in $x\text{Ba}(10-x)\text{Al}$ (see figs 4-1 and 4-7) while the molar volume decreased with increasing ZnO in $x\text{B}(15-x)\text{Zn}$ but increased in $x\text{Si}(20-x)\text{Zn}$ (see figs 4-11 and 4-16). Increase in both molar volume and density with BaO have been previously reported by (Abd El-Moneim, Youssof et al. 2006). ZnO is reported to increase molar volume as seen in the case of $x\text{Si}(20-x)\text{Zn}$ (see reports by (Mohd Sabri Mohd, Mohd Hafiz Mohd et al. 2012). BaO is more effective than ZnO in increasing the molar volume because molar volume increases as the ionic radius of the divalent modifier increases (not atomic weight) eg in the order $\text{Mg}^{2+} > \text{Zn}^{2+} > \text{Ca}^{2+} > \text{Sr}^{2+} > \text{Ba}^{2+}$. This is due to tighter binding between

oxygen and smaller cations (Smedskjaer, Youngman et al. 2013). In addition molar volume of glasses is also atomic packing density dependent as the ionic radii of the modifier increases molar volume increases and therefore packing density defined as the ratio of the minimum fraction of volume occupied by ions and the effective volume of the glass inversely decreases (Rouxel 2006). A different behaviour is observed in the $x\text{Ba}(40-x)\text{Si}$ series as the molar volume both increases and decreases which is not seen in the other series. The molar volume minimum is associated with structural densification and occurred at 22.5mol% BaO which is slightly less than the range $25 < X < 48\text{mol}\%$ in which the molar volume minimum was observed for barium borosilicate by (Bourgel, Malki et al. 2009).

As BaO is increased a decrease in T_g was observed in both $x\text{Ba}(40-x)\text{Si}$ and $x\text{Ba}(10-x)\text{Al}$ series while their TEC increased, the depolymerisation of the silicate sub-network seems to have the dominant effect on these properties. On the other hand the effect of ZnO addition on the T_g and TEC of $x\text{B}(15-x)\text{Zn}$ and $x\text{Si}(20-x)\text{Zn}$ are different because both T_g and TEC increased as ZnO replaced B_2O_3 in the $x\text{B}(15-x)\text{Zn}$ series (fig 4-13) however in $x\text{Si}(20-x)\text{Zn}$ in (fig 4-18) the T_g decreased and the TEC increased as ZnO replaced SiO_2 . The differing effects of ZnO addition on T_g in $x\text{B}(15-x)\text{Zn}$ and $x\text{Si}(20-x)\text{Zn}$ can be explained in relation to the different network formers in $x\text{B}(15-x)\text{Zn}$ and $x\text{Si}(20-x)\text{Zn}$. Therefore as silica has a high T_g so decreasing silica and increasing zinc oxide means a decrease in T_g and of course the opposite is true in the case of decreasing boron oxide and increasing zinc oxide where T_g increased. This also indicates the dominant role the network formers play in the thermal properties. Since the parent glasses are metastable and eventually would crystallise the samples in $x\text{Ba}(40-x)\text{Si}$, $x\text{B}(15-x)\text{Zn}$ and $x\text{Si}(20-x)\text{Zn}$ were heat treated and although the TEC values were lower than those of the parent glasses they all increased as BaO and ZnO increased in all the series measured. The slight reduction in TEC after crystallization is a good sign of thermal stability.

Furthermore the effect of both BaO and ZnO on electrical conductivity is similar as an increase in conductivity with increasing BaO and ZnO is seen in both glass and glass ceramics of all the measured samples. The increase in conductivity is associated with increased mobility of charge carriers in the residual glass due to network disruption (Chen, Zou et al. 2013). In addition the glass ceramics appeared to be more conductive than their parent glasses as indicated by the impedance measurement which shows that the grains are more conductive than the

residual glass, which is found in the grain boundaries in this case (see appendix 1a). Another common feature for all the series is that conductivity and dielectric constant increase with increasing temperature and frequency. The conductivity increases at higher frequencies and the dielectric constant decreases to almost a constant value at higher frequencies. The decrease in dielectric constants in both glasses and glass ceramics is due to the contribution of multi-component polarization such as electronic, ionic, dipolar or orientation and space charge effects as reported by (Morsi, Ibrahim et al. 2016). On the other hand the activation energies for conduction increase in both glass and glass ceramic $x\text{B}(15-x)\text{Zn}$ samples (figs 5-7) while in $x\text{Si}(20-x)\text{Zn}$ the E_a decreased. This suggests that the depolymerisation of the network as ZnO is added is not very severe in $x\text{B}(15-x)\text{Zn}$ compared with $x\text{Si}(20-x)\text{Zn}$ (fig 5-10). There is a similarity between the E_a of $x\text{Ba}(40-x)\text{Si}$ and $x\text{Ba}(10-x)\text{Al}$ glasses as the E_a decreased with BaO addition however in the glass ceramic form the E_a of $x\text{Ba}(40-x)\text{Si}$ increased and this is an indication of conduction pathway blockages by the crystalline phases (see figs 5-1 and 5-4).

As the glass structure was depolymerised by BaO and ZnO additions decreases in H were observed for $x\text{Ba}(40-x)\text{Si}$, $x\text{Ba}(10-x)\text{Al}$, and $x\text{B}(15-x)\text{Zn}$, while the H of $x\text{Si}(20-x)\text{Zn}$ was fairly constant with only a 0.1GPa decrease in the middle data points. In the case $x\text{Si}(20-x)\text{La}(\text{Sr})$ an increasing trend in H was observed as La_2O_3 increased against SiO_2 due to high field strength of La_2O_3 (see figs 6-1, 6-2, 6-3, 6-4 and 6-5). In series $x\text{Ba}(40-x)\text{Si}$, $x\text{B}(15-x)\text{Zn}$ and $x\text{Si}(20-x)\text{Zn}$ the hardness increased to a limited extent after crystallization. Across the $x\text{Ba}(40-x)\text{Si}$ series the increase was 0.1 to 0.3 GPa while across the $x\text{Si}(20-x)\text{Zn}$ series it was 0.5 to 0.6 GPa while for the $x\text{B}(15-x)\text{Zn}$ it was 0.1 to 0.5 GPa. Despite the increase in H of the $x\text{B}(15-x)\text{Zn}$ crystalline samples they exhibit the opposite trend to the parent glass as their H increased as ZnO increased while that of the parent glass exhibit a decreasing trend. This behaviour is not seen in $x\text{Ba}(40-x)\text{Si}$ and $x\text{Si}(20-x)\text{Zn}$ series as they both show the same trend in the hardness in both the parent glass and crystalline glasses. BaO is always reported to decrease H however ZnO behaves differently in different compositions. For example (Doweidar, Zeid et al. 1991) reported an increase in H with increasing ZnO for ternary zinc borophosphate glasses while a decrease in H was observed in binary zinc borates by (Bobkova and Khot'ko 2005). The indentation fracture toughness in $x\text{Ba}(40-x)\text{Si}$ and $x\text{Si}(20-x)\text{Zn}$ initially exhibit a slight increase, while that of $x\text{Ba}(10-x)\text{Al}$ and $x\text{B}(15-x)\text{Zn}$ series showed a decrease, with increasing BaO and ZnO and reducing network formers. However despite the increases in depolymerisation due to La_2O_3

replacing SiO₂ in the xSi(20-x)La(Sr) this series exhibits an overall increasing trend in K_{Ic} (see figs 6-1, 6-2, 6-3, 6-4 and 6-5). A clearly decreasing trend in E is seen in xBa(40-x)Si alone with increasing BaO while the E increases as ZnO and La₂O₃ increase in xB(15-x)Zn, and xSi(20-x)La(Sr) glasses. However the E of xBa(10-x)Al samples exhibits an initial increase with increasing BaO followed by a decrease as expected of BaO additions as E is linearly proportional to field strength and bond strength of the oxides in the glass so increasing BaO with lower field strength decreases the E of the glass (Ghosh, Sharma et al. 2010). While the E of xSi(20-x)Zn is fairly constant with ZnO additions (see figs 6-1, 6-2, 6-3, 6-4 and 6-5). Brittleness generally increased with BaO additions in the xBa(40-x)Si, xBa(10-x)Al series and with additions of ZnO to the xB(15-x)Zn and xSi(20-x)Zn series while La₂O₃ additions to the xSi(20-x)La(Sr) series exhibit decreasing trend. The Poisson's ratio increased with BaO additions in both xBa(40-x)Si and xBa(10-x)Al series and with ZnO in both xB(15-x)Zn and xSi(20-x)Zn series but however with La₂O₃ additions to the xSi(20-x)La(Sr) series ν tends to decrease. This is understandable because as the structure depolymerises and become more open ν tends to increase. As can be seen the ν values for all the series have an inverse correlation with K_{Ic} (compare figs 6-1, 6-2, 6-3, 6-4 and 6-5) with the plot of ν against K_{Ic} in fig 6-7).

From the perspective of TEC (measured between 300-600°C) the TEC of both glass and glass ceramics samples of 20BaSi35, 22.5BaSi32.5, 25BaSi30 mol% and glass samples of xBa(10-x)Al series meet the TEC requirement for SOFCs applications. These materials could be sealed to at least 3 components of the fuel cells namely the yttria stabilized zirconia (YSZ) with a TEC of 10-11×10⁻⁶ K⁻¹, the lanthanum strontium manganite (LSM) cathode with a TEC of 10.5-11×10⁻⁶ K⁻¹ and the metallic interconnector Crofer 22APU with a TEC of 12×10⁻⁶ K⁻¹. The nickel yttria stabilized zirconia (Ni-YSZ) cermet anode has a TEC of 14×10⁻⁶K⁻¹ and so samples 12BaAl8 and 15BaAl5 mol% with TECs of 14.37 and 13.39×10⁻⁶K⁻¹ could be compatible. It is worth noting here that the high TEC of sample 12BaAl8 is due to phase separation in that sample as it shows two T_gs. However the TECs between RT-300 °C of all the samples xB(15-x)Zn, xSi(20-x)Zn, xBa(40-x)Si, xBa(10-x)Al, and xSi(20-x)La(Sr) (as glass and glass ceramics) are not appropriate for sealing to SOFCs but they are compatible for use in sealing to the Ti-6Al-4V alloy used in electrical feed-through connectors in which the sealing glass-ceramics provides electrical insulation for the conducting metal pins and protection for the internal electronics from the outside environment. The TEC of the Ti-6Al-4V is 9.4x10⁻⁶K⁻¹ between 298 -723K and the

TEC of the glass-ceramic is $5.7-9.7 \times 10^{-6} \text{K}^{-1}$ between 303-693K. Kovar which is iron-nickel-cobalt material used as the pin has TEC of $5.2 \times 10^{-6} \text{K}^{-1}$ between 298 and 723K. Therefore, a glass-ceramic with a TEC of $6.9 \times 10^{-6} \text{K}^{-1}$ is optimal to form a compressive sealing with Kovar and Ti-6Al-4V (Staff, Fernie et al. 2016). The measurement of the TEC was limited by the fact that the TMA machine does not allow measurement beyond 650°C and the TEC also increases with temperature as can be seen by comparing the TECs of all the samples between RT-300 and $300-600^\circ\text{C}$ and the averaged TEC from RT- 600°C . However this suggest that increasing the upper limit of measuring temperature (beyond 600°C) could have increased the number of potential candidate sealing glasses in this study and so could be compatible with SOFCs operating above 650°C . See appendix 2 for the comparison between the TEC of this study and the requirement bench mark value of the TEC for SOFCs applications.

In addition to the TEC and as far as the electrical insulation of the sealing glasses for SOFCs are concerned the electrical conductivity in this study for both glass and glass ceramics $x\text{Ba}(40-x)\text{Si}$ and $x\text{B}(15-x)\text{Zn}$ samples, glass $x\text{Ba}(10-x)\text{Al}$ samples and glass ceramic $x\text{Si}(20-x)\text{Zn}$ samples measured at 600°C indicates that all these samples meet the electrical insulation requirements for use as sealant in SOFCs. See table 7.1 for comparison between the conductivity data in this study and the bench mark value given as a requirement for sealing glasses in the literature.

With regards to the mechanical properties although there is no any specified value for the mechanical properties of sealing glasses, coupled with the fact that this study only measured the mechanical properties at room temperature, robustness of the sealing glasses is crucial where the glass is brittle. Structural integrity is a requirement from room temperature during start up and through the thermal cycling back to shut down. The mechanical properties such as hardness, indentation fracture toughness and Young's modulus are higher than most normal borosilicate glasses and are also comparable to some sealing glasses reported in the literature thus indicating that the obtained values are within an acceptable range (see table 7.1) below for comparison between mechanical properties of this study and some data from the literature.

Comparison of mechanical properties						
This study	Normal borosilicate		Other sealing glasses			
	glass	glass ceramic	glass	glass	glass ceramic	
Glass code	$H_v(GPa)$				Refs	
xB(15-x)Zn	5.7-5.9	5.8-6.2	3.9-5.4	3.6-9.1	4.9-8.5	(Yoshida, Tanaka et al. 2001,
xSi(20-x)Zn	5.7-5.8	6.2-6.4				Ghosh, Sharma et al. 2010,
xBa(40-x)Si	5.2-5.7	5.3-6.2				Sellappan, Rouxel et al.
xBa(10-x)Al	4.4-5.4	no				2013),(Rodríguez-López, Wei et al. 2017),
xSi(20-x)La(Sr)	5.8-6.7	no				(Malzbender and Zhao 2012),
	$E(GPa)$					(Abdoli, Alizadeh et al. 2014),
xB(15-x)Zn	87.6-91.6	60-85		61-100	72-108	(Kothiyal, Goswami et al. 2012), (Heydari, Maghsoudipour et al. 2012),(Vullo and Davis 2004).
xSi(20-x)Zn	90.6-91.6					
xBa(40-x)Si	81.2-87.3					
xBa(10-x)Al	70.2-82.1					
xSi(20-x)La(Sr)	88.9-110					
	$K_{Ic}(MNm^{-3/2})$					
xB(15-x)Zn	0.8-0.88	0.46-9.4		0.54-0.9	0.21-1.5	
xSi(20-x)Zn	0.77-0.82					
xBa(40-x)Si	0.69-0.80					
xBa(10-x)Al	0.67-0.87					
xSi(20-x)La(Sr)	0.76-0.88					

Table 7.4: Comparison of mechanical properties in this study and the literature

8. Conclusions and recommendation for future work

One of the challenges which hinders the commercialisation of pSOFCs is the need for long term stable sealants under the operation conditions which include thermal cycle during start up and shut down of the fuel cells in a dual atmosphere environment. Based on the reliability requirements of pSOFCs which includes the robustness of the sealants, the effect of compositions on the mechanical, thermal and electrical properties of different series of glasses have been investigated. It was found that

- 1) The conductivity of all the samples tested are far above the threshold of 10^4 S cm^{-1} fixed for sealing glasses in both glass and glass ceramics see table 7.1
- 2) The E_a for conduction between 500 to 600°C is high for all tested samples, with the glasses having between 128 to 336 kJmol⁻¹ and xBa(10-x)Al glasses having the highest value and 128 to 256 kJmol⁻¹ in the glass ceramics would suggest that all the series tested have met insulation requirements to be used as sealant. Since higher E_a is an indication that more energy is needed to move charge carriers. The slight drop in E_a of the glass ceramics are due to increased conductivity of the crystalline phases see table 7.2 for the E_a of glass and glass ceramic in this study
- 3) Based on the thermal properties measurement the T_g of xB(15-x)Zn, xSi(20-x)Zn, four samples of xBa(40-x)Si except 25BaSi30 and xSi(20-x)La(Sr) are between 650-750°C which suggests that these glasses could be used for intermediate temperature pSOFCs applications. However xBa(10-x)Al series and sample 25BaSi30 could only be used for lower temperature applications because their T_g is below 650°C.
- 4) The TEC between 300 and 600°C for the whole of xBa(10-x)Al series and 20BaSi35, 22.5BaSi32.5 and 25BaSi30 mol% samples and averaged TEC from RT- 600°C for 22.5BaSi32.5 and 25BaSi30 mol% and all xBa(10-x)Al series except 10xBa(10-x)Al10 are optimal to be used for sealing to pSOFCs because they falls within the desirable value for SOFCs with an 8YSZ electrolyte, LSM cathode and ferritic stainless steel interconnectors. Series xB(15-x)Zn glass do not meet this requirement as their TEC falls between 7.9 to $8.8 \times 10^{-6} \text{ C}^{-1}$ though 8.8 is very close to the lower end of the requirement of 9. And xSi(20-x)Zn has met the lower end requirement as 3 samples have 9 to $9.2 \times 10^{-6} \text{ C}^{-1}$. However the TECs for all the xB(15-x)Zn, xSi(20-x)Zn, xBa(40-x)Si, xBa(10-x)Al, and xSi(20-x)La(Sr) glass and glass-ceramics measured between RT-300°C are not appropriate for sealing to SOFCs but

are compatible to be used in sealing Ti-6Al-4V used in electrical feed through connectors see appendix 2 for the TEC of this study and requirement bench bank for SOFCs applications given in the literature.

- 5) The formation of lanthanum borosilicate based phases in these glasses $x\text{B}(15-x)\text{Zn}$, $x\text{Si}(20-x)\text{Zn}$, and $x\text{Ba}(40-x)\text{Si}$ after crystallisation could be advantageous with regards to interfacial and thermal stability as cathode poisoning which a situation where boron in the glass seal attacks lanthanum in the LSM cathode could be avoided.
- 6) considering the properties listed in 1 to 4 above $x\text{Ba}(10-x)\text{Al}$ glasses would be preferred potential candidate for sealing glasses due to the advantage of their lowest T_g and have intermediate Young's moduli between 70-82 GPa this is because thermal stresses develop below T_g and therefore the lower the T_g the better for sealing applications. Secondly thermal stresses that developed during operations is also E dependent as can be seen in equation 2-30. which indicates that higher E could leads to higher thermal stress so the moderate E is preferred. And in trying to heat treat $x\text{Ba}(10-x)\text{Al}$ series it was found that after 50hr that the glass sealed itself to the ceramic floor of the furnace this is an indicator that $x\text{Ba}(10-x)\text{Al}$ series could be sealed to SOFCs component at temperature lower than other samples, which is also additional advantage. However unlike $x\text{B}(15-x)\text{Zn}$, $x\text{Si}(20-x)\text{Zn}$ and $x\text{Ba}(40-x)\text{Si}$ that contained La_2O_3 $x\text{Ba}(10-x)\text{Al}$ series has no La_2O_3 and therefore will not form lanthanum borosilicate phase see item 5 above.
- 7) Generally mechanical properties such as H, E and K_{Ic} are enhance by La_2O_3 addition compared to divalent oxides.
- 8) Some of the glasses in this study ($x\text{B}(15-x)\text{Zn}$, $x\text{Si}(20-x)\text{Zn}$, $x\text{Ba}(40-x)\text{Si}$) have high Poisson's ratios $0.3 < \nu < 0.33$. with the upper limit close to that of metallic glasses $x\text{Ba}(10-x)\text{Al}$ and $x\text{Si}(20-x)\text{La}(\text{Sr})$ glasses have Poisson's ratios of $0.29 < \nu < 0.3$

8.1 Recommendations for future work

- 1) Although sealing glasses are required to be insulating the interactions with other components could lead to degradation of their insulation capacity hence the need to study the interfacial behaviour of the SOFCs components eg the glass/electrolyte and glass/interconnects needs to be studied.
- 2) As suggested by Qi et al 2016, due to chemical compatibility and TEC mismatch issues, it is vital to develop different sealant compositions to match the different parts of the SOFCs system. For example the TEC of the electrolytes (YSZ, GDC, LSGM) lies between 9.5 to $12 \times 10^{-6} \text{K}^{-1}$ while for the cathode the values 12 to $14 \times 10^{-6} \text{K}^{-1}$, for anode it is 10 to $14 \times 10^{-6} \text{K}^{-1}$ and for the interconnectors it is 11 to $15 \times 10^{-6} \text{K}^{-1}$ (Qi, Porotnikova et al. 2016). No single composition could be compatible with all TECs of the different parts but rather two compositions in combination could be.
- 3) Although it is suggested in item 5 of the conclusions above that the formation of lanthanum borosilicate phase could mitigate cathode poisoning, to confirm this assertion there is the need to sinter mix powders of glasses in this study especially samples 20BaSi35, 22.5BaSi32.5, 25BaSi30 mol% and all of $x\text{Ba}(10-x)\text{Al}$ series that have met all the requirement for sealing and commercial powder of the lanthanum containing cathode to see if LaBO_3 will be formed or not.
- 4) There is the need to test the seals that met all the requirements for use as sealing glasses for SOFC in real applications to ascertain their reliability over prolonged periods. And additionally determine the wetting angle which determines the ability of the glass seals to wet and flow prior to sealing using hot stage microscopy.

References:

- Abd El-Moneim, A., I. M. Youssef and L. Abd El-Latif (2006). "Structural role of RO and Al₂O₃ in borate glasses using an ultrasonic technique." Acta Materialia **54**(14): 3811-3819.
- Abdoli, H., P. Alizadeh, D. Boccaccini and K. Agersted (2014). "Fracture toughness of glass sealants for solid oxide fuel cell application." Materials Letters **115**(0): 75-78.
- Adams, R. and P. W. McMillan (1977). "Static fatigue in glass." Journal of Materials Science **12**(4): 643-657.
- Angeli, F., D. Boscarino, S. Gin, G. Della Mea, B. Boizot and J. C. Petit (2001). "Influence of calcium on sodium aluminosilicate glass leaching behaviour." Physics and Chemistry of Glasses **42**(4-5): 279-286.
- Angeli, F., T. Charpentier, E. Molières, A. Soleilhavoup, P. Jollivet and S. Gin (2013). "Influence of lanthanum on borosilicate glass structure: A multinuclear MAS and MQMAS NMR investigation." Journal of Non-Crystalline Solids **376**: 189-198.
- Antolini, E. (2011). "The stability of molten carbonate fuel cell electrodes: A review of recent improvements." Applied Energy **88**(12): 4274-4293.
- Ardelean, I. and M. Toderas (2006). FTIR structural investigation of 3B 2 O 3 -BaO glass matrix containing manganese ions. **8**: 1118-1120.
- Aronne, A., S. Esposito and P. Pernice (1997). "FTIR and DTA study of lanthanum aluminosilicate glasses." Materials Chemistry and Physics **51**(2): 163-168.
- Arora, A., K. Singh and O. P. Pandey (2011). "Thermal, structural and crystallization kinetics of SiO₂-BaO-ZnO-B₂O₃-Al₂O₃ glass samples as a sealant for SOFC." International Journal of Hydrogen Energy **36**(22): 14948-14955.
- Barlet, M., J.-M. Delaye, T. Charpentier, M. Gennisson, D. Bonamy, T. Rouxel and C. L. Rountree (2015). "Hardness and toughness of sodium borosilicate glasses via Vickers's indentations." Journal of Non-Crystalline Solids **417**: 66-79.
- Blum, L., W. A. Meulenber, H. Nabelek and R. Steinberger-Wilckens (2005). "Worldwide SOFC Technology Overview and Benchmark." International Journal of Applied Ceramic Technology **2**(6): 482-492.
- Bobkova, N. M. and S. A. Khot'ko (2005). "Zinc Oxide in Borate Glass-Forming Systems." Glass and Ceramics **62**(5): 167-170.
- Bootjomchai, C., R. Laopaiboon, S. Pencharee and J. Laopaiboon (2014). "Elastic moduli of borosilicate glasses doped with heavy metal oxides." Journal of Non-Crystalline Solids **388**: 37-45.
- Borhan, A. I., M. Gromada, G. G. Nedelcu and L. Leontie (2016). "Influence of (CoO, CaO, B₂O₃) additives on thermal and dielectric properties of BaO-Al₂O₃-SiO₂ glass-ceramic sealant for OTM applications." Ceramics International **42**(8): 10459-10468.
- Bose, S., T. Kuila, T. X. H. Nguyen, N. H. Kim, K.-T. Lau and J. H. Lee (2011). "Polymer membranes for high temperature proton exchange membrane fuel cell: Recent advances and challenges." Progress in Polymer Science **36**(6): 813-843.
- Bourgel, C., M. Malki, M. Simon, P. Bourgel, P. Malki, P. Simon and P. Micoulaut (2009). "Molar volume minimum and adaptative rigid networks in relationship with the intermediate phase in glasses." Physical Review B - Condensed Matter and Materials Physics **79**(2).
- Braunger, M. L., C. A. Escanhoela, I. Fier, L. Walmsley and E. C. Ziemath (2012). "Electrical conductivity of silicate glasses with tetravalent cations substituting Si." Journal of Non-Crystalline Solids **358**(21): 2855-2861.
- Brow, R. K., D. R. Tallant and G. L. Turner (1996). "Raman and B-11 nuclear magnetic resonance spectroscopic studies of alkaline-earth lanthanoborate glasses." Journal of the American Ceramic Society **79**(9): 2410-2416.

Cetinkaya Colak, S., I. Akyuz and F. Atay (2016). "On the dual role of ZnO in zinc-borate glasses." Journal of Non-Crystalline Solids **432, Part B**: 406-412.

Chang, H.-T., C.-K. Lin and C.-K. Liu (2009). "High-temperature mechanical properties of a glass sealant for solid oxide fuel cell." Journal of Power Sources **189**(2): 1093-1099.

Chang, H.-T., C.-K. Lin and C.-K. Liu (2010). "Effects of crystallization on the high-temperature mechanical properties of a glass sealant for solid oxide fuel cell." Journal of Power Sources **195**: 3159-3165.

Chang, H. T., C. K. Lin, C. K. Liu and S. H. Wu (2011). "High-temperature mechanical properties of a solid oxide fuel cell glass sealant in sintered forms." Journal of Power Sources **196**(7): 3583-3591.

Chen, J., Q. Zou, F. Zeng, S. Wang, D. Tang, H. Yang and T. Zhang (2013). "Tailoring the sealing properties of TiO₂-CaO-SrO-B₂O₃-SiO₂ glass-ceramic seals: Thermal properties, chemical compatibility and electrical property." Journal of Power Sources **241**(Supplement C): 578-582.

Cheng, K. (1999). "A Criterion for Evaluating the Thermal Stability of Glasses." The Journal of Physical Chemistry B **103**(39): 8272-8276.

Cheng, K. (2001). "Evaluation of crystallization kinetics of glasses by non-isothermal analysis." Journal of Materials Science **36**(4): 1043-1048.

Choi, S. R. and N. P. Bansal (2008). Mechanical Properties of SOFC Seal Glass Composites. Advances in Solid Oxide Fuel Cells: Ceramic Engineering and Science Proceedings, John Wiley & Sons, Inc.: 275-283.

Chou, Y.-S., J. W. Stevenson and P. Singh (2007). "Novel refractory alkaline earth silicate sealing glasses for planar solid oxide fuel cells." Journal of the Electrochemical Society **154**(7): B644-B651.

Chou, Y. S., J. W. Stevenson and L. A. Chick (2002). "Ultra-low leak rate of hybrid compressive mica seals for solid oxide fuel cells." Journal of Power Sources **112**: 130-136.

Chovanec, J., D. Galusek, J. Ráheř and P. Šajgalík (2012). "Low loss alumina dielectrics by aqueous tape casting: The influence of composition on the loss tangent." Ceramics International **38**(5): 3747-3755.

Coillot, D., F. O. Méar, H. Nonnet and L. Montagne (2012). "New viscous sealing glasses for electrochemical cells." International Journal of Hydrogen Energy **37**(11): 9351-9358.

Colomban, P. (2003). "Polymerization degree and Raman identification of ancient glasses used for jewelry, ceramic enamels and mosaics." Journal of Non-Crystalline Solids **323**(1-3): 180-187.

Connelly, A. J., R. J. Hand, P. A. Bingham and N. C. Hyatt (2011). "Mechanical properties of nuclear waste glasses." Journal of Nuclear Materials **408**(2): 188-193.

Cui, L., X. Hao, Y. Tang, Z. Zheng, Y. Yuan and A. Lu (2015). "Effect of B₂O₃ on physical properties of LZAS vitrified bond and mechanical properties of diamond composites." International Journal of Refractory Metals and Hard Materials **52**: 50-54.

Darwish, H. and M. M. Gomaa (2006). "Effect of compositional changes on the structure and properties of alkali-alumino borosilicate glasses." Journal of Materials Science: Materials in Electronics **17**(1): 35-42.

DeGuire, M. R. and S. D. Brown (1984). "Dependence of Young's Modulus on Volume and Structure in Alkali Silicate and Alkali Aluminosilicate Glasses." Journal of the American Ceramic Society **67**(4): 270-273.

Dimitrov, V. and T. Komatsu (2012). "Correlation among electronegativity, cation polarizability, optical basicity and single bond strength of simple oxides." Journal of Solid State Chemistry **196**(Supplement C): 574-578.

Donald, I. (1989). "Methods for improving the mechanical properties of oxide glasses." Journal of Materials Science **24**(12): 4177-4208.

Donald, I. W. (1993). "Preparation, properties and chemistry of glass- and glass-ceramic-to-metal seals and coatings." Journal of Materials Science **28**: 2841-2886.

Donald, I. W., B. L. Metcalfe and L. A. Gerrard (2008). "Interfacial reactions in glass-ceramic-to-metal seals." Journal of the American Ceramic Society **91**: 715-720.

Donald, W. (2000). GLASS TO METAL SEALS.

Doweidar, H., Y. M. Moustafa, S. Abd El-Maksoud and H. Silim (2001). "Properties of Na₂O–Al₂O₃–B₂O₃ glasses." Materials Science and Engineering: A **301**(2): 207-212.

Doweidar, H., M. A. A. Zeid and G. M. El-Damrawy (1991). "Effect of gamma radiation and thermal treatment on some physical properties of ZnO-PbO-B₂O₃ glasses." Journal of Physics D: Applied Physics **24**(12): 2222.

Duffy, J. A. (2002). "The electronic polarisability of oxygen in glass and the effect of composition." Journal of Non-Crystalline Solids **297**(2): 275-284.

Eagan, R. J. and J. C. Swearengen (1978). "Effect of Composition on the Mechanical Properties of Aluminosilicate and Borosilicate Glasses." Journal of the American Ceramic Society **61**(1-2): 27-30.

Eden, M. (2012). "NMR studies of oxide-based glasses." Annual Reports Section "C" (Physical Chemistry) **108**(1): 177-221.

Edén, M. (2011). "The split network analysis for exploring composition–structure correlations in multi-component glasses: I. Rationalizing bioactivity-composition trends of bioglasses." Journal of Non-Crystalline Solids **357**(6): 1595-1602.

Edén, M., P. Sundberg and C. Stålhandske (2011). "The split network analysis for exploring composition–structure correlations in multi-component glasses: II. Multinuclear NMR studies of alumino-borosilicates and glass-wool fibers." Journal of Non-Crystalline Solids **357**(6): 1587-1594.

El Hayek, R., F. Ferey, P. Florian, A. Pisch and D. R. Neuville "Structure and properties of lime aluminoborate glasses." Chemical Geology.

Eldin, F. M. E. and N. A. El Alaily (1998). "Electrical conductivity of some alkali silicate glasses." Materials Chemistry and Physics **52**(2): 175-179.

Fergus, J. W. (2005). "Sealants for solid oxide fuel cells." Journal of Power Sources **147**: 46-57.

Fergus, J. W. (2006). "Electrolytes for solid oxide fuel cells." Journal of Power Sources **162**(1): 30-40.

Friauf, J. B. (1961). "Fuel cells." Advanced Energy Conversion **1**(C): 9-18.

Ganvir, V. Y. and R. S. Gedam (2017). "Effect of La₂O₃ addition on structural and electrical properties of sodium borosilicate glasses." Materials Research Express **4**(3): 035204.

Garland, N. L., D. C. Papageorgopoulos and J. M. Stanford (2012). "Hydrogen and Fuel Cell Technology: Progress, Challenges, and Future Directions." Energy Procedia **28**: 2-11.

Ghosh, S., A. Das Sharma, P. Kundu, S. Mahanty and R. N. Basu (2008). "Development and characterizations of BaO–CaO–Al₂O₃–SiO₂ glass–ceramic sealants for intermediate temperature solid oxide fuel cell application." Journal of Non-Crystalline Solids **354**(34): 4081-4088.

Ghosh, S., S. Das Sharma, S. Kundu and S. Basu (2008). "Glass-ceramic sealants for planar IT-SOFC: A bilayered approach for joining electrolyte and metallic interconnect." Journal of the Electrochemical Society **155**(5): B473-B478.

Ghosh, S., P. Kundu, A. Das Sharma, R. N. Basu and H. S. Maiti (2008). "Microstructure and property evaluation of barium aluminosilicate glass-ceramic sealant for anode-supported solid oxide fuel cell." Journal of the European Ceramic Society **28**: 69-76.

Ghosh, S., A. D. Sharma, P. Kundu and R. N. Basu (2008). "Glass-based Sealants for Application in Planar Solid Oxide Fuel Cell Stack." Transactions of the Indian Ceramic Society **67**(4): 161-182.

Ghosh, S., A. D. Sharma, A. K. Mukhopadhyay, P. Kundu and R. N. Basu (2010). "Effect of BaO addition on magnesium lanthanum aluminoborosilicate-based glass-ceramic sealant for anode-supported solid oxide fuel cell." International Journal of Hydrogen Energy **35**(1): 272-283.

Gödeke, D. and U. Dahlmann (2011). "Study on the crystallization behaviour and thermal stability of glass-ceramics used as solid oxide fuel cell-sealing materials." Journal of Power Sources **196**(21): 9046-9050.

Goel, A., D. U. Tulyaganov, A. M. Ferrari, E. R. Shaaban, A. Prange, F. Bondioli and J. M. F. Ferreira (2010). "Structure, Sintering, and Crystallization Kinetics of Alkaline-Earth Aluminosilicate Glass-Ceramic Sealants for Solid Oxide Fuel Cells." Journal of the American Ceramic Society **93**: 830-837.

Goel, A., D. U. Tulyaganov, V. V. Kharton, A. A. Yaremchenko, S. Agathopoulos and J. M. F. Ferreira (2007). "Effect of BaO addition on crystallization, microstructure, and properties of diopside-Ca-Tschermak clinopyroxene-based glass-ceramics." Journal of the American Ceramic Society **90**(7): 2236-2244.

Goel, A., D. U. Tulyaganov, V. V. Kharton, A. A. Yaremchenko, S. Eriksson and J. M. F. Ferreira (2009). "Optimization of La₂O₃-containing diopside based glass-ceramic sealants for fuel cell applications." Journal of Power Sources **189**(2): 1032-1043.

Goel, A., D. U. Tulyaganov, V. V. Kharton, A. A. Yaremchenko and J. M. F. Ferreira (2008). "The effect of Cr₂O₃ addition on crystallization and properties of La₂O₃-containing diopside glass-ceramics." Acta Materialia **56**(13): 3065-3076.

Goel, A., D. U. Tulyaganov, V. V. Kharton, A. A. Yaremchenko and J. M. F. Ferreira (2010). "Electrical behavior of aluminosilicate glass-ceramic sealants and their interaction with metallic solid oxide fuel cell interconnects." Journal of Power Sources **195**(2): 522-526.

Goel, A., D. U. Tulyaganov, E. R. Shaaban, R. N. Basu and J. M. F. Ferreira (2008). "Influence of ZnO on the crystallization kinetics and properties of diopside-Ca-Tschermak based glasses and glass-ceramics." Journal of Applied Physics **104**(4).

Gohar, I. A., H. Doweidar, R. M. Elshazly, A. A. Megahed and M. S. Meikhal (1990). "The formation of BO₄ – tetrahedra and nonbridging oxygen ions in borosilicate glasses with low silica content." Journal of Materials Science **25**(2): 1497-1502.

Gomaa, M. M., H. A. Abo-Mosallam and H. Darwish (2009). "Electrical and mechanical properties of alkali barium titanium alumino borosilicate glass-ceramics containing strontium or magnesium." Journal of Materials Science: Materials in Electronics **20**(6): 507-516.

Grandjean, A., M. Malki, C. Simonnet, D. Manara and B. Penelon (2007). "Correlation between electrical conductivity, viscosity, and structure in borosilicate glass-forming melts." Physical Review B **75**(5): 054112.

Greaves, G. N., A. L. Greer, R. S. Lakes and T. Rouxel (2011). "Poisson's ratio and modern materials." Nat Mater **10**(11): 823-837.

Gülzow, E. (2004). "Alkaline Fuel Cells." Fuel Cells **4**(4): 251-255.

Ha, M. T. and S. H. Garofalini (2017). "Local structure of network modifier to network former ions in soda-lime alumino-borosilicate glasses." Journal of the American Ceramic Society **100**(2): 563-573.

Hand, R. J. and D. R. Tadjiev (2010). "Mechanical properties of silicate glasses as a function of composition." Journal of Non-Crystalline Solids **356**(44–49): 2417-2423.

Hao, J., Q. Zan, D. Ai, J. Ma, C. Deng and J. Xu (2012). "Structure and high temperature physical properties of glass seal materials in solid oxide electrolysis cell." Journal of Power Sources **214**: 75-83.

Haseli, Y. (2018). "Maximum conversion efficiency of hydrogen fuel cells." International Journal of Hydrogen Energy **43**(18): 9015-9021.

Häßler, J. and C. Rüssel (2017). "Effect of microstructure of a phase separated sodium-borosilicate glass on mechanical properties." Ceramics International **43**(14): 11403-11409.

Hehlen, B., D. R. Neuville, D. Kilymis and S. Ispas (2017). "Bimodal distribution of Si–O–Si angles in sodosilicate glasses." Journal of Non-Crystalline Solids **469**: 39-44.

Heydari, F., A. Maghsoudipour, Z. Hamnabard and S. Farhangdoust (2012). "Mechanical properties and microstructure characterization of zirconia nanoparticles glass composites for SOFC sealant." Materials Science and Engineering: A **552**: 119-124.

Higazy, A. A. and B. Bridge (1985). "Elastic constants and structure of the vitreous system CO₃O₄-P₂O₅." Journal of Non-Crystalline Solids **72**(1): 81-108.

Hirao, K., J. Matsuoka and N. Saga (1989). "Inelastic deformation and structure of borate glasses." Journal of Non-Crystalline Solids **112**(1): 336-340.

Hirao, K., M. Yoshimoto, N. Soga and K. Tanaka (1991). "Densification of magnesium and calcium metaphosphate glasses." Journal of Non-Crystalline Solids **130**(1): 78-84.

Hosseini, S. M., T. Shvareva and A. Navrotsky (2013). "Energetics of lanthanum silicate apatite: Influence of interstitial oxygen and cation vacancy concentrations in $\text{La}_{9.33+x}(\text{SiO}_4)_6\text{O}_{2+3x/2}$ and $\text{La}_{10-x}\text{Sr}_x(\text{SiO}_4)_6\text{O}_{3-0.5x}$." Solid State Ionics **233**: 62-66.

Hsiu-Tao Chang, C.-k. I., Chien-kuo Liu (2009). High Temperature Mechanical Properties of a Crystallized BaO-B₂O₃-Al₂O₃-SiO₂ Glass Ceramic for SOFC. ASME 2009. Newport Beach, California, U S A.

Huang, J., F. Xie, C. Wang and Z. Mao (2012). "Development of solid oxide fuel cell materials for intermediate-to-low temperature operation." International Journal of Hydrogen Energy **37**(1): 877-883.

Hubert, M. and A. J. Faber (2014). "On the structural role of boron in borosilicate glasses." Physics and Chemistry of Glasses-European Journal of Glass Science and Technology Part B **55**(3): 136-158.

Hwa, L. G. and W. C. Chao (2005). "Velocity of sound and elastic properties of lanthanum gallogermanate glasses." Materials Chemistry and Physics **94**(1): 37-41.

Inaba, S., S. Fujino and K. Morinaga (1999). "Young's Modulus and Compositional Parameters of Oxide Glasses." Journal of the American Ceramic Society **82**(12): 3501-3507.

Ingram, M. D. (1989). "A new mechanism of ionic conduction in glass." Materials Chemistry and Physics **23**(1): 51-61.

Jiadong, Z., L. Ming, S. D. C., J. Wook and R. Jürgen (2014). "Impedance Spectroscopy of (Bi_{1/2}Na_{1/2})TiO₃-BaTiO₃ Ceramics Modified with (K_{0.5}Na_{0.5})NbO₃." Journal of the American Ceramic Society **97**(5): 1523-1529.

Kaky, K. M., G. Lakshminarayana, S. O. Baki, Y. H. Taufiq-Yap, I. V. Kityk and M. A. Mahdi (2017). "Structural, thermal, and optical analysis of zinc boro-aluminosilicate glasses containing different alkali and alkaline modifier ions." Journal of Non-Crystalline Solids **456**: 55-63.

Kato, Y., H. Yamazaki, S. Yoshida and J. Matsuoka (2010). "Effect of densification on crack initiation under Vickers indentation test." Journal of Non-Crystalline Solids **356**(35): 1768-1773.

Kaur, G., O. P. Pandey and K. Singh (2012). "Chemical interaction study between lanthanum based different alkaline earth glass sealants with Crofer 22 APU for solid oxide fuel cell applications." International Journal of Hydrogen Energy **37**(4): 3883-3889.

Kaur, G., O. P. Pandey and K. Singh (2012). "Effect of modifiers field strength on optical, structural and mechanical properties of lanthanum borosilicate glasses." Journal of Non-Crystalline Solids **358**: 2589-2596.

Kaur, G., O. P. Pandey and K. Singh (2012). "Interfacial study between high temperature SiO₂-B₂O₃-AO-La₂O₃ (A = Sr, Ba) glass seals and Crofer 22APU for solid oxide fuel cell applications." International Journal of Hydrogen Energy **37**: 6862-6874.

Kaur, G., O. P. Pandey and K. Singh (2014). "Self-Healing Behavior of Barium-Lanthanum-Borosilicate Glass and Its Reactivity with Different Electrolytes for SOFC Applications." International Journal of Applied Ceramic Technology **11**(1): 136-145.

Kaur, R., S. Singh and O. P. Pandey (2012). "FTIR structural investigation of gamma irradiated BaO-Na₂O-B₂O₃-SiO₂ glasses." Physica B: Condensed Matter **407**(24): 4765-4769.

Kerstan, M. and C. Rüssel (2011). "Barium silicates as high thermal expansion seals for solid oxide fuel cells studied by high-temperature X-ray diffraction (HT-XRD)." Journal of Power Sources **196**(18): 7578-7584.

Kharlamova, T., S. Pavlova, V. A. Sadykov, T. Krieger, L. Batuev, V. Muzykantov, O. Lapina, D. Khabibulin, M. Chaikina, N. Uvarov, Y. Pavlukhin, S. Petrov and C. Argirusis (2011). "Doped Apatite Type Lanthanum Silicates: Structure and Property Characterization." MRS Proceedings **1126**.

Khedim, H., H. Nonnet and F. O. Mear (2012). "Development and characterization of glass-ceramic sealants in the (CaO-Al₂O₃-SiO₂-B₂O₃) system for Solid Oxide Electrolyzer Cells." Journal of Power Sources **216**: 227-236.

Kidari, A., J. L. Dussossoy, E. Brackx, D. Caurant, M. Magnin and I. Bardez-Giboire (2012). "Lanthanum and Neodymium solubility in simplified $\text{SiO}_2\text{-B}_2\text{O}_3\text{-Na}_2\text{O-Al}_2\text{O}_3\text{-CaO}$ high level waste glass." Journal of the American Ceramic Society **95**(8): 2537-2544.

Kingery, W. D. (1961). "Introduction to Ceramics (Kingery, W. D.)." Journal of Chemical Education **38**(8): A548.

Kline, J., M. Tangstad and G. Tranell (2015). "A Raman Spectroscopic Study of the Structural Modifications Associated with the Addition of Calcium Oxide and Boron Oxide to Silica." Metallurgical and Materials Transactions B **46**(1): 62-73.

Knauth, P. and H. L. Tuller (2002). "Solid-State Ionics: Roots, Status, and Future Prospects." Journal of the American Ceramic Society **85**(7): 1654-1680.

Kohnke, H. J. (2011). "Alkaline Fuel Cells." Chem. Ing. Tech. **83**(11): 2027-2035.

Konijnendijk, W. L. and J. M. Stevels (1976). "The structure of borosilicate glasses studied by Raman scattering." Journal of Non-Crystalline Solids **20**(2): 193-224.

Kothiyal, G., M. Goswami, B. Tiwari, K. Sharma, A. Ananthanarayanan and L. Montagne (2012). "Some recent studies on glass/glass-ceramics for use as sealants with special emphasis for high temperature applications." Journal of Advanced Ceramics **1**(2): 110-129.

Kumar, V., A. Arora, O. P. Pandey and K. Singh (2008). "Studies on thermal and structural properties of glasses as sealants for solid oxide fuel cells." International Journal of Hydrogen Energy **33**: 434-438.

Kumar, V., O. P. Pandey and K. Singh (2010). "Structural and optical properties of barium borosilicate glasses." Physica B: Condensed Matter **405**(1): 204-207.

Kumar, V., Rupali, O. P. Pandey and K. Singh (2011). "Thermal and crystallization kinetics of yttrium and lanthanum calcium silicate glass sealants for solid oxide fuel cells." International Journal of Hydrogen Energy **36**(22): 14971-14976.

Kupracz, P., A. Lenarciak, M. Łapiński, M. Przeźniak-Welenc, N. A. Wójcik and R. J. Barczyński (2017). "Polaron hopping conduction in manganese borosilicate glass." Journal of Non-Crystalline Solids **458**(Supplement C): 15-21.

Kupracz, P., N. A. Szreder, M. Gazda, J. Karczewski and R. J. Barczyński (2014). "Phase Separation and Electrical Properties of Manganese Borosilicate Glasses." Procedia Engineering **98**: 71-77.

Lahl, N., K. Singh, L. Singheiser, K. Hilpert and D. Bahadur (2000). "Crystallisation kinetics in $\text{AO-Al}_2\text{O}_3\text{-SiO}_2\text{-B}_2\text{O}_3$ glasses (A = Ba, Ca, Mg)." Journal of Materials Science **35**: 3089-3096.

Laorodphan, N., P. Namwong, W. Thiemsorn, M. Jaimasith, A. Wannagon and T. Chairuang Sri (2009). "A low silica, barium borate glass-ceramic for use as seals in planar SOFCs." Journal of Non-Crystalline Solids **355**(1): 38-44.

Lara, C., M. J. Pascual, R. Keding and A. Duran (2006). "Electrical behaviour of glass-ceramics in the systems RO-BaO-SiO_2 (R = Mg, Zn) for, sealing SOFCs." Journal of Power Sources **157**(1): 377-384.

Larsen, P. H. and P. F. James (1998). "Chemical stability of $\text{MgO/CaO/Cr}_2\text{O}_3\text{-Al}_2\text{O}_3\text{-B}_2\text{O}_3\text{-phosphate}$ glasses in solid oxide fuel cell environment." Journal of Materials Science **33**: 2499-2507.

Larsen, P. H., F. W. Poulsen and R. W. Berg (1999). "The influence of SiO_2 addition to $2\text{MgO-Al}_2\text{O}_3\text{-3.3P}_2\text{O}_5$ glass." Journal of Non-Crystalline Solids **244**(1): 16-24.

Lei, D., Z. Wang, J. Li, J. Li and Z. Wang (2012). "Experimental study of glass to metal seals for parabolic trough receivers." Renewable Energy **48**: 85-91.

Leslie, H. (1964). The properties of glass surfaces. London, London : Chapman & Hall, 1964.

Lessing, P. A. (2007). "A review of sealing technologies applicable to solid oxide electrolysis cells." Journal of Materials Science **42**: 3465-3476.

Lewandowski, J. J., W. H. Wang and A. L. Greer (2005). "Intrinsic plasticity or brittleness of metallic glasses." Philosophical Magazine Letters **85**(2): 77-87.

Ley, K. L., M. Krumpelt, R. Kumar, J. H. Meiser and J. Bloom (1996). "Glass-ceramic sealants for solid oxide fuel cells .1. Physical properties." Journal of Materials Research **11**: 1489-1493.

Li, H. M., C. H. Ra, G. Zhang, W. J. Yoo, K. W. Lee and J. D. Kim (2009). "Frequency and temperature dependence of the dielectric properties of a PCB substrate for advanced packaging applications." Journal of the Korean Physical Society **54**(3): 1096-1099.

Lim, E.-S., B.-S. Kim, J.-H. Lee and J.-J. Kim (2006). "Dielectric, thermal and sintering behavior of BaO-B₂O₃-SiO₂ glasses with the addition of Al₂O₃." Journal of Electroceramics **17**(2): 359-363.

Lima, M. M. R. A., R. C. C. Monteiro, M. P. F. Graca and M. G. Ferreira da Silva (2012). "Structural, electrical and thermal properties of borosilicate glass-alumina composites." Journal of Alloys and Compounds **538**: 66-72.

Lin, S. E., Y. R. Cheng and W. C. J. Wei (2012). "BaO-B₂O₃-SiO₂-Al₂O₃ sealing glass for intermediate temperature solid oxide fuel cell." Journal of Non-Crystalline Solids **358**(2): 174-181.

Liu, C.-K., K.-F. Lin and R.-Y. Lee (2015). "Effects of lanthanum-to-calcium ratio on the thermal and crystalline properties of BaO-Al₂O₃-B₂O₃-SiO₂ based glass sealants for solid oxide fuel cells." Journal of the Ceramic Society of Japan **123**(1436): 239-244.

Liu, H., J. Huang, D. Zhao, H. Yang and T. Zhang (2016). "Improving the electrical property of CeO₂-containing sealing glass-ceramics for Solid Oxide Fuel Cell applications: Effect of HfO₂." Journal of the European Ceramic Society **36**(3): 917-923.

Liu, S., G. Zhao, H. Ying, J. Wang and G. Han (2008). "Effects of mixed alkaline earth oxides additive on crystallization and structural changes in borosilicate glasses." Journal of Non-Crystalline Solids **354**(10): 956-961.

Liu, W., X. Sun and M. A. Khaleel (2008). "Predicting Young's modulus of glass/ceramic sealant for solid oxide fuel cell considering the combined effects of aging, micro-voids and self-healing." Journal of Power Sources **185**: 1193-1200.

Lopes, A. A. S., R. S. Soares, M. M. A. Lima and R. C. C. Monteiro (2014). "Glass transition and crystallization kinetics of a barium borosilicate glass by a non-isothermal method." Journal of Applied Physics **115**(4).

Lu, C., Y. Ni, Q. Zhang and Z. Xu (2006). "NMR Study on Structural Characteristics of Rare Earth Doped Boro-Alumino-Silicate Glasses." Journal of Rare Earths **24**(4): 413-417.

Luo, D. and Z. Shen (2009). "Wetting and spreading behavior of borosilicate glass on Kovar." Journal of Alloys and Compounds **477**(1): 407-413.

Luo, L., Y. Lin, Z. Huang, Y. Wu, L. Sun, L. Cheng and J. Shi (2015). "Application of BaO-CaO-Al₂O₃-B₂O₃-SiO₂ glass-ceramic seals in large size planar IT-SOFC." Ceramics International **41**(8): 9239-9243.

Mahapatra, M. K. and K. Lu (2010). "Glass-based seals for solid oxide fuel and electrolyzer cells - A review." Materials Science & Engineering R-Reports **67**: 65-85.

Mahapatra, M. K. and K. Lu (2010). "Seal glass for solid oxide fuel cells." Journal of Power Sources **195**: 7129-7139.

Mahapatra, M. K., K. Lu and R. J. Bodnar (2009). "Network structure and thermal property of a novel high temperature seal glass." Applied Physics a-Materials Science & Processing **95**: 493-500.

Mahapatra, M. K., K. Lu and W. T. Reynolds Jr (2008). "Thermophysical properties and devitrification of SrO-La₂O₃-Al₂O₃-B₂O₃-SiO₂-based glass sealant for solid oxide fuel/electrolyzer cells." Journal of Power Sources **179**(1): 106-112.

Mahato, N., A. Banerjee, A. Gupta, S. Omar and K. Balani (2015). "Progress in material selection for solid oxide fuel cell technology: A review." Progress in Materials Science **72**: 141-337.

Maji, B. K., H. Jena and R. Asuvathraman (2016). "Electrical conductivity and glass transition temperature (T_g) measurements on some selected glasses used for nuclear waste immobilization." Journal of Non-Crystalline Solids **434**: 102-107.

Malzbender, J. and Y. Zhao (2012). "Flexural Strength and Viscosity of Glass Ceramic Sealants for Solid Oxide Fuel Cell Stacks." Fuel Cells **12**: 47-53.

Malzbender, J. and Y. Zhao (2012). "Micromechanical testing of glass-ceramic sealants for solid oxide fuel cells." Journal of Materials Science **47**: 4342-4347.

Malzbender, J., Y. Zhao and T. Beck (2014). "Fracture and creep of glass-ceramic solid oxide fuel cell sealant materials." Journal of Power Sources **246**(0): 574-580.

Manara, D., A. Grandjean and D. R. Neuville (2009). "Advances in understanding the structure of borosilicate glasses: A Raman spectroscopy study." American Mineralogist **94**(5-6): 777-784.

Manara, D., A. Grandjean and D. R. Neuville (2009). "Structure of borosilicate glasses and melts: A revision of the Yun, Bray and Dell model." Journal of Non-Crystalline Solids **355**(50-51): 2528-2531.

Matsunaga, N., D. W. Rogers and A. A. Zavitsas (2003). "Pauling's Electronegativity Equation and a New Corollary Accurately Predict Bond Dissociation Enthalpies and Enhance Current Understanding of the Nature of the Chemical Bond." The Journal of Organic Chemistry **68**(8): 3158-3172.

Mccauley, R. A. (2000). "Polymorphism and dielectric electric properties of Ba- and Sr-containing feldspars." Journal of Materials Science **35**(15): 3939-3942.

McIntosh, S. and R. J. Gorte (2004). "Direct Hydrocarbon Solid Oxide Fuel Cells." Chemical Reviews **104**(10): 4845-4866.

McMillan, P. (1984). "Structural studies of silicate glasses and melts - Applications and limitations of raman spectroscopy" American Mineralogist **69**(6-8): 622-644.

Méar, F. O., P. G. Yot, A. V. Kolobov, M. Ribes, M.-F. Guimon and D. Gonbeau (2007). "Local structure around lead, barium and strontium in waste cathode-ray tube glasses." Journal of Non-Crystalline Solids **353**(52): 4640-4646.

Medvedev, D. A., J. G. Lyagaeva, E. V. Gorbova, A. K. Demin and P. Tsiakaras (2016). "Advanced materials for SOFC application: Strategies for the development of highly conductive and stable solid oxide proton electrolytes." Progress in Materials Science **75**: 38-79.

Michalske, T. A. and S. W. Freiman (1983). "A Molecular Mechanism for Stress Corrosion in Vitreous Silica." Journal of the American Ceramic Society **66**(4): 284-288.

Milhans, J., M. Khaleel, X. Sun, M. Tehrani, M. Al-Haik and H. Garmestani (2010). "Creep properties of solid oxide fuel cell glass-ceramic seal G18." Journal of Power Sources **195**(11): 3631-3635.

Milhans, J., D. S. Li, M. Khaleel, X. Sun, M. S. Al-Haik, A. Harris and H. Garmestani (2011). "Mechanical properties of solid oxide fuel cell glass-ceramic seal at high temperatures." Journal of Power Sources **196**: 5599-5603.

Minh, N. Q. (1993). "Ceramic Fuel Cells." Journal of the American Ceramic Society **76**(3): 563-588.

Minh, N. Q. (1993). "Ceramic fuel cells." Journal of the American Ceramic Society **76**(3).

Mishra, R. K., R. Mishra, C. P. Kaushik, A. K. Tyagi, B. S. Tomar, D. Das and K. Raj (2009). "Ionic transport behavior of BaO containing sodium borosilicate glasses." Journal of Hazardous Materials **161**(2): 1450-1453.

Mohajerani, A. and J. W. Zwanziger (2012). "Mixed alkali effect on Vickers hardness and cracking." Journal of Non-Crystalline Solids **358**(12-13): 1474-1479.

Mohd Sabri Mohd, G., Z. Mohd Hafiz Mohd, Z. Azmi, A. Sidek Hj. Abdul and M. Khamirul Amin (2012). "Effect of ZnO on the Physical Properties and Optical Band Gap of Soda Lime Silicate Glass." International Journal of Molecular Sciences **13**(6): 7550-7558.

Moridi, G. R., A. Nouruzi and C. A. Hogarth (1991). "Electrical properties of barium-borosilicate glasses." Journal of Materials Science **26**(23): 6271-6274.

Morsi, R. M. M., S. Ibrahim, S. Abo-Naf and M. M. Morsi (2016). "Effect of alkaline earth metal oxides on the dielectric, structural and physico-chemical properties of lithium-zinc-lead-borates." Journal of Materials Science: Materials in Electronics **27**(4): 4147-4156.

Mysen, B. O., L. W. Finger, D. Virgo and F. A. Seifert (1982). "Curve-fitting of Raman spectra of silicate glasses." American Mineralogist **67**(7-8): 686-695.

Neyret, M., M. Lenoir, A. Grandjean, N. Massoni, B. Penelon and M. Malki (2015). "Ionic transport of alkali in borosilicate glass. Role of alkali nature on glass structure and on ionic conductivity at the glassy state." Journal of Non-Crystalline Solids **410**: 74-81.

Nguyen, H. V. P., S. A. Song, D. N. Park, H. C. Ham, J. Han, S. P. Yoon, M. R. Othman and J. Kim (2012). "Improved molten carbonate fuel cell performance via reinforced thin anode." International Journal of Hydrogen Energy **37**(21): 16161-16167.

Nicoleau, E., F. Angeli, S. Schuller, T. Charpentier, P. Jollivet and M. Moskura (2016). "Rare-earth silicate crystallization in borosilicate glasses: Effect on structural and chemical durability properties." Journal of Non-Crystalline Solids **438**: 37-48.

Nielsen, K. A., M. Solvang, S. B. L. Nielsen, A. R. Dinesen, D. Beeff and P. H. Larsen (2007). "Glass composite seals for SOFC application." Journal of the European Ceramic Society **27**(2-3): 1817-1822.

Nonnet, H., H. Khedim and F. Méar (2012). "Development and characterisation of glass and glass ceramic sealants for solid oxide electrolyser cells." International Journal of Ionics The Science and Technology of Ionic Motion **18**(5): 441-447.

Ohara, S., K. Mukai, T. Fukui, Y. Sakaki, M. Hattori and Y. Esaki (2001). "A new sealant material for solid oxide fuel cells using glass-ceramic." Journal of the Ceramic Society of Japan **109**: 186-190.

Ojha, P. K., T. K. Chongdar, N. M. Gokhale and A. R. Kulkarni (2011). "Investigation of crystallization kinetic of SrO-La₂O₃-Al₂O₃-B₂O₃-SiO₂ glass and its suitability for SOFC sealant." International Journal of Hydrogen Energy **36**(22): 14996-15001.

Ojha, P. K., S. K. Rath, T. K. Chongdar, N. M. Gokhale and A. R. Kulkarni (2011). "Physical and thermal behaviour of Sr-La-Al-B-Si based SOFC glass sealants as function of SrO content and B₂O₃/SiO₂ ratio in the matrix." Journal of Power Sources **196**: 4594-4598.

Ojha, P. K., S. K. Rath, S. K. Sharma, K. Sudarshan, P. K. Pujari, T. K. Chongdar and N. M. Gokhale (2015). "Free volume of mixed cation borosilicate glass sealants elucidated by positron annihilation lifetime spectroscopy and its correlation with glass properties." Journal of Power Sources **273**: 937-944.

Osaka, A., H. Oda and K. Takahashi (1986). "Constitution of Alkaline Earth Aluminoborate Glasses." Yogyo Kyokaishi **94**: 849-855.

Pal, I., A. Agarwal, S. Sanghi, A. Sheoran and N. Ahlawat (2009). "Conductivity and dielectric relaxation in sodium borosulfate glasses." Journal of Alloys and Compounds **472**(1): 40-45.

Park, M., J.-S. Shin, S. Lee, H.-J. Kim, H. An, H.-i. Ji, H. Kim, J.-W. Son, J.-H. Lee, B.-K. Kim, H.-W. Lee and K. J. Yoon (2018). "Thermal degradation mechanism of ferritic alloy (Crofer 22 APU)." Corrosion Science **134**: 17-22.

Parkinson, B. G., D. Holland, M. E. Smith, C. Larson, J. Doerr, M. Affatigato, S. A. Feller, A. P. Howes and C. R. Scales (2008). "Quantitative measurement of Q₃ species in silicate and borosilicate glasses using Raman spectroscopy." Journal of Non-Crystalline Solids **354**(17): 1936-1942.

Pascuta, P. and E. Culea (2011). "Structural and thermal properties of some zinc borate glasses containing gadolinium ions." Journal of Materials Science: Materials in Electronics **22**(8): 1060-1066.

Pask, J. A., Tomsia, A. P. (1991). "Wetting, Surface Energies, Adhesion, and Interface Reaction Thermodynamics." Engineered Materials Handbook **4**: 482-492.

Peighambardoust, S. J., S. Rowshanzamir and M. Amjadi (2010). "Review of the proton exchange membranes for fuel cell applications." International Journal of Hydrogen Energy **35**(17): 9349-9384.

Pönitzsch, A., M. Nofz, L. Wondraczek and J. Deubener (2016). "Bulk elastic properties, hardness and fatigue of calcium aluminosilicate glasses in the intermediate-silica range." Journal of Non-Crystalline Solids **434**: 1-12.

Prasad, A. and A. Basu (2013). "Dielectric and impedance properties of sintered magnesium aluminum silicate glass-ceramic." Journal of Advanced Ceramics **2**(1): 71-78.

Puig, J., F. Ansart, P. Lenormand, R. Conradt and S. Gross-Barsnick (2016). "Development of barium boron aluminosilicate glass sealants using a sol–gel route for solid oxide fuel cell applications." Full Set - Includes 'Journal of Materials Science Letters' **51**(2): 979-988.

Qi, S., N. M. Porotnikova, M. V. Ananyev, A. V. Kuzmin, V. A. Eremin, A. A. Pankratov, N. G. Molchanova, O. G. Reznitskikh, A. S. Farlenkov, E. G. Vovkotrub and Y. P. Zaikov (2016). "High-temperature glassy-ceramic sealants $\text{SiO}_2\text{—Al}_2\text{O}_3\text{—BaO—MgO}$ and $\text{SiO}_2\text{—Al}_2\text{O}_3\text{—ZrO}_2\text{—CaO—Na}_2\text{O}$ for solid oxide electrochemical devices." Transactions of Nonferrous Metals Society of China **26**(11): 2916-2924.

Qi, Z., F. Lihua, S. Jie, P. M. J. and Z. Teng (2015). "Tuning the Interfacial Reaction Between Bismuth-Containing Sealing Glasses and Cr-Containing Interconnect: Effect of ZnO." Journal of the American Ceramic Society **98**(12): 3797-3806.

Quinn, G. D. and R. C. Bradt (2007). "On the Vickers Indentation Fracture Toughness Test." Journal of the American Ceramic Society **90**(3): 673-680.

Rai, M. and G. Mountjoy (2014). "Molecular dynamics modelling of the structure of barium silicate glasses BaO—SiO_2 ." Journal of Non-Crystalline Solids **401**: 159-163.

Ravagnani, C., R. Keding and C. Russel (2003). "High temperature impedance spectroscopy of homogeneous and phase separated melts and glasses of the composition 48.5SiO_2 center dot $48.5\text{B}_2\text{O}_3$ center dot $3\text{Na}_2\text{O}$." Journal of Non-Crystalline Solids **328**(1-3): 164-173.

Reddy, A. A., D. Tulyaganov, G. Mather, M. Pascual, V. Kharton, S. Bredikhin, V. A. Kolotygin and J. Ferreira (2014). "Effect of strontium-to-calcium ratio on the structure, crystallization behavior and functional properties of diopside-based glasses." Int. J. Hydrog. Energy **39**(7): 3552-3563.

Reddy, R. R., Y. Nazeer Ahammed, P. Abdul Azeem, K. Rama Gopal and T. V. R. Rao (2001). "Electronic polarizability and optical basicity properties of oxide glasses through average electronegativity." Journal of Non-Crystalline Solids **286**(3): 169-180.

Rehman, I. u. (2013). Vibrational spectroscopy for tissue analysis [electronic resource]. Boca Raton, Boca Raton : CRC Press, c2013.

Reis, S. T. and R. K. Brow (2006). "Designing sealing glasses for solid oxide fuel cells." Journal of Materials Engineering and Performance **15**(4): 410-413.

Reis, S. T., M. J. Pascual, R. K. Brow, C. S. Ray and T. Zhang (2010). "Crystallization and processing of SOFC sealing glasses." Journal of Non-Crystalline Solids **356**: 3009-3012.

Rodríguez-López, S., J. Wei, K. C. Laurenti, I. Mathias, V. M. Justo, F. C. Serbena, C. Baudín, J. Malzbender and M. J. Pascual (2017). "Mechanical properties of solid oxide fuel cell glass-ceramic sealants in the system $\text{BaO/SrO—MgO—B}_2\text{O}_3\text{—SiO}_2$." Journal of the European Ceramic Society **37**(11): 3579-3594.

Rodríguez-Reyna, E., A. F. Fuentes, M. Maczka, J. Hanuza, K. Boulahya and U. Amador (2006). "Structural, microstructural and vibrational characterization of apatite-type lanthanum silicates prepared by mechanical milling." Journal of Solid State Chemistry **179**(2): 522-531.

Rouxel, T. (2006). "Elastic properties of glasses: a multiscale approach." Comptes Rendus Mécanique **334**(12): 743-753.

Rouxel, T. (2007). "Elastic properties and short-to medium-range order in glasses." Journal of the American Ceramic Society **90**(10): 3019-3039.

Rouxel, T. (2015). "Driving force for indentation cracking in glass: composition, pressure and temperature dependence." Philosophical Transactions of the Royal Society A: Mathematical, Physical and Engineering Sciences **373**(2038).

Rouxel, T. and H. Ji (2008). "Poisson's Ratio and the Densification of Glass under High Pressure." Physical Review Letters **100**(22).

Rouxel, T., P. Sellappan, F. Célarié, P. Houizot and J.-C. Sangleboeuf (2014). "Toward glasses with better indentation cracking resistance." Comptes Rendus Mécanique **342**(1): 46-51.

Salmon, P. S. (2002). "Order within disorder." Nature Materials **1**: 87.

Santha, N., S. Shamsudeen, N. T. Karunakaran and J. Isuhak Naseemabeevi (2011). "Spectroscopic, Dielectric and Optical Properties of 60ZnO–30B₂O₃–10SiO₂ Glass–Al₂O₃ Composites." International Journal of Applied Ceramic Technology **8**(5): 1042-1049.

Sasmal, N., M. Garai, A. R. Molla, A. Tarafder, S. P. Singh and B. Karmakar (2014). "Effects of lanthanum oxide on the properties of barium-free alkaline-earth borosilicate sealant glass." Journal of Non-Crystalline Solids **387**: 62-70.

Saunders, G. A., R. D. Metcalfe, M. Cutroni, M. Federico and A. Piccolo (1996). "Elastic and anelastic properties, vibrational anharmonicity, and fractal bond connectivity of superionic glasses." Physical Review B **53**(9): 5287-5300.

Schirmer, O. F., M. Imlau, C. Merschjann and B. Schöke (2009). "Electron small polarons and bipolarons in LiNbO₃." Journal of Physics: Condensed Matter **21**(12): 123201.

Schober, H. R. and B. B. Laird (1991). "Localized low-frequency vibrational-modes in glasses." Physical Review B **44**(13): 6746-6754.

Schulze, M. and E. Gülzow (2004). "Degradation of nickel anodes in alkaline fuel cells." Journal of Power Sources **127**(1–2): 252-263.

Schwickert, T., R. Sievering, P. Geasee and R. Conradt (2002). "Glass-ceramic materials as sealants for SOFC applications." Materialwissenschaft Und Werkstofftechnik **33**: 363-366.

Sehgal, J. and S. Ito (1999). "Brittleness of glass." Journal of Non-Crystalline Solids **253**(1–3): 126-132.

Sellappan, P., T. Rouxel, F. Celarie, E. Becker, P. Houzot and R. Conradt (2013). "Composition dependence of indentation deformation and indentation cracking in glass." Acta Materialia **61**(16): 5949-5965.

Shelby, J. E. (2005). Introduction to glass science and technology. Cambridge, Cambridge : Royal Society of Chemistry, c2005.

Shvanskii, E. V., N. I. Leonyuk, G. Bocelli and L. Righi (2000). "Crystallization and structural characteristics of new borosilicates." Journal of Solid State Chemistry **154**(1): 312-316.

Simner, S. P. and J. W. Stevenson (2001). "Compressive mica seals for SOFC applications." Journal of Power Sources **102**: 310-316.

Singh, R. N. (2007). "Sealing technology for solid oxide fuel cells (SOFC)." International Journal of Applied Ceramic Technology **4**: 134-144.

Singh, R. N. (2012). "Self-repairable glass seals for solid oxide fuel cells." Journal of Materials Research **27**: 2055-2061.

Singhal, S. C. (2000). "Advances in solid oxide fuel cell technology." Solid State Ionics **135**(1-4): 305-313.

Singhal, S. C. (2002). "Solid oxide fuel cells for stationary, mobile, and military applications." Solid State Ionics **152–153**: 405-410.

Smeacetto, F., M. Salvo, M. Ferraris, J. Cho and A. R. Boccaccini (2008). "Glass–ceramic seal to join Crofer 22 APU alloy to YSZ ceramic in planar SOFCs." Journal of the European Ceramic Society **28**(1): 61-68.

Smedskjaer, M. M., M. Jensen and Y. Yue (2010). "Effect of thermal history and chemical composition on hardness of silicate glasses." Journal of Non-Crystalline Solids **356**(18–19): 893-897.

Smedskjaer, M. M., R. E. Youngman and J. C. Mauro (2013). "Impact of ZnO on the structure and properties of sodium aluminosilicate glasses: Comparison with alkaline earth oxides." Journal of Non-Crystalline Solids **381**: 58-64.

Smiljanic, S. V., Grujic, Sr., M. B. Tosic, V. D. Zivanovic, S. D. Matijasevic, J. D. Nikolic and V. Topalovic (2016). "Effect of La₂O₃ on the structure and the properties of strontium borate glasses " Chem. Ind. Chem. Eng. Q. **22**(1): 111-115.

Sohn, S. B., S. Y. Choi, G. H. Kim, H. S. Song and G. D. Kim (2002). "Stable sealing glass for planar solid oxide fuel cell." Journal of Non-Crystalline Solids **297**: 103-112.

Sohn, S. B., S. Y. Choi, G. H. Kim, H. S. Song and G. D. Kim (2004). "Suitable glass-ceramic sealant for planar solid-oxide fuel cells." Journal of the American Ceramic Society **87**: 254-260.

Souquet, J. L., M. Lévy and M. Duclot (1994). "A single microscopic approach for ionic transport in glassy and polymer electrolytes." Solid State Ionics **70**: 337-345.

Środa, M. and C. Paluszkiwicz (2007). "Spectroscopic study of the influence of LaF₃ admixture on the crystallization and structure of borosilicate glass." Journal of Molecular Structure **834–836(0)**: 302-307.

Środa, M. and C. Paluszkiwicz (2008). "The structural role of alkaline earth ions in oxyfluoride aluminosilicate glasses—Infrared spectroscopy study." Vibrational Spectroscopy **48(2)**: 246-250.

Staff, M. T., J. A. Fernie, P. M. Mallinson, M. J. Whiting and J. A. Yeomans (2016). "Fabrication of a Glass-Ceramic-to-Metal Seal Between Ti–6Al–4V and a Strontium Boroaluminate Glass." International Journal of Applied Ceramic Technology **13(5)**: 956-965.

Stambouli, A. B. and E. Traversa (2002). "Solid oxide fuel cells (SOFCs): A review of an environmentally clean and efficient source of energy." Renewable and Sustainable Energy Reviews **6(5)**: 433-455.

Sun, C. and U. Stimming (2007). "Recent anode advances in solid oxide fuel cells." Journal of Power Sources **171(2)**: 247-260.

Sun, K. H. (1947). "FUNDAMENTAL CONDITION OF GLASS FORMATION." Journal of the American Ceramic Society **30(9)**: 277-281.

Sun, T., H. Xiao, W. Guo and X. Hong (2010). "Effect of Al₂O₃ content on BaO–Al₂O₃–B₂O₃–SiO₂ glass sealant for solid oxide fuel cell." Ceramics International **36(2)**: 821-826.

Tiegel, M., R. Hosseinabadi, S. Kuhn, A. Herrmann and C. Rüssel (2015). "Young's modulus, Vickers hardness and indentation fracture toughness of aluminosilicate glasses." Ceramics International **41(6)**: 7267-7275.

Timurkutluk, B., C. Timurkutluk, M. D. Mat and Y. Kaplan (2016). "A review on cell/stack designs for high performance solid oxide fuel cells." Renewable and Sustainable Energy Reviews **56**: 1101-1121.

Tiwari, B., A. Dixit and G. P. Kothiyal (2011). "Study of glasses/glass-ceramics in the SrO–ZnO–SiO₂ system as high temperature sealant for SOFC applications." International Journal of Hydrogen Energy **36(22)**: 15002-15008.

Trégouët, H., D. Caurant, O. Majérus, T. Charpentier, T. Lerouge and L. Cormier (2017). "Exploration of glass domain in the SiO₂-B₂O₃-La₂O₃ system." Journal of Non-Crystalline Solids.

Trejo, R., E. Lara-Curzio, A. Shyam, M. J. Kirkham, V. Garcia-Negron and Y. Wang (2012). "Physical and Mechanical Properties of Barium Alkali Silicate Glasses for SOFC Sealing Applications." International Journal of Applied Glass Science **3**: 369-379.

Tulyaganov, D. U., A. A. Reddy, V. V. Kharton and J. M. F. Ferreira (2013). "Aluminosilicate-based sealants for SOFCs and other electrochemical applications - A brief review." Journal of Power Sources **242**: 486-502.

Uhlmann, D. R. (1972). "A kinetic treatment of glass formation." Journal of Non-Crystalline Solids **7(4)**: 337-348.

Varshneya, A. K. (2006). Fundamentals of inorganic glasses. Sheffield, Sheffield : Society of Glass Technology, 2006.

Vullo, P. and M. J. Davis (2004). "Comparative study of micro-indentation and Chevron notch fracture toughness measurements of silicate and phosphate glasses." Journal of Non-Crystalline Solids **349**: 180-184.

Wang, P. F., Z. H. Li, J. Li and Y. M. Zhu (2009). "Effect of ZnO on the interfacial bonding between Na₂O-B₂O₃-SiO₂ vitrified bond and diamond." Solid State Sciences **11(8)**: 1427-1432.

Wang, R., Z. Lu, C. Liu, R. Zhu, X. Huang, B. Wei, N. Ai and W. Su (2007). "Characteristics of a SiO₂-B₂O₃-Al₂O₃-BaCO₃-PbO₂-ZnO glass-ceramic sealant for SOFCs." Journal of Alloys and Compounds **432**: 189-193.

Wang, S.-F., Y.-F. Hsu, H.-C. Lu, S.-C. Lo and C.-S. Cheng (2012). "B₂O₃-free SiO₂-Al₂O₃-SrO-La₂O₃-ZnO-TiO₂ glass sealants for intermediate temperature solid oxide fuel cell applications." International Journal of Hydrogen Energy **37**(7): 5901-5913.

Wang, S.-F., Y.-R. Wang, Y.-F. Hsu and C.-C. Chuang (2009). "Effect of additives on the thermal properties and sealing characteristic of BaO-Al₂O₃-B₂O₃-SiO₂ glass-ceramic for solid oxide fuel cell application." International Journal of Hydrogen Energy **34**(19): 8235-8244.

Wang, X., D. R. Ou, Z. Zhao and M. Cheng (2016). "Stability of SrO-La₂O₃-Al₂O₃-SiO₂ glass sealants in high-temperature air and steam." Ceramics International **42**(6): 7514-7523.

Wang, Y., K. S. Chen, J. Mishler, S. C. Cho and X. C. Adroher (2011). "A review of polymer electrolyte membrane fuel cells: Technology, applications, and needs on fundamental research." Applied Energy **88**(4): 981-1007.

Wang, Z., Y. Hu, H. Lu and F. Yu (2008). "Dielectric properties and crystalline characteristics of borosilicate glasses." Journal of Non-Crystalline Solids **354**(12-13): 1128-1132.

Warren, B. E. (1934). "X-RAY DETERMINATION OF THE STRUCTURE OF GLASS*." Journal of the American Ceramic Society **17**(1-12): 249-254.

Weil, K. S. (2006). "The state-of-the-art in sealing technology for solid oxide fuel cells." Jom **58**(8): 37-44.

Woldemar Anatol, W. (1964). The constitution of glasses : a dynamic interpretation. New York, New York : Interscience, 1964.

Wu, J. and J. F. Stebbins (2009). "Effects of cation field strength on the structure of aluminoborosilicate glasses: High-resolution ¹¹B, ²⁷Al and ²³Na MAS NMR." Journal of Non-Crystalline Solids **355**(9): 556-562.

Xiang, Y., J. Du, M. M. Smedskjaer and J. C. Mauro (2013). "Structure and properties of sodium aluminosilicate glasses from molecular dynamics simulations." The Journal of Chemical Physics **139**(4).

Yadav, A. K. and P. Singh (2015). "A review of the structures of oxide glasses by Raman spectroscopy." Rsc Advances **5**(83): 67583-67609.

Yamane, M. and J. D. Mackenzie (1974). "Vicker's Hardness of glass." Journal of Non-Crystalline Solids **15**(2): 153-164.

Yang, Z., G. Xia, K. D. Meinhardt, K. S. Weil and J. W. Stevenson (2013). "Chemical Stability of Glass Seal Interfaces in Intermediate Temperature Solid Oxide Fuel Cells." Journal of Materials Engineering and Performance **22**: 2892-2899.

Yang, Z. G., J. W. Stevenson and K. D. Meinhardt (2003). "Chemical interactions of barium-calcium-aluminosilicate-based sealing glasses with oxidation resistant alloys." Solid State Ionics **160**: 213-225.

Ye, Y., D. Yan, X. Wang, J. Pu, B. Chi and L. Jian (2012). "Development of novel glass-based composite seals for planar intermediate temperature solid oxide fuel cells." International Journal of Hydrogen Energy **37**(2): 1710-1716.

Yeager, E. (1961). "Fuel Cells." Science **134**(3486): 1178-1186.

Yoshida, S., H. Tanaka, T. Hayashi, J. Matsuoka and N. Soga (2001). "Scratch Resistance of Sodium Borosilicate Glass." Journal of the Ceramic Society of Japan **109**(1270): 511-515.

Yue, Y. L., X. J. Yu, H. T. Wu and X. J. Chen (2009). "Dielectric properties of quaternary calcium aluminoborosilicate system glasses." Materials Research Innovations **13**(2): 129-132.

Zhang, Q., H. Yang, F. Zeng, S. Wang, D. Tang and T. Zhang (2015). "Development of the CaO-SrO-ZrO₂-B₂O₃-SiO₂ sealing glasses for solid oxide fuel cell applications: structure-property correlation." Rsc Advances **5**(52): 41772-41779.

Zhang, T., W. G. Fahrenholtz, S. T. Reis and R. K. Brow (2008). "Borate volatility from SOFC sealing glasses." Journal of the American Ceramic Society **91**: 2564-2569.

Zhang, T. and Q. Zou (2012). "Tuning the thermal properties of borosilicate glass ceramic seals for solid oxide fuel cells." Journal of the European Ceramic Society **32**: 4009-4013.

Zhang, W., D. Yan, J. Duan, J. Pu, B. Chi and J. Li (2013). "Development of Al₂O₃/glass-based multi-layer composite seals for planar intermediate-temperature solid oxide fuel cells." International Journal of Hydrogen Energy **38**(35): 15371-15378.

Zhang, X. H., Y. L. Yue and H. T. Wu (2013). "Effects of cation field strength on structure and properties of boroaluminosilicate glasses." Materials Research Innovations **17**(3): 212-217.

Zhao, P., S. Kroeker and J. F. Stebbins (2000). "Non-bridging oxygen sites in barium borosilicate glasses: results from ¹¹B and ¹⁷O NMR." Journal of Non-Crystalline Solids **276**(1–3): 122-131.

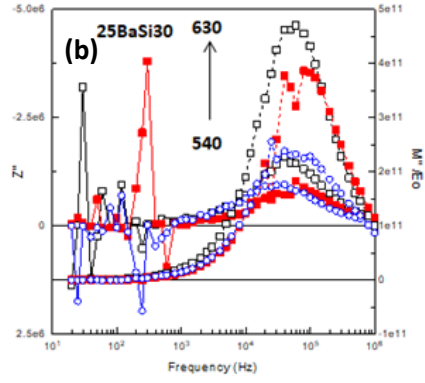
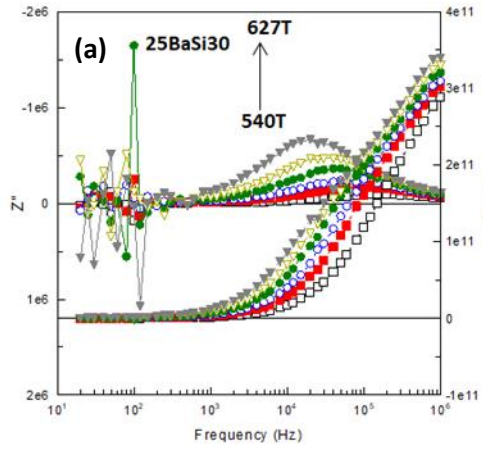
Zhao, Y. and J. Malzbender (2013). "Elevated temperature effects on the mechanical properties of solid oxide fuel cell sealing materials." Journal of Power Sources **239**(0): 500-504.

Zhao, Y., J. Malzbender and S. M. Gross (2011). "The effect of room temperature and high temperature exposure on the elastic modulus, hardness and fracture toughness of glass ceramic sealants for solid oxide fuel cells." Journal of the European Ceramic Society **31**(4): 541-548.

Zhu, W. Z. and S. C. Deevi (2003). "A review on the status of anode materials for solid oxide fuel cells." Materials Science and Engineering: A **362**(1–2): 228-239.

Appendix 1

Evidence from impedance measurement supporting increase in electrical conductivity of the grains more than residual glass (grain boundaries)



Appendix 2

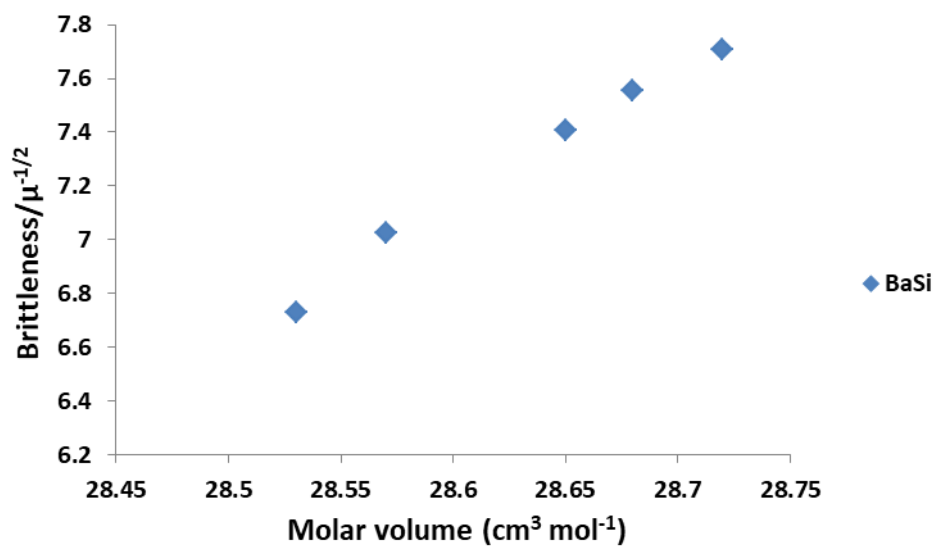
TEC comparison between TEC of this study and SOFCs requirement

samples mol%	TEC glass/ ^o C		TEC glass ceramic/ ^o C				SOFCs TEC requirements and Refs
	RT-300	300-600	RT-600	RT-300	300-600	RT-600	
10BZn15	6.6	8.8	7.9	6.8	7.5	7.2	(Mahapatra and Lu 2010), (Wang, Ou et al. 2016), (Fergus 2005, Ghosh, Sharma et al. 2008), (Ley, Krumpelt et al. 1996, Lessing 2007). (Tulyaganov, Reddy et al. 2013). (Kerstan and Rüssel 2011), (Gödeke and Dahlmann 2011), (Chou, Stevenson et al. 2007)
12.5BZn12.5	6.6	8.3	7.6	6.5	8.5	7.6	
15x BZn10	6.5	8.2	7.5	6.2	7.5	6.9	
17.5BZn7.7	6.6	7.9	7.4	5.6	7.2	6.5	
20BZn5	6.5	8.3	7.5	6.2	7.2	6.7	
40SiZn20	7.1	9.2	8.5	6.9	8.4	7.3	
42.5SiZn17.5	7.2	9.1	8.3	7	8.2	7.0	
45SiZn15	7.8	8.8	8.0	7.5	7.5	6.7	
47.5SiZn12.5	6.6	9	7.5	6.3	8.2	6.9	
15BaSi40	6.8	8.9	8.0	6.6	8.9	7.6	
17.5BaSi37.5	7.3	8.7	8.1	6.8	8.8	7.7	
20BaSi35	7.2	9.8	8.6	7.2	9.8	8.6	
22.5BaSi32.5	8.0	10.4	9.7	7.6	11.5	9.7	
25BaSi30	9.2	10.8	10.5	8.9	11.2	9.7	
10BaAl10	6.9	10.3	8.8	No			
12BaAl8	7.8	14.4	11.5	glass ceramic			
13BaAl7	7.2	12.2	9.6				
14BaAl6	7.5	11.4	9.7				
15BaAl5	8.2	13.4	10.3				
35Si15La (Sr)	7.0	9.1	8.3				
40Si10La (Sr)	6.1	8.6	7.9				

45Si5La (Sr)	5.8	7.1	7.5
--------------	-----	-----	-----

Appendix 3

Linear correlation between brittleness versus molar volume



Appendix 4

Area% of Qⁿ species obtained from deconvolution of Raman spectra of the silicate units for all series

glass code	Q0	Q1	Q2	Q3
10BZn15	18	21.9	42.2	17.8
12.5BZn12.5	15.9	21.8	44.7	17.6
15BZn10	13	22.5	45.8	18.7
17.5BZn7.5	12.6	21	48.6	17.8
20BZn5	5.4	35.3	46.2	13.2
40SiZn20	24.4	28.2	36.3	11.4
42.5SiZn17.5	20.4	23.4	41.1	15
45SiZn15	18	21.9	42.2	17.8
47.5SiZn12.5	16.4	21.4	44.2	18.1
15BaSi40	12.4	22.3	44	21.3
17.5BaSi37.5	13.9	24	43.2	18.9
20BaSi35	16.4	27	43.1	13.5
22.5BaSi32.5	17.3	28.9	39.7	14
25BaSi30	18.9	29.9	39.1	12.1
10BaAl10	9.9	15.5	48.1	26.4
12BaAl8	6.7	19	49.7	24.7
13BaAl7	9.1	19.7	46.8	24.4
14BaAl6	9	20.8	46.1	24
15BaAl5	8.6	18.9	44.1	28.4
40Si20La(Ba)	CRYST			
45Si15La(Ba)	22	21.3	43	14.2
50Si10La(Ba)	12.1	18.5	47.9	21.5
55Si5La(Ba)	11.2	18.5	47.4	22.9
30Si20La(Sr)	cryst			
35Si15La(Sr)	19.8	26	41.4	12.8
40Si10La(Sr)	11.7	21.6	48.2	18.5

45Si5La(Sr)	10.6	17.8	50.5	21.1
-------------	------	------	------	------

Appendix 5

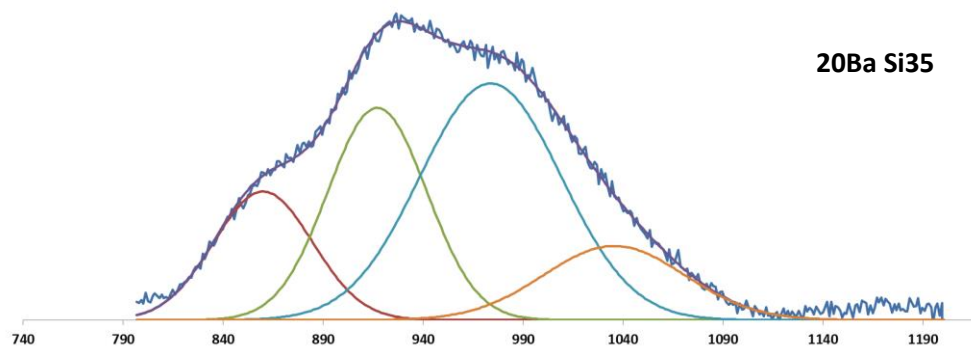
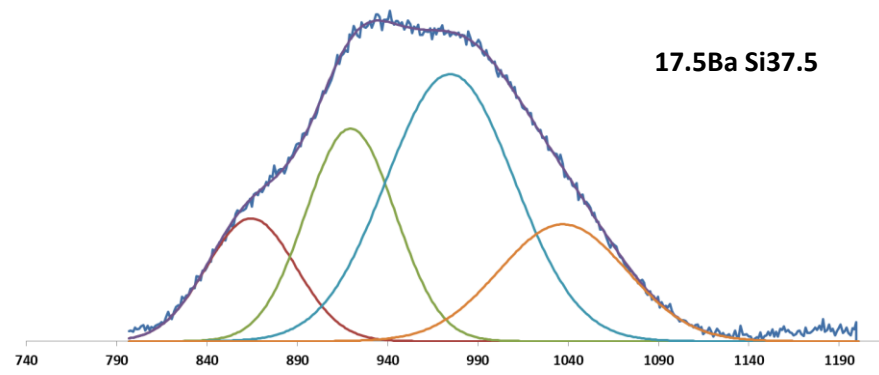
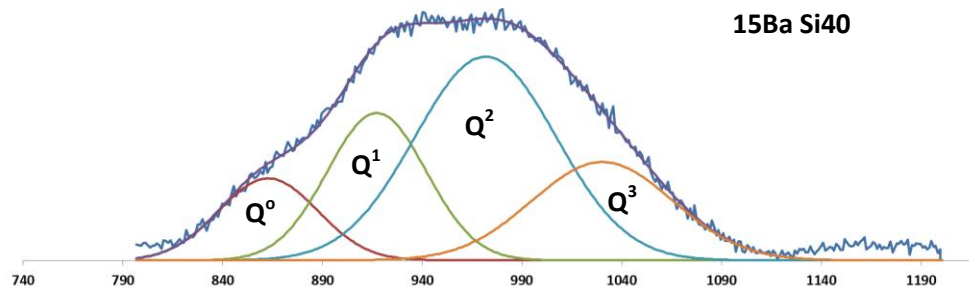
Area% of $^{[3]}\text{B}^{3+}$ and $^{[4]}\text{B}^{3+}$ obtained from the deconvolution of Raman spectra using Manara method where N_4 is BO_4 and $\text{N}_3(1)$ and $\text{N}_3(2)$ are loose BO_3 and BO_3 respectively

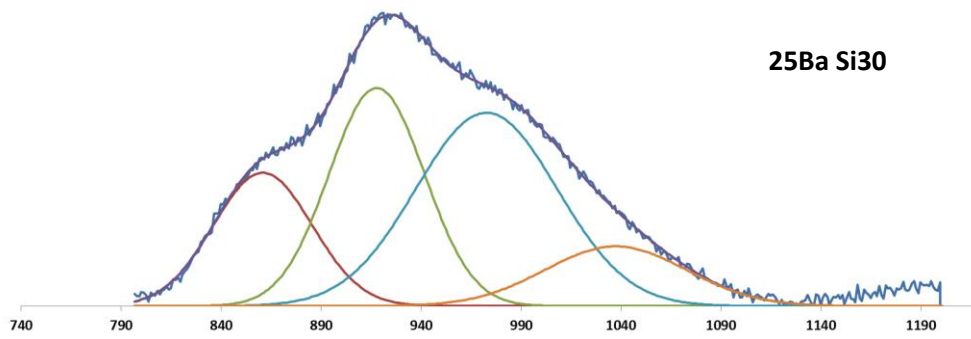
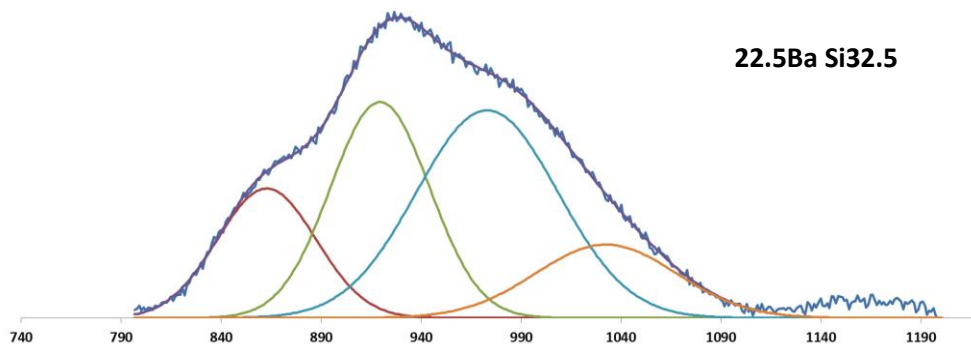
glass code	$\text{N}_3(1)$	N_4	$\text{N}_3(2)$
10BZn15	34.7	42.3	23
12.5BZn12.5	27.6	45.1	27.3
15BZn10	31.1	50.3	18.5
17.5BZn7.5	31	51.5	17.5
20BZn5	25	51	24
40SiZn20	19.6	42.6	37.7
42.5SiZn17.5	27.9	43.8	28.3
45SiZn15	32.4	49.2	18.5
47.5SiZn12.5	32.9	50.1	16.9
15BaSi40	28.7	49.7	21.6
17.5BaSi37.5	34.3	52	13.7
20BaSi35	27	50.2	21.2
22.5BaSi32.5	31.1	55	13.9
25BaSi30	25.5	60.2	14.2
10BaAl10	28.7	49.7	21.6
12BaAl8	23.5	51.7	24.8
13BaAl7	8.1	52.8	39
14BaAl6	34.3	53.9	11.8
15BaAl5	31.2	58.3	10.5
40Si20La(Ba)			
45Si15La(Ba)	39	52.2	9
50Si10La(Ba)	3	68.7	28.3
55Si5La(Ba)	8.5	82.3	9.2
30Si20La(Sr)			

35Si15La(Sr)	41	41	19
40Si10La(Sr)	36.3	56.2	7.6
45Si5La(Sr)	27	55	18

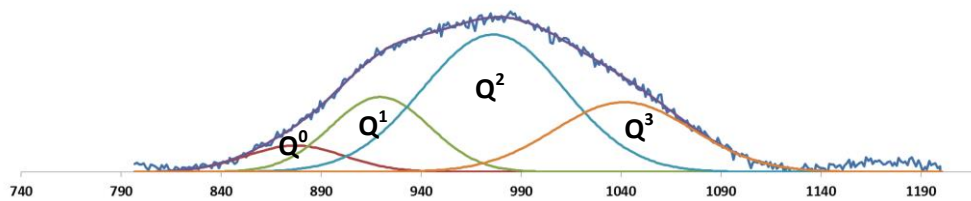
Appendix 6

Deconvoluted Raman spectra for the silicate units of all series

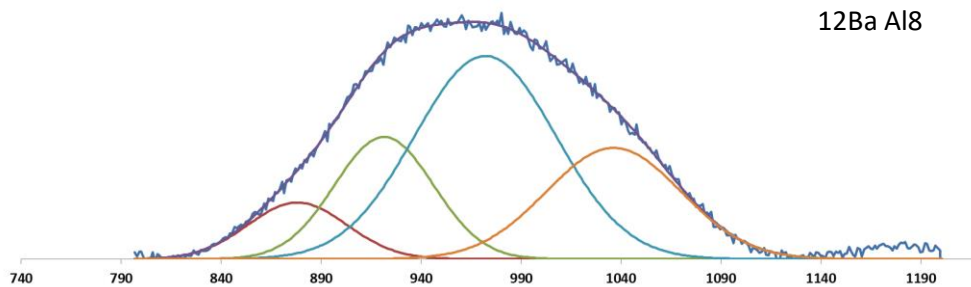




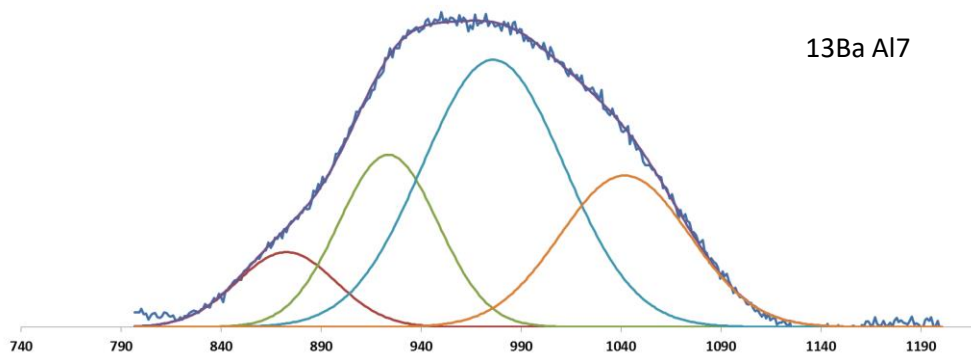
10Ba Al10



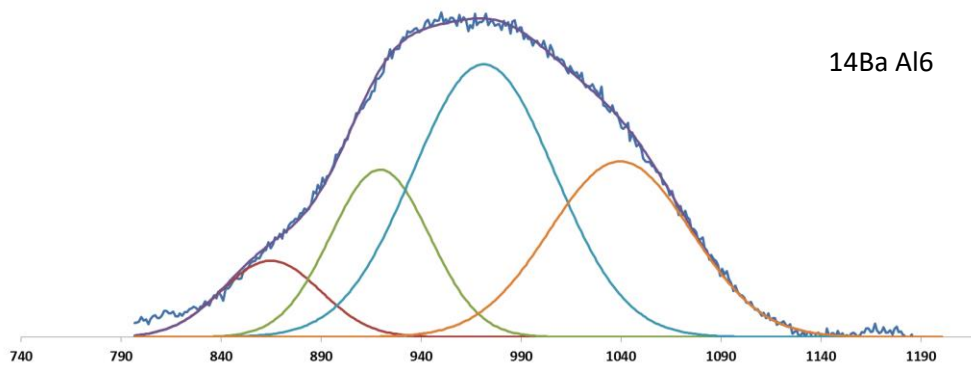
12Ba Al8

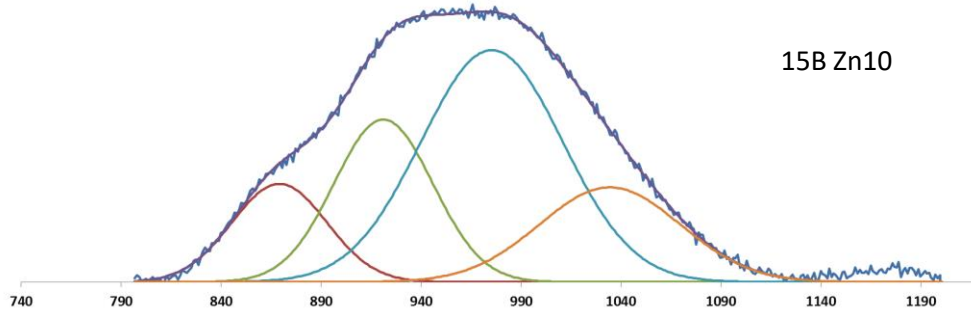
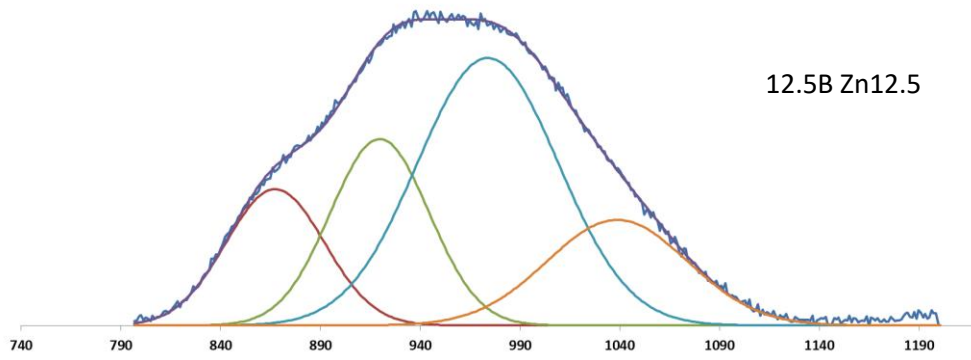
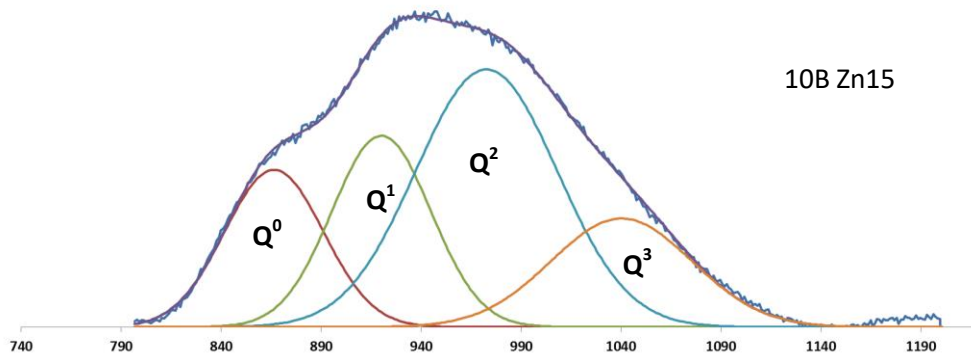


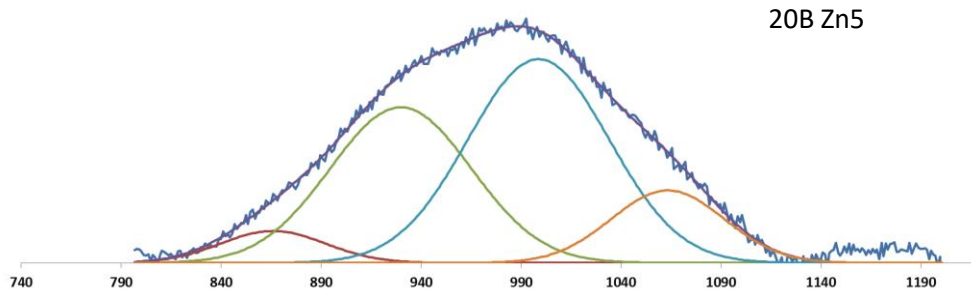
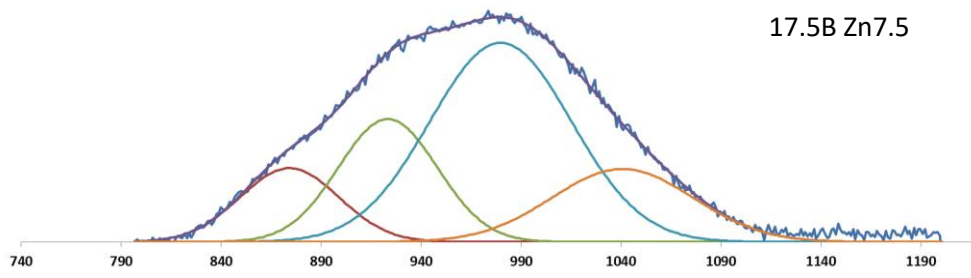
13Ba Al7



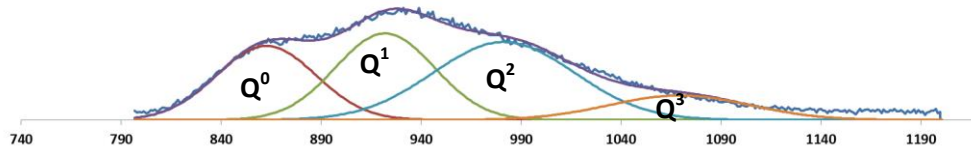
14Ba Al6



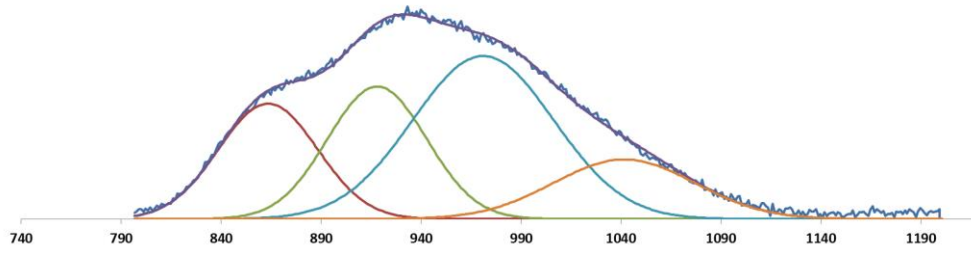




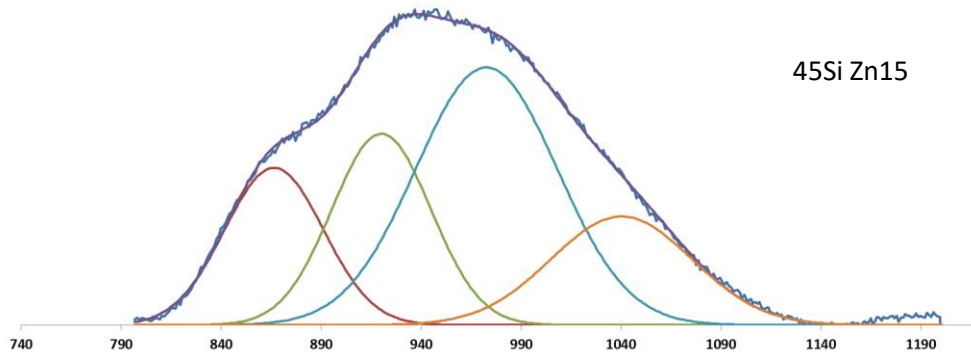
40Si Zn20



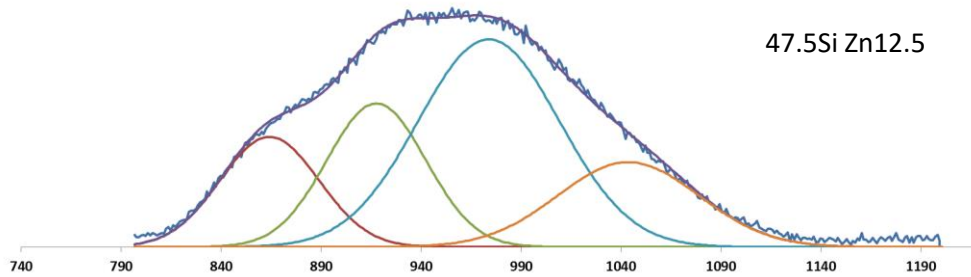
42.5Si Zn17.5

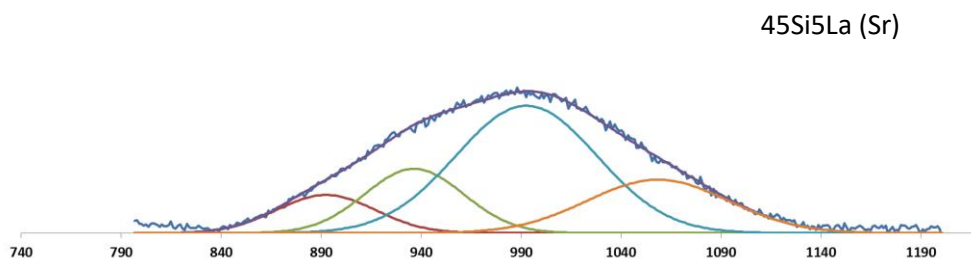
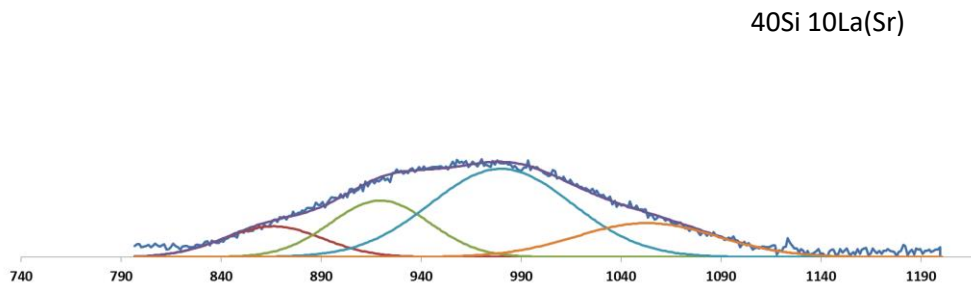
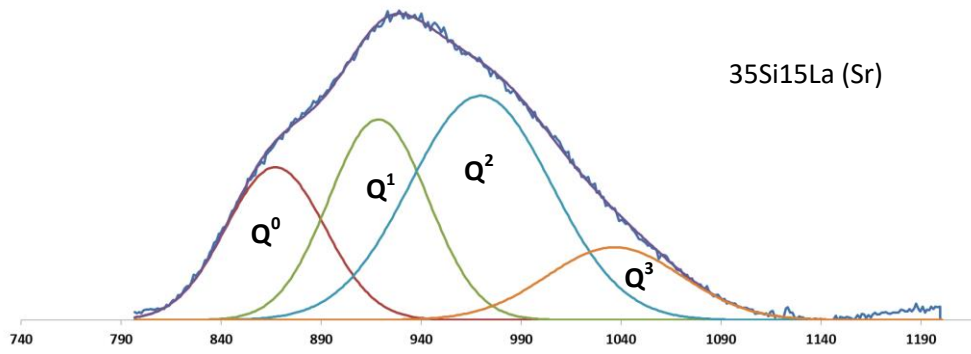


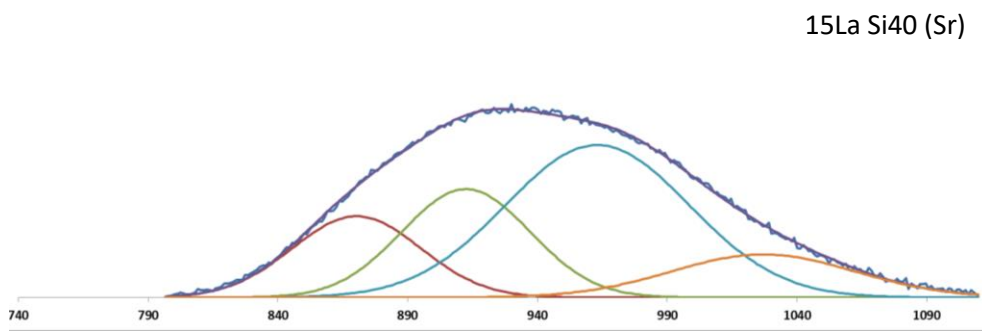
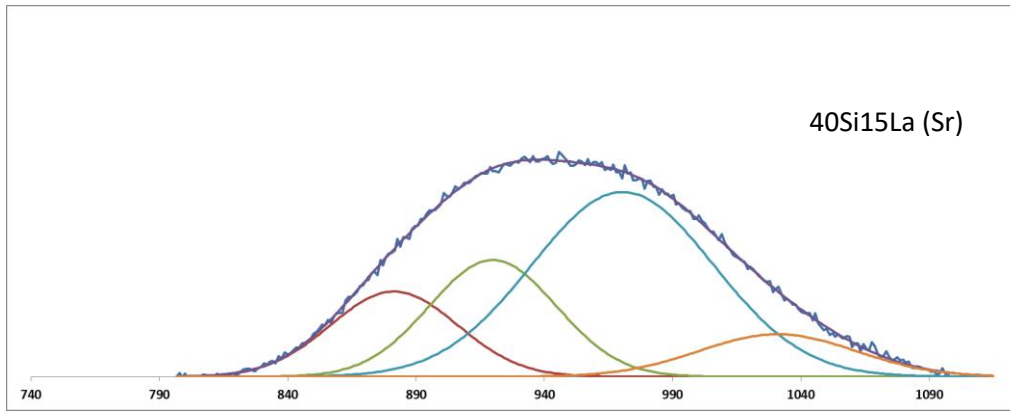
45Si Zn15



47.5Si Zn12.5

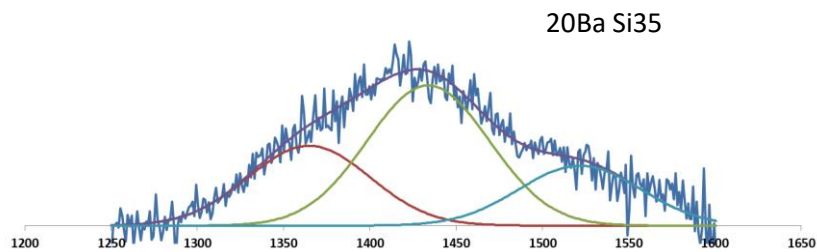
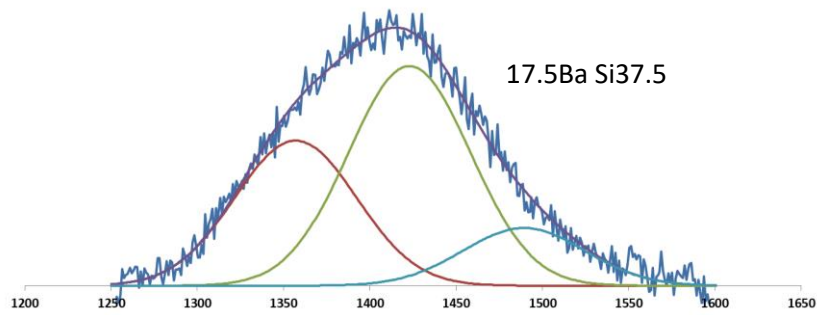
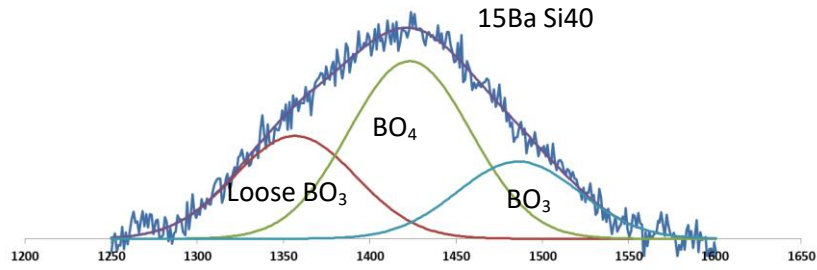


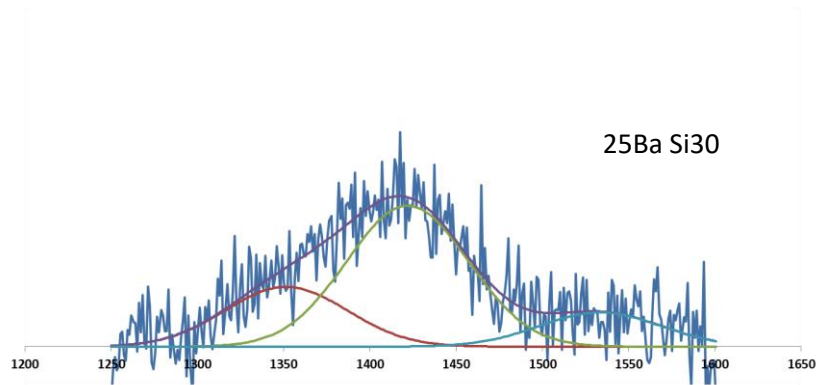
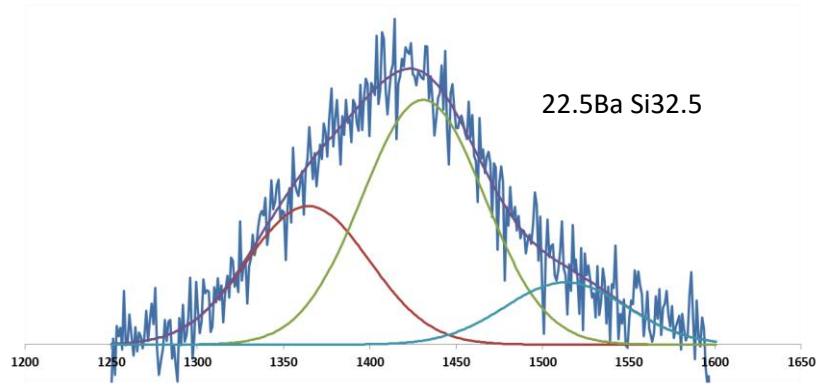


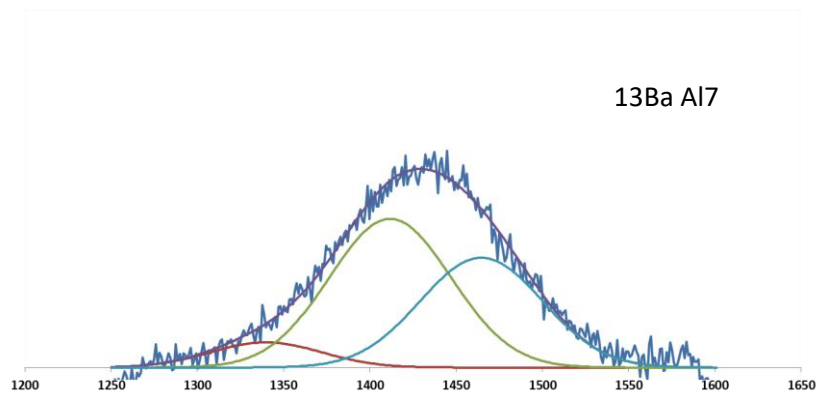
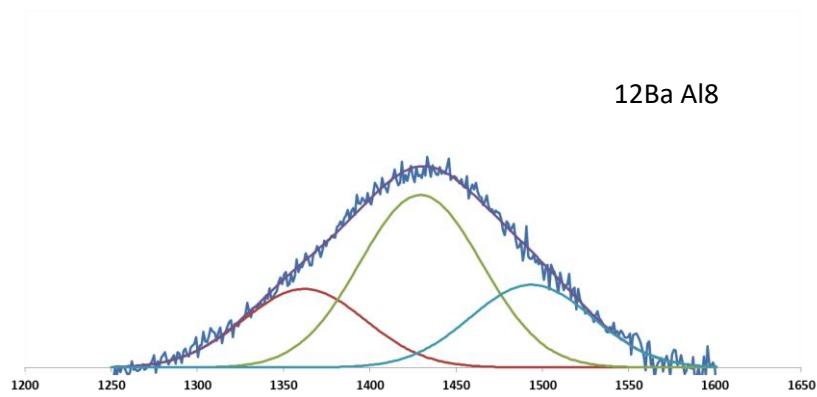
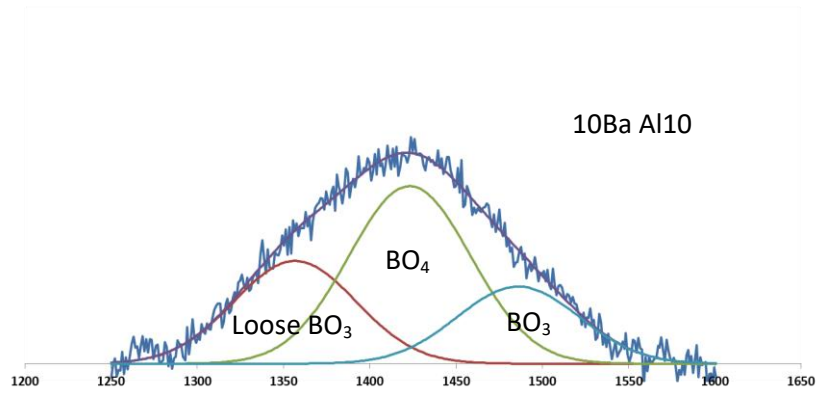


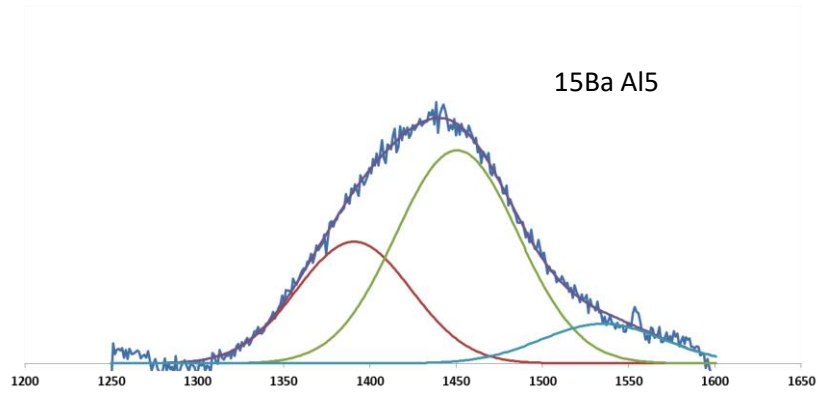
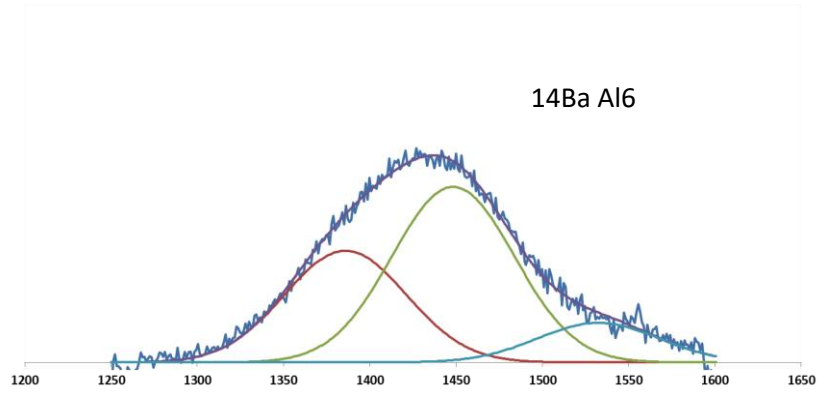
Appendix 7

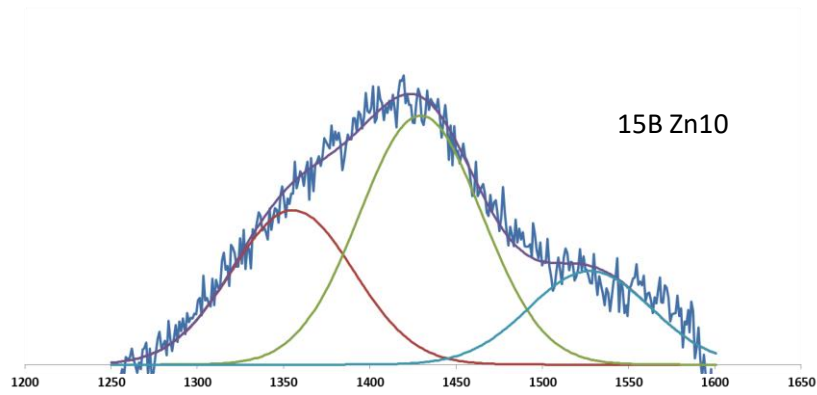
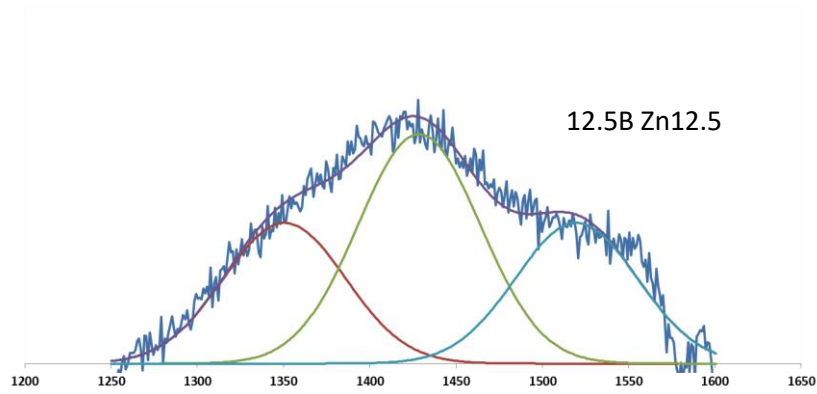
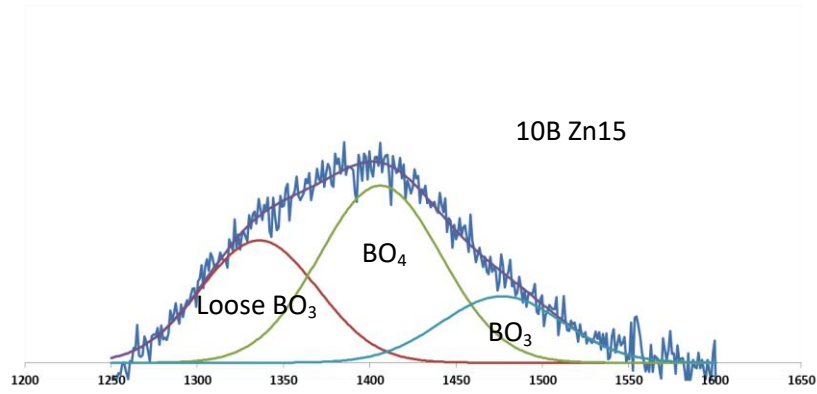
Raman spectra of Borate units for all series

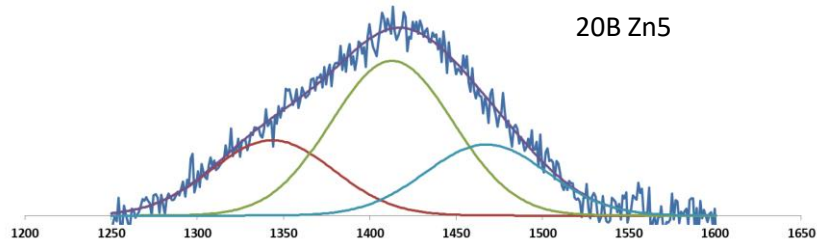
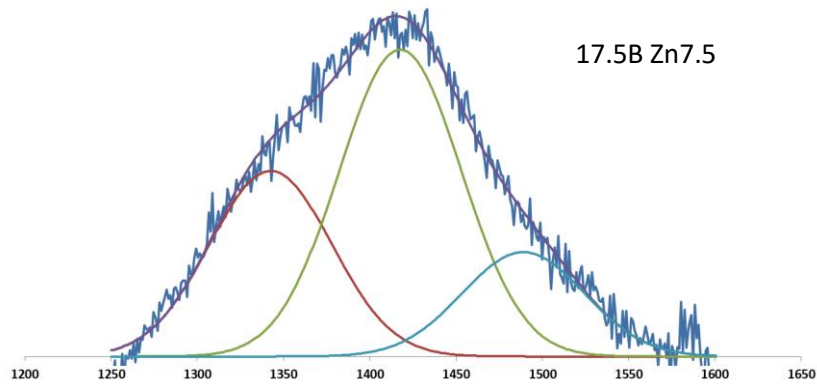


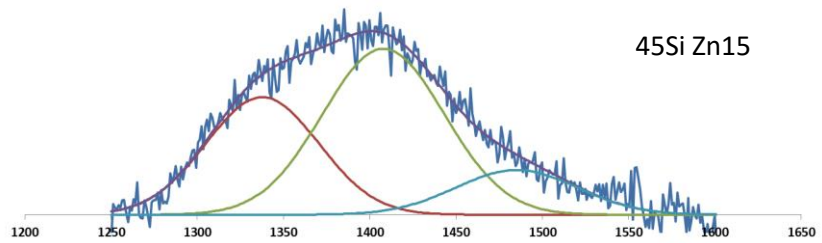
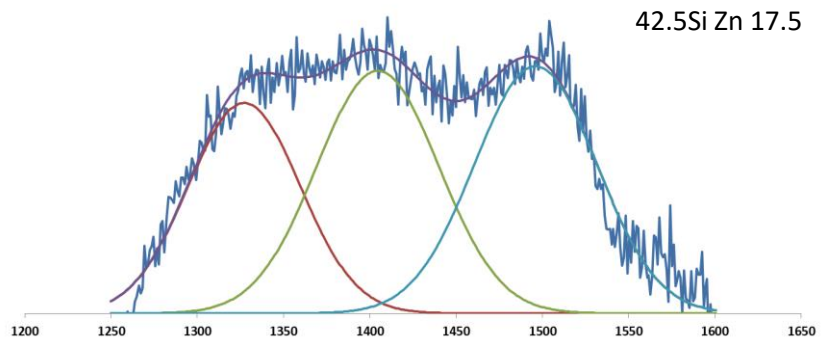
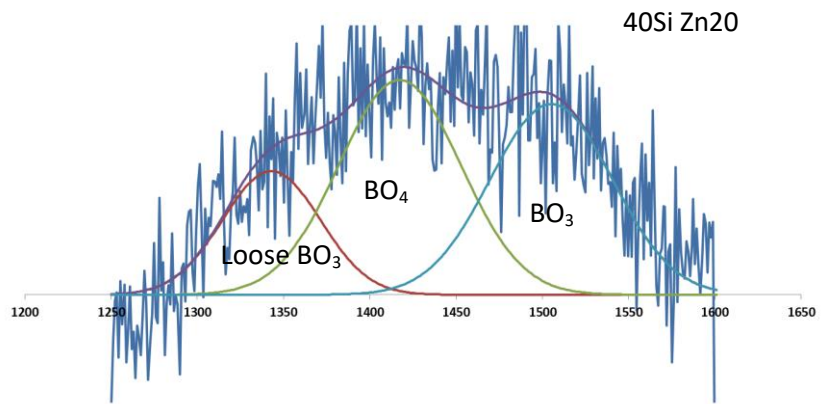




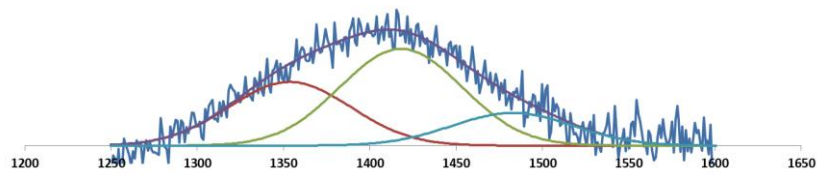




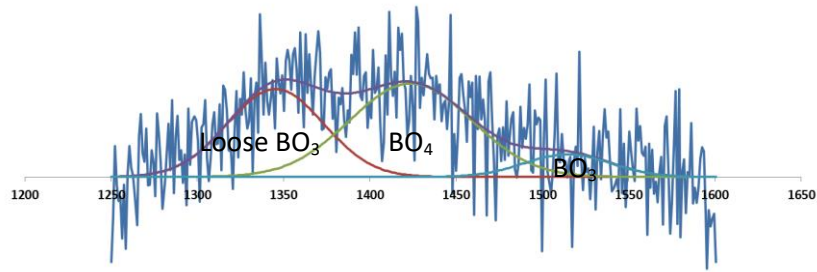




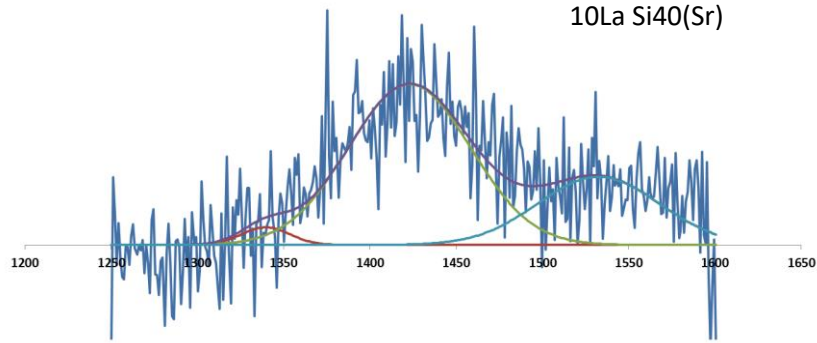
47.5Si Zn12.5



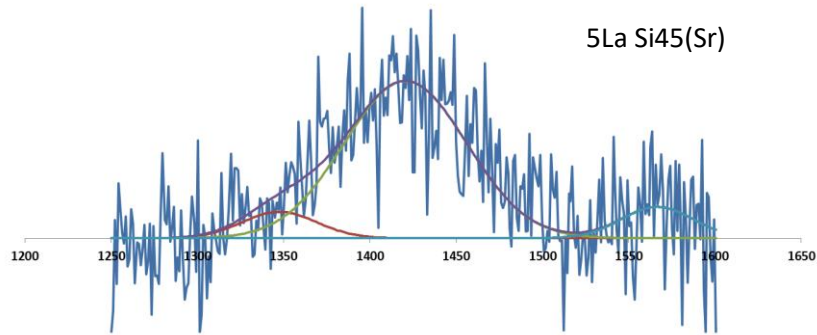
15La Si35(Sr)



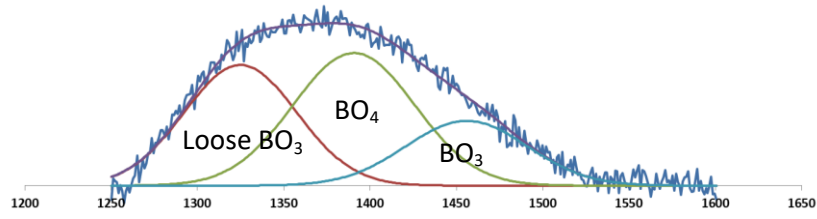
10La Si40(Sr)



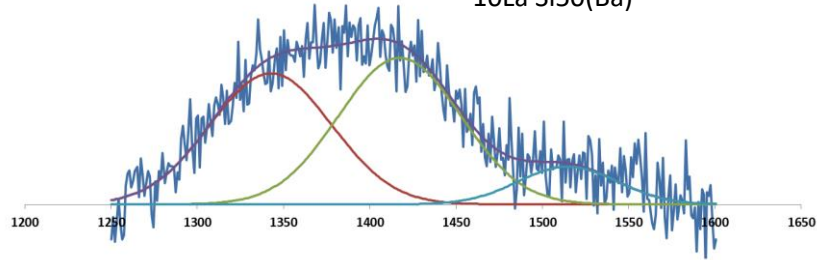
5La Si45(Sr)



15La Si45(Ba)



10La Si50(Ba)



5La Si55(Ba)

